

Université de Liège
Faculté des Sciences

**Modelling climate
and vegetation interactions**

Application to the study of
paleoclimates and paleovegetations

Dissertation présentée par
Alexandra-Jane Henrot
en vue de l'obtention du grade de
Docteur en Sciences

2010

Remerciements

Mes premiers remerciements vont à mon promoteur Guy Munhoven, qui m'a supervisé tout au long de ces années depuis mon travail de fin d'étude en Sciences Physiques, et sans qui cette thèse n'aurait pu ni commencer ni aboutir. Merci Guy pour tes conseils avisés, ton aide, ta disponibilité, ton incroyable connaissance en logiciels informatiques et langages de programmation de toutes sortes, sans oublier ton sixième sens pour repérer innombrables fautes de frappe et d'orthographe qui peuplent mes travaux. Je tiens également à remercier mon co-promoteur Louis François de m'avoir initié à l'étude des climats du passé et du fonctionnement de la végétation, d'avoir supervisé mes recherches et orienté la réalisation de ce travail. Sans ses très nombreuses idées et remarques pertinentes, mais aussi sans sa mémoire à toute épreuve, vous ne liriez pas ce travail aujourd'hui.

J'aimerais également remercier mes collègues proches ou plus lointains collaborateurs, chercheurs et doctorants qui m'ont fourni des résultats, des données, des références, ou des idées qui m'ont permis d'avancer dans mon travail. Je remercie tout d'abord mes proches collègues de l'UMCCB (dont je ne fais pas partie rappelons-le!) : Marie, Pierre, Eric, Mohamed, Jeanne-Marine et Simon (mais où es-tu maintenant?). Je vous remercie pour l'aide que vous m'avez apportée, les discussions constructives que nous avons pu avoir, mais aussi pour les discussions plus terre-à-terre dirons-nous et la bonne entente au sein du groupe. Mes remerciements vont également au professeur Volker Mosbrugger, dont la lettre de motivation m'a permis entre autre d'obtenir ce poste d'aspirant FNRS. Par conséquent merci au FNRS et à ses nombreux donateurs, ainsi qu'à l'Université de Liège pour m'avoir permis de réaliser mon doctorat dans de bonnes conditions! Merci au docteur Arne Micheels, qui m'a accueilli dans son laboratoire au tout début de ma thèse et avec qui j'ai continué d'échanger résultats et données tout au long de ces années. Merci à l'équipe de développement du modèle Planet Simulator, et plus particulièrement à Franck Lunkeit et Kerstin Haberkorn pour la résolution de problèmes techniques. Merci au groupe NECLIME, et partic-

ulièrement à Torsten Utescher, pour toutes les données qu'ils ont fournies et les contacts noués. Merci au plus récent groupe UCCC et particulièrement au docteur Martin Butzin pour avoir collaboré à la dernière partie de ce travail. Enfin, merci aux membres de mon comité de thèse, Michel Crucifix et Nathalie Fagel, pour m'avoir écouté, suivi, soutenu et conseillé lors des réunions annuelles du comité.

De près ou de loin, il y a beaucoup d'autres personnes que j'aimerais encore remercier. Elles n'étaient peut-être pas directement impliquées dans ce travail mais je leur suis redevable pour une grande part de ce dernier. Je tiens à manifester toute ma reconnaissance vis-à-vis des collègues du Laboratoire de Physique Atmosphérique et Planétaire et du professeur Jean-Claude Gérard pour m'avoir accueilli dans son service. Merci pour les midis, quatre-heures, anniversaires, tartes et cie, bref tous les bons moments passés à manger ensemble! Un tout grand merci à notre secrétaire Angela et à Nadine aussi.

Enfin, je tiens tout particulièrement à remercier ma famille pour tout ce qu'elle représente à mes yeux. Merci Maman, Momo, Bernard, Papa, Charles et Armand, Anne, Baba, Yasemin, Esma, Tahsin Hoca et bien sur mon mari chéri Yasin pour m'avoir soutenu et supporté pendant ces longues périodes de stress et de travail. Merci aussi à mes élèves de danse qui m'ont permis de m'évader un peu avec elles chaque samedi matin. Enfin, merci de loin aux mélodies de Laurent Voulzy qui m'ont bien aidé à garder le coeur CARAIB au cours des dernières semaines de rédaction!

Summary

In this study, climate and vegetation interactions are examined for several periods of the geological past with (1) a dynamic global vegetation model CARAIB, and (2) an Earth system model of intermediate complexity Planet Simulator. Both models interact through an equilibrium asynchronous coupling procedure, which consists of a series of iterations of climate and vegetation equilibrium simulations. The climate and vegetation models, as well as the coupling technique developed here and some basic results are first presented. The models are then applied to study three periods that have experienced large scale climate and vegetation changes: the Last Glacial Maximum, the Middle Pliocene and the Middle Miocene.

First, the implications of changing land surface properties on the climate at the Last Glacial Maximum (LGM) are studied. A series of sensitivity experiments is carried out to evaluate the contribution of vegetation change relative to the contributions of the ice sheet expansion and elevation, and the lowering of the atmospheric CO₂ on the Last Glacial Maximum climate. We find that the vegetation cover change at the LGM leads to significant global cooling, together with a decrease in precipitation. The change in the vegetation cover also reinforces the cooling due to other surface cover changes, such as the ice-cover, when applied together with them.

Secondly, the climate and vegetation models are used to investigate the Middle Pliocene and Middle Miocene climates and vegetations. Both periods are characterised by a warmer and wetter than present-day climate, and as a consequence, by a reduction of desert areas and an expansion and densification of forests especially at high latitudes. Our results show that the vegetation feedback on climate may have contributed to maintain and even to intensify the warm and humid conditions produced by the other climatic factors at the Middle Pliocene and Middle Miocene. Thus, considering the climate and vegetation interactions could help to reconcile model results with proxy-based reconstructions. This also suggests that vegetation-climate interactions could provide a complementary, if not an alternative mechanism,

to the large increase of CO₂ required by the models to produce the estimated warming at both periods.

The results presented in this study highlight the contribution of the biosphere in past climate changes, and therefore emphasise the study of climate and vegetation interactions to better understand past, present and future climate changes. Furthermore, our results also illustrate that considering the vegetation feedback on climate helps to improve the comparison of climate modelling results to proxy-based reconstructions for the studied periods.

Résumé

Ce travail a pour objet l'étude des interactions entre la végétation et le climat au cours de plusieurs périodes du passé géologique de la Terre, à l'aide (1) du modèle dynamique global de végétation CARAIB, et (2) du modèle climatique de complexité intermédiaire Planet Simulator. Les modèles de végétation et de climat interagissent via une procédure de couplage asynchrone à l'équilibre. Dans ce travail, les modèles ont été appliqués à l'étude de trois périodes passées, caractérisées par un changement du climat et de la couverture de végétation à grande échelle : le Dernier Maximum Glaciaire, le Pliocène Moyen et le Miocène Moyen.

Dans un premier temps, nous avons étudié l'impact de changements des propriétés de surface continentale sur le climat du dernier maximum glaciaire. Un ensemble de tests de sensibilité a été réalisés à l'aide du modèle climatique afin d'évaluer les contributions relatives de changements dans la couverture de végétation, d'une expansion des calottes de glace et d'une augmentation de leur élévation, et d'une diminution de la concentration de dioxyde de carbone dans l'atmosphère. Les résultats obtenus permettent de mettre en évidence l'impact non-négligeable du changement de végétation sur le climat. Ce dernier changement provoque en effet une diminution des températures, accompagnée d'une réduction des précipitations en moyenne globale. De plus, le changement de végétation renforce les refroidissements obtenus, lorsqu'il est combiné aux autres modifications de la couverture de surface.

D'autre part, nous avons modélisé les climats et distributions de végétation du Pliocène Moyen et du Miocène Moyen. Les résultats obtenus témoignent d'un climat plus chaud et plus humide que le climat actuel au cours de ces deux périodes, et par conséquent, d'une réduction des écosystèmes désertiques au profit d'une expansion et densification des écosystèmes forestiers, particulièrement aux hautes latitudes. Ces résultats sont en bon accord avec les résultats de précédentes études de modélisation, ainsi qu'avec les observations. Nos résultats montrent également que la rétroaction de la végétation, en réponse au changement climatique, peut avoir contribué

à maintenir, et même à intensifier, les conditions chaudes et humides au Pliocène Moyen et au Miocène Moyen produites par les autres facteurs climatiques. Cela suggère également que les interactions végétation-climat pourraient constituer un mécanisme complémentaire, si pas alternatif, à l'importante augmentation de la concentration de CO₂ atmosphérique requise par les modèles pour produire les réchauffements estimés aux périodes considérées, et dès lors réconcilier les résultats de modélisation et les estimations basées sur les données, notamment pour Miocène Moyen.

Cette étude souligne donc l'importance du rôle joué par la biosphère dans les changements climatiques passés, ainsi que la nécessité de la prise en compte des interactions végétation-climat lors de la simulation de climats passés à l'aide de modèles climatiques et de végétation. De plus, les résultats obtenus montrent, du moins pour les périodes étudiées ici, que la prise en compte des rétroactions de la végétation sur le climat aident à améliorer la comparaison des résultats de modélisation aux reconstructions basées sur des données.

Contents

Introduction	1
1 Modelling the climate and vegetation interactions	5
1.1 Climate-vegetation interactions	7
1.1.1 Climate impacts on vegetation	7
1.1.2 Vegetation impacts on climate	9
1.2 Climate and vegetation models	14
1.3 Modelling past climates and vegetations	17
2 Models	19
2.1 The Planet Simulator model	19
2.1.1 Atmosphere	20
2.1.2 Ocean	22
2.1.3 Sea-ice	24
2.1.4 Land surface and soil	25
2.1.5 Vegetation	27
2.1.6 Present-day climate simulation with the Planet Simulator	28
2.2 The CARAIB model	37
2.2.1 Hydrological module	38
2.2.2 Canopy photosynthesis and stomatal regulation	39
2.2.3 Carbon allocation and plant growth	40

2.2.4	Heterotrophic respiration and litter/soil carbon	41
2.2.5	Plant competition and biogeography	41
2.2.6	CARAIB inputs: climatic fields	43
3	Interactions between the climate and vegetation models	47
3.1	Climatic inputs for CARAIB	47
3.1.1	Climatic inputs for the present-day	48
3.1.2	Climatic inputs for the past	49
3.2	Vegetation parameters for Planet Simulator	51
3.2.1	Surface albedo	52
3.2.2	Roughness length	53
3.2.3	Field capacity	56
3.3	Coupling procedure	57
3.4	Climate-vegetation iterations	60
4	Last Glacial Maximum climate and vegetation modelling	69
–	Impacts of land surface properties and atmospheric CO ₂ on the Last Glacial Maximum climate: a factor separation analysis	71
–	Introduction	72
–	Model setup	73
–	Experimental setup	74
–	Results	77
–	Discussion	95
–	Conclusions	102
4.1	Climate-vegetation iterations for the LGM	105

5 Middle Pliocene climate and vegetation modelling	113
5.1 Introduction	113
5.2 Model setups	116
5.2.1 Climate Model	116
5.2.2 Vegetation Model	117
5.3 Experimental setup	118
5.3.1 Preindustrial conditions	118
5.3.2 Middle Pliocene conditions	121
5.3.3 Alternative vegetation cover: CARAIB setup	125
5.4 Middle Pliocene simulated climate	127
5.4.1 Global and zonal average temperature and precipitation	127
5.4.2 Regional climate responses	128
5.4.3 Vegetation effect on the Middle Pliocene climate	132
5.5 Climate comparison	137
5.6 Extra Middle Pliocene vegetation simulation with CARAIB	141
5.7 Vegetation comparison	143
5.8 CARAIB vegetation feedback on the Middle Pliocene climate	148
5.9 Conclusions	153
6 Middle Miocene climate and vegetation modelling	155
– Effects of CO ₂ , continental distribution, topography and vegetation changes on the climate at the Middle Miocene: a model study.	156
– Introduction	157
– Model and experimental design	159
– Results	167
– Discussion	190
– Conclusions	194

6.1	MMCO climate and vegetation interactions	196
6.1.1	MMCO vegetation distribution at high CO ₂ level	196
6.1.2	MMCO vegetation distribution at low CO ₂ level	204
6.1.3	Vegetation feedback on the MMCO climate	211
6.1.4	Climate-vegetation iterations at Middle Miocene	213
6.1.5	Conclusions	216
	Conclusions	221
	A Modelling Late Miocene vegetation in Europe: results of the CARAIB model and comparison with palaeovegetation data	227
	Bibliography	291

Introduction

While it is obvious that climate change affects the distribution, functioning and structure of terrestrial ecosystems, the reverse is also true. Vegetation indeed controls physical characteristics of the land surface, such as albedo, surface roughness and soil moisture storage and transport capacity, and greatly impacts on the global carbon cycle. The terrestrial biosphere thus exerts an important feedback control on climate. In times of large scale climate and vegetation changes in response to ever increasing human induced emissions of greenhouse gases, it is therefore important to improve our understanding of the climate-vegetation interactions in a more quantitative way.

For the last decades, the climate and vegetation interactions have become the subject of increasing interest from the scientific community, who have started to consider the atmosphere and terrestrial biosphere as a coupled system, interacting on a large range of time scales. Recent modelling efforts have enabled the development of coupled climate and vegetation models that can be used to study climate and vegetation interactions in the past, the present and the future. The application of climate and vegetation models to the study of paleoclimates and paleovegetations notably offers the possibility to improve our understanding of the key mechanisms that led to large scale climate and vegetation changes in the past, to study climate-vegetation interactions under varying timescales and climatic conditions, and thus to better forecast near-future climate changes involving both natural and anthropogenic factors.

In this study, we propose to examine climate-vegetation interactions with the help of two existing models: (1) CARbon Assimilation In the Biosphere CARAIB, and (2) Planet Simulator. CARAIB is a dynamic vegetation model developed at ULg-LPAP, while Planet Simulator is developed at the University of Hamburg. Here, both models interact through an equilibrium coupling procedure and are used to study the joint evolutions of climate and vegetation during relatively well documented geological events and periods

that have experienced large scale climate and vegetation changes: the Last Glacial Maximum, the Middle Pliocene and the Middle Miocene.

The first chapter introduces the different aspects of the two-way climate and vegetation interactions that are important for this study. We first discuss in a general manner how the climate may impact on vegetation, and how in turn the vegetation may impact on climate through biophysical and biogeochemical processes. We describe the recent improvements that have been made in the modelling of climate and vegetation interactions. Finally, we present the general interests in modelling past climates and vegetations.

In the second chapter, we describe comprehensively the models that have been used in this study. We first present the climate model, Planet Simulator, and its different components, focusing on the terrestrial component that is of a major interest for this study. Secondly, we present the vegetation model, CARAIB, and its different modules, as well as the plant type and biome classifications.

The third chapter describes the interactions between the climate and vegetation models that have been taken into account. First, the derivation of the climatic inputs required by the CARAIB model for present and past simulations is explained. Secondly, the calculation of the vegetation parameters that are needed by the Planet Simulator model to represent the vegetation cover effects on climate is described. Then, we present the equilibrium asynchronous coupling procedure that has been applied. Finally, we complete the presentation of the coupling technique by an application of this procedure on present-day climate and vegetation simulation experiments.

In the remaining three chapters, we present the results of climate and vegetation modelling with Planet Simulator and CARAIB on several past periods. The fourth chapter is devoted to the analysis of the impact of land surface properties and atmospheric carbon dioxide on the Last Glacial Maximum climate. A series of sensitivity experiments is carried out to evaluate the contribution of vegetation change relative to the contributions of the ice sheet expansion and elevation, and the lowering of the atmospheric carbon dioxide on the Last Glacial Maximum climate. The fifth chapter deals with the modelling of Middle Pliocene climate and vegetation with Planet Simulator and CARAIB. The results of climate and vegetation simulations are presented and compared to previous modelling and data-based studies. In the sixth chapter we present the results of Middle Miocene climate and vegetation modelling. Several sensitivity experiments are performed in order to evaluate the vegetation feedback on the Middle Miocene climate against the effects of land-sea configuration, oceanic heat transfer, topography and atmo-

spheric CO₂ concentration changes. Finally, we compare the Middle Miocene vegetation distributions simulated with CARAIB under various carbon dioxide concentrations with available proxy-based vegetation reconstructions, and also compare their potential feedback on climate.

We close our study with a short summary and discussion of the results, completed by a general conclusion concerning future research.

Chapter 1

Modelling the climate and vegetation interactions

The Earth's climate system is a complex interactive system consisting of the atmosphere, land surface, snow and ice, ocean and other bodies of water and living things (LE TREUT et al., 2007). Each of the components of the climate system influences and is influenced by all of the others (see Figure 1.1). They are linked by flows of energy and matter. The energy flow occurs as solar and infrared radiation, as sensible and latent heat, and through the transfer of momentum between the components. The major mass flows involve water and carbon (hydrological and carbon cycle). Thus, the behaviour of the climate system depends on how these energy and mass flows change as the system changes, on how the flows themselves influence the system, and on the multiple time scales with which the system responds to change in the mass and energy flows. The climate system evolves in time under the influence of its own internal dynamics and due to changes in external factors that affect climate (called forcings), such as volcanic eruptions, solar variations, as well as human-induced changes in atmospheric composition. Some of the driving factors of climatic change operate at time scales of hundreds of millions of years, whereas others fluctuate over a time period of only a few years or less. Climate responds directly to such changes, as well as indirectly, through a variety of feedback mechanisms. The feedback mechanisms in the climate system may either amplify (positive feedback) or diminish (negative feedback) the effects of a change in climate forcing (LE TREUT et al., 2007).

The atmosphere and the terrestrial biosphere are two components of the climate system, which interact in a complex non linear way at a wide range of time scales (CLAUSSEN, 1994). The atmospheric climate has a profound

impact on the phenology and physiological processes of the biosphere, and exerts the dominant control on the geographical distribution of the major vegetation types on a global scale. In turn, vegetation cover affects climate via alteration of the physical characteristics of the land surface, such as albedo, roughness, water availability (biophysical effects), and of the concentrations of gases in the atmosphere, such as carbon dioxide and methane (biogeochemical effects) (BROVKIN, 2002). The atmosphere and terrestrial biosphere (including the soils) must therefore be studied as a coupled system, interacting on a large range of time scales. On time scales of seconds to hours, their interaction is dominated by the exchange of energy, mass (water, carbon) and momentum. On time scales of days to months, important processes are the storage of water in soil and the vegetation cycle. At seasonal, annual and decadal time scales, the vegetation structure itself may undergo important transformations (stand growth, disturbance, extinction of plant types) (FOLEY et al., 2000).

In times of ever increasing human induced emissions of greenhouse gases – the most important among them being carbon dioxide, CO_2 , which is also known to act to some extent as a fertilising agent on plants – it is therefore important to improve our understanding of the climate-vegetation interactions, which we only qualitatively depicted above, in a more quantitative way. There are also a number of instances in the recent and more distant past of Earth’s climate history where global climate change went together with large-scale vegetation change.

However, the actual influence of terrestrial ecosystems is difficult to predict. Vegetation changes induced by climate change might in some regions lead to a positive feedback, which might be offset by negative feedbacks in other regions. Climatic change induced by modification of the vegetation cover in some regions may lead to adaptations of ecosystems elsewhere on the globe that may either dampen or amplify the initial climate change. Sufficiently realistic models for both climatic and biospheric parts, and which can still be coupled in a fully bi-directional way are therefore required for a quantitative study of the response of the coupled climate-biosphere system to perturbations. Contrasting settings from the geological past can be used to better constrain and validate the coupled system and to understand the mechanisms that drove the observed changes.

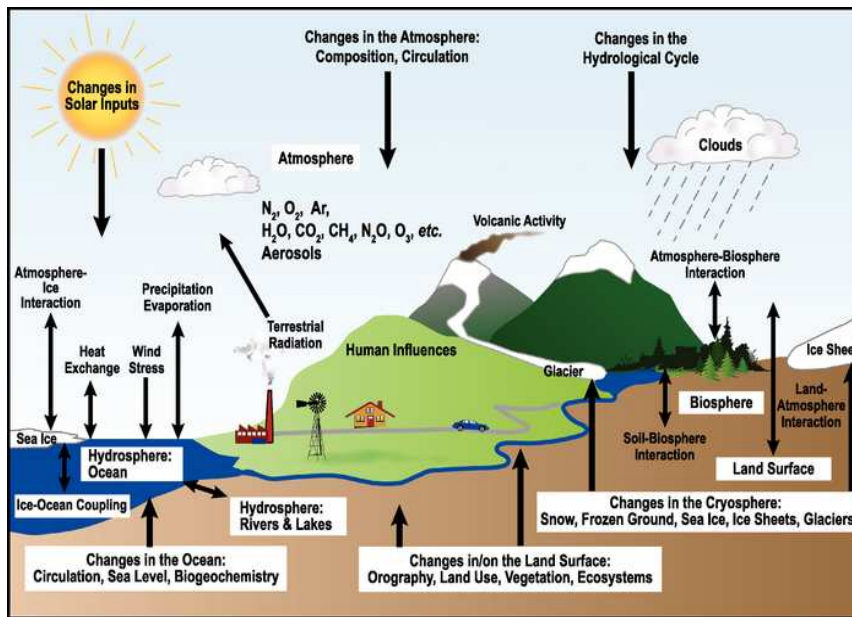


Figure 1.1: Schematic view of the components of the climate system, their processes and interactions (LE TREUT et al., 2007).

1.1 Climate-vegetation interactions

1.1.1 Climate impacts on vegetation

The climatic constraints on the activity of the biosphere are certainly the most obvious manifestations of the climate-vegetation interactions. The distribution of the major vegetation types, such as deserts, tropical rainforests, and tundra (see Figure 1.2), is obviously determined by climate, while soil type and topography influence the vegetation distribution to a smaller extent (BROVKIN, 2002). The distribution of the tropical rainforest, for example, closely follows the equatorial climate zone with year-round rain and warm conditions occurring in the Amazon Basin, Central Africa, Central America and South-East Asia (ADAMS, 2010). Climatic conditions, such as temperature, radiation and soil water availability, profoundly influence the structure and functioning of ecosystems on regional and global scale, determining the predominant type of vegetation, e.g., grassland or forest, and the biogeochemical properties of the surface, e.g., carbon stocks in the biomass and the soil. Trees, notably, have a greater requirement for warmth, water and nutrients than grasses. Below certain thresholds of temperature or water availability,

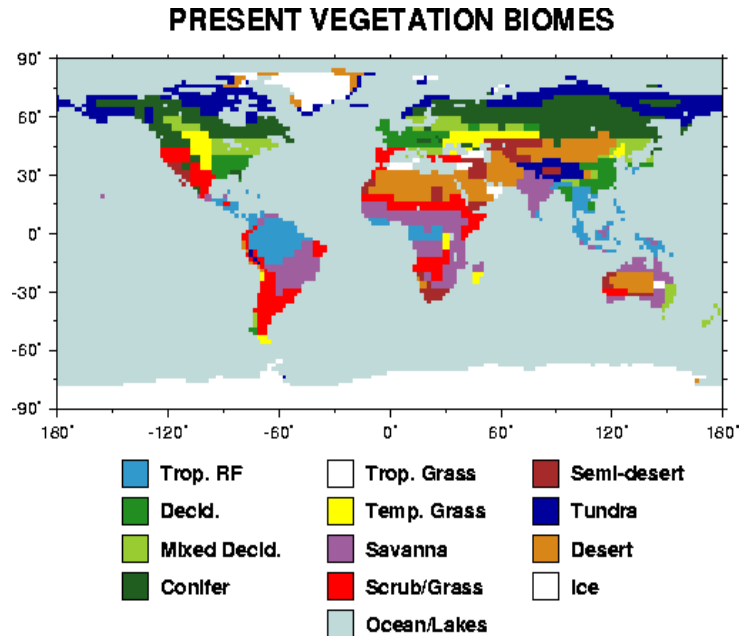


Figure 1.2: Map of major biome distributions as it is supposed to have been before major anthropogenic disturbances (CROWLEY, 1995).

the only plants that can survive are shrubs and herbaceous plants. Therefore, changes in climate directly affect the geographic distribution of global vegetation (ADAMS, 2010). Carbon dioxide may also affect plants by changing the climate, but also influence them through its direct effects on plant physiology. CO_2 is a determining factor for photosynthesis and the opening or closing of stomata, the small pores of the leaves that regulate the exchange of water and gases between the plant and the atmosphere. Thus, an increase of the atmospheric CO_2 concentration generally benefits to plant activity because it allows plants to photosynthesize faster. It also allows the plant leaves to close their stomata, which diminishes the risk of dying by dehydration. Moreover, over the next few centuries, this direct CO_2 effect might turn out to be ecologically important and lead to changes in the structure of vegetation around the world (ADAMS, 2010).

The impact of climate change on the vegetation distribution can be seen nowadays. Analysis of satellite-sensed vegetation greenness and meteorological station data suggest an enhanced plant growth and lengthened growing season duration at northern high latitudes since the 1980s (ZHOU et al.,

2003; NEMANI et al., 2003). This effect is supported by modelling linked to observed climate data (LUCHT et al., 2002; NOTARO et al., 2005). However, the time scale of vegetation re-growth is up to hundred years for forest ecosystems. The alteration of the soil organic profile in response to vegetation changes is even slower. Therefore, the evolution of ecosystems towards the equilibrium with the environment takes up to several thousands of years. However, systematic observations of changes in vegetation and soils are only available for up to several decades. Moreover, in the most explored regions, such as Europe, the natural vegetation cover has been replaced by croplands and planted forests. Due to these limitations in available time-series, a conventional approach in biogeographic analysis is the substitution of time by space via the analysis of geographical climate-vegetation regularities, under the assumption that observed natural ecosystems are in equilibrium with climate (BROVKIN, 2002).

1.1.2 Vegetation impacts on climate

The climate exerts the dominant control on the vegetation. The terrestrial biosphere can in turn strongly affect the climate, through both positive and negative feedbacks due to biophysical and biogeochemical processes (FOLEY et al., 2003). The biophysical mechanisms affect the exchange of energy, water and momentum between the biosphere and the atmosphere. The biogeochemical mechanisms influence the flux of carbon between the biosphere and the atmosphere. This section covers mainly the biophysical processes that have been studied here, and shortly present the biogeochemical interactions.

Biophysical processes

The land surface climate is determined by the surface fluxes between the biosphere and the atmosphere, which are influenced by radiative (e. g., albedo) or non-radiative (e. g., roughness, soil water) variables (see Figure 1.3). Both radiative and non-radiative variables are controlled by vegetation.

Surface Albedo

The surface albedo (the fraction of reflected solar radiation by the surface) and emissivity (the ratio of thermal radiation of the surface to that of a black body) are important variables for the radiative balance at the surface. Light surfaces have high albedos and are able to reflect more radiation to space than dark surfaces with lower albedos. Thus, forested and densely vegetated

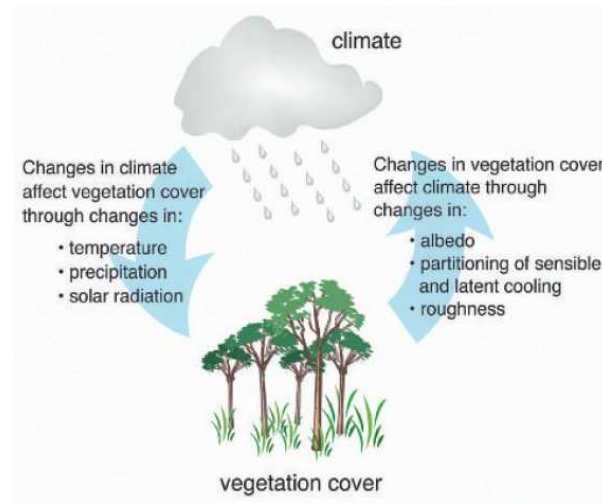


Figure 1.3: Biophysical feedbacks between climate and vegetation (FOLEY et al., 2003).

areas that are commonly darker than those covered with grasslands or sparse vegetation are characterised by low albedo values and absorb more solar radiation. Table 1.1 lists the albedos attributed to various surface types. Thus, a change in the vegetation cover modifies the albedo of the surface, thereby affecting the energy balance and the surface temperature. This, in turn affects the energy partitioning between sensible heat flux, which is the amount of energy released by the surface during a change of temperature, and latent heat flux, which is the amount of energy released during the evaporation of surface water (FOLEY et al., 2003). For example, high-latitude climate is strongly influenced by the darkening effect of vegetation. Numerous studies investigated the effect on modern climate of reforestation at high latitudes (BONAN et al., 1992; THOMAS and ROWNTREE, 1992; GANOPOLSKI et al., 1998; LEVIS et al., 2000; CRUCIFIX and LOUTRE, 2002). They all demonstrated that the replacement of tundra by boreal and even deciduous forests at high latitudes, in response to climate warming, significantly reduces the albedo of snow covered surfaces. This in turn increases the surface temperature and induces an earlier snow melt during the snow season that allows the trees to grow more easily. Thus, the development of forests at high latitudes amplifies the system response to the original forcing (positive feedback).

Roughness length

On the other hand, vegetation height and density affect the roughness of the

Table 1.1: Albedos of various surface types (GUYOT, 1999).

Surface Type	Albedo
Water	0.03-0.5
Snow	0.45-0.95
Land-ice	0.2-0.4
Sea-ice	0.3-0.4
Urban surface	0.1-0.27
Bare soil	0.2
Desert	0.2-0.45
Grassland	0.16-0.26
Cropland	0.1-0.25
Coniferous forest	0.05-0.15
Deciduous forest	0.1-0.2

land surface. The roughness of the surface is represented by the roughness length, which is a parameter of the vertical wind profile equations that model the horizontal mean wind speed near the ground. In the logarithmic wind profile, the roughness length is equivalent to the height at which the wind speed tends to zero. Trees have a high roughness length compared to grasses and deserts. Typical roughness length values for various surface types are given in Table 1.2. The roughness length affects the mixing of air close to the ground. Rough surface mixes air more efficiently, enhancing both latent and sensible surface heat fluxes, whereas smooth surfaces imply stronger winds near the ground (FOLEY et al., 2003). Therefore, deforestation, such as the tropical deforestation that is being carried out in South-America, Africa and South-east Asia, induces a strong decrease of roughness length, which in turn reduces the surface fluxes and the evapotranspiration that is an important component of the hydrological cycle of tropical rainforest. The reduced evaporation results in less water being pumped into the atmosphere, thereby contributing to decrease of the tropical rainfall and increase in surface temperature (BONAN, 2002; COSTA and FOLEY, 2000).

Rooting depth

The biosphere also influences the hydrological cycle via its control on the evapotranspiration and soil moisture. The rooting depth plays an important role in the hydrological cycle, because it determines the quantity of water that can be extracted by the vegetation from the soil and recycled back into the atmosphere through evapotranspiration (HAGEMANN and KLEIDON, 1999; ARORA, 2002). Trees have typically deeper roots and are able to extract

Table 1.2: Roughness lengths of various surface types (JACOBSON, 2005).

Surface Type	Roughness length (m)
Rough sea	$1.5 \times 10^{-5} - 1.5 \times 10^{-4}$
Calm sea	10^{-5}
Ice	10^{-5}
Snow	$5 \times 10^{-4} - 10^{-4}$
Short grass (<10 cm)	$10^{-3} - 4 \times 10^{-2}$
Long grass (>25 cm)	$4 \times 10^{-2} - 0.1$
Tropical forest	2.2
Coniferous forest	4.8
Deciduous forest	2.6
Cropland	0.12
Desert	3×10^{-4}

water from deep soil layer, while grasses and herbaceous plants are effective in using soil moisture at shallow depths. Table 1.3 lists the maximum rooting depth of various plant types. With deeper roots, more soil volume is explored and more soil water is available for evapotranspiration during dry periods. Such a behaviour is observed in several parts of East Africa and in the Amazon forest. In the case of tropical deforestation, the replacement of tropical forest with grassland or pasture notably decreases the rooting depth, which contributes to reduce evapotranspiration from the surface. This in turn substantially decreases the local rainfall and increases the surface temperature (BONAN, 2002; COSTA and FOLEY, 2000). As a result, the warming induced by the reduction of evapotranspiration surpasses the surface cooling induced by an increase of the surface albedo due to the replacement of forests by grasslands. The net effect of the tropical deforestation is thus a local warming (COSTA and FOLEY, 2000).

As mentioned above, changes in vegetation cover influence the regional climate, but also the neighbouring regions. The local effect is most pronounced for temperature, as vegetation changes modify the surface albedo, which directly affects the local radiative budget (BROVKIN, 2002). However, the changes in vegetation also affect the evaporation, which may result in remote effects due to the long-distance transport of moisture. Thus, the changes in climate linked to vegetation changes depend on both local and remote vegetation changes. Furthermore, the effects of vegetation on regional climate are not the same around the globe. They may be either dampened or amplified depending on the various mechanisms and feedbacks that are

Table 1.3: Maximum rooting depths of various vegetation types (CANADELL et al., 1996).

Vegetation Type	Maximum rooting depth (m)
Desert	9.5 ± 2.4
Grassland	2.6 ± 0.2
Cropland	2.1 ± 0.2
Tundra	0.5 ± 0.1
Boreal forest	2 ± 0.3
Temperate coniferous forest	3.9 ± 0.4
Temperate deciduous forest	2.9 ± 0.2
Tropical evergreen forest	7.3 ± 2.8

involved in these climate-vegetation interactions. Therefore, the climate-vegetation interactions remain difficult to predict, and the research on these interactions concentrates for the present on some "hot spots" where the interactions are the most pronounced, e. g. boreal reforestation and tropical deforestation (BROVKIN, 2002; FOLEY et al., 2003).

Biogeochemical processes

Various processes in terrestrial ecosystems also influence the flux of carbon between land and the atmosphere (see Figure 1.4). These biogeochemical feedbacks results from the two-way interactions between climate and vegetation (FOLEY et al., 2003). The photosynthetic productivity of the terrestrial ecosystems changes in response to changes in temperature, precipitation, atmospheric CO₂ and nutrients. For example, the productivity increases and the carbon uptake from the atmosphere is enhanced if climate is favourable for vegetation growth (e.g., increased rainfall in a semi-arid system). Thus, shifts in ecosystem structure in response to climate changes can alter the partitioning of carbon between the atmosphere and the land surface. For example, the replacement of tundra by boreal forests at high latitudes, in response to climate warming, would initially lead to an increase of carbon storage in the biosphere, due to the larger biomass of trees than herbs (DENMAN et al., 2007). However, over a longer time scale (e. g., over centuries), changes in soil carbon would need to be considered to determine the net effect of this vegetation change. On the other hand, a deforestation of tropical forests would result in a net flux of carbon to the atmosphere (DENMAN et al., 2007). These biogeochemical effects will play an important role in the

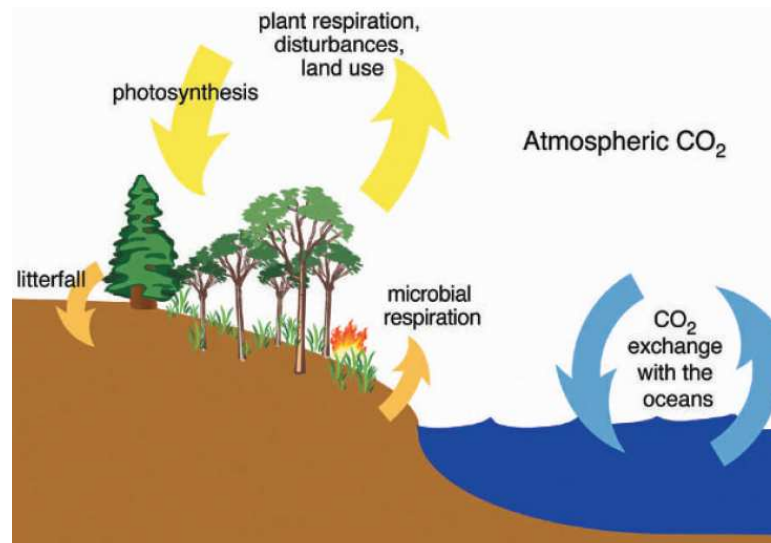


Figure 1.4: Biogeochemical feedbacks between climate and vegetation (FOLEY et al., 2003).

climate changes of the next centuries. The amount of CO₂ in the atmosphere will be determined not only by human activity, but also by the response of the terrestrial biosphere and the ocean (FOLEY et al., 2003).

1.2 Climate and vegetation models

During the last centuries, both the terrestrial biosphere and the physical climate system have been undergoing fundamental changes in response to human activities. Therefore, the scientific community has become increasingly interested in developing tools, such as models, to improve our understanding of global-scale climatic and biospheric processes. Recent efforts have been made to model climate and vegetation and to incorporate the two-way climate-vegetation interactions into coupled climate-vegetation models (e. g., FOLEY et al. (1998); LEVIS et al. (2004); GALLIMORE et al. (2005); NOTARO et al. (2005))

The rapid development of vegetation models has notably expanded the number of applications for which they can be used, and therefore the usefulness of the models themselves. Based on the assumption that native vegetation would be the best expression of climate, or in other words, that the

equilibrium distribution of major vegetation types can be explained by climate, the first climate classification models of biogeography were developed (KÖPPEN, 1923; HOLDRIDGE, 1947; BUDYKO, 1974; PRENTICE et al., 1992). These models use basic climatic parameters (growing degree days, minimum winter time temperature, rainfall, etc.) to allow the prediction of the geographic distribution of many plant ecosystems or biomes on the global scale. For example, HOLDRIDGE (1947) determined 38 climatic life zones using three climatic variables (annual precipitation, temperature above 0°C, and ratio of mean annual potential evapotranspiration to mean annual precipitation). These models have been widely used with climate models to investigate the equilibrium response of vegetation to climate changes (HENDERSON-SELLERS, 1993; BETTS et al., 1997; CLAUSSEN, 1994, 1998).

However, these biogeography models do not account for all the mechanisms of the climate-vegetation interactions. They do not consider ecological and biochemical processes, such as photosynthesis and carbon allocation. They do not explicitly represent the structural attributes of vegetation, like leaf area index (the ratio between the total leaf surface of vegetation and the land surface area on which the vegetation grows), or stomatal conductance (a measure of the rate of transfer of either water vapour or carbon dioxide through the stomata). During the last decades, Dynamic Global Vegetation Models (DGVMs) have been developed to better represent these processes and account for the terrestrial biochemistry (e. g., FOLEY et al. (1996); OTTO et al. (2002); BROVKIN et al. (1997); COX et al. (2000); SITCH et al. (2003)). DGVMs notably simulate photosynthesis, growth of the vegetation, allocation of carbon into the plants, and soil water budget. They are also able to simulate the transient changes in the carbon balance and vegetation structure in response to climate changes. DGVMs generally take into account the competition between the plant types in function of their productivity, and account for vegetation growth and carbon storage disturbances, due to wildfires for example. They have been largely used to simulate the changes in terrestrial vegetation cover and carbon storage in response to global climate change in the recent past or future climate change scenarios (COX et al., 2001; BROVKIN et al., 2002; OTTO et al., 2002; FRANÇOIS et al., 2006; LUCHT et al., 2006; JIAN et al., 2005; CRUCIFIX et al., 2005).

On the other hand, modelling efforts have been made to link these vegetation models to Atmospheric General Circulation Models (AGCMs). For over a decade, many AGCMs have used static or at best prescribed land surface characteristics, including parameters related to or controlled by vegetation. Neither did they respond to climate change, nor possibly fed back on it. This fact also proved problematic when applying GCMs to the study

of past climates, for which adequate information on vegetation distribution is not available. Thus, in order to simulate the vegetation-climate interactions, fully coupled global climate models including dynamical vegetation models started to be developed (FOLEY et al., 1998; DELIRE et al., 2003; LEVIS et al., 2004; GALLIMORE et al., 2005; NOTARO et al., 2005; CRUCIFIX and HEWITT, 2005). These fully-coupled atmosphere-vegetation models (AVGCMs) or atmosphere-vegetation-ocean models (AOVGCMS) are now used for past, present and future climate modelling (e. g., BRACONNOT et al. (2007a,b)). Their ability to simulate past, present and future climate and vegetation are evaluated in the frame of intercomparison projects, such as the Paleoclimate Modelling Intercomparison Project (PMIP2) (HARRISON et al., 2002).

These complex models remain, however, difficult and expensive to use, especially in terms of computing resources. Two other approaches have therefore more commonly been chosen to study the two-way climate-vegetation interactions. The first one calls upon Earth System Models of Intermediate Complexity (EMICs) with extremely simplified physics or coarse resolution components. It was chosen, e. g., by CLAUSSEN et al. (2001) and BROVKIN et al. (2002), who used CLIMBER-2 (PETOUKHOV et al., 2000), and by RENNSSEN et al. (2003) who used ECBILT-CLIO-VECODE (OPSTEEGH et al., 1998; GOOSSE and FICHEFET, 1999; BROVKIN et al., 1997). However, the vegetation feedback is not always completely represented in these models. In RENNSSEN et al. (2003), e. g., it only feeds back via surface albedo. Furthermore, these models remain to a large extent rooted into present-day settings, because of their statistical dynamical foundation, or because of specific, statically prescribed boundary conditions or flux corrections required. The second approach is based upon asynchronous coupling of state-of-the-art GCMs with vegetation models (DE NOBLET et al., 1996; BETTS et al., 1997; CLAUSSEN et al., 1998). Asynchronous coupling, however, only allows to analyse equilibrium vegetation-climate interaction. It does not allow consistent transient simulation experiments.

In order to study the joint evolutions of climate and vegetation during various past periods, we have chosen here an approach mixing the two approaches cited above. Thus, we have chosen to couple asynchronously a state-of-the-art DGVM, CARAIB, that has proven its reliability in simulating present and past vegetation distributions (e. g., NEMRY et al. (1996); LAURENT et al. (2008); OTTO et al. (2002); FRANÇOIS et al. (2006)), to an AGCM of intermediate complexity, Planet Simulator (FRAEDRICH et al., 2005a,b). The Planet Simulator has the advantage to be portable and quick to reach equilibrium. It includes an atmospheric component with an explicit representation of the three-dimensional atmospheric dynamics that is

adapted to simulate easily past climates. In the next two chapter we give a comprehensive description of the climate and vegetation models, and of the asynchronous coupling procedure that have been used in this study. The subsequent chapters are devoted to the application of the models to relatively well documented geological past events and periods that have experienced large scale climate and vegetation changes, i. e., the Last Glacial Maximum, the Middle Pliocene and the Middle Miocene.

1.3 Modelling past climates and vegetations

A variety of natural climate and vegetation states have been present in the Earth's history. There are also a number of instances in the recent and more distant past where global climate changes went together with large-scale vegetation changes. Therefore, modelling past climate and vegetation provides a means to improve our understanding of climate changes and climate-vegetation interactions under varying timescales and climatic conditions, and thus to better forecast near-future climate changes involving both natural and anthropogenic factors.

Furthermore, paleoclimate and paleovegetation reconstructions offer the possibility of testing climate models and their ability to simulate realistic climate and vegetation changes. Indeed, even if models could simulate modern climate and vegetation perfectly, this would not guarantee an accurate simulation of climate changes (JOUSSAUME et al., 1999; FRANÇOIS et al., 2002). Moreover, many parameterisations describing sub-grid scale processes (e. g., cloud parameters, turbulent mixing) have been developed using present-day observations. During the last decades, paleoclimate proxies for a range of climate observations had expanded greatly. A climate proxy is a local quantitative record (e. g., thickness and chemical properties of tree rings, pollens of different species) that is interpreted in terms of a climate variable (e. g., temperature or rainfall) using a transfer function that is based on physical principles and recently observed correlations between the two records (JANSEN et al., 2007). Thus, numerous paleoclimate and paleovegetation reconstructions based on various data, including pollen records, insect and animal remains, oxygen isotopes and other geological data from lake varves, loess, ocean sediments, ice cores and glacier termini, are now available for the recent past.

At this stage, modelers are usually interested in typical past climate intervals or events, with significantly different climate and vegetation conditions

from the modern and large amounts of reliable proxy data to compare and validate their modelling results. For instance, the Last Glacial Maximum (LGM), around 21 000 years before present (21 kBP), has been widely simulated to assess the ability of models to reproduce extreme cold conditions, and to understand how massive ice sheets and lower atmospheric CO₂ concentration impact climate (JOUSSAUME and TAYLOR, 2000). The response of the vegetation to extremely cold and arid climatic conditions, leading to a broad expansion of deserts and grasslands, and its feedback on the LGM climate has also been widely studied (e. g., CROWLEY and BAUM (1997); WYPUTTA and MCAVENEY (2001); CRUCIFIX and HEWITT (2005)). Further in the recent past, warmer than present-day periods have been identified and started to be studied. These periods offer the advantage of having a geographical configuration close to the modern one and are relatively well documented by proxy data. Thus, they provide potential guidance to improve our knowledge on the global warming in the near future. For example, the Middle Pliocene (3.29 to 2.97 Ma BP) is the most recent geological period during which global climate was 2 to 3°C warmer than the present, with higher than preindustrial atmospheric carbon dioxide concentrations (estimated to be close to 400 ppmv), and with significant greening documented at northern high latitudes and desert reductions at middle latitudes (HAYWOOD et al., 2009b). Recent efforts have also been developed to model and document the warm climate and vegetation of the Middle Miocene (about 17 to 15 Ma BP) (MOSBRUGGER et al., 2005). However, the responsible mechanisms for the Middle Pliocene and Middle Miocene warmths are still highly debated, as the models qualitatively capture the basic trends of proxy data on a global scale, but fail to quantitatively reproduce the reconstructed climate in the amplitude and the climate and vegetation spatial patterns for these periods.

Chapter 2

Models

The present chapter is intended to give a global and comprehensive description of the climate and vegetation models that have been used in this study. The first section handles the climate model, Planet Simulator, and its components. The second section describes the vegetation model, CARAIB, and details its different modules, as well as the climatic inputs needed to run simulations.

2.1 The Planet Simulator model

The Planet Simulator (FRAEDRICH et al., 2005a,b) is an Earth system Model of Intermediate Complexity (EMIC) (CLAUSSEN et al., 2002). The dynamical core of the Planet Simulator is PUMA-2, a spectral General Circulation Model (GCM) of medium complexity with triangular truncation, based upon the Portable University Model of the Atmosphere PUMA (FRAEDRICH et al., 1998). Besides the central atmospheric component, the Planet Simulator includes other compartments of the climate system, for example, an ocean with sea-ice, a land surface with a simple biosphere (see Figure 2.1). These other compartments are reduced to linear systems, and interact with the atmospheric component via various linear processes that parameterise the variability of the subsystems in terms of their energy and mass balances.

The Planet Simulator has been used before for present-day climate modelling studies (FRAEDRICH et al., 2005b; GROSFELD et al., 2007; JUNGE et al., 2005) as well as for various paleoclimatic studies focusing on different past periods (ROMANOVA et al., 2006; MICHEELS et al., 2009a,b; HENROT

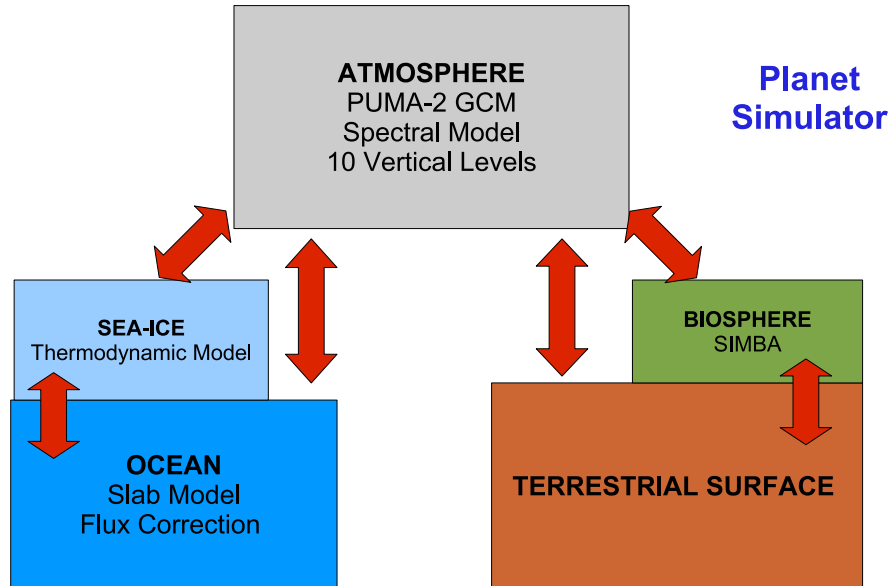


Figure 2.1: Components of the Planet Simulator.

et al., 2009, 2010). The model has proven its usefulness in the comparison to proxy data (HENROT et al., 2009; MICHEELS et al., 2009a). The Planet Simulator present-day climate compares fairly well to ERA-40 reanalysis, although it is affected by two major climatological biases: (1) a cold bias at high latitudes in winter of the hemisphere and (2) a global overestimation of the surface evaporation (HABERKORN et al., 2009). For a complete model description, we refer the reader to the documentation of the Planet Simulator (FRAEDRICH et al., 2005a; LUNKEIT et al., 2007). It should be noticed that we used version 15.3 of the Planet Simulator (updated version of version 15.0 (LUNKEIT et al., 2007)).

2.1.1 Atmosphere

Model dynamics and resolution

The atmospheric component of the Planet Simulator is PUMA-2, a spectral GCM with triangular truncation, based upon the Portable University Model of the Atmosphere PUMA (FRAEDRICH et al., 1998). PUMA-2 solves the primitive equations, consisting of the conservation of momentum and mass,

the first law of thermodynamics and the equation of state, simplified by the hydrostatic approximation.

The primitive equations are solved numerically in the $(\lambda, \varphi, \sigma)$ coordinate system, where λ represents the longitude, φ the latitude, and σ the pressure normalized by the surface pressure

$$\sigma = \frac{p}{p_S}. \quad (2.1)$$

In this vertical coordinate system, the top of the atmosphere corresponds to $\sigma = 0$ ($p = 0$ at the top of the atmosphere), whereas the base of the atmosphere corresponds to $\sigma = 1$ ($p = p_S$ at the surface). In the horizontal direction, the conventional spectral approach with the spectral transform method is applied (ORSZAG, 1970). Finite differences are used in the vertical, with the vertical velocity being defined between full (temperature, moisture, vorticity and divergence) levels. The equations are integrated in time with a leap-frog semi-implicit time stepping scheme (HOSKINS and SIMMONS, 1975; SIMMONS et al., 1978) with Robert/Asselin time filter (ROBERT, 1981; ASSELIN, 1972).

By default, the atmosphere is subdivided into five equidistant vertical σ levels. However, we preferred to use ten equidistant vertical σ levels in order to better represent the atmospheric processes (HENROT, 2006). The horizontal resolution depends on the truncation used, either a T21 or a T42 resolution. The Planet Simulator's grid consists of 32 gaussian latitudes and 64 equally-spaced longitudes for the T21 resolution, and of 64 latitudes and 128 longitudes for the T42 resolution.

For more details concerning the atmosphere dynamics of the model, we refer to the Planet Simulator reference guide (LUNKEIT et al., 2007), the master thesis of HENROT (2006), and also to the ECHAM3 and ECHAM5 models reports (DKRZ, 1993; ROECKNER et al., 2003), because of the similarities to the Planet Simulator in their structures.

Atmospheric processes

Radiation The radiation parameterisations are based on the scheme of LACIS and HANSEN (1974) for the short wave radiation and SASAMORI (1968) for the long wave radiation. The short wave radiation scheme follows the ideas of LACIS and HANSEN (1974) for the cloud free atmosphere, with Rayleigh scattering, ozone absorption and water vapor absorption. For the cloudy part, albedos and transmissivities for high-, middle- and low-level clouds are parameterised following STEPHENS (1984). Long wave radiation

for the clear sky uses a broad band emissivity method (SASAMORI, 1968). The cloud flux emissivity is obtained from the cloud liquid water content (STEPHENS, 1984). The ozone concentration used in the radiation scheme is prescribed following an idealized annual cycle (GREEN, 1964). The atmospheric carbon dioxide (CO_2) concentration is manually prescribed by the user. However, neither the concentration of methane (CH_4) and nitrous oxide (N_2O), nor that of atmospheric dust content are taken into account.

Precipitation The precipitation parameterisation is based on the work of KUO (1965, 1974). Precipitation is partitioned into convective precipitation, large scale precipitation and snow fall. The cumulus convection is parameterised following the convection scheme of KUO (1965, 1974). Large scale condensation occurs if the air is supersaturated. Condensed water falls out instantaneously as precipitation. No storage of water in clouds is considered. However, a distinction is made between rain and snow fall at the surface. If the temperature of the lowermost atmospheric level is lower than 273.16 K, precipitation is assumed to be snow, otherwise all precipitation falls out as rain. Cloud cover and cloud liquid water content are diagnostic quantities. The fractional cloud cover of a grid-cell is parameterised according to SLINGO and SLINGO (1991).

Surface fluxes Surface fluxes, i.e., zonal and meridional momentum, sensible and latent heat fluxes, are parameterised using the bulk aerodynamic formulas. The calculation of the drag and transfer coefficients is based on the work of LOUIS (1979) and ROECKNER et al. (1992). Vertical diffusion representing the non-resolved turbulent exchange is applied to the horizontal wind components, the potential temperature and the specific humidity. The horizontal diffusion parameterisation follows the LAURSEN and ELISASEN (1989) scheme.

2.1.2 Ocean

The ocean model consists of a slab model, only representing the ocean mixed-layer. The mixed-layer depth is kept fixed to 50 m. The mixed-layer temperatures are computed from a prognostic equation at each ocean point. The transport of heat by oceanic surface currents is represented by an additional source or sink of heat, varying monthly and spatially that is prescribed within the mixed-layer and the sea-ice. Heat flux adjustments are applied to ocean

grid-cells to mimic heat transport by ocean currents that is not an explicitly represented process in the model.

The sea surface temperature at each ocean point is calculated following the equation:

$$\frac{dT_S}{dt} = \frac{Q_{atm} + Q_c}{\rho_w c_{pw} h_{mix}},$$

where ρ_w and c_{pw} represent respectively the density and specific heat of sea water. h_{mix} is the depth of the mixed layer, fixed to 50 m. Q_{atm} is the net atmosphere to ocean heat flux, which in the absence of sea-ice is defined as the sum of solar flux absorbed by the ocean, long wave cooling flux, sensible heat flux from the ocean into the atmosphere, and latent heat flux from the ocean to the atmosphere.

The impact of oceanic heat transport Q_c on the sea surface temperature (SST) is parametrised following the traditional flux correction procedure¹. First, a calibration run is performed, in which the mixed-layer temperatures are held to climatology. Then, the heat flux adjustment or flux correction, i.e., extra ocean-atmosphere flux that would be needed to keep the model ocean in balance, is computed from the temperature differences between the climatological and calculated ocean temperatures:

$$Q_c = \rho_w c_{pw} h_{mix} \frac{T_{Sclim} - T_S}{\tau}.$$

Here, T_{Sclim} and T_S respectively represent the climatological and calculated sea surface temperatures, and the time scale τ is about 50 days.

Prescribing heat flux adjustments helps to minimise the cold bias that occur at high latitudes in the Planet Simulator (HENROT, 2006; HABERKORN et al., 2009). Furthermore, prescribing heat flux adjustments, rather than using fixed sea-surface temperatures, allows the slab-ocean model to respond with a greater sensitivity to boundary condition changes. The climate sensitivity of the model to a doubling of CO₂ from a preindustrial level of 280 ppmv to 560 ppmv, and with fixed sea surface temperatures, is +0.8°C under a present-day configuration. The prescription of the oceanic heat fluxes and the calculation by the model of the sea surface temperatures and sea-ice cover increase the climate sensitivity to CO₂ doubling to +4.5°C. The difference in the model responses under fixed and calculated oceanic conditions may be mainly attributed to the response of sea-ice to the warming

¹Following the description of the HadAM3 model in *Wikipedia, the Free Encyclopedia*, web site : <http://en.wikipedia.org/wiki/HadCM3>, visited the 10/31/10

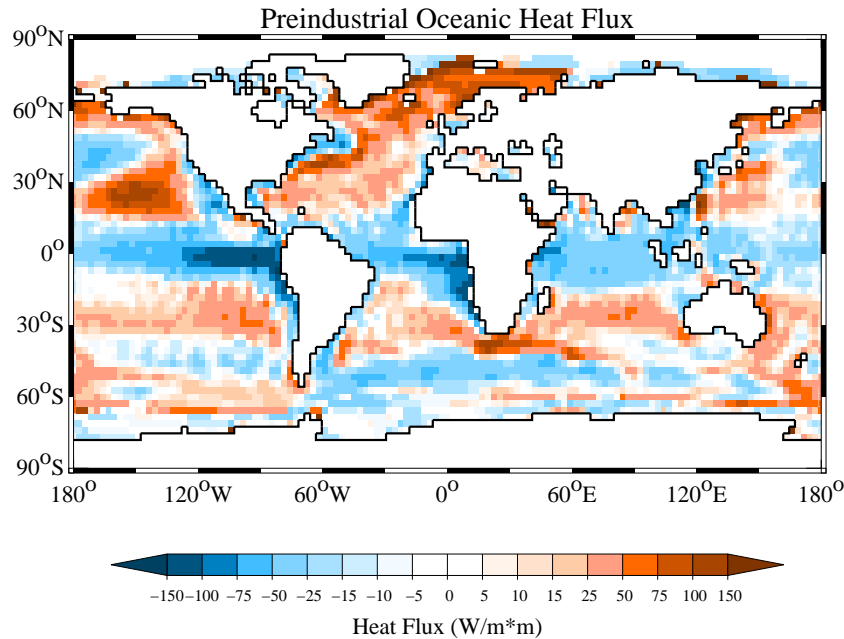


Figure 2.2: Ocean heat fluxes for a preindustrial T42 simulation experiment.

effect induced by the increase of CO_2 concentration. The climate sensitivity of the Planet Simulator under calculated oceanic conditions is consistent, but slightly larger than the climate sensitivities, from $+2.6^\circ\text{C}$ to 4.4°C , of atmospheric GCMs coupled to slab ocean models given in the IPCC report (CUBASCH et al., 2001).

The oceanic heat fluxes distribution we obtained for a preindustrial experiment in T42 is shown in Figure 2.2. The warm and cold currents are respectively characterized by positive and negative values. The ocean heat fluxes reproduce well the main warm currents of the Northern Hemisphere, such as the Gulf Stream and the Kuro-Sivo, and the cold currents, notably the Antarctic circumpolar, Benguela and Humboldt currents.

2.1.3 Sea-ice

The Planet Simulator also includes a thermodynamic sea-ice model, based on the zero layer model of SEMTNER (1976). The sea-ice model computes the thickness of the sea-ice from the thermodynamic balances at the top and the bottom of the sea-ice. The sea-ice temperature is calculated from the energy

balance at the ice surface. The zero layer model is based upon the assumption that the temperature gradient in the ice is linear and that the capacity of the ice to store heat can be neglected. The ice concentration over each ocean point is represented by a prognostic variable, which is equal to zero if the ocean point is ice-free, or equal to 1 if the ocean point is ice-covered.

Sea-ice is formed if the ocean temperature drops below the freezing point for sea-water (271.25 K for a standard salinity of sea-water (JACOBSON, 2005)), and is melted if the ocean temperature increases above this point. The freezing point for sea-water is a critical threshold in the model. Indeed, the ice-free ocean points where the temperature drops just below the freezing point, are completely covered by ice with an ice concentration equal to 1. The transition from ice-free to ice-covered points, and conversely, is therefore very sensitive to temperature changes.

Similarly to the ocean module, a flux correction can be prescribed on the ice-covered points. The flux correction for sea-ice is calculated as

$$Q_c = \frac{\rho_i L_i}{\epsilon} (h_i - h_{clim}),$$

where ρ_i represents the density and L_i the latent heat of fusion of sea-ice. h_i and h_{clim} are respectively the calculated and the climatological ice thickness, and ϵ is a relaxation constant.

The sea-ice model is equipped with a snow cover, and the thickness of the snow cover is calculated. The presence of snow on the grid-cell changes the albedo properties, as snow has a slightly higher albedo than ice. The albedo of sea-ice is calculated in function of the ice temperature, T_{ice} , as

$$Alb^{ice} = \min(Alb_{max}^{ice}, 0.5 + 0.025(273.16 - T_{ice})).$$

By default, the maximum ice albedo Alb_{max}^{ice} is equal to 0.7, or 0.8 in the presence of snow. Therefore, if an ocean point becomes ice-covered, its surface albedo shifts from 0.069 (standard sea-water albedo in the Planet Simulator) to 0.7 or 0.8 which strongly impacts the energy balance at the surface.

2.1.4 Land surface and soil

The terrestrial component includes the calculation of temperatures for the surface and the soil, a soil hydrology and a river transport scheme. In addition, surface properties like the albedo, the roughness length or the evaporation efficiency are provided. Glaciers are treated like other land points, but with surface and soil properties appropriate for ice.

The surface temperature is computed from the linearised energy balance of the uppermost meters of the ground (0.2 m by default).

$$c_{top}z_{top}\frac{\Delta T_S}{\Delta t} = F_S - G + \Delta T_S \frac{\partial(Q_a - Q_g)}{\partial T_S} - Q_m, \quad (2.2)$$

where c_{top} is the volumetric heat capacity and z_{top} is the uppermost layer thickness. Q_a denotes the total heat flux from the atmosphere, which consists of the sensible heat flux, the latent heat flux, the net short wave radiation and the net long wave radiation. Q_g is the flux into the deep soil. Q_m is the snow melt heat flux. F_S and G are respectively the conductive heat fluxes from the surface to the ground and from the ground to the surface.

Below the uppermost layer, the soil column is discretised into 5 layers, which thicknesses increase with depth. The temperature of each soil layer is calculated from an energy balance taking into account the conductive heat flux between the layers.

The parameterisation of soil hydrology comprises the budgets for snow amount and the soil water amount. The soil water reservoir is represented by a single-layer bucket model (MANABE, 1969). Soil water is increased by precipitation and snow melt, and is depleted by the surface evaporation. In this simple bucket model, the soil water is limited by a field capacity, which geographical distribution can be prescribed or set to a default value of 0.5 m everywhere. If the soil water exceeds the field capacity, the excessive water builds the runoff. The local runoff is transported to the ocean by a river transport scheme with linear advection (SAUSEN et al., 1994).

Modifications of the field capacity (maximum bucket size) may significantly affect the hydrological cycle, by limiting or increasing the surface evaporation that in turn affects the precipitation rate and the surface temperature. An increase of the rooting depth (the depth at which plants are able to grow roots), linked for example to the replacement at high latitudes of tundra by boreal forest, contributes to increase the field capacity, and therefore to increase the surface evaporation.

The geographical distribution of other land surface parameters, such as the surface albedo and the roughness length, can also be prescribed. However, the seasonal variations of these parameters are not taken into account, and only an annual distribution can be prescribed. The background albedo is only modified in the presence of snow on the land point following:

$$A_S = A_S^{clim} + (A_S^{snow} - A_S^{clim}) \frac{z_{snow}}{z_{snow} + 0.01}, \quad (2.3)$$

where A_S^{clim} is the prescribed surface albedo, z_{snow} is the snow depth, and A_S^{snow} the snow albedo, which depends on surface temperature

$$A_S^{snow} = A_{max}^{snow} + (A_{min}^{snow} - A_{max}^{snow}) \frac{T_S - 263.16}{10}, \quad (2.4)$$

with $A_{min}^{snow} \leq A_S^{snow} \leq A_{max}^{snow}$ and default values $A_{max}^{soil} = 0.8$ and $A_{min}^{soil} = 0.4$.

A change in the surface albedo directly affects the energy balance at the surface, which in turn impacts on the surface temperatures and surface heat fluxes. An increase of the surface albedo, linked notably to the formation of snow cover, or to the replacement of forests by grasslands or deserts, induces a decrease of surface temperature. The Planet Simulator is very sensitive to the surface albedo changes, as observed in FRAEDRICH et al. (2005b), HENROT (2006) and HENROT et al. (2009).

The roughness length is used to calculate the zonal and meridional momentum, sensible and latent heat fluxes, and influences the movements of the atmospheric masses near the surface. The prescribed roughness length distribution is not modified on land. Roughness length is modified over the ocean points following the Charnock formula (LUNKEIT et al., 2007). The Planet Simulator is less sensitive to roughness length changes, notably induced by modification of the vegetation cover (HENROT, 2006, 2007). In most cases, the roughness length effect is dominated and masked by the surface albedo effect.

2.1.5 Vegetation

In order to complete the description of the Planet Simulator, we also present here briefly the simple vegetation model that it includes. SIMBA (Simulator of Biospheric Aspects) uses a simple dynamic parameterization to calculate the dynamics of those land surface parameters that are strongly affected by terrestrial vegetation, i.e., background albedo, roughness length, and depth of the rooting zone. These parameters are simulated as functions of two carbon pools, a fast pool to represent leaf area, and a slow pool to represent woody biomass.

Nevertheless, we did not use this vegetation component in this study, since we preferred to work with the more complex dynamic vegetation model CARAIB, described in the following section.

2.1.6 Present-day climate simulation with the Planet Simulator

In order to assess the ability of the Planet Simulator to reproduce correctly present-day climate, we briefly present here the results of two present-day climate simulations with the Planet Simulator on T21 and T42 grids, and compare these results with the NCEP/NCAR reanalysis data (KALNAY et al., 1996). A more complete description of the model's standard climate and evaluation against ERA-40 reanalysis data has been done by HABERKORN et al. (2009).

The two simulations discussed here have been forced with standard sets of boundary conditions on respectively T21 and T42 grids, described notably in the following chapters (Chapters 4 and 5) and also in more details in HENROT (2007). The T21 and T42 reference simulations have been forced with a present-day orbital configuration (eccentricity 0.016724, obliquity 23.446° and longitude of perihelion 102.04°) and solar constant (1365 W/m^2). The atmospheric CO_2 concentration was set to the value of 360 ppmv. The present-day land-sea distribution, land-ice cover and topography have been reconstructed from Peltier's ICE-5G ice sheet reconstruction (PELTIER, 2004). The surface boundary condition parameters controlled by the vegetation cover (surface albedo, roughness length and field capacity) have been derived from the CARAIB modern vegetation distributions presented in Section 3.1.1. As initial conditions over ocean grid-cells, we used monthly present-day sea-surface temperature and sea-ice distributions derived from the AMIP2 database (AMIP2, 2004). We prescribed the heat transfer calculated by the Planet Simulator for a present-day climate, following the procedure described in Section 2.1.2. The results of the reference simulations (averages over the last 20 years of 50-year simulations) are compared in terms of global and zonal climate with the NCEP/NCAR reanalysis data KALNAY et al. (1996). The reanalysis climatic variables used here (surface air temperature and total precipitation) have been derived from data assimilation using data from 1948 to 1996. The horizontal resolution of the NCEP/NCAR reanalysis data is T62 (192 longitudes and 94 gaussian latitudes).

Both T21 and T42 control simulations are characterised by a global annual mean surface temperature around 13.5°C that is in good agreement with the global annual mean surface temperature of 13.8°C derived from the NCEP/NCAR reanalysis (see Table 2.1). The global temperatures are about 1°C cooler over the oceans, whereas they are slightly warmer over the continents, relative to the global oceanic and continental temperatures of the

Table 2.1: Global, continental and oceanic annual mean near-surface temperature T_{2m} ($^{\circ}\text{C}$) and precipitation (mm/yr) for the T21, T42 simulations and NCEP/NCAR reanalysis. The continental mean excludes the contribution from Antarctica.

	T_{2m} ($^{\circ}\text{C}$)			Prc (mm/yr)		
	<i>Global</i>	<i>Ocean</i>	<i>Continent</i>	<i>Global</i>	<i>Ocean</i>	<i>Continent</i>
CTRL T21	13.6	15.3	12.8	1097	1161	941
CTRL T42	13.5	15.1	13.2	1119	1203	942
NCEP/NCAR	13.8	16.2	12.0	986	1050	876
	JJA T_{2m} ($^{\circ}\text{C}$)					
CTRL T21	15.2	15.6	19	1118	1151	1051
CTRL T42	14.9	15.3	19.1	1130	1187	1032
NCEP/NCAR	15.4	16.3	18.8	1040	1017	1075
	DJF T_{2m} ($^{\circ}\text{C}$)					
CTRL T21	11.8	15.0	5.9	1076	1167	850
CTRL T42	11.9	14.9	6.1	1115	1224	862
NCEP/NCAR	12.3	16.1	4.9	967	1055	789

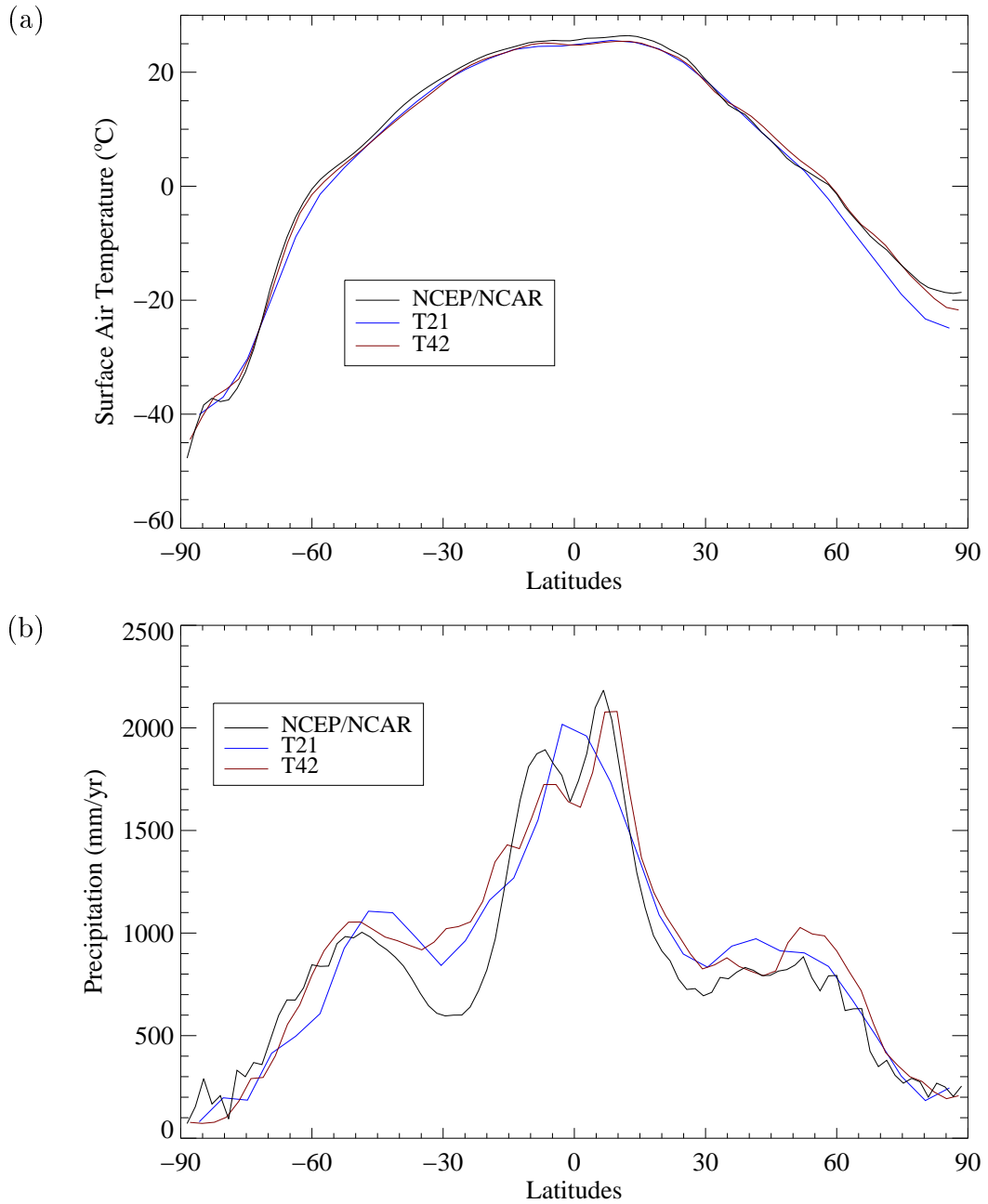


Figure 2.3: Zonal annual mean (a) surface air temperature and (b) precipitation for the control simulations and the NCEP/NCAR reanalysis.

2.1. THE PLANET SIMULATOR MODEL

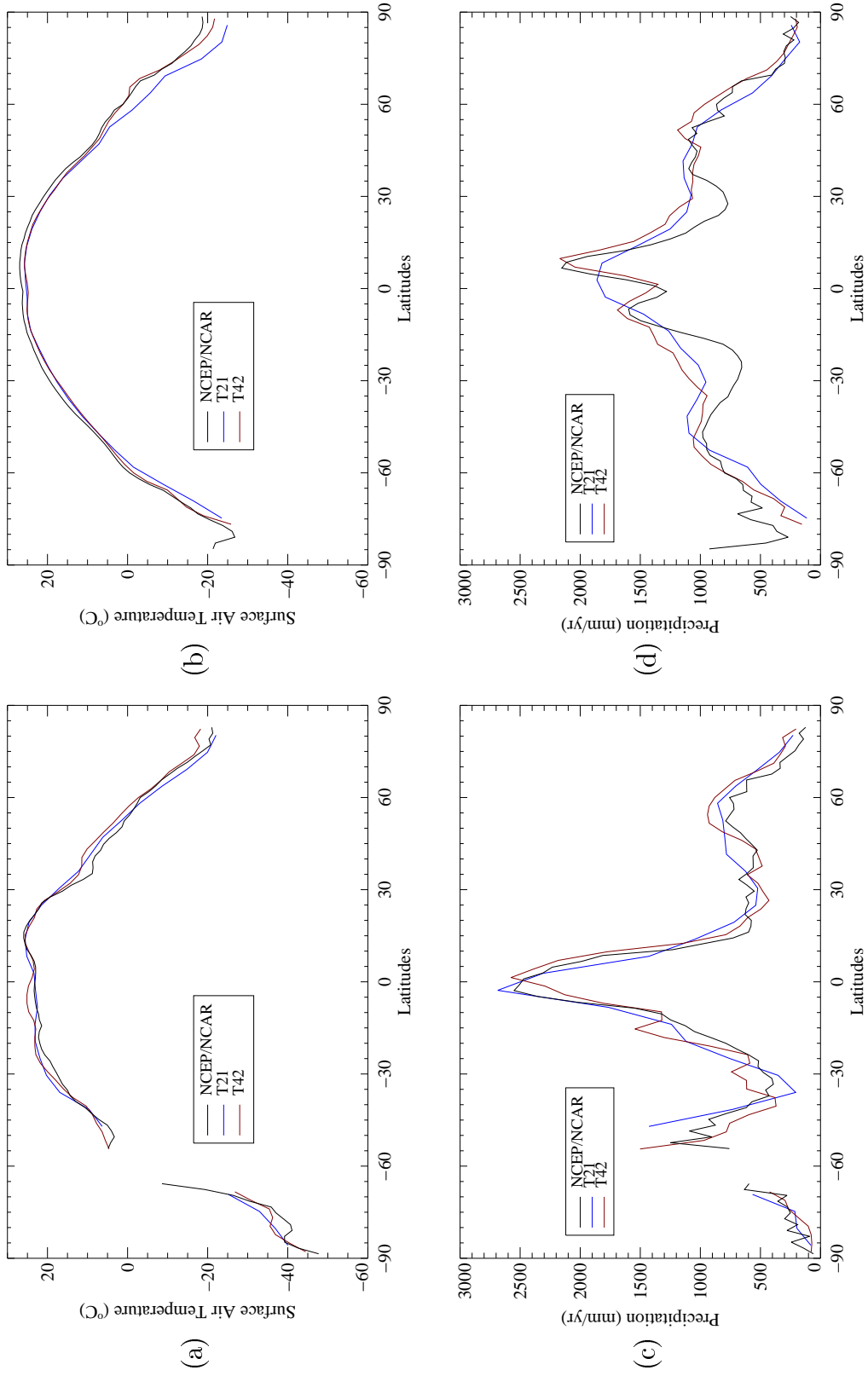


Figure 2.4: Zonal annual mean surface air temperature (a) over the continents and (b) over the oceans, and zonal annual mean precipitation (c) over the continents and (d) over the oceans for the control simulations and the NCEP/NCAR reanalysis.

reanalysis. Thus, the cooler global temperatures obtained here can mainly be attributed to a cold bias of the model at high latitudes, and especially in winter and over the oceans. HABERKORN et al. (2009) found similar results and attributed the cold bias of the model to the use of prescribed sea-ice cover in their setup. Here, the cold bias is less marked because we let sea-ice cover adjust as a function of the prescribed heat transfers in the oceans and sea-ice. Zonally, both simulations reproduce well the temperature profile (see Figure 2.3). However, passing from T21 to T42 resolution improves the temperatures estimations, especially northward of 50°N . In contrast, at both resolutions, the model gives warmer temperatures in summer of the Northern Hemisphere, and tend to slightly overestimate the continental temperatures around 30 to 40°N and S.

On the other hand, the model systematically overestimates the precipitation rates, as also found by HABERKORN et al. (2009). This tendency subsists all year long, but is more marked over the oceans during the summer of the Northern Hemisphere. As shown in Figure 2.3, the model well reproduces the zonal distribution of the precipitation. The two maxima of precipitation around the equator, corresponding to the location of the Intertropical Convergence Zone (ITCZ) are only represented in T42. However, at both resolution the model overestimates the precipitation around 30°N and S, mainly over the oceans, and also at middle latitudes around 50°N and S. This is a consequence of the overestimation of the surface evaporation in the Planet Simulator (HABERKORN et al., 2009). This effect is more marked at higher resolution.

Regionally, besides the differences in resolution, both control simulations give very similar temperature and precipitation distributions. Figures 2.5 and 2.6 show the annual, the December, January, February (DJF) and the June, July, August (JJA) mean surface air temperature and precipitation for the T21 control simulation. Figures 2.7 and 2.8 show the same variables for the T42 control simulation. The differences in the simulated climate can mainly be explained by resolution-dependent effects. A finer resolution notably enables a better representation of local effects. For example, the more accurate representation of the topography in T42 allows a more detailed representation of the topography induced effects on temperature (decreasing temperature with increasing altitude, and conversely), e. g., over the high reliefs of Asia and South America.

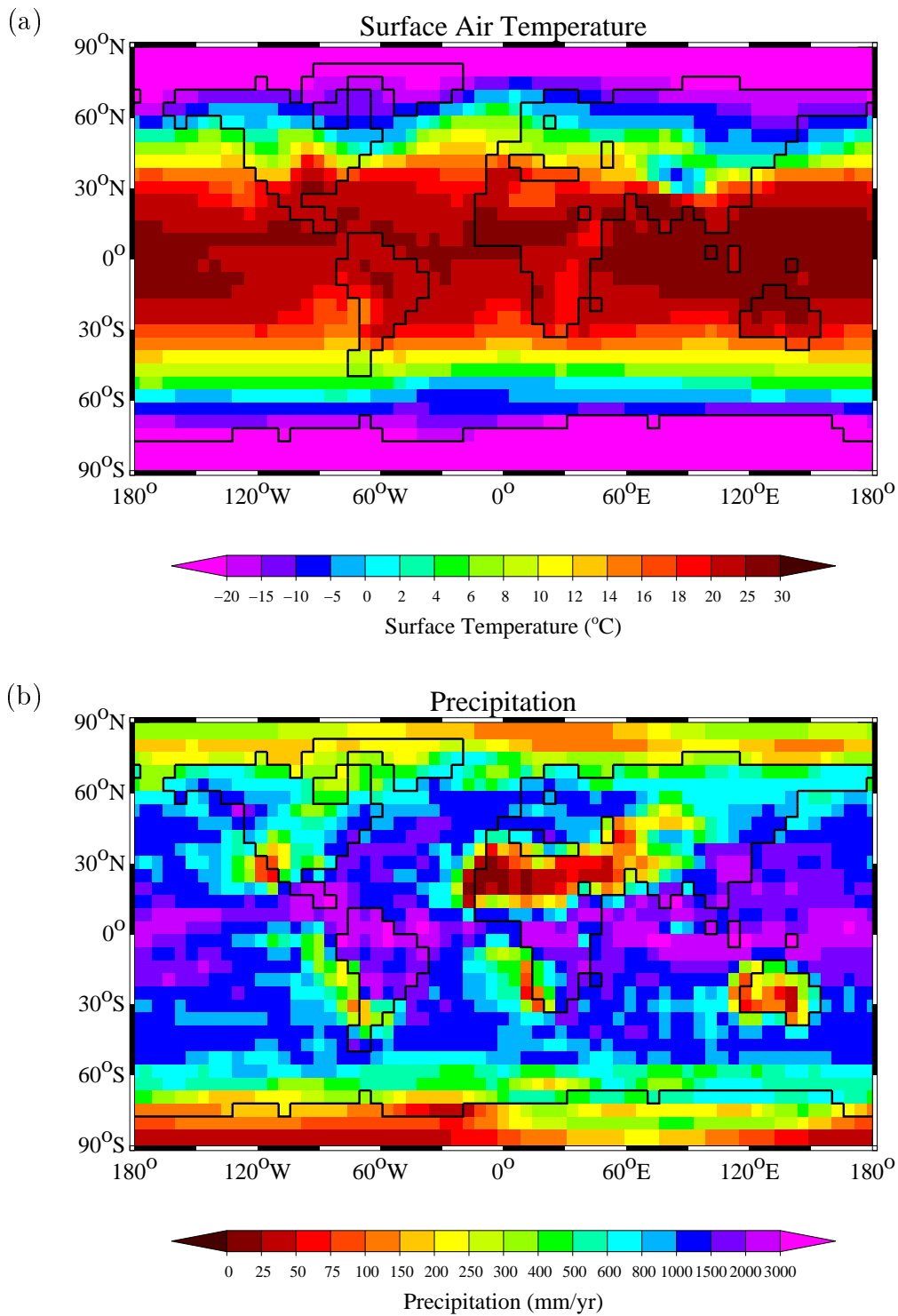


Figure 2.5: Annual mean (a) surface air temperature and (b) precipitation for the control simulation in T21.

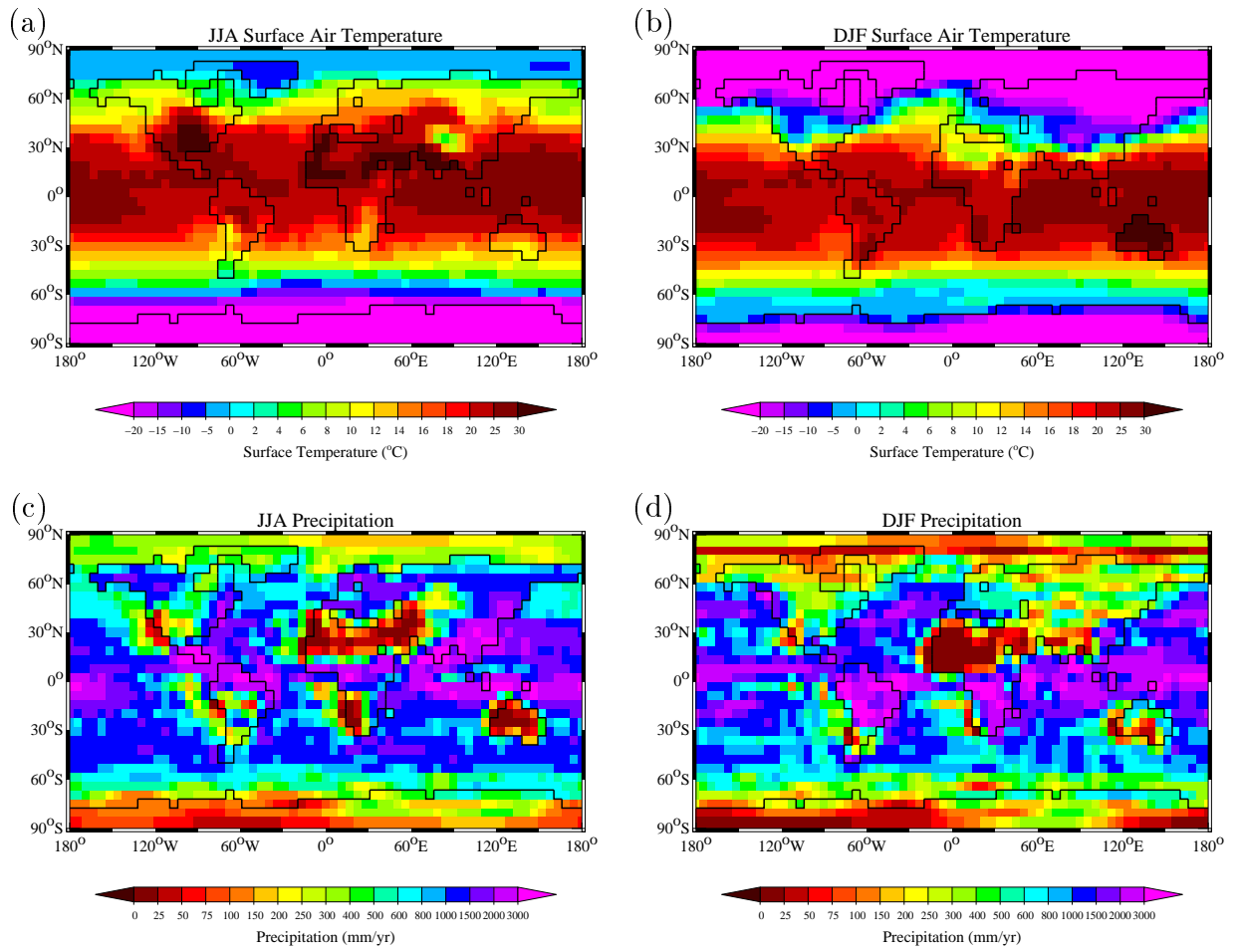


Figure 2.6: (a) JJA and (b) DJF surface air temperatures, and (c) JJA and (d) DJF precipitation for the control simulation in T21.

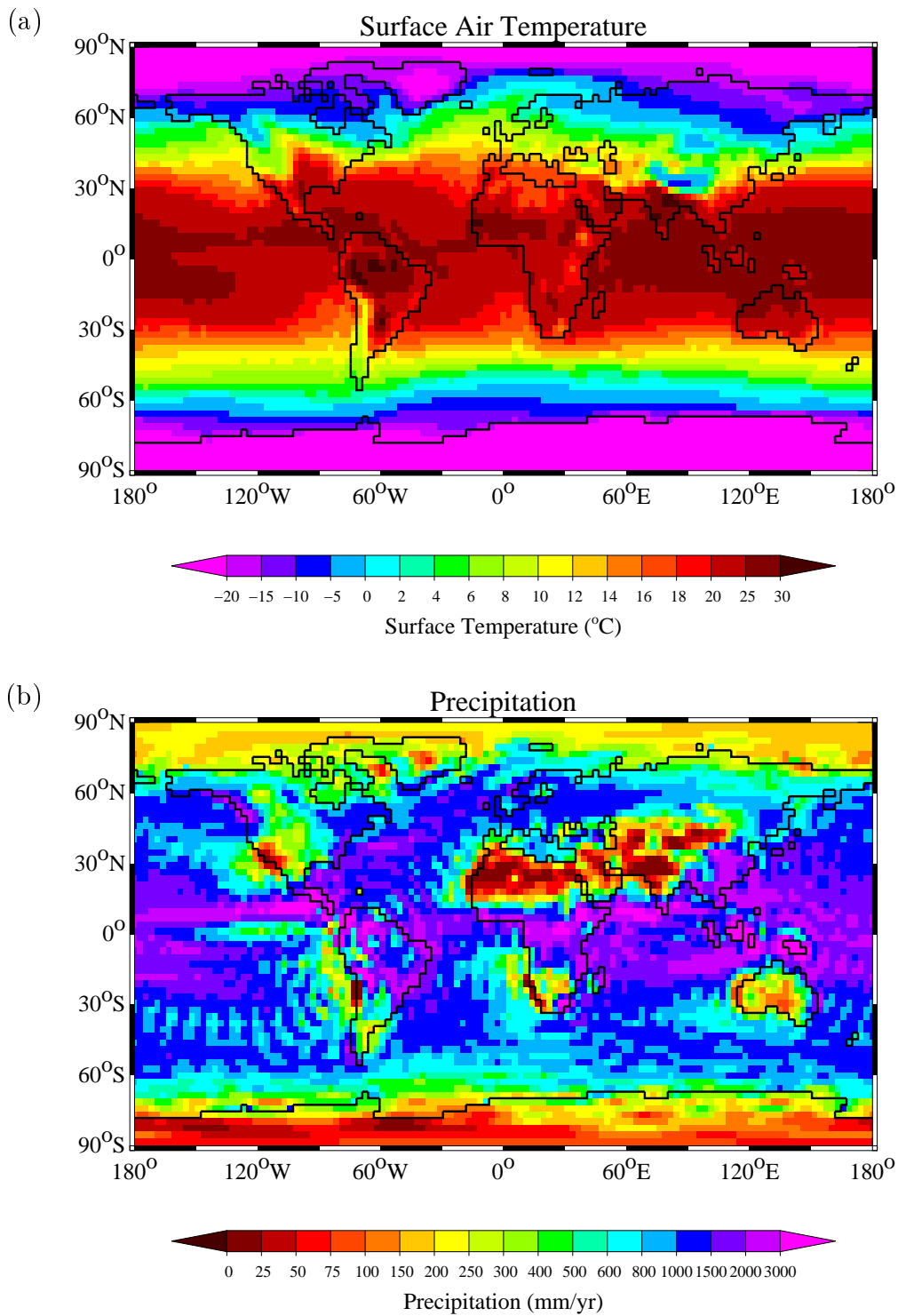


Figure 2.7: Annual mean (a) surface air temperature and (b) precipitation for the control simulation in T42.

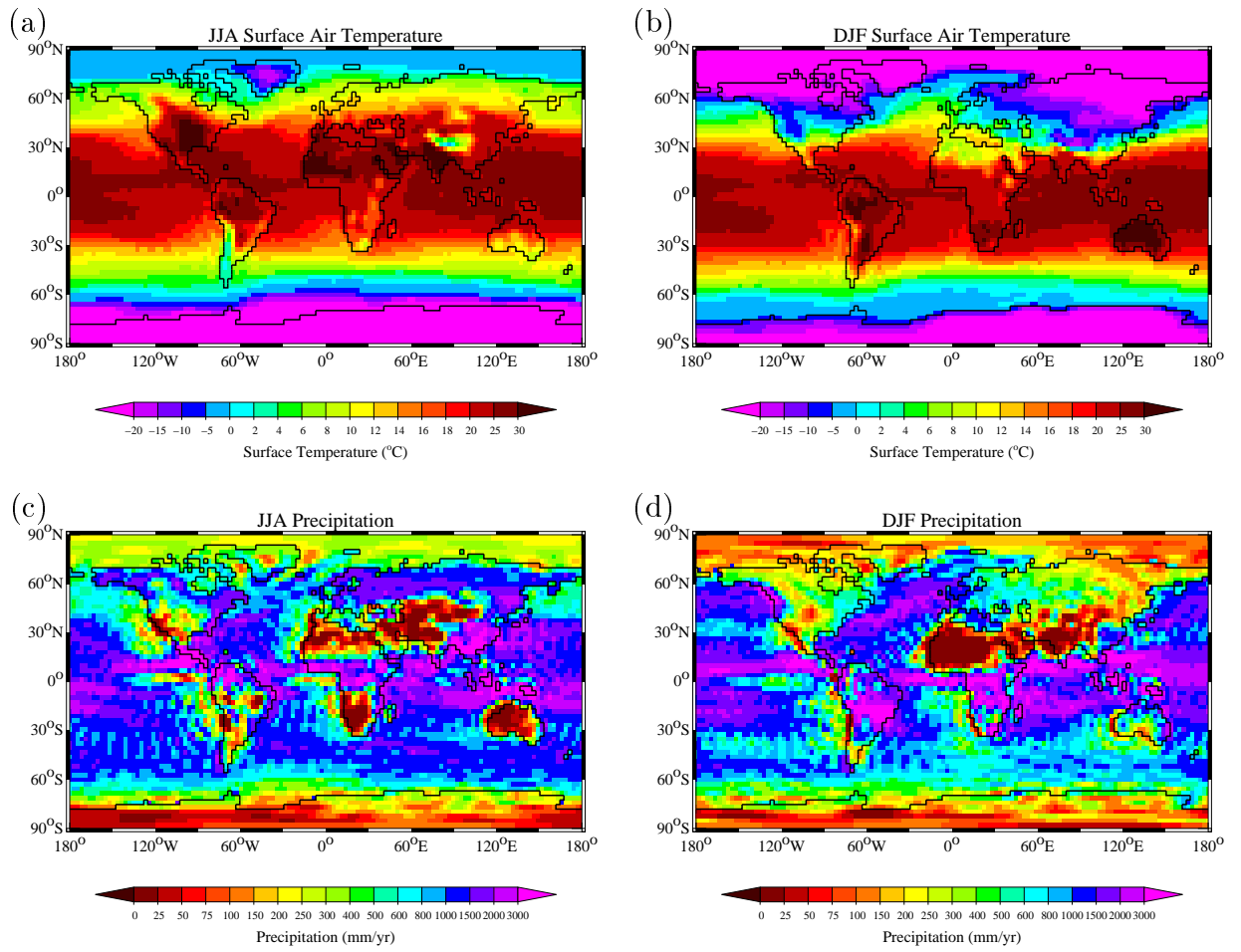


Figure 2.8: (a) JJA and (b) DJF surface air temperatures, and (c) JJA and (d) DJF precipitation for the control simulation in T42.

2.2 The CARAIB model

The CARAIB model (CARbon Assimilation In the Biosphere) is a global dynamic vegetation model developed at the Laboratory for Planetary and Atmospheric Physics (LPAP) and Unité de Modélisation du Climat et des Cycles Biogéochimiques (UMCCB) of the University of Liège. CARAIB has been originally designed to study the carbon cycle in the terrestrial biosphere and especially the role of the land ecosystems in atmospheric CO₂ sequestration. Since its first version in 1994 (WARNANT et al., 1994), several parameterisations and modules of the model have been improved and implemented (NEMRY et al., 1996; GÉRARD et al., 1999; WARNANT, 1999; OTTO et al., 2002; LAURENT et al., 2008; DURY et al., submitted).

The CARAIB model has been widely used to study the role of vegetation in the global carbon cycle and to reconstruct vegetation distributions at present (WARNANT et al., 1994; NEMRY et al., 1996; GÉRARD et al., 1999; LAURENT et al., 2008), and in the past, notably at Last Glacial Maximum and Mid-Holocene times (FRANÇOIS et al., 1998, 1999; OTTO et al., 2002; CHEDDADI et al., 2006; GALY et al., 2008; HENROT et al., 2009), and at different time slices of the Miocene (FRANÇOIS et al., 2006; FAVRE et al., 2007; FRANÇOIS et al., submitted; HENROT et al., 2010). Recently, it has been used for future projections (DURY et al., submitted). It should be noticed that we have worked here with the CARAIB version described in GALY et al. (2008).

As illustrated in Figure 2.9, in its current version the CARAIB model is composed of five modules describing respectively (1) the hydrological budget, (2) canopy photosynthesis and stomatal regulation, (3) carbon allocation and plant growth, (4) heterotrophic respiration and litter/soil carbon dynamics, and (5) plant competition and biogeography.

The model takes into account a set of herbaceous and tree Plant Functional Types (PFTs), which can coexist on the same grid cell. The PFT concept groups plants according to their function in ecosystems and their use of resources. The classification of plants into PFTs takes into account phylogentic (taxonomic groups) and life-form characteristics (such as plant size, leaf size, leaf shape, seasonality of leaves, rooting depth, etc.). For each of these PFTs, the model calculates the temporal evolution of two carbon reservoirs in the plant (metabolic and structural carbon) and three in the soil (metabolic and structural litter, soil organic carbon). The model time step is one day for updating all water and carbon reservoirs, but photosynthesis and plant respiration are calculated every two hours, in order to

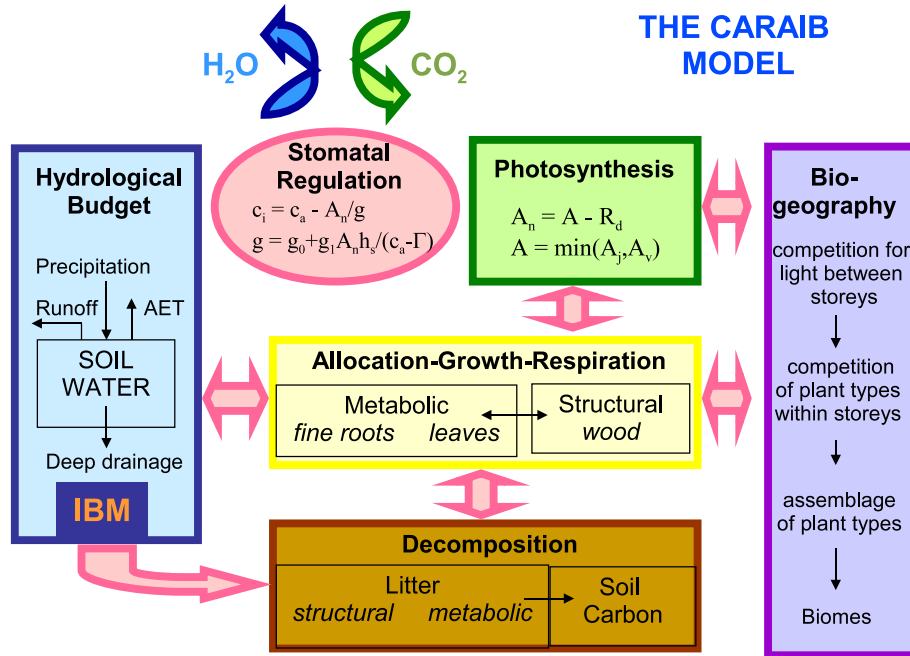


Figure 2.9: Components of the CARAIB model.

take into account non-linear effects associated with the variation of photosynthetic/respiration fluxes over the day. Vegetation cover is updated once a month for herbs and once a year for trees. Spatially, the CARAIB model is a grid-point model, and it can be used with different spatial resolution. Furthermore, several plant functional types and Bioclimatic Affinity Groups (BAGs) classifications have been developed to be used within the CARAIB model (OTTO et al., 2002; LAURENT et al., 2004; UTESCHER et al., 2007).

2.2.1 Hydrological module

The hydrological module IBM (Improved Bucket Model) calculates the soil water content, the amount of snow and the associated hydrological fluxes (HUBERT et al., 1998; FRANÇOIS et al., 2006). The model consists of one reservoir of soil water corresponding to the root zone. The evolution of the soil water content in the root zone is calculated for all PFTs together, assuming that all PFTs share the same soil water reserve. Root depths are in

the range of 0.5-1.7 m depending on vegetation type (SCHENK and JACKSON, 2002). The soil water budget is calculated as

$$\frac{dW}{dt} = P + SM - E - D - SR, \quad (2.5)$$

where W is the soil water content. The inputs of the soil water reservoir are the precipitation P and snowmelt SM . The output fluxes of the reservoir are the evapotranspiration E , the drainage D and the surface runoff SR .

Daily precipitation P is the only prescribed water flux. It is separated into its rain and snow contributions, according to the values of the minimum and maximum temperatures over the day. Snow precipitation feeds the snow reservoir. The output fluxes of this reservoir are snowmelt and snow evaporation. Snow evaporates at the Potential EvapoTranspiration rate (PET). Snowmelt occurs if the maximum temperature exceeds 0°C. A fraction of rain precipitation can be intercepted by the foliage and re-evaporated before reaching the ground. This fraction is parameterised as a function of the canopy Leaf Area Index (LAI, defined as the ratio of total upper leaf surface of vegetation divided by the surface area of the land on which the vegetation grows) and of the ratio P/PET . This parameterisation was developed on the basis of a reservoir model for leaf surface water using a 1-minute time step and assuming a statistical distribution of the precipitation during the day. Potential evapotranspiration PET is calculated according to Penman's equation (MINTZ and WALKER, 1993). The fraction of rainwater reaching the ground, and the snowmelt are therefore the input fluxes to the soil water reservoir. Surface soil evaporation and vegetation transpiration are represented as a single flux in the model, which is calculated as a function of PET and soil water amount. Soil water is assumed to be drained out at the bottom of the root zone at a rate equal to the soil hydraulic conductivity, which is evaluated as a function of soil water content and soil texture (SAXTON et al., 1986). When the soil layer reaches saturation, the excess water is evacuated as surface runoff.

2.2.2 Canopy photosynthesis and stomatal regulation

The photosynthetic calculation is performed separately for all model PFTs. It is based on FARQUHAR et al. (1980) model for C_3 plants and on COLLATZ et al. (1992) for C_4 plants. C_3 plants, accounting for the majority of earth's plant species, use enzyme rubisco to make a three-carbon compound as the first stable product of carbon fixation. C_3 plants flourish in cool, wet, and

cloudy climates, where light levels may be low, because the metabolic pathway is more energy efficient, and if water is plentiful, the stomata can stay open and let in more carbon dioxide. However, water losses are high. C_4 plants use biochemical and anatomical mechanisms to raise the intercellular carbon dioxide concentration at the site of fixation and the first stable product of carbon fixation is a four-carbon compound. By limiting the carbon losses through photorespiration, C_4 plants have higher photosynthesis efficiency than C_3 plants. C_4 plants are therefore better adapted to hot and dry environments.

Stomatal conductance is calculated using the parameterisation of BALL et al. (1987), modified by WIJK et al. (2000) to account for soil water dependence. Photosynthetic rates and stomatal conductance are evaluated in a series of 16 canopy layers of 0.5 thickness in LAI. Each layer is subdivided into its sunlit and shaded components. Radiative transfer of Photosynthetic Active Radiation (PAR) is treated according to the model of GOUDRIAAN and VAN LAAR (1994). Herbs are assumed to grow below trees, except if environmental conditions are such that no tree can survive on the grid cell. Consequently, herb photosynthesis is limited by the amount of light transmitted through the tree canopy.

2.2.3 Carbon allocation and plant growth

The photosynthetic products are allocated to two carbon reservoirs corresponding to metabolic (leaves and fine roots) and structural (wood and coarse roots) tissues. The partitioning of this carbon allocation among the two pools is specific to each PFT and depends on environmental conditions (OTTO et al., 2002). The output fluxes of these vegetation pools are autotrophic respiration and litter production. Autotrophic respiration is divided into maintenance and growth respiration. The maintenance respiration is proportional to the carbon content of the pool and varies exponentially with temperature. The growth respiration is proportional to the biomass increase. Only part of the structural pool is subject to respiration. Litter is produced by the mortality of metabolic and structural tissues, through seasonal leaf fall of deciduous species, plant death due to natural regeneration of the canopy, and plant death due to unfavorable climatic conditions (OTTO et al., 2002).

2.2.4 Heterotrophic respiration and litter/soil carbon

This module calculates heterotrophic respiration rates, as well as the time evolution of metabolic litter, structural litter and soil carbon reservoirs. Heterotrophic respiration is a function of temperature, soil moisture and depends linearly on the reservoir content (NEMRY et al., 1996).

2.2.5 Plant competition and biogeography

This last module evaluates steady state distribution of all tree and herb PFTs on each grid-cell of the studied geographical area. Seed production, as well as their dispersal and germination is not explicitly described in the current version of CARAIB. The share of the area (cover fraction) in a given storey between PFTs is performed according to the net primary productivities (NPP=photosynthesis-autotrophic respiration) of the relevant PFTs. The model canopy is divided into two storeys: overstorey corresponding to trees and understorey to grasses. Grass PFTs fill the lower layers of the canopy and exhibit substantial photosynthesis only if the overstorey canopy is not fully developed, i.e., if the number of canopy layers occupied by trees is small enough to allow the penetration of significant sunlight.

PFT classification

In the current version of the CARAIB model, the plant species are classified into plant functional types PFTs. A PFT comprises botanical species that share common morphological and phenological attributes, and therefore play a similar role within an ecosystem (UTESCHER et al., 2007). Here we used a classification including 15 PFTs, described in UTESCHER et al. (2007) and GALY et al. (2008). This 15-type classification has been obtained by grouping several plant types (Bioclimatic Affinity Groups, BAGs) of the classification developed by LAURENT et al. (2004) for modern European trees (PFTs 3, 4, 5, 7, 9, 11, 12 and 13), by adding some new classes corresponding to warm temperate trees (PFTs 6, 8 and 10) and by keeping the classes of the original CARAIB classification (OTTO et al., 2002) for tropical trees (PFTs 14, 15) and herbs (PFTs 1 and 2). The 15-PFT classification comprises two types for the herbs (C_3 and C_4 herbs), and thirteen types for the trees, mainly distributed in needleleaved evergreen, needleleaved summergreen, broadleaved deciduous, broadleaved raingreen, and broadleaved evergreen trees. Tree types are differentiated on the basis of climatic thresholds. The list of the 15 PFTs is given in Table 2.2.

Table 2.2: Plant functional types (PFTs) of the 15-PFTs classification.

PFTs	Example of species
1. C_3 herbs	<i>Asteraceae, Poaceae, campanula</i>
2. C_4 herbs	<i>Amaranthaceae, Bambusoideae</i>
3. Needleleaved evergreen boreal/temperate cold	<i>Cupressaceae, Juniperus, Abies</i>
4. Needleleaved evergreen temperate cool	<i>Abies alba, Taxus, Sequoia sempervirens</i>
5. Needleleaved evergreen temperate dry warm	<i>Cedrus, Cupressus, Pinus halepensis</i>
6. Needleleaved evergreen temperate perhumid warm	<i>Cathaya, Sciadopitys</i>
7. Needleleaved summergreen boreal/temperate cold	<i>Larix decidua</i>
8. Needleleaved summergreen temperate warm	<i>Taxodium, Glyptostrobus</i>
9. Broadleaved evergreen temperate dry warm	<i>Olea europaea, Pistacia, Quercus ilex</i>
10. Broadleaved evergreen temperate perhumid warm	<i>Alangium, Castanopsis, Magnolia</i>
11. Broadleaved summergreen boreal/temperate cold	<i>Alnus, Quercus robur, Populus, Tilia, Betula, Salix</i>
12. Broadleaved summergreen temperate cool	<i>Acer campestre, Fagus sylvatica, Ulmus</i>
13. Broadleaved summergreen temperate warm	<i>Castanea, Juglans, Ostrya, Halesia</i>
14. Broadleaved rainingreen tropical	<i>Acacia, Bursera, Dendropanax</i>
15. Broadleaved evergreen tropical	<i>Annona, Bombax, Cupiana</i>

Biome assignment scheme

In an off-line scheme, the PFT assemblages are converted into biomes on the basis of several criteria, involving mostly vegetation parameters predicted by the model (dominant PFT and its cover fraction, total NPP, total LAI, LAI of trees, and ratio between grass NPP and tree NPP). A simplified biome prediction scheme is given in Table 2.3. We refer to FRANÇOIS et al. (submitted) for a more detailed description of the biome scheme (see Appendix A). Deserts correspond to areas where the NPP of all PFTs is equal to zero. The ice/polar desert biome is not assigned on the basis of vegetation characteristics, but from growing degree-days limits (GDD5 is the growing degree-days based on a temperature threshold of 5°C).

The biome distribution calculated here is based on plant physiology rather than on empirical climate-vegetation relationships. The advantage is that PFT assemblages and biome distributions can be calculated even for climatic or environmental configurations that do not have present-day analogues. The only limitation is that the model PFT classification is based on present-day vegetation and its known characteristics. To reconstruct past vegetation, we therefore have to assume that plants were relatively close to modern plants in terms of physiology and metabolism, following the nearest living relative or coexistence approach (MOSBRUGGER and UTESCHER, 1997). The biome distribution is useful for visualizing the model results. Preferably, it should not be used for comparison with data. Indeed, the biome limits are rather imprecise and the biome classification generally varies from one author to the other. The relative proportions of the various PFTs are more directly comparable with palaeobotanical or palynological data.

2.2.6 CARAIB inputs: climatic fields

The inputs of the CARAIB model are meteorological variables, which can be taken from meteorological databases or can be outputs from GCMs. The required variables are: daily mean air temperature, diurnal amplitude of air temperature (maximum-minimum air temperature over the day), precipitation, fraction of sunshine hours during daylight period, air relative humidity, and wind speed. CARAIB also needs the soil texture (percentage of silt, sand and clay) used in the hydrological module.

The climatic inputs must be provided at a daily frequency. However, global databases, such as those of LEEMANS and CRAMER (1991) or NEW et al. (2002), generally provide monthly means of the required variables.

Table 2.3: CARAIB biome assignment scheme. NPP_{tot} is the total NPP of the grid cell, LAI_{tot} the total leaf area index of the grid cell (herbs+trees), LAI_{tree} the leaf area index of the trees, and R is the ratio between herb NPP and tree NPP. f_{C4} is the fraction of C_4 herbs in the under-storey. f_{cold} is the fraction of boreal/temperate cold trees, f_{bdec} the fraction of broadleaved summergreen boreal/temperate trees, f_{ndll} the fraction of temperate needle-leaved trees, f_{med} the fraction of temperate dry warm trees, f_{strop} the fraction of humid warm trees, and f_{trop} the fraction of tropical trees in the over-storey.

Biomes	GDD5	NPP_{tot}	LAI_{tot}	R	other conditions
1. Ice/Polar Desert	<50				
2. Desert	≥ 50	0			
3. Semi-desert	>500	$\neq 0$	<0.3		
4. Tundra	[50-500]	$\neq 0$			$LAI_{trees} < 0.8$
5. Tropical grassland	>500	$\neq 0$	≥ 0.3	>0.8	$LAI_{trees} < 0.8, f_{C4} > 0.5$
6. Temperate grassland	>500	$\neq 0$	≥ 0.3	>0.8	$LAI_{trees} < 0.8, f_{C4} \leq 0.5$
7. Tropical savanna		$\neq 0$	≥ 0.3	>0.8	$LAI_{trees} \geq 0.8, f_{C4} > 0.5$
8. Warm temperate open woodland		$\neq 0$	≥ 0.3	>0.8	$LAI_{trees} \geq 0.8, f_{C4} \leq 0.5,$ $f_{med} + f_{strop} > 0.5$
9. Cold temperate/boreal open woodland		$\neq 0$	≥ 0.3	>0.8	$LAI_{trees} \geq 0.8, \leq 0.5,$ $f_{med} + f_{strop} \leq 0.5$
10. Tropical rainforest		$\neq 0$	≥ 0.3	≤ 0.8	$f_{trop} > 0.67, \text{ dominant PFT } 15$
11. Tropical seasonal forest		$\neq 0$	≥ 0.3	≤ 0.8	$f_{trop} > 0.67, \text{ dominant PFT } 14$
12. Subtropical forest		$\neq 0$	≥ 0.3	≤ 0.8	$f_{strop} + f_{trop} > 0.67$
13. Warm temperate broadleaved evergreen forest		$\neq 0$	≥ 0.3	≤ 0.8	$f_g > 0.67$
14. Warm temperate conifer forest		$\neq 0$	≥ 0.3	≤ 0.8	$f_{ndll} > 0.67, \text{ dominant PFT } 5$
15. Warm temperate mixed forest		$\neq 0$	≥ 0.3	≤ 0.8	$f_{strop} + f_{trop} \leq 0.67,$ dominant PFTs 5,9
16. Temperate broadleaved deciduous forest		$\neq 0$	≥ 0.3	≤ 0.8	$f_{bdec} > 0.67$
17. Cool temperate conifer forest		$\neq 0$	≥ 0.3	≤ 0.8	$f_{ndll} > 0.67,$ dominant PFTs 3,4,7
18. Cool temperate mixed forest		$\neq 0$	≥ 0.3	≤ 0.8	$f_{cold} \leq 0.8$
19. Boreal/montane forest		$\neq 0$	≥ 0.3	≤ 0.8	$f_{cold} > 0.8$

GCM outputs are also generally longterm monthly climatological means. Consequently, CARAIB includes a stochastic generator to transform the available monthly values into the daily inputs required by the model (HUBERT et al., 1998). The probabilities and distribution functions for daily temperatures and precipitation are assigned for 176 geo-climatic zones defined by combining Koppen's classification with a geographic division. For sunshine hours and relative humidity, two different values are produced every month, one for dry days and one for wet days. The wind speed is linearly interpolated between months. After stochastic generation the daily values are renormalised to conserve the monthly values.

Chapter 3

Interactions between the climate and vegetation models

This chapter presents the interactions between the climate and vegetation models that have been taken into account in this study. The first section describes how the outputs of the Planet Simulator are derived to obtain the climatic inputs required by the CARAIB model for present and past simulations. The correction of the GCM outputs using the anomaly method is also presented in the second part of this section. The second section deals with the calculation of the vegetation parameters that are needed by the Planet Simulator model to represent the vegetation cover effects on climate. The derivation of the surface albedo, roughness length and field capacity from the CARAIB outputs are described in detail here. The third section of this chapter presents the equilibrium asynchronous coupling procedure that has been applied in this work. Finally, we present the results of this coupling procedure on present-day climate and vegetation simulation experiments.

3.1 Climatic inputs for CARAIB

In order to produce vegetation distributions with CARAIB, several meteorological variables are required as input fields: mean temperature, diurnal temperature amplitude, precipitation, percentage of sunshine hours (derived from cloudiness), air relative humidity and wind speed. These variables can be taken from meteorological databases or can be outputs from GCM climate simulation experiments (see Section 2.2.6). However, there is currently no global proxy-based data set including all necessary input fields for

CARAIB, that could be used to produce vegetation distributions for past periods. Moreover, present-day vegetation reconstructions directly based on GCM outputs show systematic errors linked to biases in the GCM simulated climate in comparison to observations. Therefore, as explicated below, anomalies calculated between past and present simulated climate and added to a reference climatology are used to produce past vegetation distributions, rather than direct GCMs outputs.

3.1.1 Climatic inputs for the present-day

Present-day climatic inputs can be derived from global climatological databases, such as LEEMANS and CRAMER (1991) and NEW et al. (2002). The climatology of the CLIMATE database version 2.1 (unpublished data) used here is an updated version of the IIASA database LEEMANS and CRAMER (1991), originally at 0.5° by 0.5° resolution. The NEW et al. (2002) climatology is a $10'$ monthly mean climatology, interpolated from a data set of station means for the period 1961 to 1990. These climatologies have been used to force CARAIB in various previous studies (e. g., OTTO et al. (2002); FRANÇOIS et al. (2006); HENROT et al. (2010); DURY et al. (submitted) and FRANÇOIS et al. (submitted) (see Appendix A), to mention only the most recent ones).

The biome distributions at a 0.5° by 0.5° resolution obtained from equilibrium runs of CARAIB forced with 280 ppmv of atmospheric CO_2 and respectively the Cramer and Leemans and NEW et al. (2002) climatologies are illustrated in Figure 3.1. It should be noticed that these vegetation distributions represent potential vegetation in equilibrium with the climate. Neither urban zones nor human land-use are taken into account. Furthermore, the vegetation maps do not show Antarctica, because the climatologies do not include any data for Antarctica.

Little differences are observed in the biome distributions obtained with the two data sets. Deserts are more expanded in the Cramer and Leemans distribution, whereas tropical rainforests are slightly less developed in Africa and South America in comparison to the NEW et al. (2002) distribution. Temperate forests expand further north in North America and northeastern Europe in the Cramer and Leemans distribution, due to slightly warmer winter temperatures in these regions in comparison with the NEW et al. (2002) climatology.

Both CARAIB biome distributions show reasonably good agreement with published potential natural vegetation maps (MELILLO et al., 1993; CROW-

LEY and BAUM, 1997). They are also consistent with the biome distributions reconstructed from satellite observations (WOODWARD et al., 2004), and from modern pollen samples of the Palaeovegetation Mapping Project BIOME 6000 (PRENTICE et al., 2000a). Differences in the biome distributions may partly be attributed to the different biome classifications used by these authors and the differences in resolutions. CARAIB correctly predicts the tundra and boreal forests distribution at high latitudes of the Northern Hemisphere (WOODWARD et al., 2004; PRENTICE et al., 2000a). However, the eastward expansion of temperate forests in northeastern Europe in the Cramer and Leemans distribution disagrees with the reconstruction of PRENTICE et al. (2000a) that presents boreal forests in this region. Furthermore, both CARAIB distributions yield boreal forests over western Canada where the MELILLO et al. (1993) and CROWLEY and BAUM (1997) biome reconstructions have grassland biomes. Deserts and semi-deserts are generally well located, but too expanded in southwestern North and South America where the reconstructions of MELILLO et al. (1993) and CROWLEY and BAUM (1997) support grasslands and shrublands. This last difference could be linked to the absence of shrubs in the 15-PFT classification used with CARAIB for this exercise (see Section 2.2.5). Finally, tropical rainforests are less extended in Africa and South America in the CARAIB distributions in comparison to MELILLO et al. (1993) and WOODWARD et al. (2004).

3.1.2 Climatic inputs for the past

Past vegetation reconstructions are obtained using climatic anomalies calculated between past and present simulated climate and added to a reference climatology, following the methodology described in FRANÇOIS et al. (1999) and OTTO et al. (2002). The anomaly Δq of a climatic variable q is a combination of absolute Δq_{abs} and relative Δq_{rel} anomalies between the past q_{past} and present-day q_{pres} values of the climatic variable simulated with the Planet Simulator (or any other climate model, or possibly even proxy data-based estimation).

$$\Delta q = \epsilon \Delta q_{abs} + (1 - \epsilon) \Delta q_{rel}, \quad (3.1)$$

with the absolute and relative anomalies calculated as

$$\Delta q_{abs} = q_{past} - q_{pres}, \quad (3.2)$$

$$\Delta q_{rel} = \frac{q_{ref}}{q_{pres}} (q_{past} - q_{pres}), \quad (3.3)$$

where q_{ref} represents the corresponding variable of the present-day climatology used as reference, e. g. the Cramer and Leemans, or NEW et al. (2002)

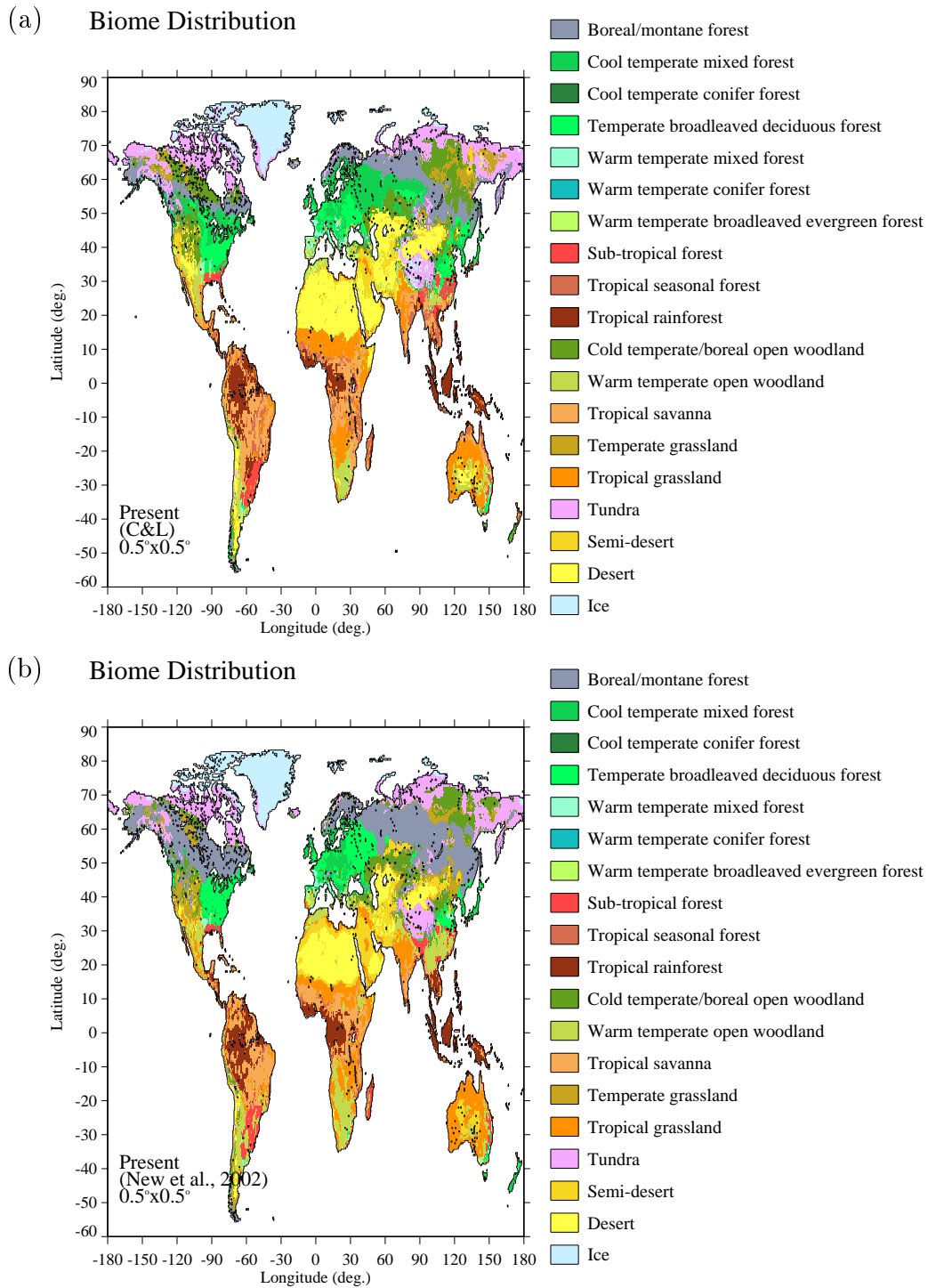


Figure 3.1: CARAIB biome distributions using (a) the Cramer and Leemans and (b) the NEW et al. (2002) climate data sets.

climatology.

The climatic variable actually used to force CARAIB is then q_{cor}

$$q_{cor} = q_{ref} + \Delta q. \quad (3.4)$$

For temperature and diurnal temperature amplitude, only absolute anomalies are used, i. e., $\epsilon=1$. For wind speed, only relative anomalies are used, i. e., $\epsilon=0$. For the other variables (precipitation, relative humidity and sunshine hours), mixed anomalies are used, i. e., ϵ is generally close to 1, but gradually decreases to 0 when the absolute correction tends to yield negative values of the variable which are not physically meaningful.

3.2 Vegetation parameters for Planet Simulator

The surface boundary condition parameters controlled by the vegetation cover in the Planet Simulator are: surface albedo, roughness length and field capacity. The annual distributions of these parameters can be derived from equilibrium runs of CARAIB.

The land surface is subdivided into three main classes: bare soil (no vegetation at all), trees and herbs. The fractions of grid-cell covered by bare soil, trees and herbs are calculated using a probabilistic approach based on the partition of the canopy in terms of leaf area index (LAI). It should be noticed that the annual mean LAI of each PFT is used to produce the annual mean surface albedo and roughness length distributions that will be used as boundary conditions to force the Planet Simulator in its standard version.

The annual mean LAIs attributed to the tree and herb classes are calculated as

$$\overline{LAI} = \sum_i f_i LAI_i, \quad (3.5)$$

where i denumbers the PFTs of the class: 2 for the herbs and 13 for the trees in the 15-PFT classification. LAI_i and f_i respectively represent the LAI and the fraction of the PFT i , belonging to the corresponding herb or tree class.

The vegetation canopy is divided into a series of thin layers of constant thickness. The thickness of each canopy layer can be defined in terms of LAI as $\Delta L = LAI_{tot}/n$, where n is the number of layers of the canopy, and LAI_{tot} the total LAI of the canopy. LAI_{tot} corresponds to the sum of the mean

trees and herbs LAIs defined above, $LAI_{tot} = \overline{LAI}_{trees} + \overline{LAI}_{herbs}$, since the herbs are allowed to grow below the trees in CARAIB.

Thus, using a probabilistic approach based on the propagation of sunlight into the canopy, the fraction of bare soil f_{soil} can be defined as the probability for the sunlight to reach the ground without being intercepted by leaves.

$$f_{soil} = \prod_{i=1}^n (1 - \Delta L) = (1 - LAI_{tot}/n)^n \cong \exp(-LAI_{tot}), \quad (3.6)$$

since we consider that the canopy is formed by a large number of layers (typically $n > 5000$).

Consequently, the fraction of vegetation of the grid-cell, f_{veg} , is given by $1 - f_{soil}$. f_{veg} represents the sum of the fraction of trees, f_t , and the fraction of herbs, f_h , which are not covered by trees (the fraction of herbs that grow below trees is included in the fraction of trees). The fraction of trees can be calculated as the probability for the sunlight to be intercepted by the trees leaves. However, the fraction of herbs that are not covered by trees is calculated as the difference between the vegetation and trees fractions:

$$f_{veg} = 1 - \exp(-(\overline{LAI}_{trees} + \overline{LAI}_{herbs})) \quad (3.7)$$

$$f_{soil} = 1 - f_{veg} \quad (3.8)$$

$$f_{trees} = 1 - \exp(-\overline{LAI}_{trees}) \quad (3.9)$$

$$f_{herbs} = f_{veg} - f_{trees}. \quad (3.10)$$

3.2.1 Surface albedo

The surface albedo of the grid-cell is obtained from the linear average of the trees, herbs and bare soil albedos following:

$$Alb_{tot} = \left(\sum_i f_i Alb_i \right) f_{trees} + \left(\sum_j f_j Alb_j \right) f_{herbs} + Alb_{soil} f_{soil}, \quad (3.11)$$

where i denumbers tree and j herb PFTs. f_i and f_j are respectively the fractions of tree-PFTs and of herb-PFTs calculated by CARAIB. Alb_i and Alb_j are the albedos of the tree-PFTs and the herb-PFTs.

The albedo attributed to each PFT is the arithmetic mean of the short wave ($\lambda < 0,7 \mu\text{m}$) and long wave ($\lambda \geq 0,7 \mu\text{m}$) albedos of each PFT, following PITMAN et al. (1991). The surface albedos attributed to the PFTs of

the 15-PFT classification are given in Table 3.1. The bare soil albedo is calculated from the soil colour and humidity, following the approach described in PITMAN et al. (1991):

$$\begin{aligned} Alb_{sw} &= 0.1 + 0.1 C + 0.07 (1 - W) \\ Alb_{lw} &= 2 Alb_{sw} \\ \Rightarrow Alb_{soil} &= Alb_{sw} + Alb_{lw} = 1.5 (0.1 + 0.1 C + 0.07 (1 - W)) \end{aligned} \quad (3.12)$$

C is the soil colour of the grid-cell, varying from 0 for dark soils to 1 for light soils, following the standard scale in CARAIB (PITMAN et al., 1991). W is the ratio of the soil water and the field capacity calculated in the Planet Simulator.

The annual mean surface albedo distribution obtained from the results of an equilibrium run of CARAIB on a T42 longitude-latitude grid, forced with 280 ppmv of atmospheric CO_2 and the NEW et al. (2002) climatology is illustrated in Figure 3.2. The surface albedo distribution shown here is consistent with the reconstruction of present-day surface albedo based on a 1 km ecosystem type distribution (HAGEMANN et al., 1999; HAGEMANN, 2002) and with the surface albedo distribution used in ECHAM4 (CLAUSSEN et al., 1994). Deserts and arid areas are characterised by albedos greater than 0.35. The albedo of temperate forests is around 0.16 to 0.18, and the albedo of tropical forests is slightly weaker, around 0.12. It should be noticed that the surface albedo over Antarctica is initially set to the default value of 0.2, used for bare soil in the Planet Simulator, due to the absence of data in Antarctica. The albedo of the ice covered regions, notably in Antarctica and Greenland, will then be set to 0.8 in the Planet Simulator, according to the glacier mask. Moreover, in the Planet Simulator, the presence of snow will modify the surface albedo of the pixel (see Section 2.1.4).

3.2.2 Roughness length

As described in CLAUSSEN et al. (1994), the calculation of roughness length by linear averaging is not valid at coarse resolution. Therefore, the concept of blending height is used here (MASON, 1988). Instead of roughness length values, drag coefficients at the blending height are averaged (HAGEMANN et al., 1999). The drag coefficients are defined as:

$$c_d = \left(\frac{\kappa}{\ln \frac{z_b}{z_{veg}}} \right)^2, \quad (3.13)$$

Table 3.1: Short-wave albedos, long-wave albedos and rooting depths attributed to the 15 PFTs.

PFTs	Short-wave albedo	Long-wave albedo	Rooting depth (mm)
1. C ₃ herbs	0.14	0.26	910
2. C ₄ herbs	0.14	0.26	1200
3. Needleleaved evergreen boreal/temperate cold	0.09	0.19	580
4. Needleleaved evergreen temperate cool	0.09	0.19	1040
5. Needleleaved evergreen temperate dry warm	0.09	0.19	1710
6. Needleleaved evergreen temperate perhumid warm	0.09	0.19	1060
7. Needleleaved summergreen boreal/temperate cold	0.09	0.18	580
8. Needleleaved summergreen temperate warm	0.09	0.18	1040
9. Broadleaved evergreen temperate dry warm	0.09	0.18	1710
10. Broadleaved evergreen temperate perhumid warm	0.09	0.18	1040
11. Broadleaved summergreen boreal/temperate cold	0.09	0.27	580
12. Broadleaved summergreen temperate cool	0.09	0.27	1040
13. Broadleaved summergreen temperate warm	0.09	0.27	1210
14. Broadleaved raingreen tropical	0.09	0.17	1440
15. Broadleaved evergreen tropical	0.09	0.17	910

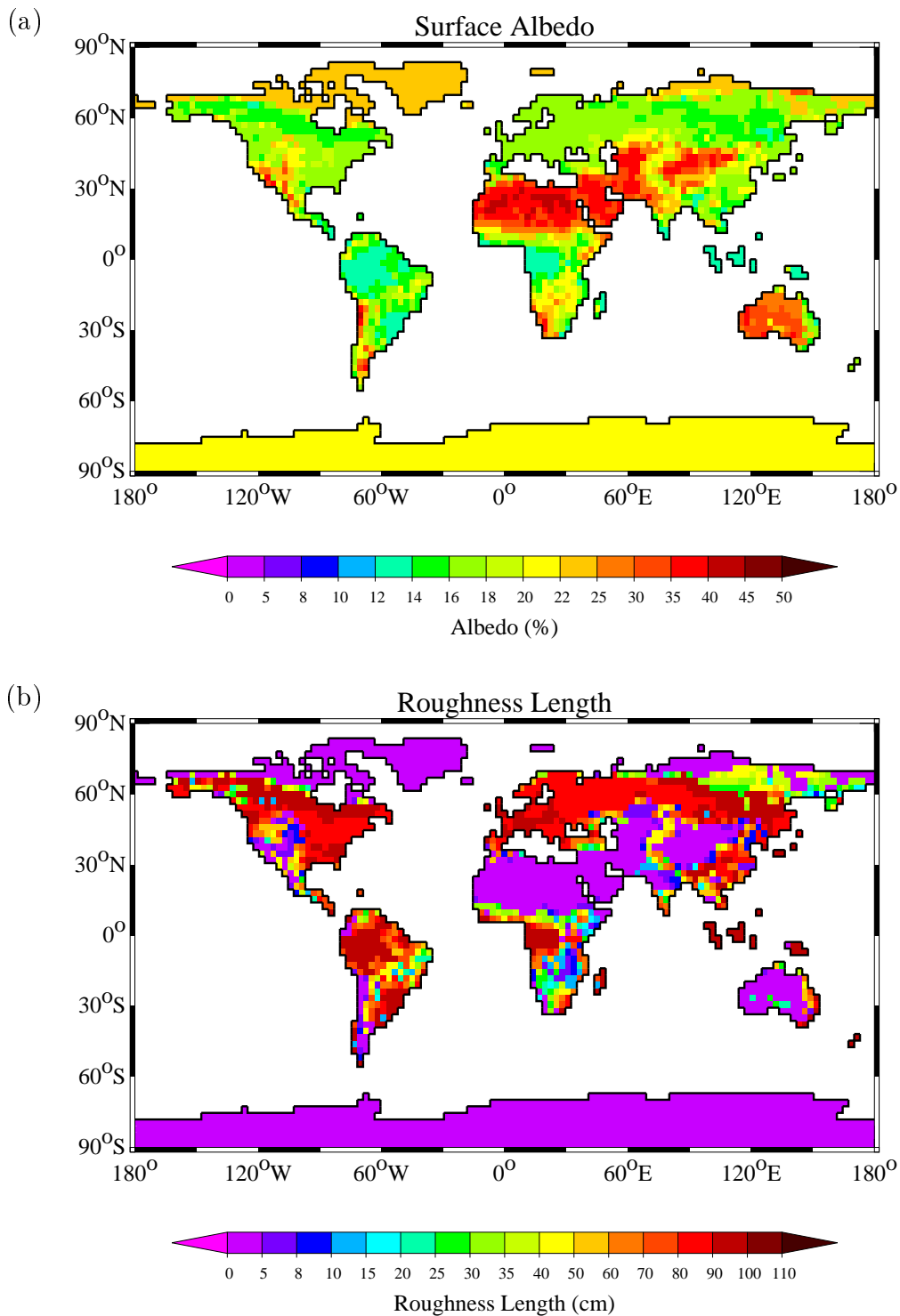


Figure 3.2: Annual mean (a) surface albedo and (b) roughness length distributions for the Planet Simulator obtained from a T42 preindustrial simulation with CARAIB.

where κ is the von Kármán's constant, z_{veg} the roughness length of the grid-cell, and z_b is the blending height, fixed to 100 m (CLAUSSEN et al., 1994).

The roughness length of the grid-cell is obtained from the average of the drag coefficients defined for the three classes (trees, herbs and bare soil):

$$\frac{1}{\ln^2\left(\frac{z_b}{z_{veg}}\right)} = \sum_j \left(\frac{f_j}{\ln^2\left(\frac{z_b}{z_{veg,j}}\right)} \right), \quad (3.14)$$

where f_j are the fraction of the trees, herbs and bare soil given in equation (3.7), and $z_{veg,j}$ is the roughness length attributed to each class (1 m for the trees, 0.1 m for the herbs and 0.001 m for bare soil, following PITMAN et al. (1991)).

The annual mean roughness length distribution obtained from the results of an equilibrium run of CARAIB in T42 forced with 280 ppmv of atmospheric CO₂ and the NEW et al. (2002) climatology is illustrated in Figure 3.2. It broadly agrees with the distributions of HAGEMANN et al. (1999); HAGEMANN (2002) and CLAUSSEN et al. (1994). Roughness length of a few centimeters are attributed to the deserts and grassland ecosystems. Roughness length of 1 m are attributed to temperate and tropical forests. Nevertheless, we used a roughness length of 1 m for all types of trees, according to the values given by PITMAN et al. (1991), whereas a roughness length of 2 m is attributed to tropical trees in HAGEMANN et al. (1999); HAGEMANN (2002).

3.2.3 Field capacity

In the Planet Simulator, the maximum soil water holding capacity is limited by the field capacity that can be derived from the vegetation cover. The field capacity of each grid-cell, W_{fci} , is calculated in the CARAIB model in function of the rooting depth and the soil texture: $W_{fci} = Rootd * fci$. The rooting depth of the grid-cell, $Rootd$, is calculated by linear averaging, in function of the rooting depths and fractions of PFTs defined on the vegetated part of the pixel. A default value of 200 mm is attributed to bare soil, and a default value of 580 mm is used for permafrost regions. The rooting depths attributed to the 15 PFTs of the CARAIB classification are given in Table 3.1. The volumetric fraction of water at field capacity fci is derived from the soil texture classes (percentages of silt, sand and clay), following the parameterisation of SAXTON et al. (1986).

The distributions of rooting depth and field capacity obtained from the T42 preindustrial equilibrium run of CARAIB are shown in Figure 3.3. The CARAIB field capacity distribution broadly agrees with the field capacity distribution associated with the 1 km ecosystem data (HAGEMANN et al., 1999), and with the one used in the ECHAM4 model (PATTERSON, 1990). Field capacities of more than 500 mm are associated with warm temperate broadleaved forest, whereas lower values are attributed to cooler forest types. The field capacity values derived from the CARAIB run are deeper than the values used for the ECHAM4 model, which are too low especially in the tropics (KLEIDON and HEIMANN, 1998). However, the CARAIB field capacities remain shallower than the ones given in HAGEMANN et al. (1999), especially below 50°N, due to the difference in the rooting depth and soil texture values used here.

3.3 Coupling procedure

In order to link the climate and vegetation models, we have applied an equilibrium asynchronous coupling procedure, as defined by FOLEY et al. (1998). This coupling procedure consists of an iterative procedure where the climate resulting from an equilibrium run of the climate model is used to drive changes in the equilibrium distribution of vegetation types, which in turn are fed back into the land surface scheme of the climate model (see Figure 3.4). Long term mean climate (averaged over the last 20 years of simulation or more) is used to force CARAIB, following the procedure described in CLAUSSEN (1994). In turn, the vegetation parameters derived from the CARAIB equilibrium simulation are used to force Planet Simulator. This iterating cycle of equilibrium climate and vegetation simulations is repeated until the results of both models converge to equilibrium, i.e., until no significant trend could be detected in global and local land surface parameters and climatic variables between successive simulations.

The equilibrium asynchronous coupling procedure has been applied in previous climate and vegetation modelling studies, on different geological periods, and with various climate and vegetation models (CLAUSSEN, 1994, 1998; DE NOBLET et al., 1996, 2000; DECONTO et al., 1999; BETTS et al., 1997). DE NOBLET et al. (1996) used the LMD AGCM asynchronously coupled to the BIOME equilibrium vegetation model in order to examine the impact of changes in the position of the boreal forests and tundra on the Quaternary climate, and their potential role in the initiation

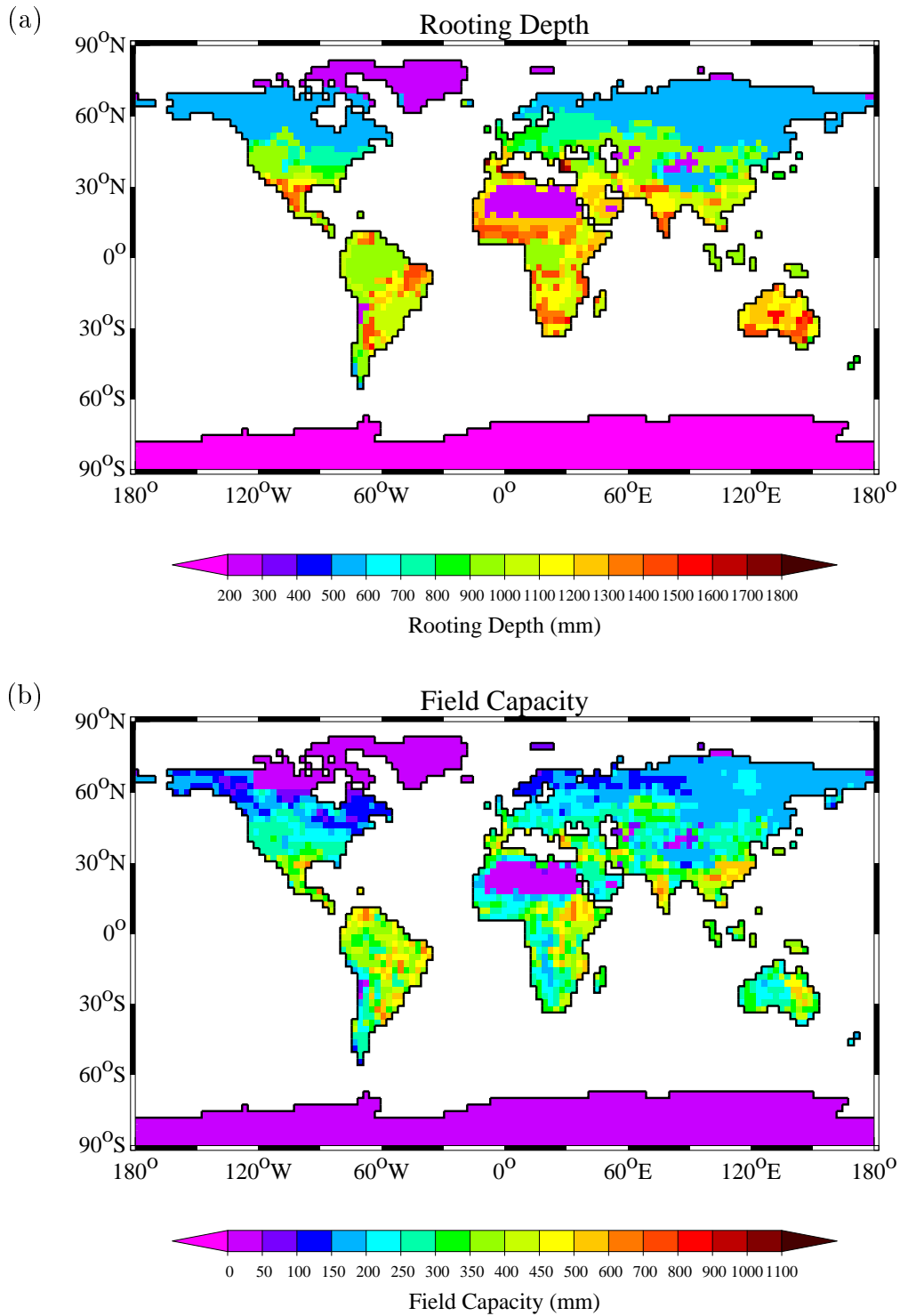


Figure 3.3: Annual mean (a) rooting depth and (b) field capacity distributions obtained from a T42 preindustrial simulation with CARAIB.

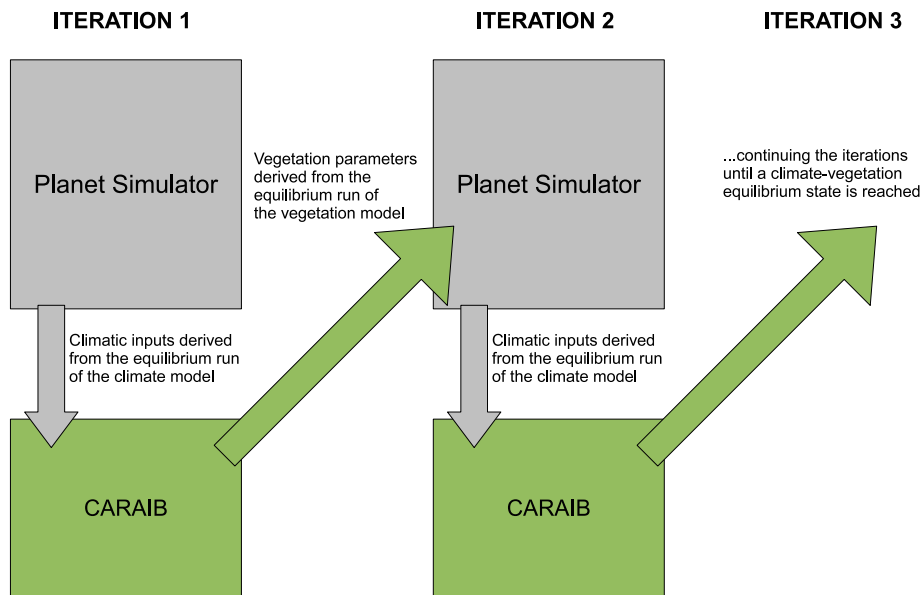


Figure 3.4: Asynchronous equilibrium coupling of the Planet Simulator and CARAIB models.

of glaciations. CLAUSSEN (1998) used the asynchronously coupled ECHAM-BIOME model to investigate the influence of initial vegetation conditions on changes in the African and Indian monsoon during the Holocene. DE NOBLET et al. (2000) compared the ability of the asynchronously coupled models LMD-BIOME and ECHAM3-BIOME to reproduce a green Sahara at 6000 years BP. DECONTO et al. (1999) used the GENESIS-EVE coupled model to study high-latitude climate vegetation interactions during the Cretaceous (around 80 million years BP). Finally, BETTS et al. (1997) used several coupled vegetation models to investigate the potential role of vegetation feedbacks on future climate changes.

The equilibrium asynchronous coupling between climate and vegetation models has proved its usefulness in the study of climate and vegetation interactions, and has highlighted the importance of incorporating representations of a changing vegetation cover within climate models. However, this coupling technique has several limitations, as observed by FOLEY et al. (1998, 2000). Indeed, the equilibrium asynchronous coupling procedure, by definition, only simulates equilibrium responses of the vegetation and the climate to respective climate and vegetation changes. It is therefore not suitable for simulating transient changes in vegetation and climate, and to address

the time-dependent nature of the atmosphere-biosphere response to climate variability. Furthermore, the vegetation models and AGCM land surface parameterisations are not always physically consistent. For example, in the PlanetSimulator-CARAIB asynchronously coupled model, there are two independent treatments of the surface radiation and water budget. Planet Simulator includes its own land-atmosphere exchanges processes, whereas CARAIB estimates its soil water requirements for plants. The surface evaporation is notably calculated from the bulk aerodynamic formulas in the Planet Simulator land surface scheme, whereas is it calculated according to Penman's equation in the CARAIB model. To provide a more direct linkage between the atmospheric and ecological processes, the CARAIB model should have been fully incorporated within the Planet Simulator, replacing its terrestrial component. However, due to several incompatibilities between both Planet Simulator and CARAIB models, we were not able to develop a more efficient and direct coupling procedure to apply in this work. Some of the additional developments that have been done to produce a fully-coupled PlanetSimulator-CARAIB model will be described in a separate report (in preparation). For this work, we therefore have to bear in mind the limitations of the asynchronous coupling procedure.

3.4 Climate-vegetation iterations for the preindustrial period

In order to assess the equilibrium asynchronous coupling procedure described above, we carried out a series of five iterations for the preindustrial period with the Planet Simulator and CARAIB. For the first iteration, CARAIB was forced with the NEW et al. (2002) climatology, and an atmospheric CO₂ concentration of 280 ppmv, to produce a first set of surface parameters to force the Planet Simulator. The Planet Simulator was run in T21 (in order to limit the computing time requirements of the climate runs). This set of vegetation and climate simulations completed the first iteration. Then, for the rest of the iterations, the long term monthly means of the climatic variables over the last 20 years of 50-year runs were used to force the CARAIB model. CARAIB was run in T21 and directly forced with the Planet Simulator outputs. We analyse the climate and vegetation iterations in terms of trends and differences between global surface patterns, climatic variables and biome patterns.

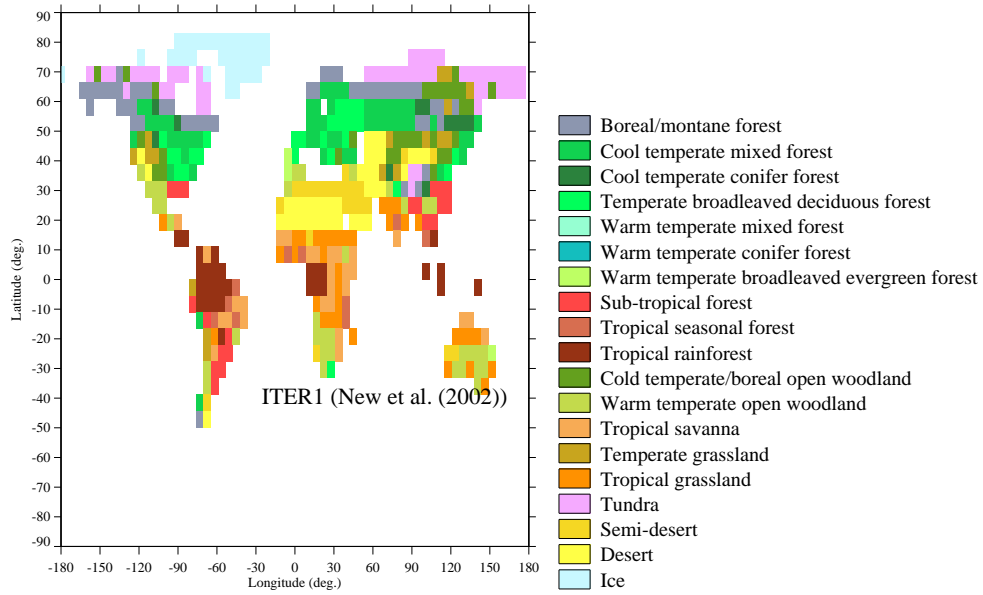
The biome distributions derived with CARAIB from the NEW et al.

(2002) climatology (first vegetation iteration ITER1) and from the climate of the first climate iteration with Planet Simulator (second vegetation iteration ITER2) are shown in Figure 3.5. The global mean Net Primary Productivity (NPP) obtained at each vegetation iteration is shown in Figure 3.6. The major differences in biome distributions occur between the climatology induced biome distribution and the biome distribution computed with CARAIB from the first climate simulation. The climate simulated by the Planet Simulator mainly induces an opening of the global landscape, characterised by an expansion of deserts, e.g., in Central Asia, southwestern North America and especially in Australia, and an expansion of grasslands, essentially in South Africa. These vegetation changes are mainly linked to the differences between the climatological and the simulated precipitation distributions during the climatological year. Indeed, the seasonal precipitation contrast is much larger in the climate simulated by the Planet Simulator that includes drier months, as well as wetter months relative to the NEW et al. (2002) climatology. Low precipitation rates during some months can thus cause water stress to the vegetation, and limit the growth of the trees, or even kill the plants. However, in response to the high precipitation rates that are simulated in the tropics, the NPP of the tropical forest types largely increases from the first to the second vegetation iteration, which in turn increases the global NPP. Furthermore, broadleaved temperate forests are more expanded, notably in northeastern Asia and Canada, in the second vegetation distribution, in comparison to the climatology induced vegetation distribution. This can be explained by the warmer temperature that are simulated in winter over these regions, allowing temperate trees to subsist.

After the second vegetation iteration (ITER2), the series of biome distributions and global NPP differ only slightly. We quantified the differences in the biome distributions obtained at successive iterations by calculating the total area, in terms of percentage of the land surface, in which biomes differ when comparing two global biome distributions (see Figure 3.6). Only the climatology induced distribution (ITER1) and the first computed biome distribution (ITER2) differ by much more than 10%. We can therefore consider that the vegetation distributions do not significantly change after the second iteration. There is no important expanding or shifting of biomes, and the differences in the successive biome distributions can be attributed to the crossing of the thresholds used to classify the vegetation types, rather than to actual climate changes. These small changes in the vegetation distributions could also be seen as small oscillations around the equilibrium state (case of a stable harmonic oscillator).

Figure 3.7 shows the continental annual mean surface albedo, roughness

(a) Biome Distribution



(b) Biome Distribution

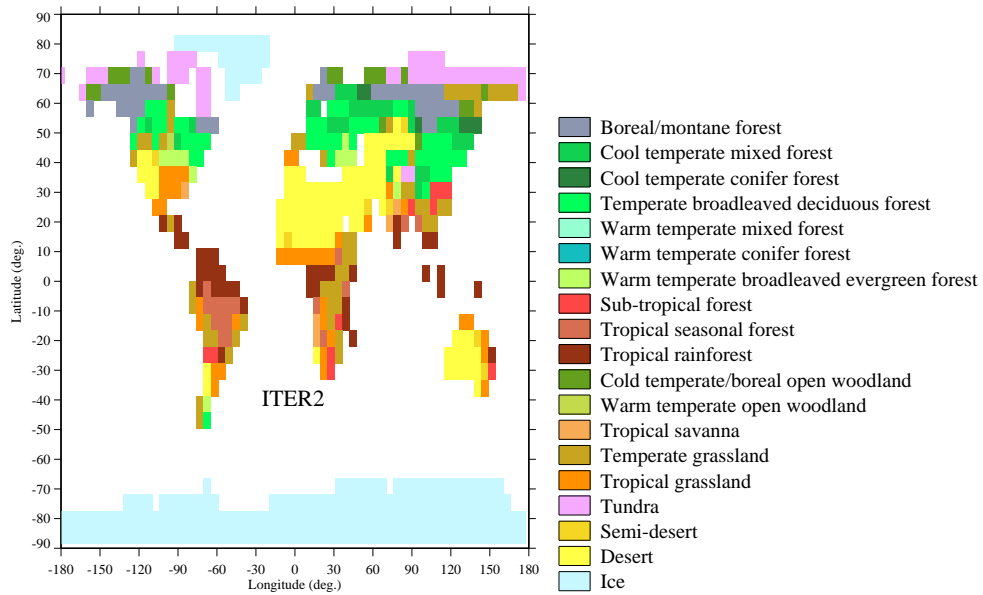


Figure 3.5: CARAIB biome distributions for (a) the first vegetation iteration (ITER1) and (b) the second vegetation iteration (ITER2).

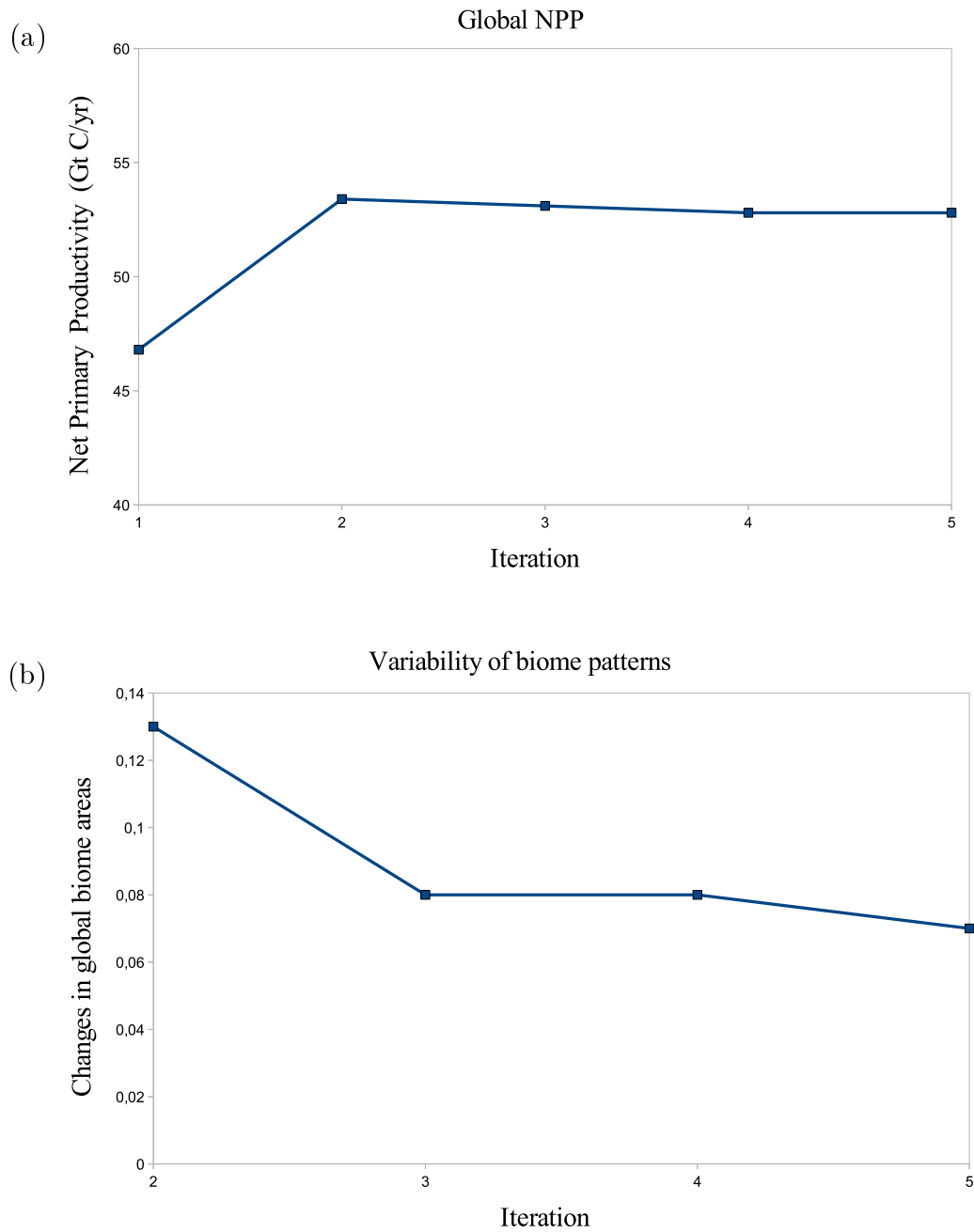


Figure 3.6: (a) Global Net Primary Productivity (Gt C/yr) for each vegetation iteration, and (b) Total area in term of percentage land surface in which biomes differ from two successive vegetation iterations.

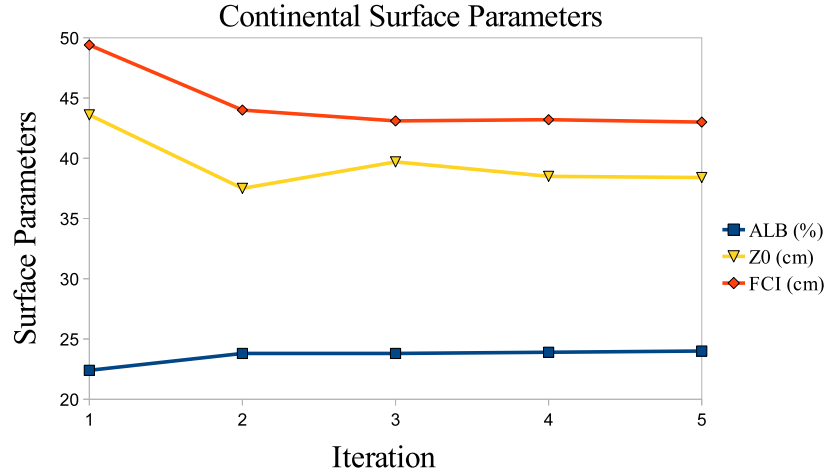


Figure 3.7: Continental annual mean surface albedo (%), roughness length (cm) and field capacity (cm) for each iteration.

length and field capacity used to force the Planet Simulator at each iteration. The continental annual, summer (JJA) and winter (DJF) mean surface air temperatures (SAT) and precipitation (PRC) are shown in Figure 3.8. The largest change in the climatic variables and surface parameters occurs at the second climate iteration. Continental SAT and PRC decrease respectively by 1°C and 22 mm/yr . This effect is essentially due to the decrease of the surface albedo and the field capacity caused by the differences between the vegetation distributions derived from the NEW et al. (2002) climatology (ITER1) and the vegetation distribution computed from the first Planet Simulator run (ITER2) that is used for the second climate iteration. After the second iteration, neither the global climatic variables, nor the surface parameters exhibit any statistically significant trend.

Locally, larger changes in surface temperature and precipitation occur between the first and the second climate iterations, as illustrated in Figure 3.9. The expansion of deserts and grasslands in the vegetation distribution ITER2 leads to surface albedo increases, that in turn contribute to decrease the SAT of about 2°C on the concerned regions, i. e., North Africa, Central Asia, North America and Australia. The continental temperature decreases also induce slight temperature decreases over the oceans, particularly at high latitudes, due to the high sensitivity of sea-ice to temperature changes. The precipitation decreases essentially occur over the Equatorial Atlantic ocean and over

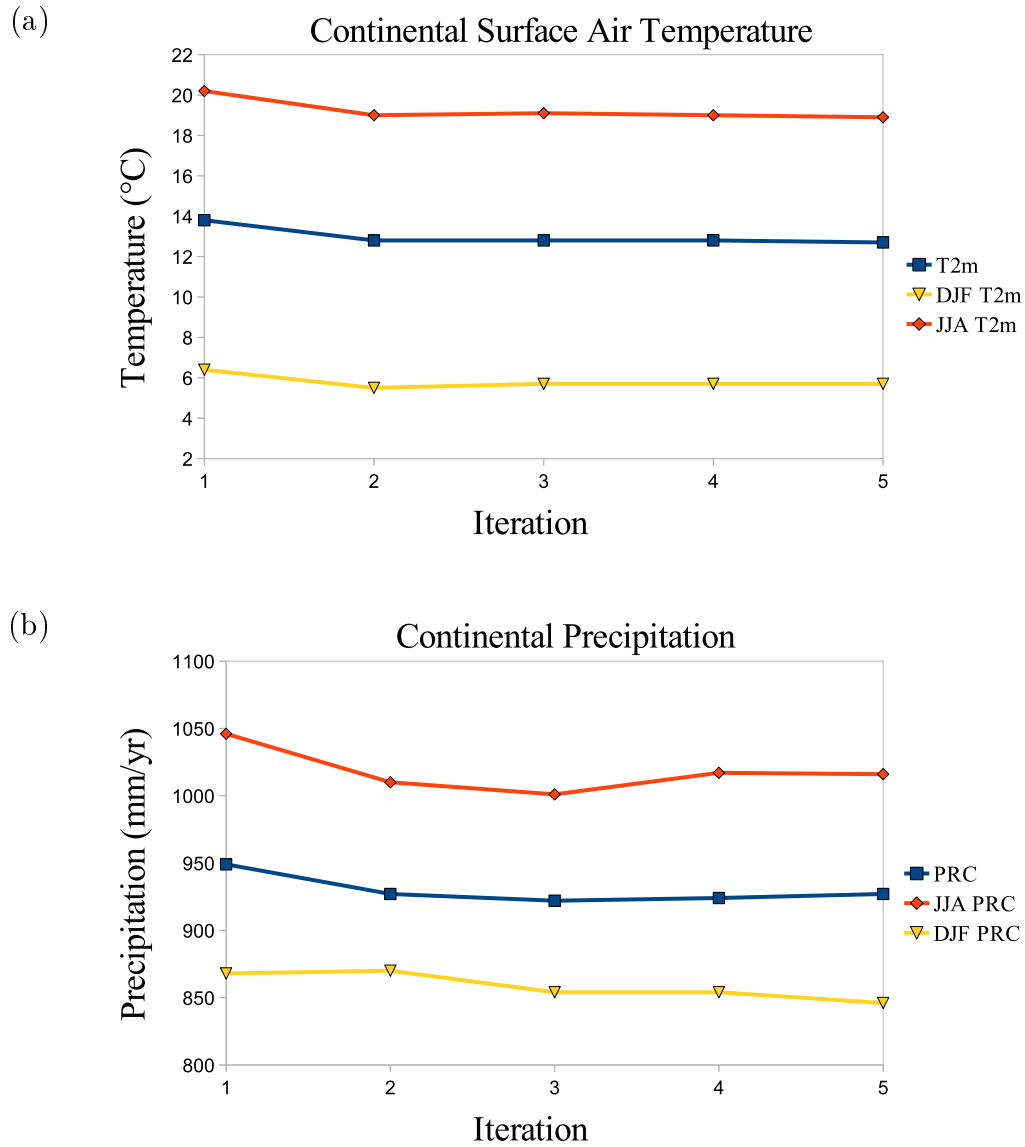


Figure 3.8: Continental annual and seasonal (JJA and DJF) (a) mean surface air temperature (°C) and (b) precipitation (mm/yr) for each iteration.

some land grid-cells. However, after the second iteration, local temperature differences do not exceed 2°C in absolute value, and mainly concern the sea-ice covered regions, which respond strongly to slight temperature changes. Figure 3.10 shows the SAT and PRC differences between the third and the second climate iterations. After the second iteration, the temperature differences in some regions oscillate between two successive iterations, which does not induce significant climatic trend (positive and negative temperature anomalies of the same order of magnitude can occur in a specific region between successive iterations). After the second climate iteration, the precipitation anomalies only concern a few grid-cells, and no significant trend is observed in the precipitation distribution. Therefore, we can consider that the incorporation of the CARAIB derived surface parameters does not induce a significant trend in the global annual and seasonal surface climate. However, the equilibrium climate reached by the Planet Simulator after the series of iterations is cooler and drier than the one reached after the first iteration, using the vegetation derived from the NEW et al. (2002) climatology. This is a consequence of the expansion of deserts and grasslands in the vegetation distribution derived from the Planet Simulator climate. Thus, the climate-vegetation interactions analysed here do not really contribute to improve the simulated preindustrial climate. Indeed, the vegetation impact on climate tends to amplify the cold bias of the model, by decreasing the temperatures over the continents. However, the vegetation impact improves the representation of the precipitation distribution in the model, by reducing the precipitation rates in the tropics where they are overestimated in using the standard configuration of the model.

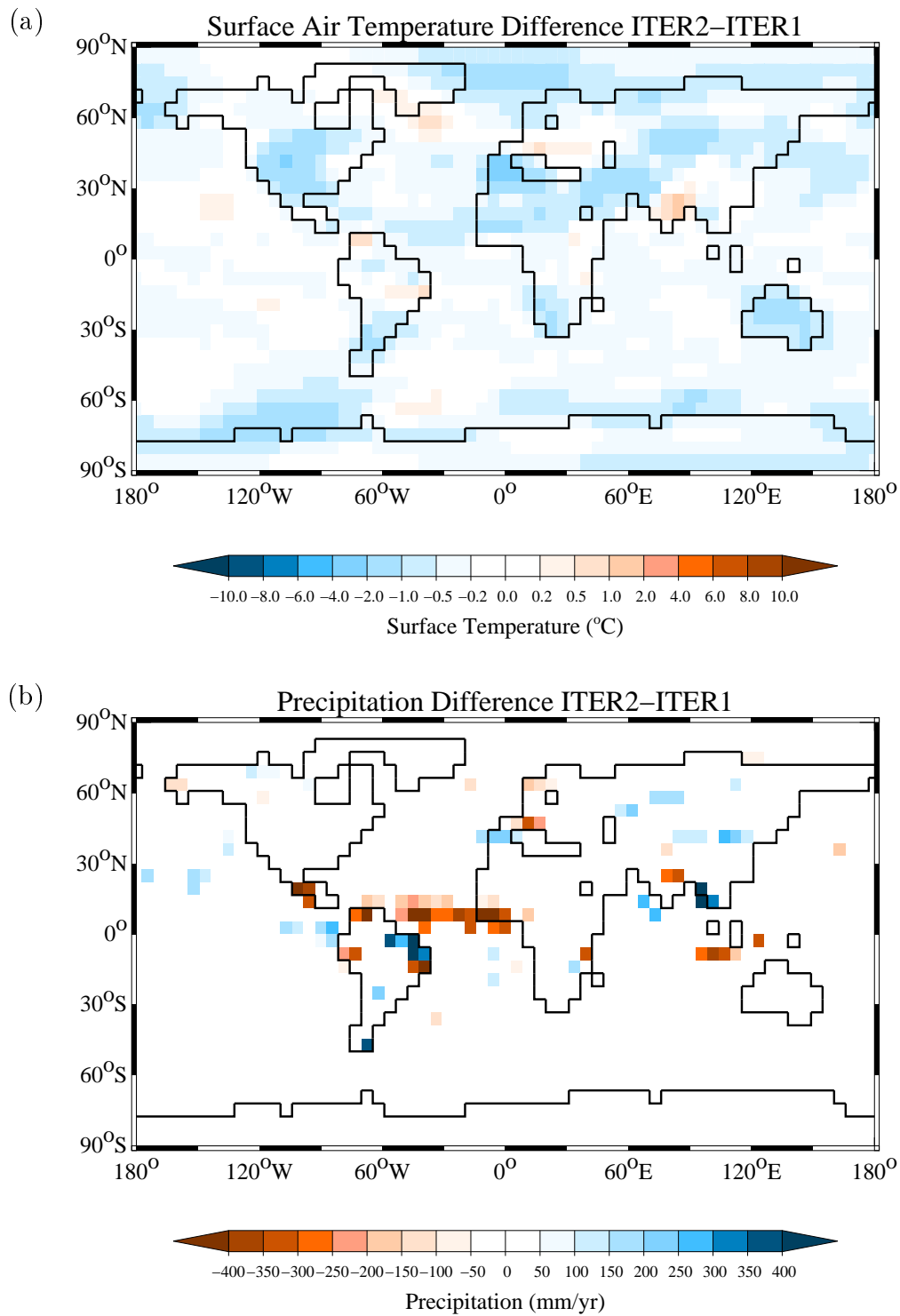


Figure 3.9: (a) Surface air temperature and (b) precipitation annual mean differences between the second and the first climate iterations (ITER2-ITER1).

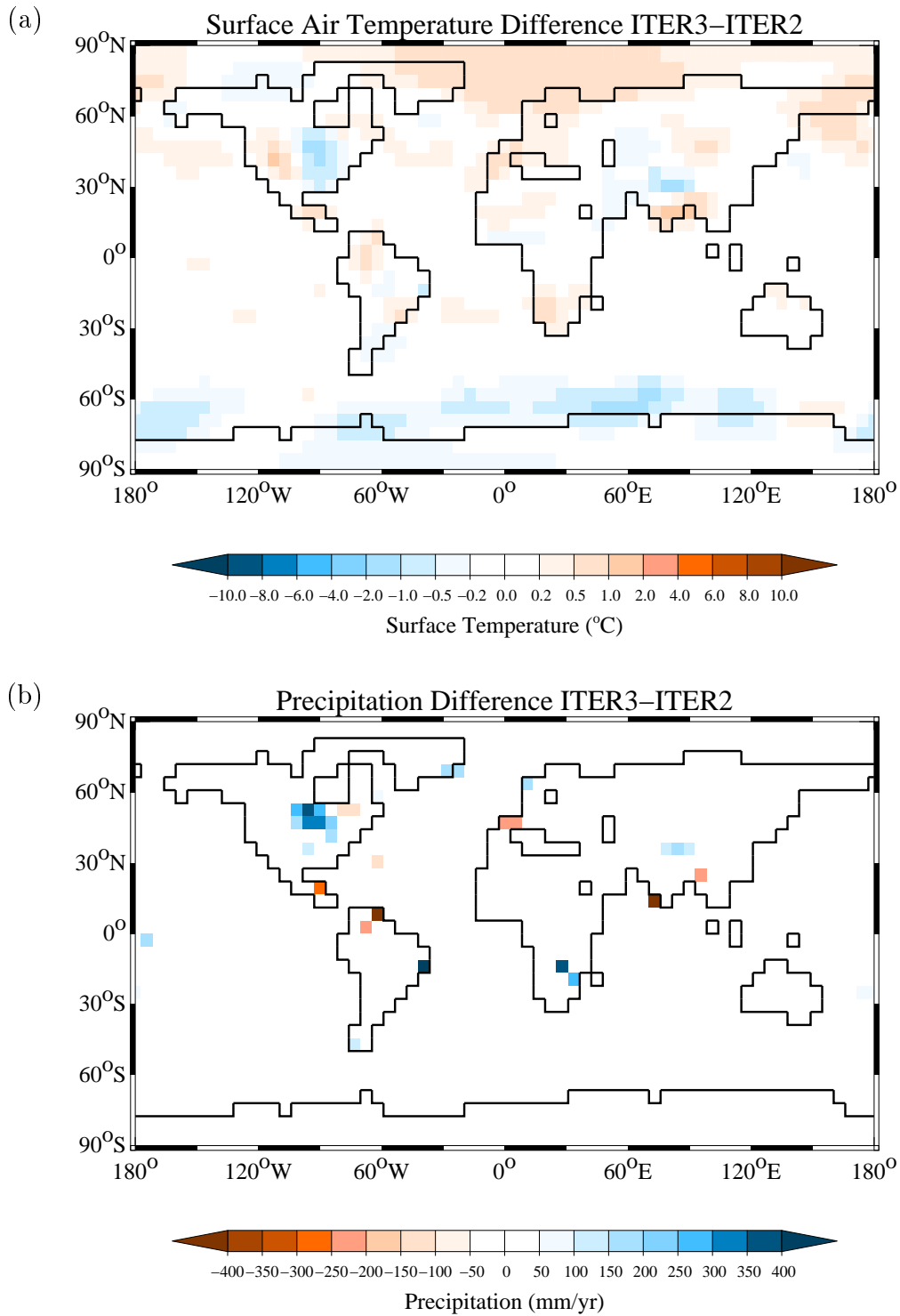


Figure 3.10: (a) Surface air temperature and (b) precipitation annual mean differences between the third and the second climate iterations (ITER3-ITER2).

Chapter 4

Last Glacial Maximum climate and vegetation modelling

The purpose of the present chapter is the study of land surface cover change implications on Last Glacial Maximum (LGM) climate. This first application of the Planet Simulator and CARAIB allows us to test the ability of the models to simulate a climate and vegetation distribution that significantly differ from the modern ones, and to evaluate the model results against the large number of previous modelling studies results and proxy-based climatic reconstructions that cover the period.

During the last decades, several studies have tried to analyse and isolate the vegetation impact on the LGM climate. We can notably mention the study of WYPUTTA and MCAVENEY (2001) who modelled the impact of a vegetation change on the atmospheric circulation at the LGM. They found that the vegetation changes produced an additional cooling of about 1 to 2°C in Western Europe and till 6°C in Siberia, as well as a precipitation reduction of more than 30% in the tropics. More recently, CRUCIFIX and HEWITT (2005) obtained an additional cooling of 0.6°C, a decrease of precipitation, and a perturbation of the Asian monsoon, when changing the vegetation cover in the coupled climate-vegetation model HADSM3-TRIFFID.

Here, we carried out a series of climate simulation experiments with the Planet Simulator, considering in turn the effect of changing vegetation cover (via surface albedo and roughness length derived from CARAIB simulations), ice sheet cover and orography, and atmospheric CO₂ concentration between a preindustrial state and the LGM. We applied the factor separation method of STEIN and ALPERT (1993) in order to rigorously determine the vegetation cover change impact.

The results of this first study, including a complete discussion of the boundary conditions and vegetation impacts on LGM climate, and a comparison of the simulated climate with proxy-based reconstructions have been published as HENROT et al. (2009). The text of that paper is reproduced on the next pages.

Following the text of that paper, we present the results of an additional series of climate and vegetation model iterations. The vegetation results and feedbacks on climate of the first iteration are briefly discussed in that addendum to the paper.

Impacts of land surface properties and atmospheric CO₂ on the Last Glacial Maximum climate: a factor separation analysis

A.-J. Henrot¹, L. François², S. Brewer^{2,*} and G. Munhoven¹

¹ Laboratory of Atmospheric and Planetary Physics, University of Liège, Liège, Belgium

² Unité de Modélisation du Climat et des Cycles Biogéochimiques, University of Liège, Liège, Belgium

* now at: Botany Department, University of Wyoming, Laramie, Wyoming, USA

Abstract Many sensitivity studies have been carried out, using climate models of different degrees of complexity to test the climate response to Last Glacial Maximum boundary conditions. Here, instead of adding the forcings successively as in most previous studies, we applied the separation method of U. Stein et P. Alpert 1993, in order to determine rigorously the different contributions of the boundary condition modifications, and isolate the pure contributions from the interactions among the forcings. We carried out a series of sensitivity experiments with the model of intermediate complexity Planet Simulator, investigating the contributions of the ice sheet expansion and elevation, the lowering of the atmospheric CO₂ and of the vegetation cover change on the LGM climate.

The separation of the ice cover and orographic contributions shows that the ice albedo effect is the main contributor to the cooling of the Northern Hemisphere, whereas orography has only a local cooling impact over the ice sheets. The expansion of ice cover in the Northern Hemisphere causes a disruption of the tropical precipitation, and a southward shift of the ITCZ. The orographic forcing mainly contributes to the disruption of the atmospheric circulation in the Northern Hemisphere, leading to a redistribution of the precipitation, but weakly impacts the tropics. The isolated vegetation contribution also induces strong cooling over the continents of the Northern Hemisphere that further affects the tropical precipitation and reinforce the southward shift of the ITCZ, when combined with the ice forcing. The combinations of the forcings generate many non-linear interactions that reinforce or weaken the pure contributions, depending on

the climatic mechanism involved, but they are generally weaker than the pure contributions. Finally, the comparison between the LGM simulated climate and climatic reconstructions over Eurasia suggests that our results reproduce well the south-west to north-east temperature gradients over Eurasia.

Introduction

The Last Glacial Maximum (LGM), around 21 000 years before present (21 kBP), represents the largest climate change of the recent past. It is characterized by an expansion and a thickening of the ice sheets at high latitudes, a large reduction in atmospheric CO₂ concentration and a less dense vegetation cover. Several projects, using palaeoclimatic data, have reconstructed the surface conditions at the LGM, like CLIMAP (CLIMAP PROJECT MEMBERS, 1976), or more recently MARGO (KUCERA et al., 2005), making the LGM one of the best documented periods of the recent geological past.

As a result, the LGM has become the subject of numerous General Circulation Model (GCM) studies, in order to test the ability of the models to simulate a climate markedly different from the present, and to better understand the mechanisms that lead to abrupt climate changes. Many sensitivity studies have been carried out, using GCMs to test the climate response to various glacial boundary conditions (BROCCOLI and MANABE, 1987b; HEWITT and MITCHELL, 1997; GANOPOLSKI, 2003; SCHNEIDER VON DEIMLING et al., 2006).

In these studies, boundary condition changes and forcings were generally applied in a sequential procedure that con-

sisted of a successive addition of the forcings leading to the final LGM state. In that case, the response of the model to a particular change in a given boundary condition is determined by the comparison of the runs with and without that change, neglecting in the analysis the possible interactions between the forcings that can take place and contribute to the final climate state. To overcome this shortcoming, STEIN and ALPERT (1993) developed a rigorous method to carry out sensitivity studies that separates the pure contributions of the forcings from the interactions resulting from their combination.

BERGER et al. (1996) and JAHN et al. (2005) used the STEIN and ALPERT (1993) factor separation method to analyse different contributions to the LGM climate. BERGER et al. (1996) used a 1-D radiative-convective climate model to assess the individual and synergistic effects of the ice sheet albedo feedback and atmospheric CO₂ changes at LGM. JAHN et al. (2005) used CLIMBER-2 (PETOUKHOV et al., 2000; GANOPOLSKI et al., 2001) to separate the pure contributions of CO₂, ice sheet and vegetation changes from their combinations. Here, we applied the STEIN and ALPERT (1993) method to a LGM sensitivity study carried out with the Earth system model Planet Simulator. We carried out a series of sixteen simulation experiments, where we have

assessed the effects from differences in the vegetation cover, the ice sheet cover, the orography, and the effect of reduced atmospheric carbon dioxide between a pre-industrial state and the LGM. We reconstructed the vegetation distributions with the CARAIB dynamic vegetation model (described in Sect. 4). We then examined the response of surface temperature and precipitation to the different forcings and discuss the pure contribution of the four factors on the LGM climate, as well as the interactions among them. Finally, we evaluated our LGM results over Eurasia and Africa against LGM climate reconstruction produced by WU et al. (2007).

Model setup

The Planet Simulator (FRAEDRICH et al., 2005a) is an Earth system Model of Intermediate Complexity (EMIC). Its central component is PUMA-2, a spectral GCM with triangular truncation, based upon PUMA (FRAEDRICH et al., 1998). PUMA-2 solves the moist primitive equations, representing the conservation of momentum, mass and energy, on σ coordinates in the vertical. It also includes boundary layer, precipitation, interactive clouds and radiation parameterisations. For the present study, we configured it to use a T21 truncation and ten vertical equally spaced σ levels. The atmospheric module is coupled to a 50 m deep mixed-layer ocean, a thermodynamic sea-ice and a land surface and soil model. Sea surface temperatures are computed from the net atmospheric heat flux in the surface. The

transport of heat by oceanic surface currents is represented by an additional source or sink of heat, varying monthly and spatially that is prescribed within the mixed-layer and the sea-ice. Heat flux adjustments are applied to ocean grid-cells to mimick heat transport by ocean currents that is not an explicitly represented process in the model. Their distribution was determined from a preindustrial experiment, where sea surface temperature and sea-ice distributions were prescribed from the AMIP2 dataset (AMIP2, 2004). This preindustrial heat flux distribution has been used throughout the full set of experiments. We did not consider any change in the oceanic circulation at the LGM. The land surface and soil models calculate the surface temperatures from a linearized energy balance equation and predict soil moisture on the basis of a simple bucket model. The influence of vegetation is represented by background albedo and roughness length. Their annual distributions are prescribed, and albedo may only change in grid-cells where snow is present.

The distributions of surface albedo and roughness length were obtained from the dynamic vegetation model CARAIB (CARbon Assimilation In the Biosphere) (WARNANT et al., 1994; NEMRY et al., 1996; LAURENT et al., 2008). CARAIB calculates the carbon fluxes between the atmosphere and the terrestrial biosphere and deduces the evolution of carbon pools, together with the relative abundances of a series of plant types. Its different modules respectively focus on the hydrological cycle, photosynthesis and stomatal regulation, carbon allocation and

biomass growth, heterotrophic respiration and litter and soil carbon, and the distribution of the model plant types, as a function of productivity. Here we used a classification with fifteen Plant Functional Types (PFTs), described in GALY et al. (2008). Model derived PFT assemblages were then translated into biomes to produce vegetation maps. The inputs of the model are meteorological variables, which can be taken from meteorological databases or outputs from GCMs. CARAIB has been used before to produce LGM vegetation distributions, using climatic forcings derived from a range of GCM simulation experiments (FRANÇOIS et al., 1998, 1999; OTTO et al., 2002; CHEDDADI et al., 2006; GALY et al., 2008). For the present study, we have derived a new global LGM vegetation distribution, which we discuss in Sect. 4.

Experimental setup

We carried out a series of sensitivity experiments with the Planet Simulator, implementing the factor separation method of STEIN and ALPERT (1993). This approach calculates and isolates the pure contribution of any factor, as well as the contributions due to interactions among two or more factors, using a linear combination of a number of simulations. 2^n simulations are then required to separate the pure and interaction contributions of n factors. Following the factor separation method, we carried out a series of sixteen sensitivity experiments, considering all the possible perturbations of a given control run configuration by prescribing changes of ice

sheet cover, orography, vegetation cover (through albedo and roughness length) and atmospheric carbon dioxide. Table 4.1 lists the changes in boundary conditions used for the sixteen experiments. The control experiment (CTRL) does not consider any of the changes, while the LGM experiment includes all of them. We included the LGM land-sea distribution and orbital forcing in the control configuration, taking into account their contributions to produce a complete LGM climate at the end of the series, but neglecting the contribution of their interactions with the other factors, since they are comparatively weak (Sect. 4).

A more complete study would have to further consider the effects of ocean circulation changes on the LGM climate. The simple mixed-layer model included in the Planet Simulator precludes the interactive calculation of such circulation changes that would thus have to be prescribed in a similar fashion to the land surface property changes, which we focus on in this study. An adequate prescribed sea surface temperature (SST) distribution, such as those provided by CLIMAP (CLIMAP PROJECT MEMBERS, 1976) or MARGO (KUCERA et al., 2005) reconstructions, would implicitly take into account such a change. However, there are two main reasons for *not* adopting this approach. First of all, BRACONNOT et al. (2007a) show the limitation of the use of CLIMAP SSTs with slab models, since they fail to produce the magnitude of the glacial cooling, especially in the tropics. Secondly, the use of fixed SSTs constrains the model sensitivity that reduces notably the impacts

of vegetation changes outside of land areas (GANOPOLSKI et al., 2001).

Table 4.1: Characteristics of the 16 simulation experiments. – refers to control values and + refers to LGM values. Each of the 4 columns corresponds to one of the four factors analysed: atmospheric CO₂, ice cover, orography and surface albedo.

Acronym	CO ₂	ICE	ORO	VEG
CTRL	–	–	–	–
C	+	–	–	–
I	–	+	–	–
O	–	–	+	–
V	–	–	–	+
CI	+	+	–	–
CO	+	–	+	–
CV	+	–	–	+
IO	–	+	+	–
IV	–	+	–	+
OV	–	–	+	+
CIO	+	+	+	–
CIV	+	+	–	+
COV	+	–	+	+
IOV	–	+	+	+
LGM	+	+	+	+

Alternatively, we could have derived a LGM heat flux distribution from a coupled ocean-atmosphere or a forced oceanic GCM simulation experiment. However, these simulation experiments do not yet provide a consistent picture on how the ocean circulation changed at the LGM (WEBER et al., 2007; LYNCH-STIEGLITZ et al., 2007). WEBER et al. (2007) analysed the results from nine different coupled PMIP model simulations. They find that the Atlantic Meridional Overturning Circulation was 10–40% more intense at the LGM than

at present-day in four out of nine models, 20–40% less intense in four other models, and slightly reduced only in one model.

We therefore decided to follow the PMIP1 protocol and we prescribed the present-day (control run) oceanic heat flux distributions even for the LGM. As a consequence, the model may respond with a larger sensitivity and simulate cooling closer to coupled ocean-atmosphere ones, if compared to fixed SSTs runs (BRACONNOT et al., 2007a). We must nevertheless keep in mind that some feedbacks and regional impacts of oceanic circulation changes at the LGM (as shown, e.g. by HEWITT et al. (2003) or KIM et al. (2003)) cannot be represented.

Boundary conditions and model configuration

All of the experiments, including the CTRL run, use common orbital forcings, land-sea distribution and oceanic configuration. The orbital parameters correspond to 21 kBP (excentricity 0.018 994, longitude of perihelion 114.42° and obliquity 22.949°). The solar constant is kept fixed at 1365 W/m². The model’s land distribution takes into account the emergence of land points due to the lower sea-level at 21 kBP. The land-sea mask used with the model has been derived from Peltier’s ICE-5G 1° by 1° resolution ice sheet reconstruction (PELTIER, 2004), interpolated onto the model’s grid.

In order to have a common land-sea mask for all of the sixteen simulation experiments, the CTRL run al-

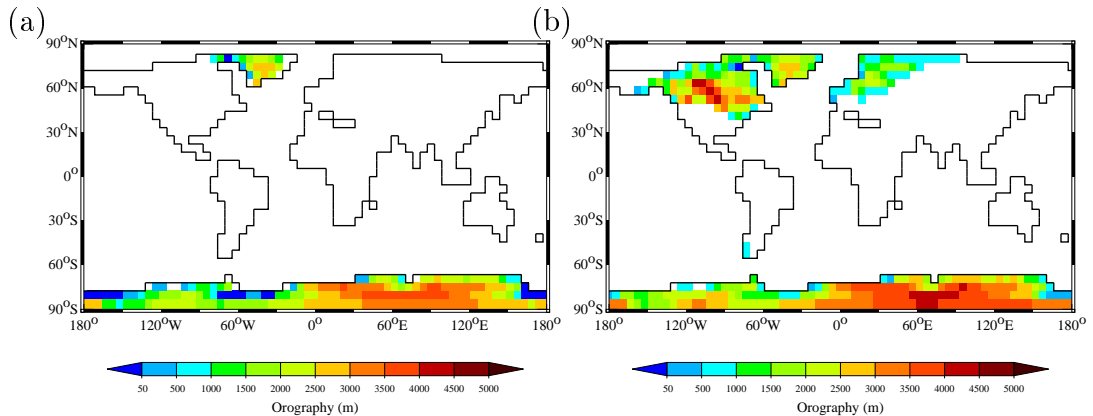


Figure 4.1: Land-sea mask and orography over the glacier mask for (a) the CTRL configuration and (b) the LGM configuration. The ice sheet expansion is shown by the colored pixels.

ready takes into account the exposure of land at the LGM that results from ice sheet growth. We chose not to include this land-sea mask change in the orography changes, since it brings about additional changes, such as vegetation cover or ice cover, which are analysed separately. Therefore, the effect of orography changes on the LGM climate considered here only relates to the increase of elevation at high latitudes. The emerging cells from the LGM land-sea distribution therefore also kept their oceanic albedo and roughness length in the CTRL run, making it as similar as possible to a pre-industrial configuration.

As initial conditions over ocean grid-points, we used the preindustrial SST and sea-ice distributions. The boundary conditions in time are given by the heat transfer calculated by the Planet Simulator for a preindustrial climate, following the PMIP1 protocol.

The CTRL experiment used a prein-

dustrial atmospheric CO_2 concentration of 280 ppmv. The control continental ice cover and orography have also been reconstructed from Peltier's ICE-5G for the preindustrial state, considering that grid-cells covered by an ice fraction greater than 50% are completely covered by ice (see Fig. 4.1). The vegetation parameters have been derived from a preindustrial vegetation distribution calculated from an equilibrium run of CARAIB, forced with 280 ppmv of CO_2 and the climatology of the CLIMATE database version 2.1 (W. Cramer, Potsdam, pers. comm.).

To obtain the LGM climate, we lowered the atmospheric CO_2 concentration to an ice age level of 200 ppmv (PETIT et al., 1999). We reconstructed the continental ice cover and orography from Peltier's ICE-5G for the LGM (see Fig. 4.1). The vegetation parameters have been replaced by their LGM distributions derived from a LGM vegeta-

tion distribution produced by CARAIB, except over the land points that are covered by ice sheets at LGM, in order to not overestimate the vegetation impact. We used an equilibrium run of CARAIB forced with 200 ppmv of CO₂ and a climate derived from the ECHAM4 GCM (ROECKNER et al., 1996) (revised version of the distribution shown by FRANÇOIS et al. (2003)). We calculated the anomalies of the GCM climatic fields between the LGM and the preindustrial, added to the CLIMATE database version 2.1, as climatic inputs for the LGM simulation, following the approach described in OTTO et al. (2002).

Neither the effects of lower CH₄ and N₂O concentrations in the atmosphere, nor those of the higher atmospheric dust content at the LGM have been taken into account here. These three agents are not included in the radiation scheme of the Planet Simulator. Their variations could lead to important additional cooling and provide feedbacks for the LGM climate system. This is well documented by the results of SCHNEIDER VON DEIMLING et al. (2006) who show that the increase of atmospheric dust at the LGM yields a net global cooling that is of the same order of magnitude than the vegetation induced cooling.

Results

Simulated LGM vegetation

The biome maps (Fig. 4.2) show the simulated preindustrial and LGM vegeta-

tion distributions, with a resolution of 0.5° by 0.5°. Globally, the simulated LGM vegetation cover is less dense than the preindustrial one. Grasslands and deserts expand, mainly at the expense of forest ecosystems, in response to the extremely cold and dry LGM conditions. CARAIB simulates a reduction of the total carbon stock (vegetation plus soil) of 734 Gt C, which is at the lower end of the LGM carbon stock reduction range suggested from reconstructions of palaeovegetation from palynological and sedimentological proxy data (-700 to -1600 Gt C), but slightly higher than estimates obtained with biospheric model forced with outputs of general circulation models (0 to 700 Gt C, after PEDERSEN et al. (2003)).

Regionally, the simulated LGM vegetation distribution is broadly consistent with the results of the Palaeovegetation Mapping Project BIOME 6000¹ (PRENTICE et al., 2000b; HARRISON et al., 2001; BIGELOW et al., 2003; PICKETT et al., 2004). Polar desert and tundra are modelled in a large part of the Northern Hemisphere continents. In Siberia and in the part of Alaska not covered by ice sheets, they replace the boreal forests (taïga), when in western Europe tundra replaces the temperate forests. Note that the polar desert or ice biome, extremely expanded in our LGM simulation, does not represent permanent ice, but the absence of vegetation, due to extremely cold and dry conditions. The warm temperate and mixed forests of southwestern Europe are replaced by semi-deserts. Colder

¹available under http://www.bridge.bris.ac.uk/resources/Databases/BIOMES_data

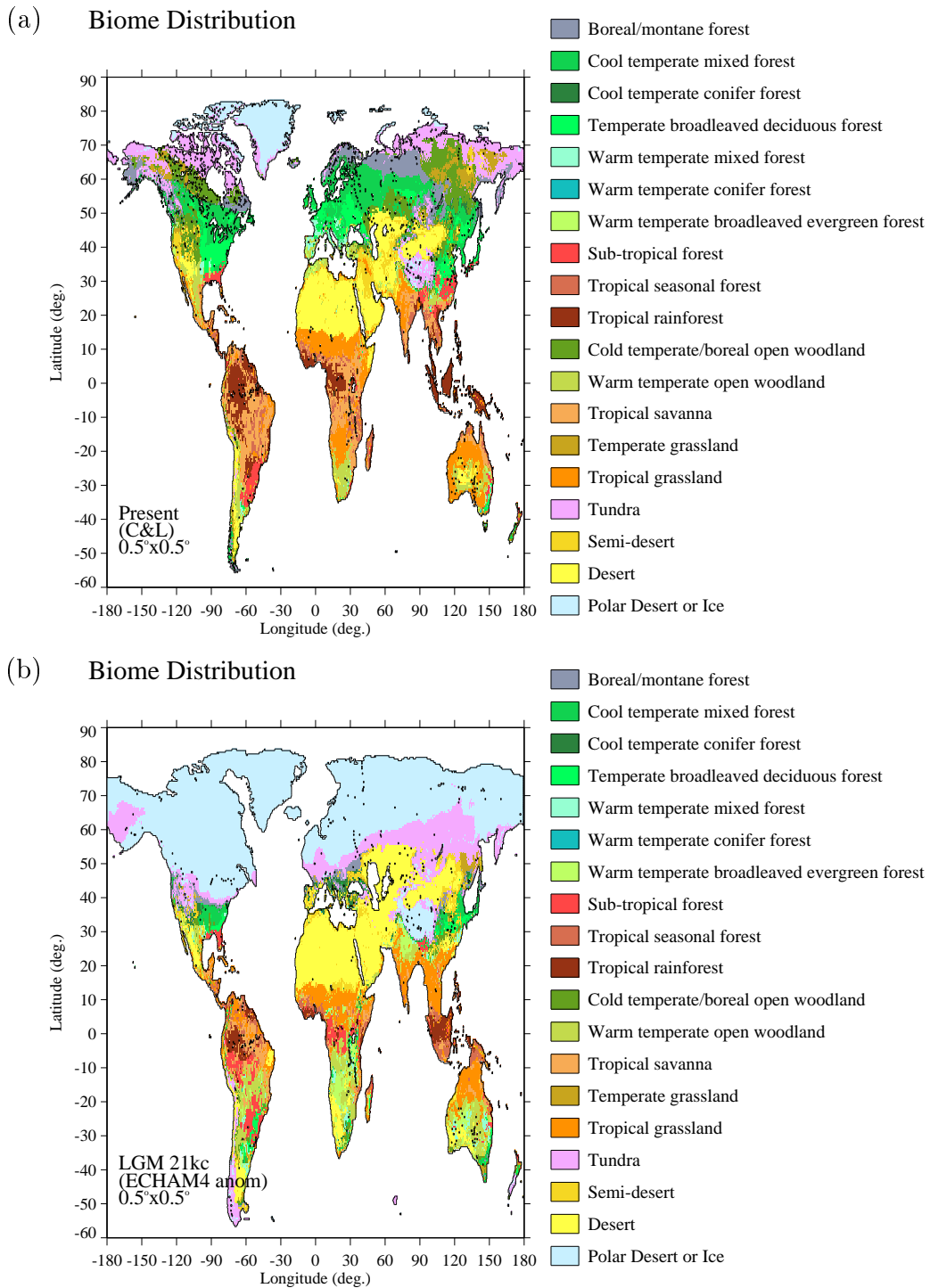


Figure 4.2: Biome distributions from CARAIB (a) preindustrial and (b) LGM equilibrium runs.

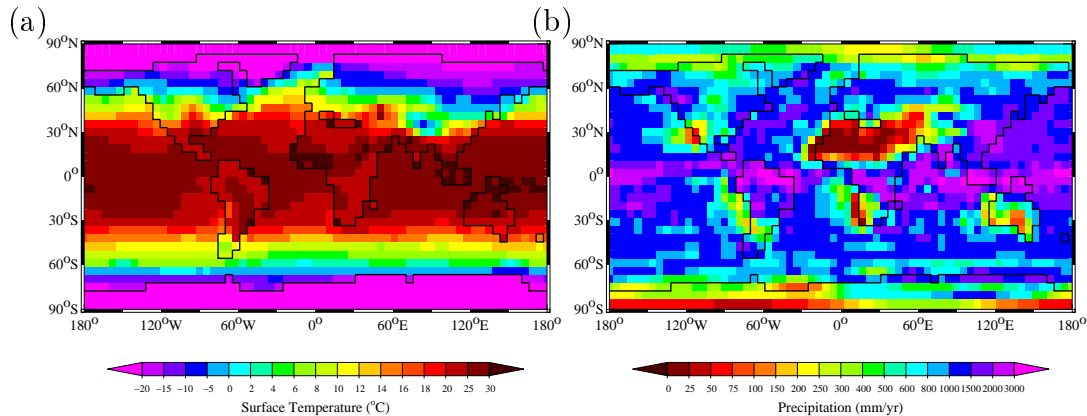


Figure 4.3: Control experiment (CTRL) results: (a) annual surface temperature; (b) precipitation.

forest types also appear in our results, as in the reconstruction of CHEDDADI et al. (2006). This latter reconstruction differs from the BIOME 6000 one and shows only semi-deserts in the region. North Africa is covered by deserts, with a southward expansion of the Sahara by less than 5° in latitude, replacing tropical grasslands or savannas. In Equatorial Africa the tropical rainforest is reduced, except in the western part. In Asia, deserts and grasslands expand, with an extension of deserts to the east in the centre of Asia, and the replacement of subtropical and temperate forests by tropical grasslands essentially in southeastern Asia. In North America, the forest biomes are shifted southward and replaced by tundra or polar deserts, and the subtropical types are limited to Florida. However, the predominance of deserts and grasslands in the west coast of North America, simulated by CARAIB, does not agree with the reconstructions of WILLIAMS et al. (2000) used in the BIOME6000 results,

which show mainly cool mixed forests and open woodlands in this region. It is more in line with the reconstruction of ADAMS et al. (1990). A fragmentation of the tropical rainforest and its replacement by savannas or subtropical forests occur in the north of South America, while the southern part is dominated by tundra and deserts. Finally, the tropical grasslands and deserts prevailing in the centre and the Southwest of Australia in the simulated preindustrial distribution are replaced by warm and open forests.

Control experiment

As mentioned before, the control state differs from a preindustrial one by the 21kBP orbital configuration and land-sea distribution that we separate from the other factors, due to the weak contributions of their interactions. Nevertheless, the pure effects of both factors contribute to the LGM climate. The change in the orbital forcing reduces the global

Table 4.2: Comparison of the pure contributions with the effects of the interactions between the factors on the global, oceanic and continental annual surface temperature (in °C). (See Fig. 4.5 for additional information.)

Acronym	Global	Ocean	Continent
C	-2	-1.9	-1.9
I	-2.7	-1.4	-5.7
O	+0.1	+0.4	-0.9
V	-1.3	-0.8	-2.5
CI	+0.1	+0.0	+0.1
CO	+0.1	+0.1	+0.1
CV	-0.0	-0.1	+0.2
IO	+0.2	+0.1	+0.4
IV	+0.2	+0.1	+0.5
OV	+0.1	+0.1	+0.0
CIO	+0.1	+0.1	-0.1
CIV	+0.1	+0.2	-0.2
COV	+0.0	+0.2	-0.3
IOV	+0.0	+0.1	-0.1
LGM	-0.0	-0.1	+0.1

mean surface temperature by 0.4°C from 15.2°C at preindustrial times, but it does not significantly affect the precipitation. Local cooling does not exceed -0.5°C over the continents and the open ocean. It may nevertheless reach -4°C over sea-ice, especially in the Antarctic ocean, due to the persistence of sea-ice in summer, following the lowering of the obliquity at 21kBP that reduces insolation at high latitudes in both hemispheres during their respective summers. The modification of the land-sea mask (with emerging grid-cells keeping oceanic surface albedo) warms the global mean temperature by 0.3°C. This warming is mainly due to the replacement of ocean by land grid-cells, preventing the formation of sea-ice on some grid-cells at high latitudes and the resulting strong albedo

feedback to take place, and limiting the evaporation on some emerged grid-cells in the tropics. Finally, the CTRL climate, combining both forcings, is close to a preindustrial climate (with a global surface temperature lowered by -0.1°C only). The surface temperature and precipitation distributions for the control state are shown on Fig. 4.3.

Global responses

We present here the global impacts of the pure contributions of the four factors, as well as the contributions of their interactions. The magnitude of the impacts of boundary condition changes on surface temperature and precipitation are shown in Fig. 4.4, represent-

Table 4.3: Comparison of the pure contributions with the effects of the interactions between the factors on the global, oceanic and continental annual precipitation (in mm/yr). (See Fig. 4.5 for additional information.)

Acronym	Global	Ocean	Continent
C	-33	-29	-33
I	-47	-23	-99
O	-1	-2	-1
V	-29	-5	-77
CI	+4	+4	+5
CO	+0	-4	+9
CV	+2	-0	+8
IO	+5	+4	+7
IV	+13	+5	+31
OV	+2	-1	+6
CIO	+1	+6	-9
CIV	+2	-0	+6
COV	+2	+5	-4
IOV	+1	+4	-3
LGM	-4	-8	-0

ing the anomalies between each experiment and the control run. Ice cover change (experiment I) is the factor producing globally the largest cooling and dryness, followed by CO₂ (experiment C) that gives an additional cooling effect when added to the ice cover change (experiment CI). Vegetation cover changes also significantly cool and dry the climate (experiment V), when orography changes slightly tend to warm the global climate (experiment O). The experiment CIV, adding ice, CO₂ and vegetation changes, is then the coolest and the driest of the series, even more than the complete LGM one, due to the absence of orography change. The global LGM cooling is -5.2°C (-10.4°C on the continents and -1.8°C on the oceans), and the global LGM precipitation reduction

is -79 mm/yr (-105 mm/yr on the continents and -45 mm/yr on the oceans).

The LGM cooling obtained here is consistent with the cooling simulated by the models used in PMIP1 (from -2 to -6°C for atmospheric GCMs with computed sea surface temperatures (JOUSSAUME and TAYLOR, 2000)) and PMIP2 (between -3.6 and -5.7°C for coupled atmosphere-ocean models (BRACONNOT et al., 2007a)), but it is at the cooler end of this range. This may be due to the lack of an explicit representation of ocean circulation in our model, as the slab models used in PMIP1 tended to produce stronger cooling over the Northern Hemisphere than the coupled ocean-atmosphere models (BRACONNOT et al., 2007a). However, none of the PMIP1 models and only a few of the PMIP2

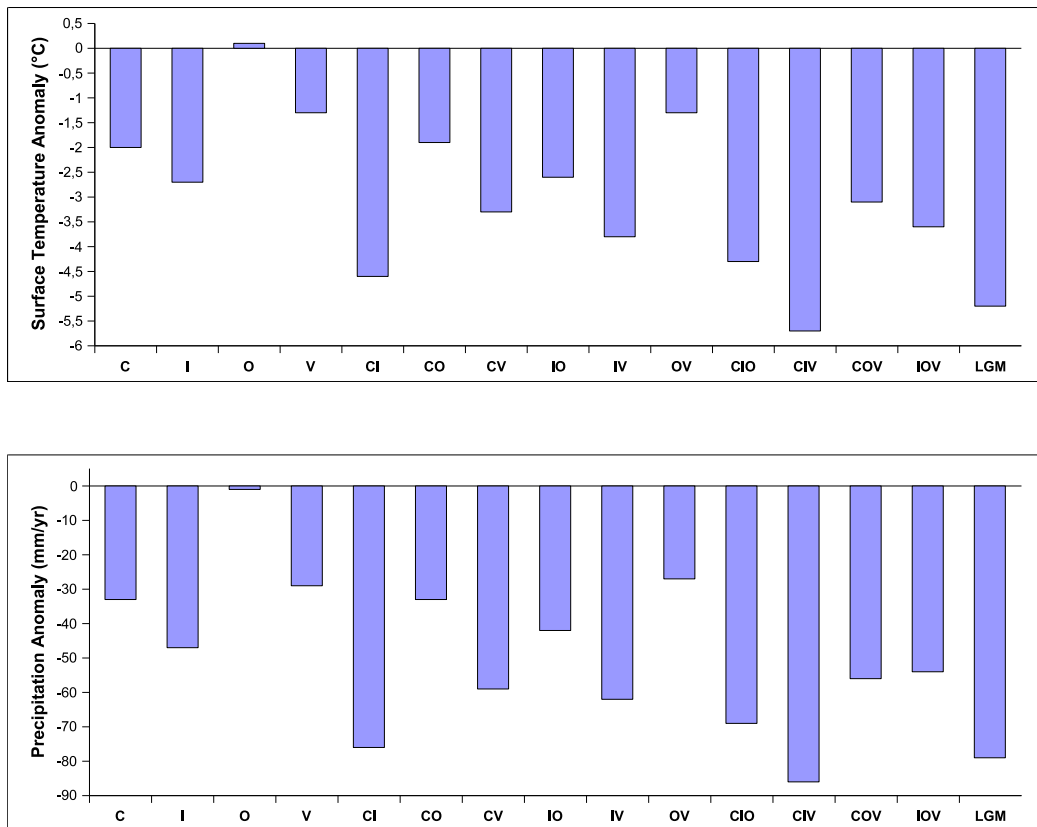


Figure 4.4: Global surface temperature and precipitation anomalies (EXPERIMENT-minus-CTRL). All results reported here are global means over the last 20 years of 50-year simulations, allowing 30 years for the model to equilibrate.

models have taken into account vegetation changes at LGM. The additional cooling simulated in our experiments may therefore be also due to the additional contribution of vegetation change. This is partially supported by the CIO experiment, which does not include vegetation changes. This simulated a global temperature anomaly of -4.3°C , which better fits the range of the PMIP1 and PMIP2 model cooling than the total LGM cooling of -5.2°C .

The impacts of the interactions of two or more factors on global, continental and oceanic surface temperature are shown respectively on Fig. 4.5a and Table 4.2, and on Fig. 4.5b and Table 4.3. The contributions of the pure factors (ice, CO_2 , vegetation and orography anomalies) are also shown for comparison. Note that we do not consider Antarctica in the calculation of the continental mean. Large changes especially in surface temperature that have only a weak impact on local climate and are not indicative of large scale climate change, can occur there. The interactions should be taken into account in the climate analysis, since they show evidence of the non linear feature of effects caused by the different factor combinations. For example, the combination of the ice and vegetation cover changes (experiment IV) produces non linear effects that result in an increase of surface temperature and precipitation. These effects act in the opposite direction of the pure contributions of ice and vegetation. The total cooling due to ice and vegetation cover changes (-3.8°C on global surface temperature, see Fig. 4.4) is then weaker than the simple addition of both pure contributions (-2.7°C for ice plus

-1.3°C for vegetation that is -4°C), since the interaction between both forcings gives a slight warming (of $+0.2^{\circ}\text{C}$ globally). Nevertheless, the interaction effects remain weaker than the pure contributions effects. Only the interactions between ice and vegetation, and ice and orography (experiments IV and IO) have comparable effects to the pure contribution ones, especially on the continents. The interaction IO notably warms the continental surface temperature by 0.4°C , while the pure orographic contribution leads to a continental warming of 0.9°C (Fig. 4.5). The increase of precipitation caused by the interaction IV ($+31\text{ mm/yr}$) also compares to the decrease of precipitation due to the CO_2 contribution (-33 mm/yr) (Fig. 4.5).

Spatial responses

Surface temperature

Figs. 4.6 and 4.7 illustrate the surface temperature responses to the prescription of the boundary condition forcings. The presence of ice sheets increases the albedo of ice covered grid-cells by more than 40% in comparison to the control state. The pure ice cover effect (experiment I, Fig. 4.6a) produces the largest cooling only in the Northern Hemisphere, in comparison to the other pure contributions of the series, but weakly affects the Southern Hemisphere. The weak impact of the ice cover effect in the Southern Hemisphere is due to the lack of oceanic circulation changes in our model. Only the small ice cap covering Patagonia leads to a pronounced local cooling. The largest decreases of surface temperature are located over the ice sheets and over the North Atlantic

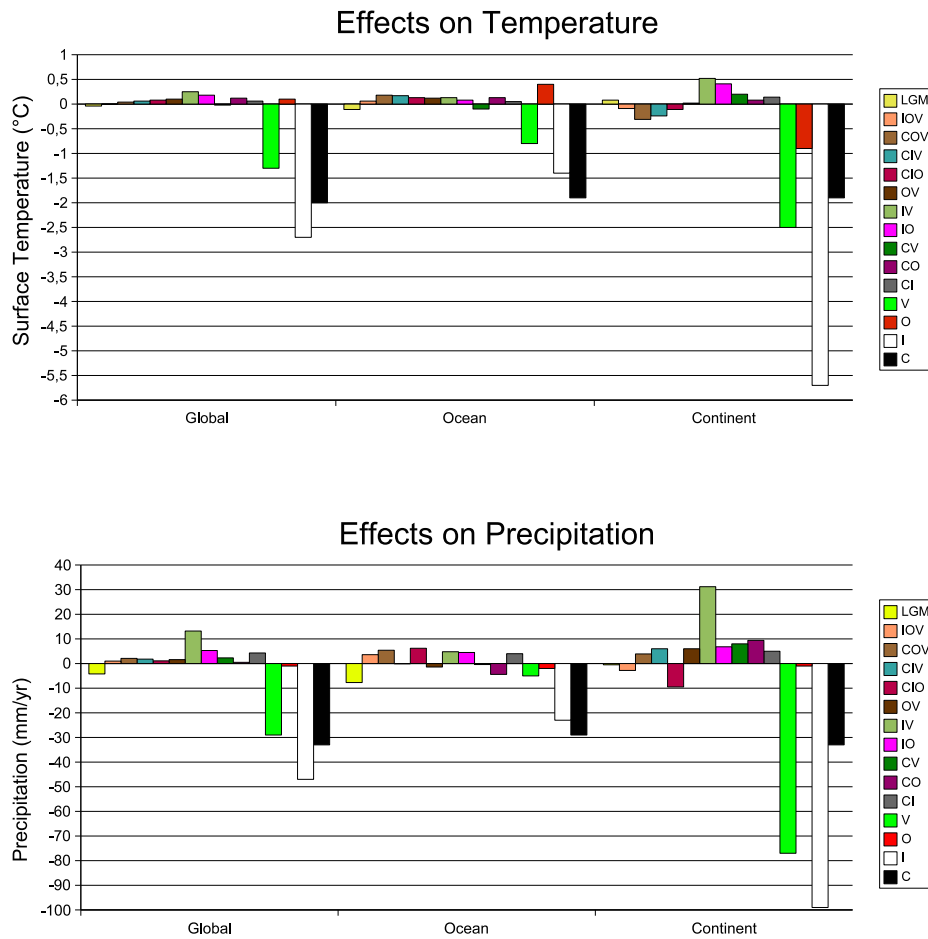


Figure 4.5: Comparison of the pure contributions with the effects of the interactions between the factors on the global, oceanic and continental annual (a) surface temperature and (b) precipitation. The C, I, O, V effects represent the pure contributions of each factor. The CI to LGM effects represent the contributions of the *interactions* among the corresponding factors, not the actual effects, shown on Fig. 4.4.

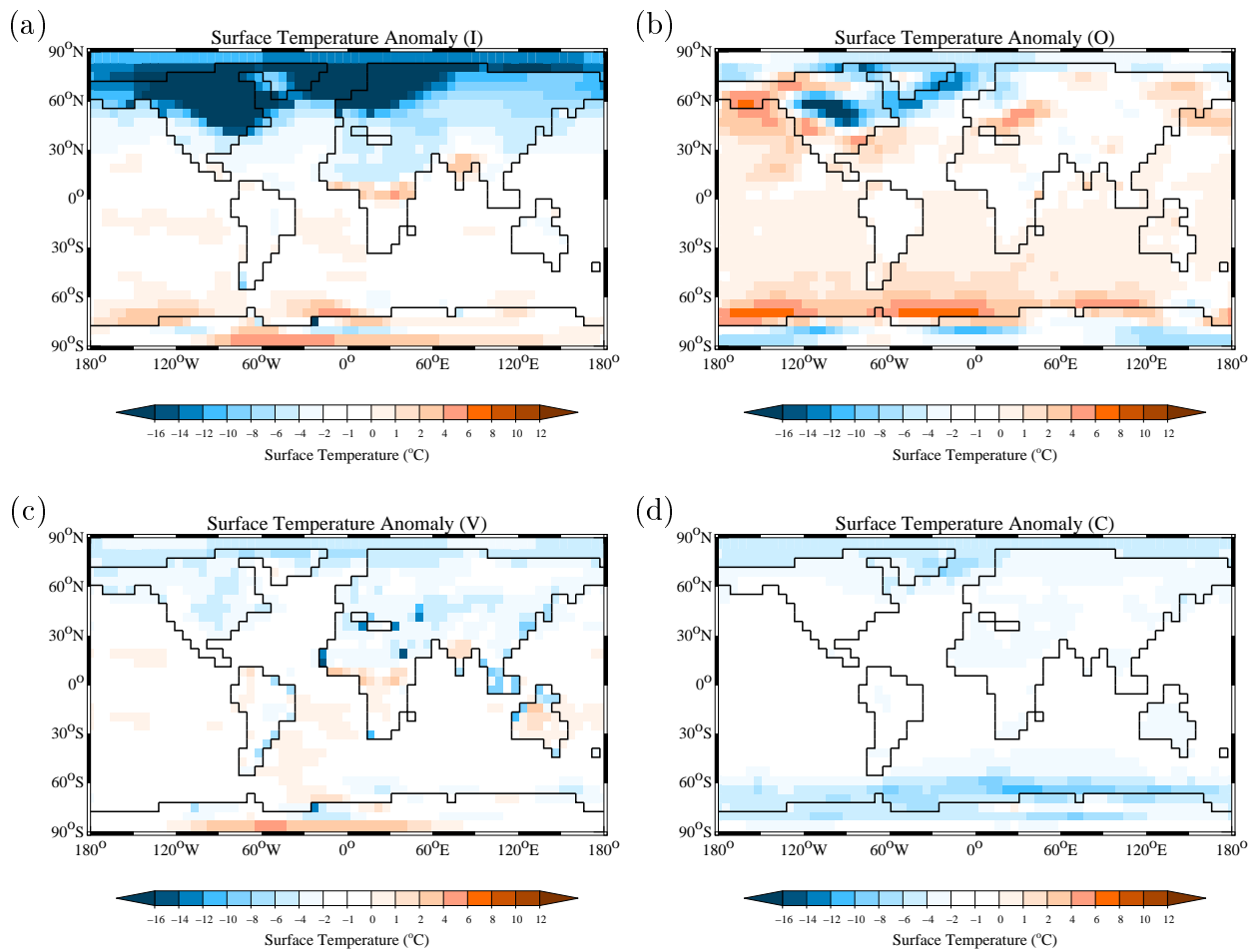


Figure 4.6: Annual surface temperature anomalies (EXPERIMENT-minus-CTRL) for (a) experiment I; (b) experiment O; (c) experiment V; (d) experiment C.

and the Arctic Oceans, resulting from an extension and thickening of sea-ice. The mid and low northern latitudes are also affected by some weaker cooling, but some tropical regions, as Equatorial Africa and India, are subjected to warming that is more pronounced during summer and linked to a decrease of summer rainfall.

Vegetation cover changes result in a large cooling on the Northern Hemisphere, mainly over the continents (experiment V, Fig. 4.6c). The vegetation contribution is comparable in terms of magnitude to the ice cover effect over the mid and low latitudes of the Northern Hemisphere. As described above, vegetation cover changes affect surface albedo and roughness length, but the albedo impact on surface temperature is dominant, because of its direct impact on the energy balance. The cooling produced on the continents of the Northern Hemisphere is directly linked to the increase of surface albedo by more than 10%, caused by the replacement of boreal and temperate forests by tundra or semi-deserts. Further, the induced cooling can be reinforced by the snow albedo feedback, on grid-cells covered by snow. However, Equatorial Africa and India also show some warming, related to a decrease of evaporation and summer rainfall, as in experiment I. Surface temperatures also increase in Australia and South Africa, but are caused instead by the increase of surface albedo, caused by the replacement of deserts and grasslands by forest biomes. Finally, there is pronounced but localized cooling over emerging land grid-cells at LGM, due to the replacement of their control oceanic albedos of 7% directly by LGM vegeta-

tion albedo greater than 15%. In experiment IV (Fig. 4.7a), the application of vegetation changes together with the presence of ice sheets reinforces and expands southward the cooling induced by the ice cover effect, especially over the high latitudes and the continents in the Northern Hemisphere. A stronger warming occurs in Equatorial Africa and India. However, the Southern Hemisphere remains weakly affected by both factors. Only vegetation changes produce a weak warming, due to a decrease in albedo.

The CO_2 contribution causes a rather uniform temperature cooling, of about -2°C (experiment C, Fig. 4.6d). The magnitude of the cooling is similar over continents and oceans, and in both Northern and Southern Hemispheres, making it the most important contributor to sea surface temperature cooling. Further, the CO_2 contribution results in a stronger cooling around the poles, especially over the Antarctic ocean, linked to an expansion and thickening of sea-ice. This reinforces the cooling trend in the Northern Hemisphere initiated by ice sheet and vegetation albedo effects, when all three forcings are combined (experiment CIV, Fig. 4.7c), and gives an additional cooling in the Southern Hemisphere, notably stronger than the vegetation warming impact in Australia and South Africa.

In contrast to the previous contributions, orography changes do not have a net cooling effect in the Northern Hemisphere (experiment O, Fig. 4.6b). The increased elevation produces large cooling over the ice sheets, especially over the Laurentide ice sheet, which has

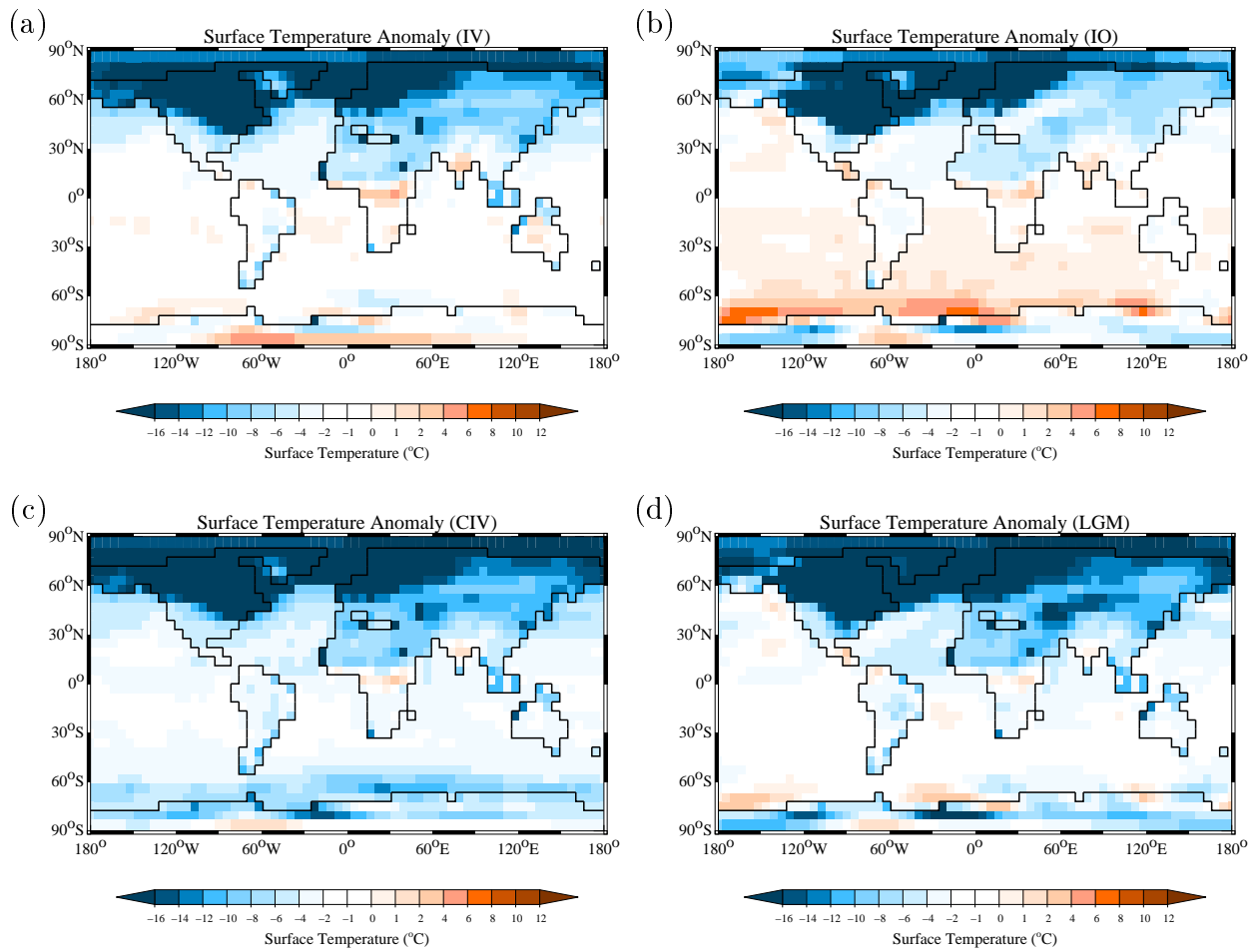


Figure 4.7: Annual surface temperature anomalies (EXPERIMENT-minus-CTRL) for (a) experiment IV; (b) experiment IO; (c) experiment CIV; (d) experiment LGM.

its surface at 3000 m.a.s.l. in the LGM reconstruction. The cooling also affects the Arctic and North Atlantic oceans. However, North America, Europe and also the West Pacific and North Atlantic experience large warming linked to precipitation changes, caused by wind track perturbations at mid and high latitudes, as discussed below. The combination of the ice sheet cover and orography forcings, representing the full contribution of the ice sheets on surface temperature of the ice sheets at LGM, leads to an additional cooling over the ice sheets (Fig. 4.7b). The cooling is weaker over the southern borders of the ice sheets, due to the orographic contribution. The cooling trend induced by the ice cover remains dominant over the continents of the Northern Hemisphere, whereas the orography changes minimize the cooling at the mid latitudes and slightly warm some oceanic regions, e.g. North West Pacific and Southern Ocean, where the ice albedo has weaker impacts.

The combination of the four factors (experiment LGM, Fig. 4.7d), keeps the cooling profile induced by ice cover, vegetation and CO₂ changes, as in the experiment CIV. However, experiment LGM is warmer than experiment CIV, due to the contribution of orography changes, warming the oceans and some continental regions of the mid latitudes in the Northern Hemisphere.

Precipitation

Figs. 4.8 and 4.9 illustrate the significant precipitation responses to the prescribed boundary condition forcings. In experiment I (Fig. 4.8a), the cooling induced by the ice cover effect dries out the

atmosphere, and reduces precipitation. Large reductions occur in the Northern Hemisphere, over the ice sheets, Siberia, Alaska and the North Atlantic Ocean. Further, the intense cooling of the continents strengthens the westerlies of the Northern Hemisphere, giving rise to precipitation in North America and North Pacific. Nevertheless, the impact of ice cover is not limited to the high latitudes and also strongly influences the tropical precipitation system by a southward shift of the control location of the Inter Tropical Convergence Zone (ITCZ). The strong cooling impact of ice cover on the surface and sea surface temperature in the Northern Hemisphere causes an increase of the inter-hemispheric temperature gradient, sufficient to lead to a displacement of the ITCZ to the warmer Southern Hemisphere. This explains the reduction of precipitation over the oceans and the continent and the weakening of the monsoon systems (except over southeastern China) in the northern part of the tropics (ITCZ control location), and the increase of precipitation to the south.

Vegetation changes in experiment V (Fig. 4.8c) in turn dry out the continents of the Northern Hemisphere, mainly due to the cooling effect of the increase of albedo. The cooling effect again strengthens the westerlies, increasing precipitation over the centre of North America, and is similar, but weaker in magnitude, to the ice cover effect. The tropics also undergo a strong reduction of precipitation, as in experiment I. By the same mechanism, the contribution of the vegetation changes is then sufficient to shift the ITCZ location southward, reducing oceanic and continental precipi-

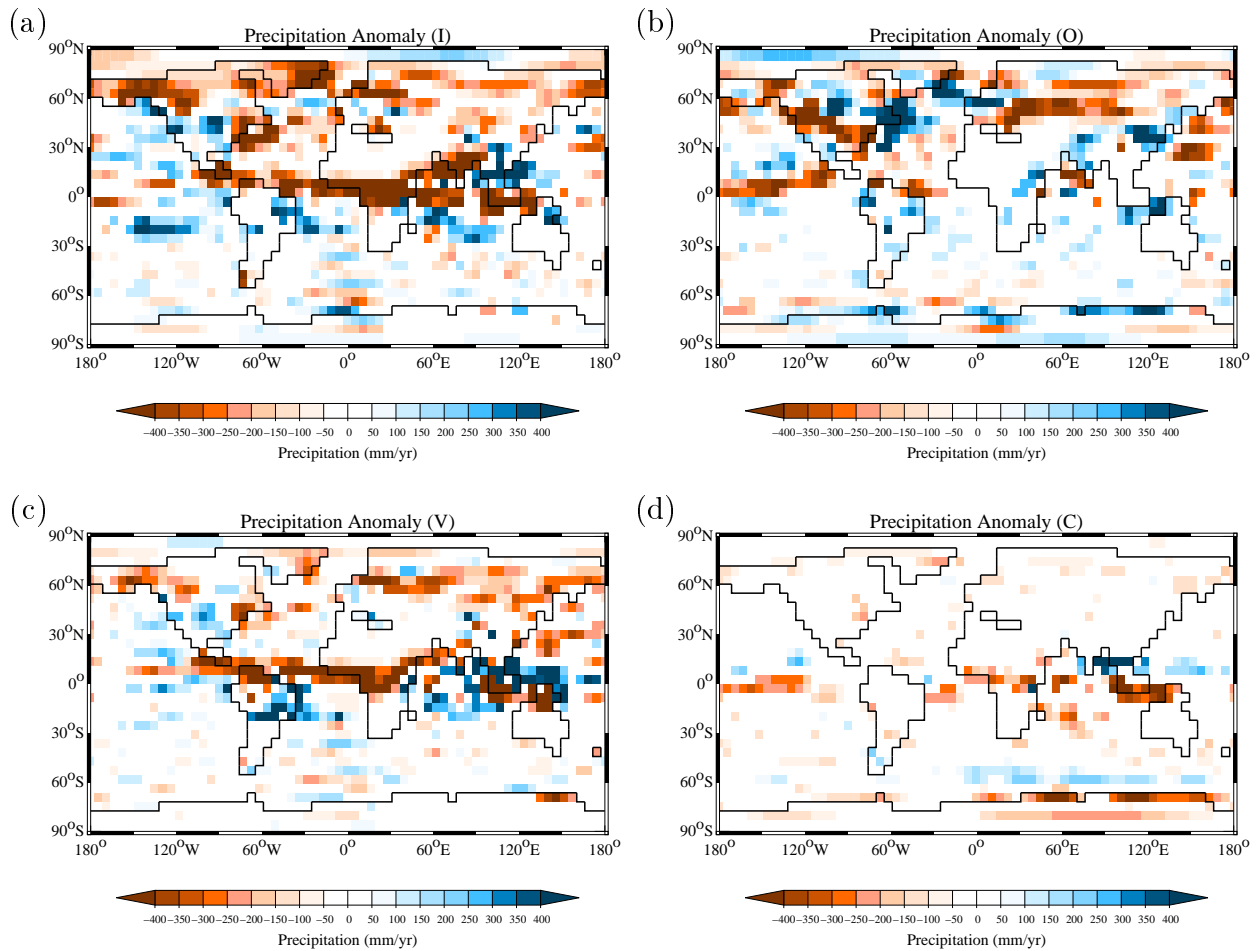


Figure 4.8: Annual precipitation anomalies (EXPERIMENT-minus-CTRL) for (a) experiment I; (b) experiment O; (c) experiment V; (d) experiment C. Only anomalies greater than one standard deviation for the long-term annual mean over the last 20 simulation years are shown.

tation in the northern part of the tropics. Nevertheless, the reduction of the rainforest in Amazonia, Equatorial Africa or Indonesia could also be responsible for the reduction of precipitation over these regions. The change of vegetation from rainforest to grasslands or savannas decreases the roughness length that in turn decreases the surface evaporation, thus warming and drying the air. The change in precipitation could be linked to the roughness length more than to the albedo effect. The combination of vegetation changes with ice cover (Fig. 4.9a) reinforces the dryness induced by ice albedo in the Northern Hemisphere, and intensifies the ITCZ shift, further decreasing rainfall over the ITCZ control location and increasing them southward.

Orography changes strongly affect precipitation over the mid and high latitudes of the Northern Hemisphere, by disrupting the atmospheric circulation (Fig. 4.8b). The presence of the high Laurentide ice sheet causes a split flow of the westerlies into two branches, one passing northward of the ice sheet and the other southward, and rejoining over the North Atlantic. As we can see on Fig. 4.10, showing the surface winter winds for the experiments CTRL and O, the split flow causes at the surface a deflection of the westerlies over Alaska and the formation of an anticyclonic circulation over the western portion of the Laurentide ice sheet. The northern part of the ice sheet is then crossed by a strong surface flow that increases precipitation there, while the southern part and the rest of North America is crossed by north to northwest flow originating from the anticyclone that causes a decrease of rainfall in these region. These

conditions prevail during winter, spring and autumn, but weaken during summer. Over the North Atlantic, where both flows merge together, precipitation generally increases. The deflection of the westerly wind belt over the North Atlantic, with south to southwest winds arriving to the southern part of the Fennoscandian ice sheet, increases precipitation on the ocean. However, it decreases the wind strength over western Europe, causing a large reduction of precipitation in the main part of Eurasia, explaining the net warming of the surface temperature described above. The Fennoscandian ice sheet also blocks the westerlies that contributes to the decrease of precipitation over Eurasia. The total ice sheet contribution, combining ice cover and orography forcings (experiment IO, Fig. 4.9b), keeps the precipitation profile imposed by orography changes in the Northern Hemisphere, and imposed by the ice albedo in the tropics. Nevertheless, the ice albedo cooling effect tends to increase the dryness of the continents of the Northern Hemisphere, except over North America, where the intensification of the westerlies causes more precipitation. The shift of the ITCZ over the ocean is more pronounced that can be linked to the further increase of the surface temperature gradient, due to warmer sea surface temperatures in the south, induced by orography changes.

The CO_2 contribution has the weakest impact on precipitation in the Northern Hemisphere, and dries out equally both hemispheres (Fig. 4.8d). Only the equatorial band is affected by a more pronounced decrease of precipitation, still weaker than the other pure contributions that can be

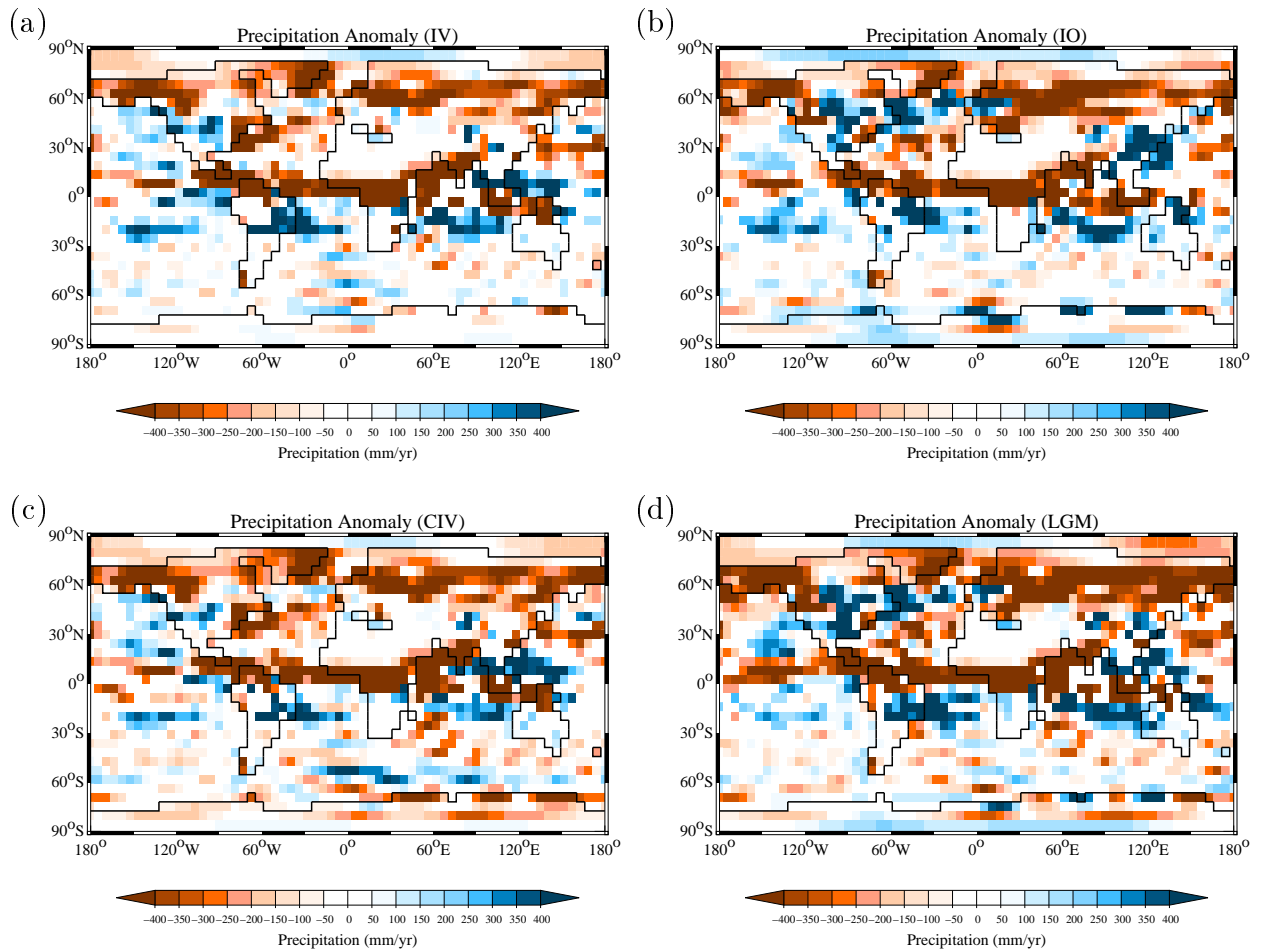


Figure 4.9: Annual precipitation anomalies (EXPERIMENT-minus-CTRL) for (a) experiment IV; (b) experiment IO; (c) experiment CIV; (d) experiment LGM. Only the anomalies greater than one standard deviation for the long-term annual mean over the last 20 simulation years are shown.

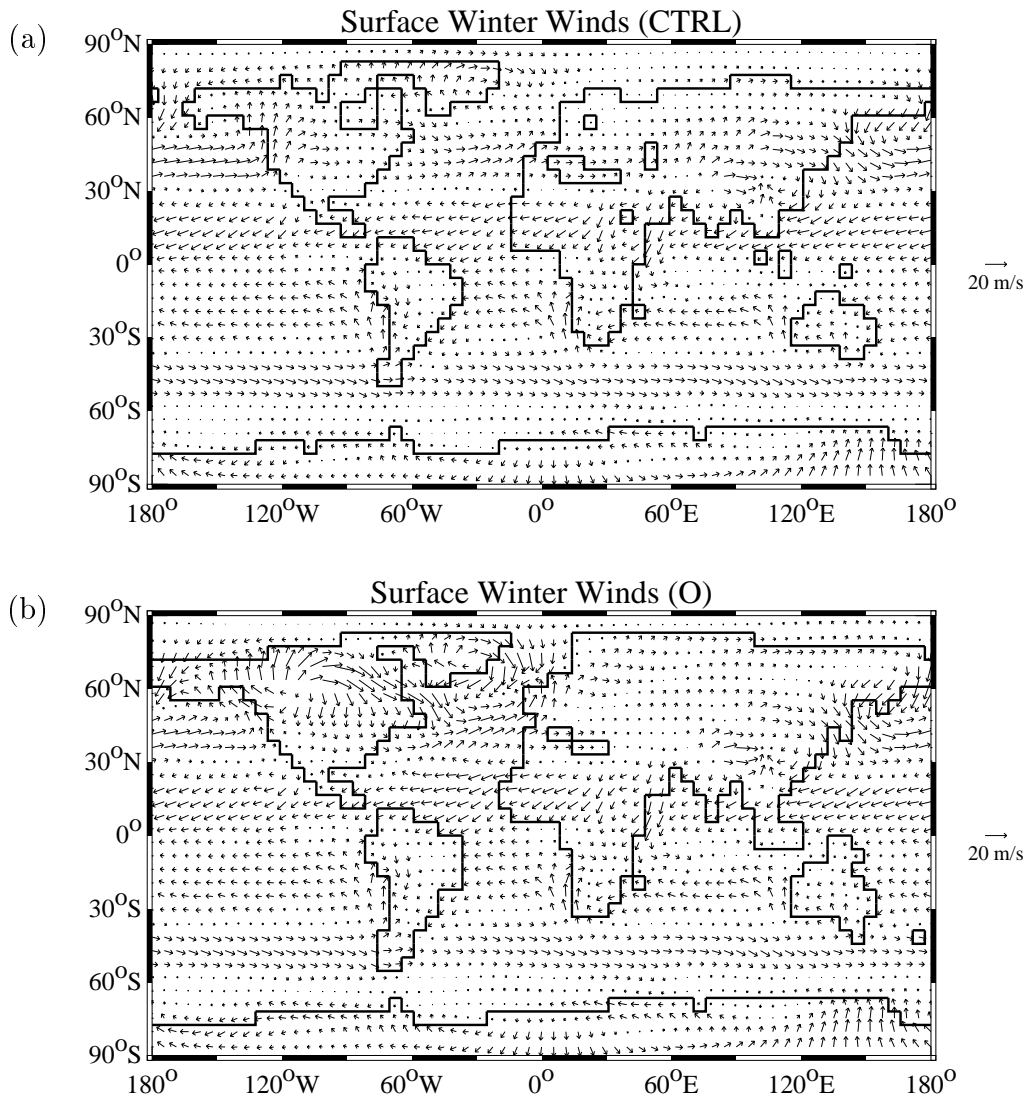


Figure 4.10: Surface winter winds resulting for (a) experiment CTRL (b) experiment O

related to the CO₂ induced sea surface temperature cooling. The combination of the CO₂ effect with the ice cover and vegetation change effects (Fig. 4.9c), generates the driest experiment of the series (experiment CIV), causing strong reductions of precipitation over the continents and a pronounced southward shift of the ITCZ. The addition of the orography contribution, in the experiment LGM (Fig. 4.9d), essentially modifies the precipitation distributions in the Northern Hemisphere, generating more precipitation over the north and north-west of the Laurentide ice sheet, in comparison to the experiment CIV. However, the drying over the continents of the Northern Hemisphere is reinforced, as well as the decrease of rainfall over the ITCZ control location.

Interaction effects

The global effect of the interactions among factors generally tend to increase temperatures and precipitation. However, the interactions have much more contrasted local effects, which may weaken or reinforce the pure contribution effects, depending on the region. We discuss here only the strongest interactions of the series, which are the interactions between ice cover and vegetation change (IV), and between ice cover and orography changes (IO), respectively. The other interactions of the series (OV, IOV, etc.) show similar patterns in their effects, but are weaker. We can also remark that the interactions between CO₂ changes and the other factors generates the weakest effects of the series. Fig. 4.11 shows the effects on surface temperature and precipitation of the interactions IV and IO.

Both interactions IV and IO warm the surface temperature over sea-ice in the Arctic Ocean, with the interaction IO causing a greater warming, even affecting the northern borders of the continents. The interactions here weaken the pure contributions of the three factors that tend to increase the sea-ice extent and thickness in the Arctic, reducing the regional climate cooling. In contrast, in the Antarctic Ocean, the interactions favor the sea-ice extent and thickening.

The interaction IV produces strong continental cooling, comparable in magnitude to the pure contributions, e.g. in Alaska (Fig. 4.11a). The increase of surface albedo due to both contributions cools the surface temperature, allowing snow to persist and the positive snow albedo feedback to reinforce the initial cooling induced by both pure contributions. However, over Equatorial Africa and India, the interaction leads to a cooling together with a precipitation increase (Fig. 4.11c). These effects can be related to a more important surface evaporation, permitted by the decrease of the sensible heat flux, due to the southward extension of the cooling trend caused by both I and V forcings. In this case, the interaction acts in the opposite direction of both pure contributions, and lowers their regional warming impacts.

The interaction IO produces strong cooling over the continents, particularly over North America, with an increase of rainfall (Figs. 4.11b and 4.11d). The interaction effect is opposite to the orographic warming effect in the concerned region. This regional cooling can be related to the ice induced cooling, rein-

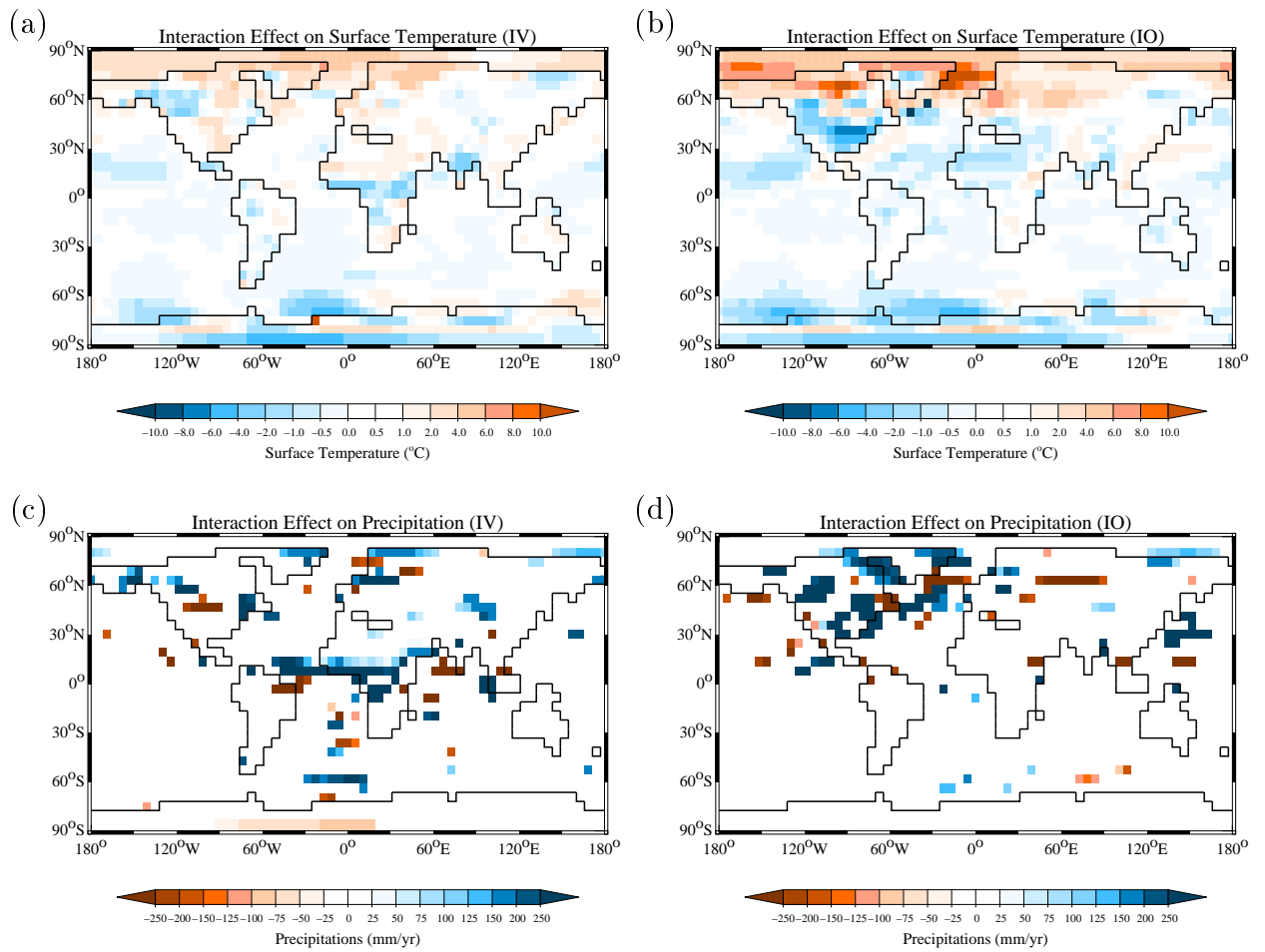


Figure 4.11: Effects of (a) interaction IV on surface temperature; (b) interaction IO on surface temperature; (c) interaction IV on precipitation; (d) interaction IO on precipitation.

forced by the snow albedo feedback, and possibly to the local topographic cooling induced by the orography change. However, precipitation also increases, related to the combined effects of the strengthening of the winds due to the ice contribution and the intensification of the northern branch of the jet stream due to the orography contribution. However, the interaction IO mainly affects the precipitation in the Northern Hemisphere, while the interaction IV essentially affects the tropics.

Discussion

Effects on surface temperature

The complete series of experiments allows us to analyse and distinguish several climatic impacts on the LGM climate, linked to the development of ice sheets, the lowering of atmospheric CO₂ and vegetation changes. The factor separation method of STEIN and ALPERT (1993) used here allows us to compare the relative roles of the factors, starting from the same control state. This procedure was previously adopted in the LGM climate studies of BERGER et al. (1996) and JAHN et al. (2005). It differs from the sequential procedure used in most previous sensitivity studies on the climate forcings at the LGM (BROCCOLI and MANABE, 1987b; HEWITT and MITCHELL, 1997; GANOPOLSKI, 2003; SCHNEIDER VON DEIMLING et al., 2006). The results derived from the sequential additive procedure are particularly sensitive to threshold effects, that could trigger large non-linear changes in the system when crossed. In

consequence, the magnitude of a given effect would be dependent on the order in which the forcings are applied. The factor separation method suffers less from this shortcoming. With this method, non-linear climate response is included in the interaction terms that the method allows to isolate from the pure contributions of the factors. Once the joint action of two or more processes makes the system cross a threshold, care needs to be taken to interpret the physical meaning of the interaction terms, as discussed by JAHN et al. (2005). The major disadvantage of the factor separation method is that it requires a large number of experiments to be carried out that can be minimized by a rigorous choice of the forcing studied. It is also best suited for use with EMICs, which allow to keep the required computing time within reasonable bounds.

In the following section, we compare our results to those of GANOPOLSKI (2003) and JAHN et al. (2005), who performed sensitivity studies with the CLIMBER-2 model. GANOPOLSKI (2003) used a sequential additive procedure, JAHN et al. (2005) the factor separation method. We obtain a global LGM cooling of -5.2°C that compares well with the global cooling of -5.1°C obtained by JAHN et al. (2005). The magnitudes of the global contributions show the dominant cooling effect of the ice sheets (combined albedo-temperature and altitude-temperature effects) that is -3°C in GANOPOLSKI (2003) and in JAHN et al. (2005) and -2.6°C in our experiment IO. The reduction of atmospheric CO₂ is the second major factor responsible for cooling the LGM climate globally, as al-

ready shown by BROCCOLI and MANABE (1987b). Reducing the concentration to 200 ppm (GANOPOLSKI, 2003) and to 190 ppm (JAHN et al., 2005) respectively cools the climate by 1.2°C and 1.5°C . Here, the lowering of the concentration to 200 ppm (experiment C) cools the climate by 2°C , due to the high sensitivity of PLASIM to CO_2 (FRAEDRICH et al., 2005b).

Locally, the presence of ice sheets cools mainly the high latitudes of the Northern Hemisphere in both models. However, due to the lack of oceanic circulation in our model, we do not reproduce the strengthening of the northward oceanic heat transfer that weakens the cooling in the Northern Hemisphere and reinforces the cooling in the Southern Hemisphere (JAHN et al., 2005). This explains the greater cooling produced in the Northern Hemisphere and some warming obtained in the Southern Ocean in experiment IO, in comparison to JAHN et al. (2005).

The lowering of atmospheric CO_2 mainly contributes to the sea-ice formation at high latitudes. In experiment C, it has a homogeneous cooling and drying effect in both hemispheres. Its local contribution, especially on the continents in the Northern Hemisphere, is the weakest of the four pure contributions. In JAHN et al. (2005), the lower CO_2 also impacts on the oceanic circulation, and reinforces once more the heat transfer to the North, leading to a stronger cooling in the Southern Hemisphere, if compared to our experiment C. Further, CO_2 induces in our results very weak non linear interactions with the other factors and always tends to rein-

force the cooling and the drying induced by the other factors. Due to the lack of oceanic circulation, we have possibly missed further oceanic feedbacks and their interactions. JAHN et al. (2005) obtained a switch from a warm ocean mode to a cold ocean mode (GANOPOLSKI and RAHMSTORF, 2001), when adding the ice sheet and CO_2 effects together. Overall, our results fairly agree with results of GANOPOLSKI (2003) and JAHN et al. (2005). Some differences may be attributed to the lack of oceanic circulation changes in our model, although differences in the magnitude of the results can also come from the different structures of the Planet Simulator and CLIMBER-2.

Focus on vegetation impact

The vegetation cover change produces a cooling of -1.3°C in the experiment V. Its pure contribution is globally lower than the ice and CO_2 contributions. However, its local impacts are comparable and even larger than the local impacts of CO_2 , especially on the continents and the northern latitudes of Eurasia, due to the taiga-tundra feedback (GANOPOLSKI et al., 2001). The magnitude of the vegetation effect in our results, confirms once again the importance of the vegetation contribution to the LGM climate. The additional cooling induced by LGM vegetation cover can be seen in the difference between experiments LGM and CIO. This cools the climate by -0.9°C , which is in line with the cooling obtained by GANOPOLSKI (2003) and JAHN et al. (2005) (respectively -0.6°C and -0.7°C). It is

also at the lower end (strongest cooling) of the range of temperature variations due to vegetation changes reported by SCHNEIDER VON DEIMLING et al. (2006) (-0.5°C to -1°C). The larger cooling in our results can therefore be attributed to a larger difference in the prescribed vegetation cover that nevertheless agrees well with the data. The additional vegetation impact in our results is also stronger than the impacts of prescribed vegetation reconstructions in previous studies (CROWLEY and BAUM, 1997; LEVIS et al., 1999; WYPUTTA and MCAVENEY, 2001). However, the weaker effects of vegetation in these studies could also be due to the use of fixed sea surface temperatures that leads to an underestimation of vegetation impacts, as shown by GANOPOLSKI et al. (2001).

Ice and orography impacts

The separation of the ice cover and orography contributions shows that the ice albedo effect is the main contributor to the cooling of the Northern Hemisphere, whereas orography has only a local cooling impact over the ice sheet. Several studies have already investigated these two effects, but on the basis of a sequentially additive procedure (RIND, 1987; KAGEYAMA and VALDES, 2000). The isolation of both contributions allows us to attribute the atmospheric circulation changes in the Northern Hemisphere to the orography effect, but the strengthening of the westerlies of the Northern Hemisphere to the ice albedo effect. Similarly to MANABE and BROCCOLI (1985) and BROCCOLI and MANABE (1987a) we find that the presence of

the Laurentide ice sheet has a predominant impact on the atmospheric circulation, causing a split flow of the westerlies into two branches that in turn leads to a disruption of the precipitation distributions in the Northern Hemisphere, and affects the surface temperature. We can also remark that the orographic contribution alone would have caused some warming in Europe and in the centre of North America. This warming is more than compensated by the cooling effect of the ice cover. The resulting impact of the ice sheets (orography plus ice albedo) in these regions is weaker than the pure ice albedo effect.

Effects on precipitation

Nevertheless, the ice sheet impact is not limited to the climate in the Northern Hemisphere. The ice cover contribution significantly affects the tropical regions and is even the main contributor to tropical precipitation decrease over the continents and the oceans. CHIANG et al. (2003), CHIANG and BITZ (2005) and BROCCOLI et al. (2006) already related the reduction of convective activity and precipitation in the tropics and particularly to the southward shift of the ITCZ (BRACONNOT et al., 2000) to the presence of ice in the Northern Hemisphere. In our case, the pure contribution of the ice sheet cover is sufficient to produce a reduction of the sea surface temperature in the Northern Hemisphere as well as in the northern part of the tropics (more particularly in the Equatorial Atlantic and Indian oceans). The meridional gradient across the equator is increased and the ITCZ shifted southward.

Interestingly, the addition of the orographic contribution intensifies the disruption of the tropical precipitation by warming the sea-surface temperature in the Southern Hemisphere.

The intense cooling of the continents in the Northern Hemisphere produced by the ice cover contribution and the persistence of snow also weakens the Asian summer monsoon, as in DEMENOCAL and RIND (1993). However, our results show an increase of precipitation over North East Asia that can be related to the strengthening of the Asian winter monsoon, as already obtained by YANASE and ABE OUCHI (2007) with simplified and coupled models of the PMIP2 simulations. The precipitation maximum during winter is also displaced to the Pacific, southward of Southeast Asia. This can be linked to the southward shift of the westerly jet stream, as in YANASE and ABE OUCHI (2007).

Ice cover is not the only effect that leads to a disruption of tropical rainfall. The vegetation contribution also strongly affects the tropics. As noted by KUBATZKI and CLAUSSEN (1998), the vegetation impacts remain essentially local, due partly to the use of fixed sea surface temperatures. However, the cooling produced over the continents of the Northern Hemisphere, mostly due to the albedo effect, is sufficient to reduce the convective activity of the ITCZ, as described in CRUCIFIX and HEWITT (2005), and to shift the ITCZ southward. Nevertheless the vegetation effect remains weaker than the ice albedo effect. Further, the addition of the vegetation contribution to the ice cover contribution reinforces the cooling and drying

over the Northern Hemisphere, as well as the precipitation decrease over the ITCZ control location, even if the interactions of both factors tend to act in opposite directions. The vegetation contribution also warms and dries the tropical regions of South America and Africa, as mentioned by LEVIS et al. (1999). This effect is linked to the reduction of the tropical rainforest, decreasing the roughness length in the model that in turn reduces the surface evaporation.

For completeness, we should mention that neither the effects of lower CH_4 and N_2O concentrations in the atmosphere, nor those of the higher atmospheric dust content at the LGM have been taken into account in the present study. As mentioned in Sect. 4, their variations could lead to important additional cooling and provide feedbacks for the LGM climate system. SCHNEIDER VON DEIMLING et al. (2006) notably show that the increase of atmospheric dustiness at the LGM yields a net global cooling of the same order of magnitude as the vegetation induced cooling.

Consistency with palaeo data

In order to estimate the consistency of the simulated LGM climate and of the boundary conditions impacts, we evaluated our results over Eurasia and Africa against the LGM climate reconstructed by WU et al. (2007). We have restricted our comparison to the continental areas in order to limit the oceanic influence, since our model does not include an OGCM. The WU et al. (2007) reconstruction was produced with an improved inverse vegetation model, using

a recent version of BIOME4 (KAPLAN, 2001) and pollen biome scores from the BIOME6000 project (PRENTICE et al., 2000b). Further, the improved inverse modelling method takes into account the direct physiological impact of the lower CO₂ concentration at LGM, reducing the bias in palaeoclimatic reconstruction (RAMSTEIN et al., 2007).

We compare our model results to reconstructions by using zonal averages, following the approach of KAGEYAMA et al. (2001). In order to keep the model averages comparable with the data coverage, we partitioned them into two sectors representing western Europe and Africa (20° W–20° E) on one hand, and eastern Europe, eastern Africa and western Siberia (20° E–60° E), on the other. The differentiation between two sectors allows us to clearly display the model results and the data with error bars, keeping the data points sufficiently well distributed in longitude over each one of the two sectors. It also allows us to highlight the meridional gradients in the studied climatic variables. Please notice that the anomalies are calculated between a modern climate run (same conditions as for preindustrial, except for an atmospheric CO₂ concentration of 340 ppm) and the LGM run described above, in order to be compatible with the reconstructed anomalies. The averages are taken over land points only. Figs. 4.12 and 4.13 show the zonal averages of the model anomalies and the data anomalies between LGM and modern climate for the mean temperature of the coldest month (MTCO), the mean temperature of the warmest month (MTWA), the mean annual temperature and precipitation (MAT and MAP, respectively). The

data error bars are also shown, representing the 5–95% confidence interval for each reconstruction and the ± 2 standard deviation curves, representing the longitudinal dispersion of the model results.

The simulated MTCO anomalies are generally colder in Eurasia than in Africa, and colder over latitudes over 40°N, suggesting a stronger LGM meridional gradient, compared to present-day. The model tends to overestimate the cooling over Siberia in comparison with the data, but the results remain within the data error bars, which are quite large over this region (interval of possible values of the order of 25°C). The cooling over northwestern Europe, linked to the presence of the Fennoscandian ice sheet, may also be overestimated, but no pollen data are available to confirm or contradict our results. The cooling is clearly underestimated over Africa. The model even gives a slight warming near the Equator.

The MTWA anomalies show a general cooling trend at the LGM, with some warming, especially over the eastern sector. The model reproduces quite well the absence of a net meridional gradient, but the variability of the model results is much stronger than the data error bars. This is due to the low resolution of the model and the average of the model results over large zones. The model tends to underestimate the cooling over western Europe, but still produces a strong cooling over the ice sheet. The discrepancies are still present over western Africa.

MAT values show a similar pattern to MTCO, even if the MAT anomalies are smaller than the MTCO ones. The

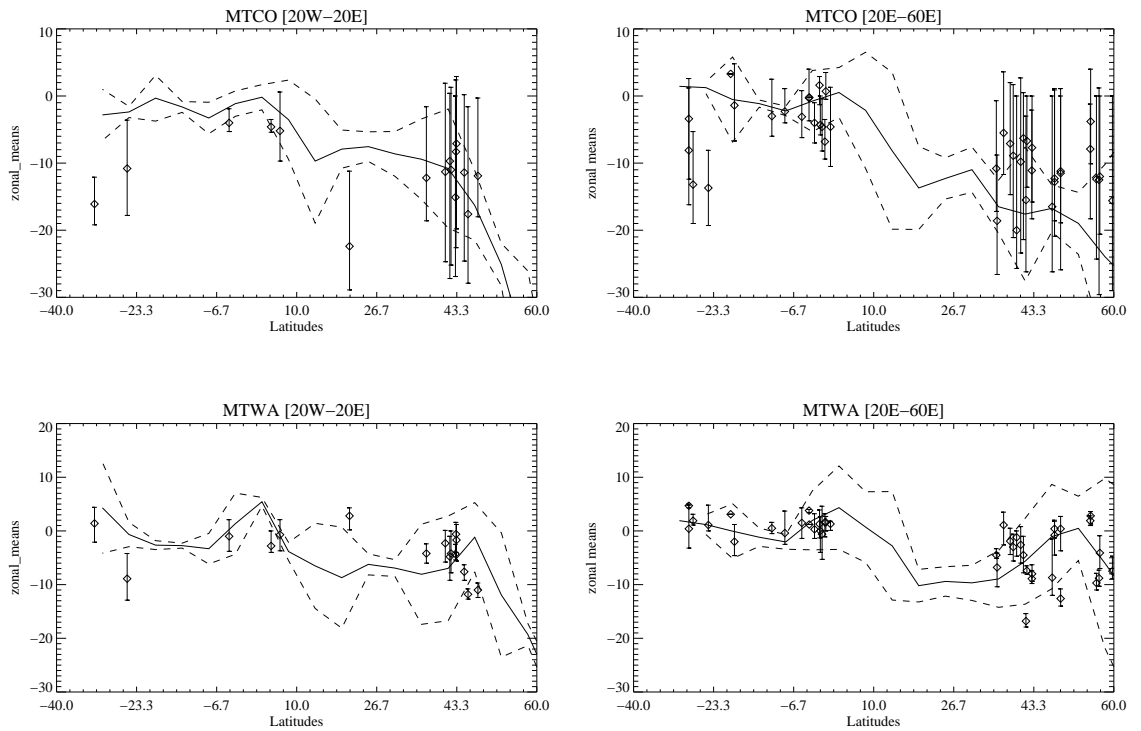


Figure 4.12: Comparison between model results and data for the LGM-minus-PRESENT anomalies of the mean temperature of the coldest month (MTCO) and the mean temperature of the warmest month (MTWA), in the two sectors (20° W– 20° E) and (20° E– 60° E). For the model, the longitudinal averages over land points (solid lines) are shown with the ± 2 standard deviation curves (dashed lines). Data points are represented by dots and shown with the 5–95% confidence intervals.

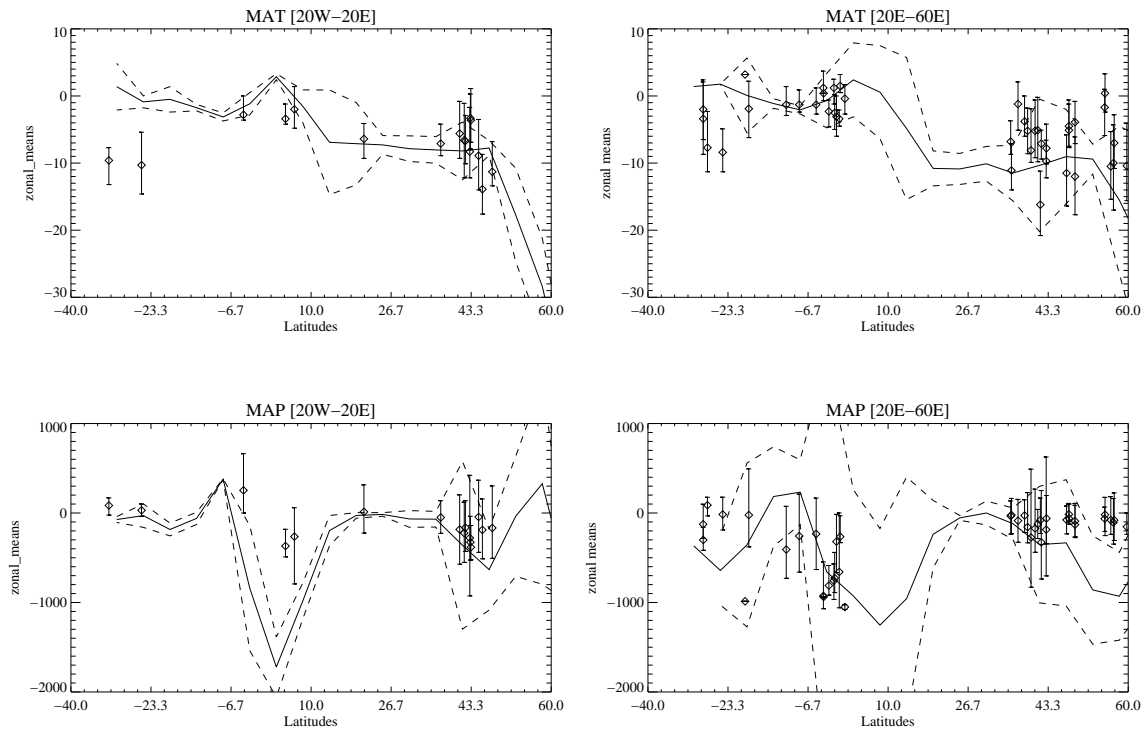


Figure 4.13: Comparison between model results and data for the LGM-minus-PRESENT anomalies in the mean annual temperature (MAT) and the mean annual precipitation (MAP) — see Fig. 4.12 for more details.

model also simulates drier conditions than today, with a decrease of MAP that agrees with data. The model tends to overestimate the decrease in precipitation over high latitudes, but gives a slight increase of precipitation over the ice sheet. A strong decrease is produced in Equatorial Africa that is not reproduced in the data. However the MAP anomalies over Africa are generally in better agreement with the data than the MAT anomalies, especially over the western sector.

Our results agree fairly well with the climatic reconstructions of WU et al. (2007) over Europe and western Siberia. They reproduce the south-west to north-east temperature gradient, with a decrease of MTCO cooling from Europe to Siberia, and the absence of significant MTWA gradient, as in the PMIP1 and PMIP2 model-pollen data comparisons carried out by KAGEYAMA et al. (2001, 2006). Our results show a better agreement with the data, in particular over western Europe, as we include the vegetation contribution, not taken into account in the PMIP1 simulations. Nevertheless, there are still regions where discrepancies remain significant. The model tends to overestimate the MTCO cooling and the dryness over Siberia, similar to several models in the PMIP1 project (KAGEYAMA et al., 2001). As explained in KAGEYAMA et al. (2001), it may also be due to the perturbation of atmospheric circulation produced by North Atlantic sea surface temperatures and sea-ice extent, computed by the slab ocean model. However, the MTCO cooling over northwestern Europe is generally stronger than the ones produced by the models with computed sea surface

temperatures used by KAGEYAMA et al. (2001). Therefore, it is in better agreement with the data over this sector.

On the other hand, the MTWA cooling is underestimated over western Europe (around 45°N), due to a decrease of MAP. These results may be related to too warm sea surface temperature computed by the slab model in the Mediterranean Sea, influencing the continental temperature and precipitation of this region and giving warmer and drier summers than in the reconstruction. The weakening of the westerlies due to orography changes (see Sect. 4) can also explain the warming of the region especially in summer. We cannot ascribe these discrepancies to the low resolution of the model or the poor representation of orography in this region. JOST et al. (2005) indeed find that these discrepancies persist at higher resolutions.

Over eastern and southern Africa, the model systematically underestimates the MTCO and MTWA cooling. This underestimation of the cooling by the model can be explained by the higher elevation of the data points (above 1500 m), in comparison to the model elevation (not exceeding 500 m). The reduction of the reconstructed temperature are then larger at higher elevation, as suggested by the reconstruction of temperature changes at the LGM from the snowline changes in East Africa carried out by MARK et al. (2005).

Conclusions

In this study, we used the Planet Simulator, an Earth System model of intermediate complexity to investigate the

contributions of the ice sheet expansion and elevation, the lowering of the atmospheric CO₂ and of the vegetation cover change on the LGM climate. The vegetation distributions for the preindustrial and the LGM were obtained with the dynamic vegetation model CARAIB. They compare fairly well in terms of biomes with the results of the Palaeovegetation Mapping Project BIOME6000 (PRENTICE et al., 2000b).

We applied here the factor separation method of STEIN and ALPERT (1993), in order to rigorously determine the different contributions of the boundary condition modifications. The method also allowed us to isolate the pure contributions, as well as the interactions among the factors. This same method was previously adopted in studies of BERGER et al. (1996) and JAHN et al. (2005) e.g. who focused on a smaller set of factors.

Our results highlight once more the dominant cooling and drying effect of the ice sheet expansion on the global scale LGM climate. This finding confirms the conclusions of GANOPOLSKI (2003) and JAHN et al. (2005). The next most important factors are the lower CO₂ concentration in the atmosphere and the vegetation cover change. Similarly to BROCCOLI and MANABE (1987b), we find that, locally, the ice albedo effect is also responsible for the strongest cooling in the Northern Hemisphere, while the reduction in atmospheric CO₂ is the main contributor to the Southern Hemisphere cooling. However, due to the lack of oceanic circulation changes in our model, we do not produce a strengthening of the north-

ward heat transfer, as in JAHN et al. (2005). Therefore our results show a generally colder and dryer effect of the ice sheet in the Northern Hemisphere and a more homogeneous impact of the CO₂ reduction in comparison to JAHN et al. (2005).

The separation of the ice cover and orographic contributions shows that the ice albedo effect is the main contributor to the cooling of the Northern Hemisphere, whereas orography has only a local cooling impact over the ice sheet, and gives the weakest global impact on temperature of the series of pure contributions. Further, the ice cover expansion in the Northern Hemisphere is identified for being responsible for the tropical precipitation disruption and the southward shift of the ITCZ, as already mentioned in CHIANG et al. (2003). The orographic changes at high latitudes mainly contribute to the disruption of the atmospheric circulation in the Northern Hemisphere, but do not have any significant impact in the tropics. According to BROCCOLI and MANABE (1987a), the presence of the Laurentide ice sheet has a predominant impact on the atmospheric circulation, causing a split flow of the westerlies into two branches, leading to a redistribution of the precipitation. This disruption of the precipitation causes some warming over the continents of the Northern Hemisphere and over the oceans. The cooling brought about by the ice cover, however, overcompensates for this warming.

In our experiments, the vegetation contribution induces strong cooling over the continents of the Northern Hemisphere, mainly caused by the increase of

albedo, even comparable in magnitude to the ice cover and CO₂ induced cooling in some regions. Further, the vegetation effects are also sufficient to affect the tropical precipitation on land and on the oceans, causing a southward shift of the ITCZ, which is reinforced when we combine the ice and vegetation contributions. The additional effect of vegetation changes under LGM boundary conditions gives a global cooling in line with the results of GANOPOLSKI (2003), JAHN et al. (2005) and SCHNEIDER VON DEIMLING et al. (2006), but slightly stronger due to the more contrasting vegetation reconstruction prescribed here.

The combinations of the factors generate many interactions, globally opposed to the pure contributions and weaker. However, locally the interaction effects are more complex and may either reinforce or weaken the pure contributions, depending on the regions of the globe and on the climatic mechanism involved.

Finally, our LGM climate results agree fairly well with the climatic reconstructions of WU et al. (2007) over Europe and western Siberia, notably due to the inclusion of vegetation changes. Our results reproduce well the south-west to

north-east MTCO gradient from Europe to Siberia, and the absence of significant MTWA gradient, as in the PMIP1 and PMIP2 model-pollen data comparisons carried out by KAGEYAMA et al. (2001, 2006). However, our results do not support the strong cooling over Africa that are due to the use of elevated data points for the paleoclimatic reconstructions.

Acknowledgements

We thank Michel Crucifix for helpful discussions and for pointing out the STEIN and ALPERT (1993) method to us. We acknowledge the efforts of the Planet Simulator team (especially Klaus Fraedrich, Edilbert Kirk and Frank Lunkeit) for making available their model as Open Source Software and for the sustained development and help. We thank Stefan Lorenz for providing the ECHAM4 data. Comments by Andrey Ganopolski and one anonymous reviewer helped to improve the manuscript submitted for discussion. A.-J. Henrot is a Research Fellow and G. Munhoven a Research Associate with the Belgian Fund for Scientific Research (F.R.S.-FNRS). Support for the work of S. Brewer was provided by FRFC convention no. 2.4555.06.

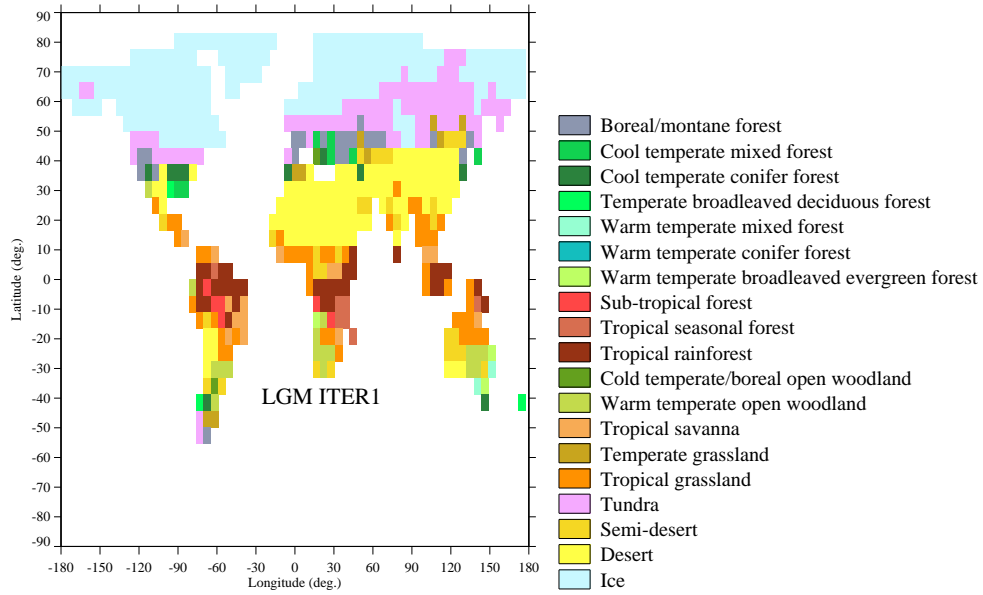
4.1 Climate-vegetation iterations for the LGM

In order to complete the analysis of climate-vegetation interactions in our LGM experiments, we tested here the effect of the LGM climate simulated with the Planet Simulator on the vegetation distribution produced with CARAIB. Starting from the climate of the full LGM experiment with the Planet Simulator (experiment LGM in HENROT et al. (2009)), we carried out a series of five iterations with CARAIB and Planet Simulator, applying the asynchronous coupling procedure described in the previous chapter (see Section 3.3). For the first iteration, CARAIB was forced with an atmospheric CO₂ concentration of 200 ppmv and with the climatic anomalies between the LGM and the CTRL experiments, added to the NEW et al. (2002) climatology, following the approach described in Section 3.1.2. Then, the Planet Simulator was forced with the vegetation parameters derived from the first vegetation distribution obtained with CARAIB. This set of vegetation and climate simulations completed the first iteration. It should be noticed that both models have been run on a T21 grid.

The results of the first vegetation iteration (LGM ITER1) yield an open and desertic vegetation at the LGM, as illustrated by the biome distribution shown in Figure 4.14. This biome distribution compares fairly well with the biome distribution obtained from a CARAIB simulation forced with the LGM climate simulated by ECHAM4 and shown in Figure 4.2. Besides the differences in the resolutions (0.5° and T21 here), and in the climatic inputs, derived from two different models (ECHAM4 and Planet Simulator), both distributions yields polar deserts expansion as south as 40°N over the continents. In agreement with the ECHAM4-CARAIB vegetation distribution, desert and tundra ecosystems are dominant at middle latitudes in the LGM ITER1 distribution, while the vegetation distribution over the continents in the tropics and in the Southern Hemisphere is less affected by vegetation changes relative to the preindustrial state. Nevertheless, in the biome distribution LGM ITER1, deserts are much more expanded in Asia, in response to very dry conditions produced in the experiment LGM over that region (see Section 4). In contrast, the tropical forest biome is more expanded in East and Equatorial Africa, indicating that despite the strong precipitation decreases that occur in the tropics in experiment LGM, the precipitation rates are sufficient to maintain tropical forests in these regions. This last result does not agree with previous LGM vegetation reconstructions, which suggest a reduction of the tropical rainforest areas at LGM (CROWLEY and BAUM, 1997; WYPUTTA and MCAVENEY, 2001).

After the first vegetation iteration, no significant changes occur in the

(a) Biome Distribution



(b) Biome Distribution

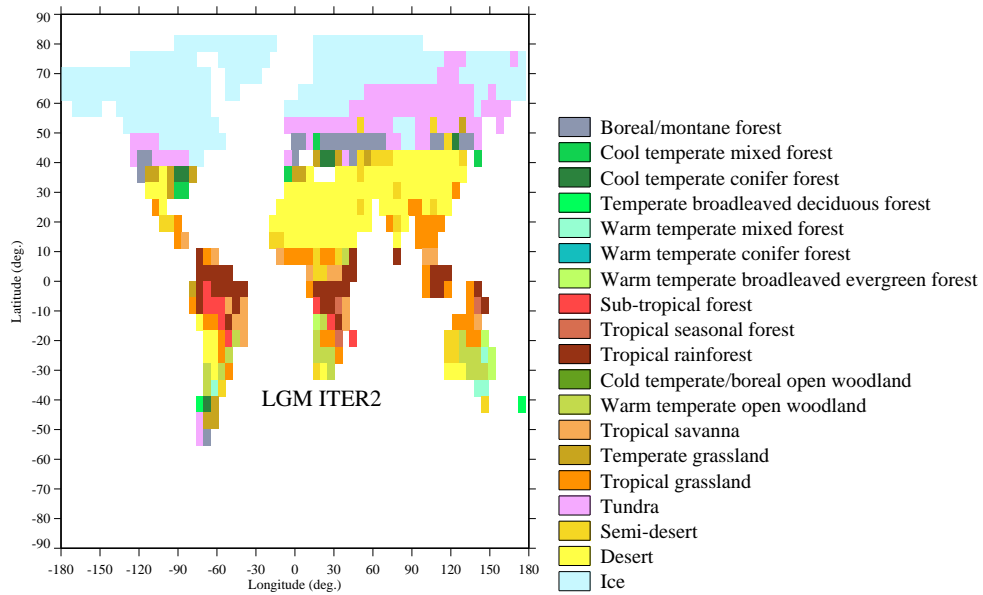


Figure 4.14: CARAIB biome distributions for (a) the first vegetation iteration (LGM ITER1) and (b) the second vegetation iteration (LGM ITER2).

vegetation distributions simulated in the series of iterations. Only a few grid-cells are concerned by biome changes from the LGM ITER1 distribution to the LGM ITER2 (see Figure 4.14). After the first iteration, the differences in biome distributions (calculated as in Section 3.4) differ by less than 12% (see Figure 4.15). The global NPP only significantly varies from the ECHAM4-CARAIB simulation to the LGM ITER1 one. The NPP decrease that occurs at the first iteration is mainly due to the expansion of desert and semi-desert ecosystems in Asia in the LGM ITER1 simulation. Thus, we can consider that the vegetation distributions do not significantly change after the first iteration. As for the series of iterations performed for the preindustrial period, the differences in the successive biome distributions can be attributed to the crossing of the thresholds used to classify the vegetation types, rather than to significant climate changes.

The effect of the simulated CARAIB vegetation LGM ITER1 on climate in the first iteration is shown in Figure 4.17. The vegetation effect slightly reinforces the continental cooling at middle and high latitudes, particularly in Asia in response to the increase of surface albedo due to the expansion of deserts. However, the expansion of tropical forests induces surface albedo decreases that lead to slight temperature increases in tropical regions. The precipitation distribution is weakly affected by the vegetation effect, except over the tropics where the expansion of the tropical forests in Equatorial Africa leads to increases of surface evaporation and consequently of precipitation, which helps to maintain warm and moist conditions that are favourable for the subsistence of tropical forests in the region. This effect is notably opposed to the first large scale effect of vegetation on the simulated LGM climate that tended to decrease precipitation in the tropics (see results of experiment V in HENROT et al. (2009)). However, we did not take into account field capacity changes linked to vegetation changes in the previous experiments (experiments V and LGM). Only surface albedo and roughness length were modified in the experiments V and LGM, whereas we modified the field capacity in the series of climate iterations described here. Thus, the reduction of tropical forest areas obtained in the ECHAM4-CARAIB vegetation distribution should have reinforced the decreases of precipitation in the tropics induced by the increase of surface albedo in experiments V and LGM, if field capacity changes were considered. This would be in line with the results of WYPUTTA and MCAVENEY (2001) who simulated precipitation decreases in the tropics in response to the replacement of tropical forests by savannas.

Nevertheless, the vegetation effects on climate at the first iteration remain relatively weaker than the first effects of vegetation on climate studied in experiment V. This may be explained by the fact that vegetation effects were

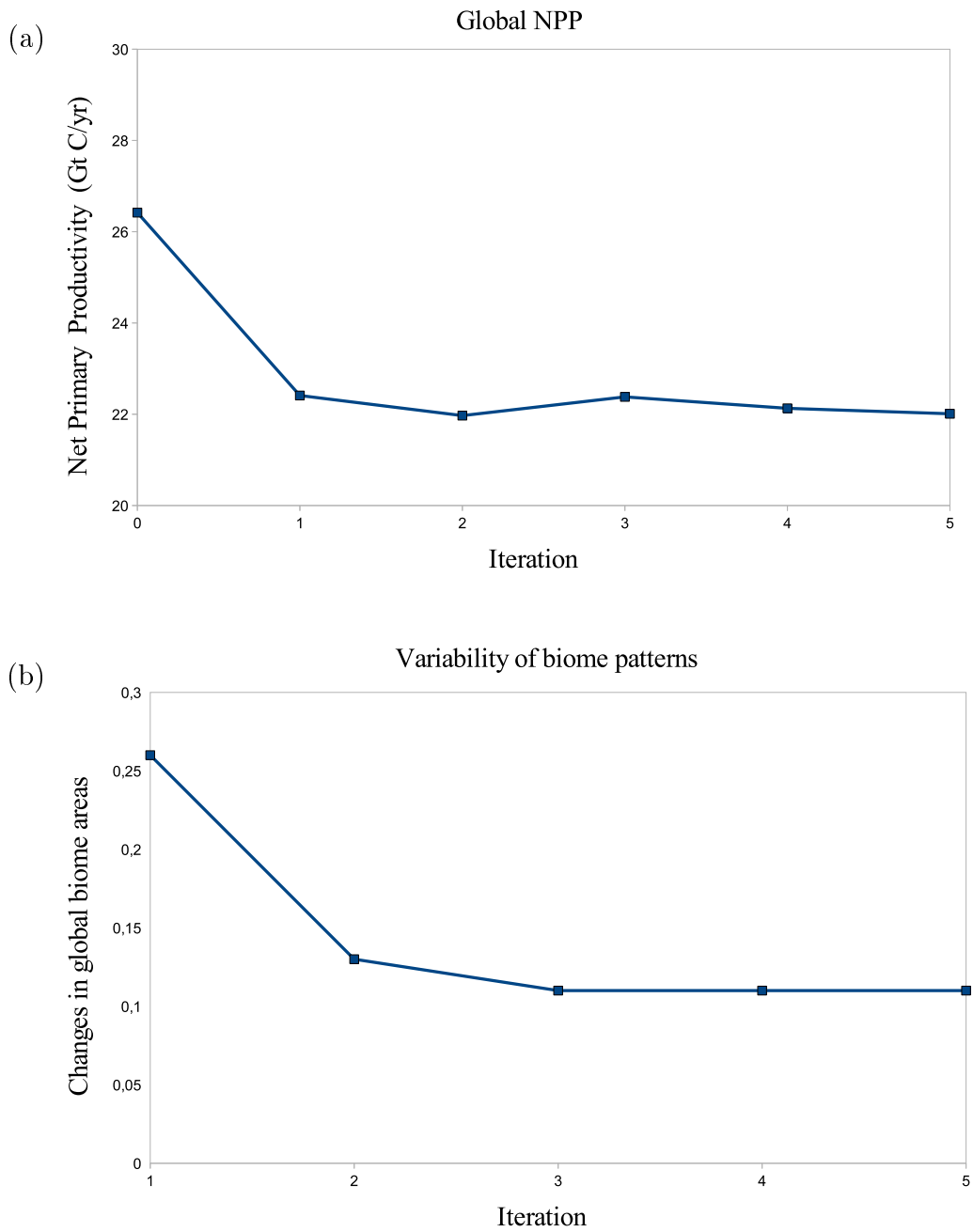


Figure 4.15: (a) Global Net Primary Productivity (Gt C/yr) for each vegetation iteration, and (b) Total area in term of percentage land surface in which biomes differ from two successive vegetation iterations, including the ECHAM4-CARAIB vegetation distribution as iteration 0.

already taken into account in the experiment LGM from which we started the series of iterations, and that the vegetation produced here differs only slightly from the ECHAM4-CARAIB vegetation distribution used to force the experiments V and LGM. After the first iteration, no significant trend in the climate variables is observed (see Figure 4.16). The extent of deserts remains hardly constant in the following vegetation distributions. The tropical forests also remain well installed in Equatorial Africa and in the other tropical regions. However, tropical forests do not further expand in the next vegetation iterations. Consequently, no significant increase of precipitation occurs in the climate experiments. Therefore, we can consider that the incorporation of the CARAIB derived surface parameters does not induce a significant trend in the LGM climate simulated by the Planet Simulator after the first iteration. The vegetation simulated at the first iteration produces some additional cooling effects over continental regions, which confirms the cooling effect of vegetation changes on the LGM climate. On the other hand, the consideration of soil water changes in response to vegetation changes leads to precipitation increases in the tropics that are opposed to the other vegetation effects that contribute to decrease the precipitation in the tropics. The expansion of the tropical forests in Equatorial Africa we obtained here disagrees with previous vegetation reconstructions (CROWLEY and BAUM, 1997; PRENTICE et al., 2000b; WYPUTTA and MCAVENEY, 2001). However, interestingly, the increase of precipitation simulated here in response to the expansion of tropical forests in the CARAIB vegetation distribution LGM ITER1 could help to improve the comparison of the simulated mean annual precipitation rates (MAP) with the proxy-based reconstructions of MAP over eastern Equatorial Africa (see Section 4).

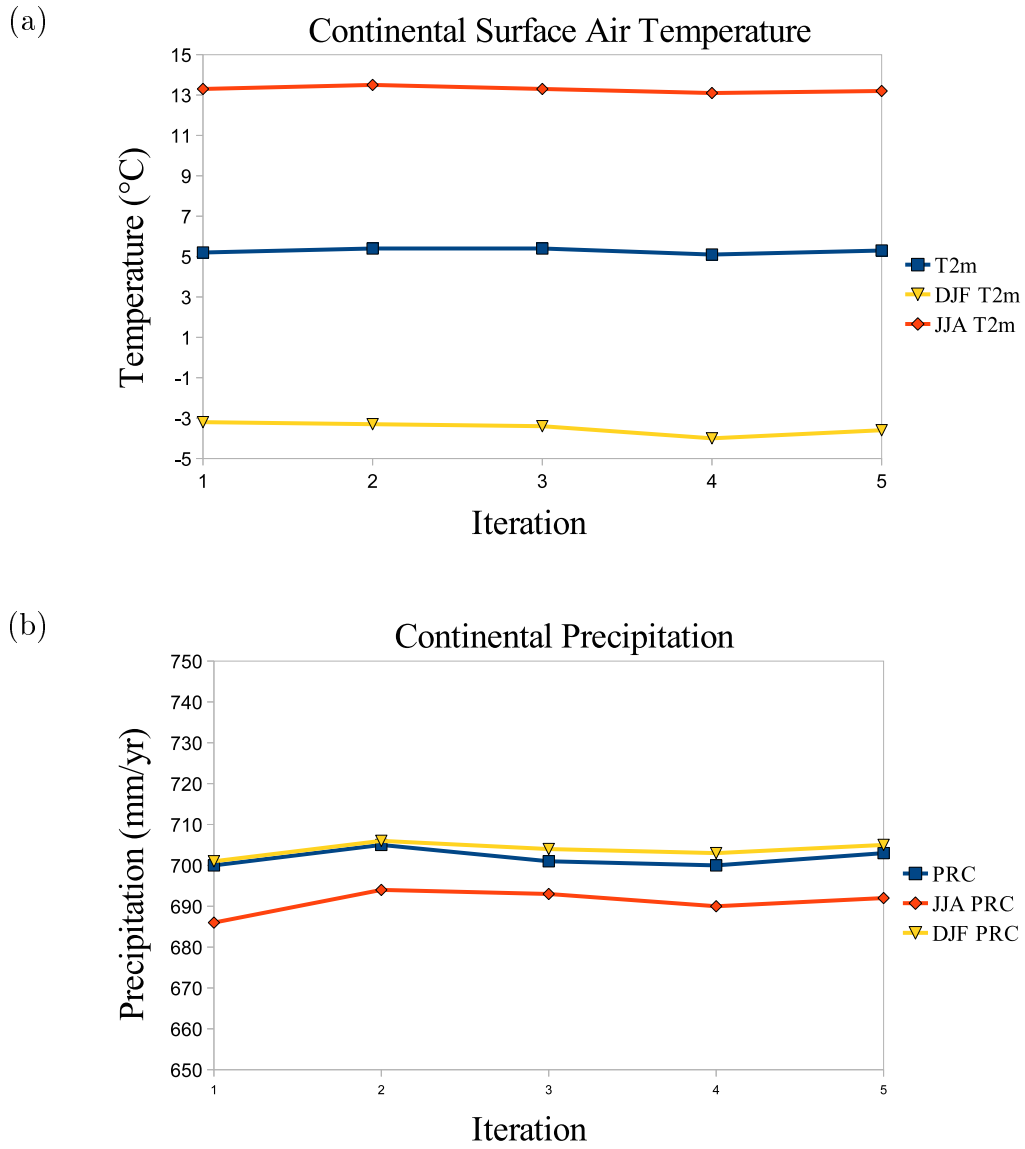


Figure 4.16: Continental annual and seasonal (JJA and DJF) (a) mean surface air temperature ($^{\circ}\text{C}$) and (b) precipitation (mm/yr) for each iteration.

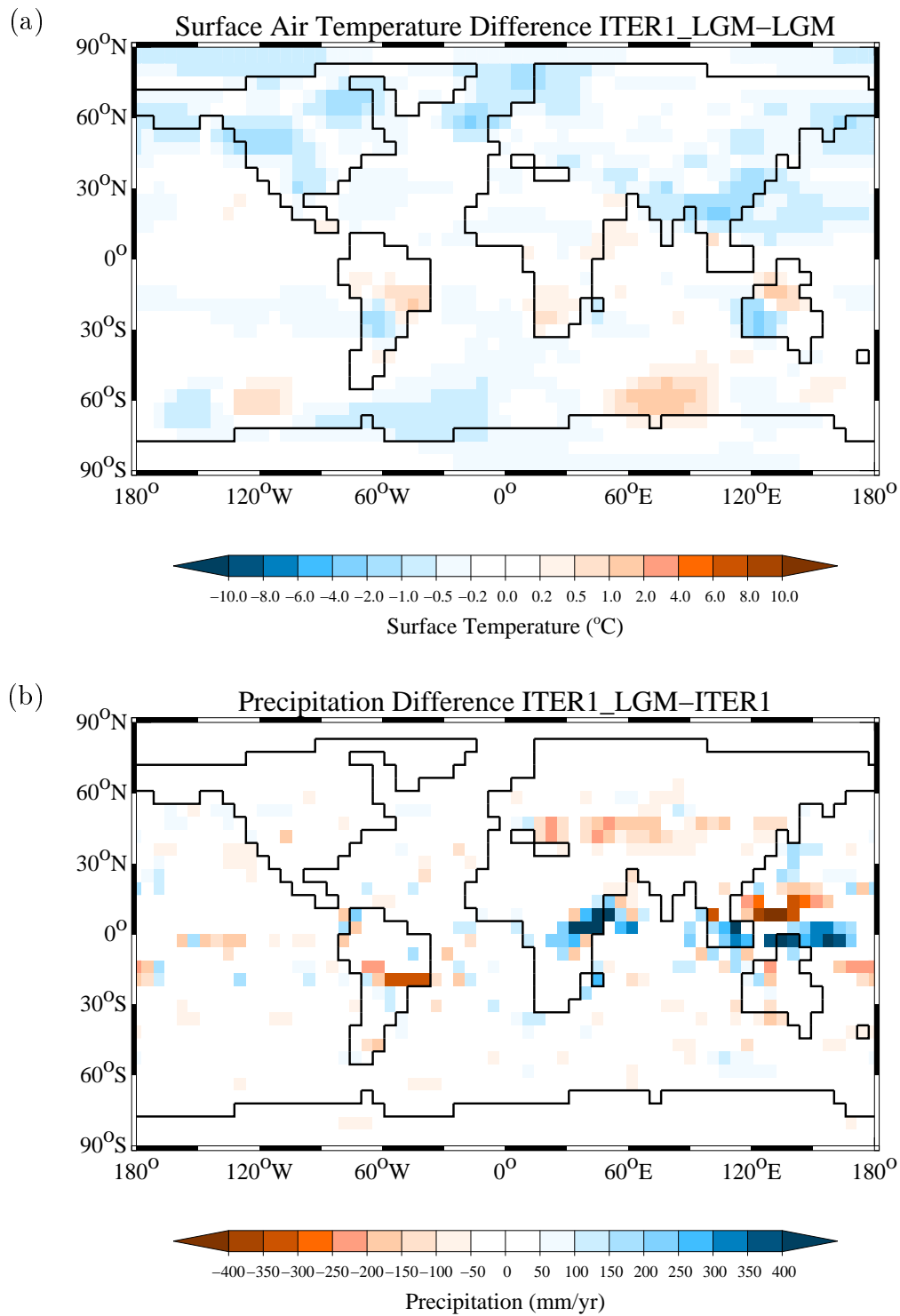


Figure 4.17: (a) Surface air temperature and (b) precipitation annual mean differences between the first climate iteration and the experiment LGM (LGM ITER1-LGM).

Chapter 5

Middle Pliocene climate and vegetation modelling

In this chapter, we present the results of Middle Pliocene climate and vegetation modelling with the Planet Simulator and CARAIB. The Middle Pliocene has become a period of increasing interest for modelling studies since it is considered as a potential analogue for the near future climate. This period is also well documented by proxy-data, thanks to the PRISM project (Pliocene Research, Interpretations, and Synoptic Mapping). Recently, the Pliocene Paleoclimate Modelling Intercomparison Project (PlioMIP), which is a section of the Paleoclimate Modelling Intercomparison Project (PMIP), has been entirely devoted to the systematic modelling of the Middle Pliocene climate with GCMs. Here, we have rigorously followed the PlioMIP protocol in order to allow an evaluation of the ability of the Planet Simulator to simulate warm climate, such as the Pliocene one. The climate and vegetation modelling results presented in the following sections are the subject of an article in preparation. The presentation of the results is thus written in the style of an article with its own introduction and conclusions.

5.1 Introduction

In the perspective of future climate changes, past warm climates have been widely studied, as they provide potential guidance to understand future climate changes and global warming (HAYWOOD et al., 2009b). In this context, the Pliocene, and more precisely the Middle Pliocene, which is considered as

a potential analogue for the climate of the twenty-first century (JANSEN et al., 2007), has become the subject of increasing interest.

The Pliocene epoch (5.3 to 1.8 Ma B.P.) appears to have been on average warmer than present-day (DOWSETT, 2007), especially during the Middle Pliocene warm interval or Middle Pliocene Warm Period (MPWP, 3.29–2.97 Ma), as defined by the United States Geological Survey’s PRISM group (HAYWOOD et al., 2010). The MPWP therefore represents the most recent known interval exhibiting significant warmth over a relatively long period, and in almost similar to present geographic configuration (HAYWOOD et al., 2010). The MPWP is well documented by geological proxies, witnessing of warmer than present-day climate over the oceans (DOWSETT et al., 1996; BARRON, 1996), as well as over the continents (KÜRSCHNER et al., 1996; SALZMANN et al., 2008). Data-based vegetation reconstructions notably suggest that boreal forests shifted northward, whereas warm-temperate forests expanded at middle latitudes at the expense of deserts (THOMPSON and FLEMING, 1996). Moreover, the estimates of atmospheric CO₂ levels for the MPWP, between 360 and 380 ppmv (KÜRSCHNER et al., 1996; RAYMO et al., 1996), are comparable to the CO₂ levels that have already been reached today.

Many modelling studies have been conducted to investigate the climate mechanisms that could explain the Middle Pliocene warmth. Several studies proposed an enhanced meridional ocean heat transport together with higher than present-day atmospheric CO₂ concentrations to account for the Middle Pliocene warmth (DOWSETT et al., 1996; RAYMO et al., 1996). RIND and CHANDLER (1991) proposed that palaeogeographic changes, such as the reduction of the elevations of the major mountain chains, could have played a significant role on the Middle Pliocene climate. Climatic feedbacks, related to altered vegetation cover, ice-sheet extent, and cloud cover have also been invoked (HAYWOOD and VALDES, 2004, 2006; SALZMANN et al., 2008; JOST et al., 2009). More recently, HAYWOOD et al. (2007) and LUNT et al. (2008) suggested that permanent El Niño-like conditions could explain the Middle Pliocene warmth.

Though numerous modelling studies have been performed on the Middle Pliocene, most of them did not apply a systematic methodology that would have made direct comparison possible between the different models simulations, such as the use of same boundary conditions. However, the initiation of the PRISM project by the U. S. Geological Survey (DOWSETT et al., 1994), made the reconstruction of comprehensive global data sets that can be used as standard boundary conditions for GCM simulations of the MPWP

(DOWSETT et al., 1996, 1999; HAYWOOD et al., 2010).

Various versions of the PRISM data set have been used in several modelling studies. SLOAN et al. (1996) simulated the Middle Pliocene climate using the PRISM1 data set (DOWSETT et al., 1996) to prescribe boundary conditions for the atmospheric NCAR GENESIS GCM. The PRISM2 data set (DOWSETT et al., 1999) has been widely used to force atmospheric GCMs (HAYWOOD et al., 2000b,a; JIANG et al., 2005; HAYWOOD and VALDES, 2006; JOST et al., 2009; HAYWOOD et al., 2009a), as well as fully coupled ocean-atmosphere GCMs (HAYWOOD and VALDES, 2004; HAYWOOD et al., 2007). HAYWOOD et al. (2000b,a) used the PRISM2 data set and the atmospheric HadAM3 version of the UKMO model to analyse respectively the MPWP regional warming over Europe, over the Mediterranean and at the global scale. HAYWOOD and VALDES (2004) simulated the climate of the MPWP using the PRISM2 data set and the fully coupled ocean-atmosphere UKMO GCM. JIANG et al. (2005) examined the Middle Pliocene climate with the IAP global grid-point atmospheric GCM (JIANG et al., 2003), and particularly compared their results to paleoclimatic reconstructions in East Asia. Furthermore, HAYWOOD and VALDES (2006) and JOST et al. (2009) investigated the vegetation feedback on Middle Pliocene climate, respectively using the TRIFFID dynamic vegetation model together with the HadAM3 atmospheric GCM, and the ORCHIDEE dynamic vegetation model with the LMDZ atmospheric GCM. Recently, HAYWOOD et al. (2009a) initiated the Pliocene Model Intercomparison Project (PlioMIP) and compared the Middle Pliocene climate simulated by the atmospheric HadAM3 and GISS GCMAM3 GCMs, forced with the same set of boundary conditions derived from the PRISM2 data set.

In this study, we simulated the climate of the Middle Pliocene with the Planet Simulator and compared it to the preindustrial simulated climate. In order to enable a direct comparison of the Pliocene results presented here to other model results, we applied the Pliocene Model Intercomparison Project (PlioMIP) protocol (experiment 1, preferred conditions), fully described in HAYWOOD et al. (2010). We therefore used the last version of the PRISM3D data set (HAYWOOD et al., 2010), to prescribe initial and boundary conditions for the Planet Simulator. In addition to the experiments defined by the PlioMIP protocol, we called upon the dynamic vegetation model CARAIB OTTO et al. (2002); FRANÇOIS et al. (2006); GALY et al. (2008) to reconstruct the vegetation distribution in response to the warm Middle Pliocene climate we simulate.

We first present the Planet Simulator (Section 5.2) and describe in de-

tail the initial and boundary conditions we applied to force the control and Pliocene experiments (Section 5.3). We examine the response of surface global and local climate (temperature, precipitation, cloud cover and low level winds) to the different boundary condition changes imposed, and particularly to the vegetation changes (Section 5.4). We compare our results to the results of previous modelling studies, taking into account the differences in the set of PRISM boundary conditions used (Section 5.5). Finally, we discuss the Middle Pliocene vegetation distribution produced by CARAIB (Section 5.6), compare it to previous model- and data-based vegetation reconstructions (Section 5.7), and analyse the vegetation feedback on the Middle Pliocene climate (Section 5.8).

5.2 Model setups

5.2.1 Climate Model

The Planet Simulator (FRAEDRICH et al., 2005a,b) is an Earth system Model of Intermediate Complexity (EMIC). It has been used for present-day climate modelling studies (FRAEDRICH et al., 2005b; GROSFELD et al., 2007; JUNGE et al., 2005) as well as for various paleoclimatic studies focusing on different past periods (ROMANOVA et al., 2006; MICHEELS et al., 2009a,b; HENROT et al., 2009, 2010). The model has proved usefulness in the comparison to proxy data (HENROT et al., 2009; MICHEELS et al., 2009a). The Planet Simulator present-day climate compares fairly well to ERA-40 reanalysis although it is affected by two major climatological biases: (1) a cold bias at high latitudes during winter in each hemisphere and (2) a global overestimation of the surface evaporation (HABERKORN et al., 2009). The central component of the Planet Simulator is PUMA-2, a spectral GCM with triangular truncation, based upon the Portable University Model of the Atmosphere PUMA (FRAEDRICH et al., 1998). PUMA-2 solves the moist primitive equations, representing the conservation of momentum, mass and energy, on σ coordinates in the vertical. It also includes boundary layer, precipitation, interactive clouds and radiation parameterisations. For the present study, we configured it to use a T42 truncation and ten vertical equally spaced σ levels. The model atmosphere is coupled to a 50 m deep mixed-layer ocean, a thermodynamic sea-ice and a land surface and soil model.

Sea surface temperatures are computed from the net atmospheric heat flux at the surface. The transport of heat by oceanic surface currents is

represented by an additional distribution of heat sources and sinks that is prescribed within the mixed-layer and the sea-ice. That distribution varies monthly and spatially. It is applied to ocean grid-cells to mimic heat transport by ocean currents that is not an explicitly represented process in the model. This procedure allows the model to respond with a larger sensitivity to boundary condition changes than with prescribed sea-surface temperatures.

The land surface and soil models calculate the surface temperatures from a linearised energy balance equation and predict soil moisture on the basis of a simple bucket model. The influence of vegetation is represented by background albedo, roughness length and rooting depth. Their annual distributions are prescribed, and albedo may only change in grid-cells where snow is present.

5.2.2 Vegetation Model

In order to produce extra preindustrial and Middle Pliocene vegetation distributions and analyse the impact of vegetation changes on the Middle Pliocene climate, we used the dynamic vegetation model CARAIB (OTTO et al., 2002; FRANÇOIS et al., 2006; LAURENT et al., 2008; GALY et al., 2008). CARAIB calculates the carbon fluxes between the atmosphere and the terrestrial biosphere and deduces the evolution of carbon pools, together with the relative abundances of a series of plant functional types. Its different modules respectively focus on the hydrological cycle, photosynthesis and stomatal regulation, carbon allocation and biomass growth, heterotrophic respiration and litter and soil carbon, and the distribution of the model plant types, as a function of productivity. Here we used a classification with fifteen Plant Functional Types (PFTs), described in UTESCHER et al. (2007) and GALY et al. (2008). Model derived PFT assemblages can be translated into biomes to produce vegetation maps. The inputs of the model are meteorological variables, taken from meteorological databases or GCM simulation experiments. CARAIB has been widely used to reconstruct past vegetation distributions, notably for the Last Glacial Maximum (FRANÇOIS et al., 1999; OTTO et al., 2002; CHEDDADI et al., 2006; GALY et al., 2008; HENROT et al., 2009) and several time slices of the Miocene (FRANÇOIS et al., 2006; FAVRE et al., 2007; HENROT et al., 2010).

5.3 Experimental setup

Two numerical experiments were carried out with the Planet Simulator for this study: (1) a preindustrial experiment, referred to as CTRL experiment, and (2) a Middle Pliocene one, referred to as PLIO experiment, where we applied the PRISM3D conditions for experiment 1 (preferred conditions), following the PlioMIP protocol (HAYWOOD et al., 2010). Table 5.1 lists the initial and boundary conditions applied for the CTRL and PLIO experiments. Both experiments have been run for 100 years and the results shown in Section 5.4 are means over the last 50 years of simulation, allowing 50 years for the model to equilibrate.

5.3.1 Preindustrial conditions

Orbital configuration and atmospheric CO₂

The CTRL simulation is forced with a present-day orbital configuration (eccentricity 0.016724, obliquity 23.446° and longitude of the perihelion 102.04°) and solar constant (1365 W/m²). The atmospheric CO₂ concentration is set to the preindustrial value of 280 ppmv. It should be noticed that neither the effects of CH₄ and N₂O concentrations in the atmosphere, nor those of the atmospheric dust content have been taken into account here. These three agents are not included in the radiation scheme of the Planet Simulator.

Land-sea distribution, topography and land ice

The preindustrial land-sea distribution used with the model has been derived from Peltier's ICE-5G 1° by 1° resolution ice sheet reconstruction (PELTIER, 2004), interpolated onto the model grid. The preindustrial continental ice cover and orography have also been reconstructed from Peltier's ICE-5G for the preindustrial state, considering that grid-cells covered by an ice fraction greater than 50% are completely covered by ice. Figures 5.1 and 5.2 respectively show the preindustrial and Pliocene topography and ice-sheet mask on the corresponding preindustrial and Pliocene land-sea distributions.

Sea surface temperatures and sea-ice

As boundary conditions over ocean grid-points, we prescribed monthly mean present-day sea-surface temperature and sea-ice distributions derived from

Table 5.1: Experimental design and boundary conditions for CTRL and PLIO experiments.

	CTRL	PLIO
Orbital configuration	present-day	present-day
Atmospheric CO ₂	280 ppmv	405 ppmv
Land-sea mask	from PELTIER (2004)	PRISM3D
Topography	from PELTIER (2004)	PRISM3D (anomaly)
Ice sheet mask	from PELTIER (2004)	PRISM3D
Sea surface temperature	from AMIP2 (2004)	PRISM3D (anomaly)
Sea-ice	from AMIP2 (2004)	PRISM3D
Vegetation cover	from BIOME4-based modern vegetation	PRISM3D

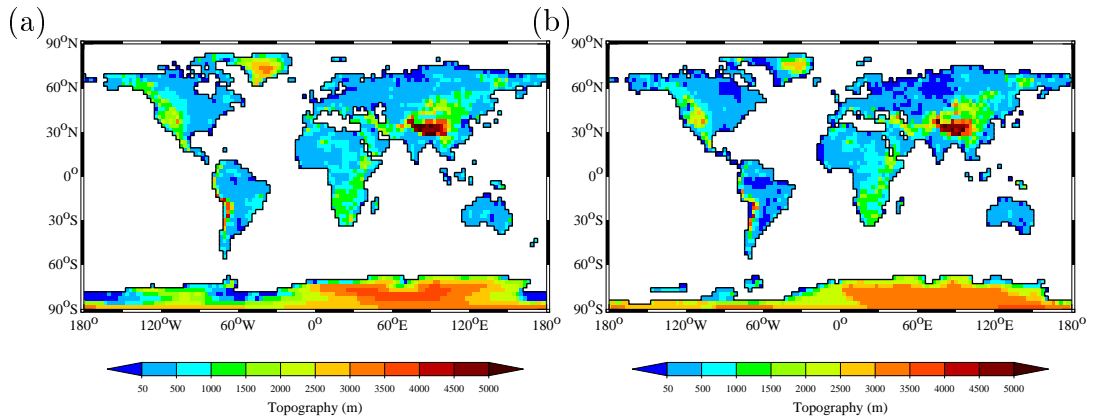


Figure 5.1: Topography on land and land-sea distribution for (a) the preindustrial and (b) the Pliocene configurations.

the AMIP2 database (AMIP2, 2004). In order to follow the PlioMIP protocol, the sea surface temperatures and sea-ice cover have been kept fixed for the CTRL simulation. However, we have also let the sea surface temperatures and sea-ice cover vary in the experiments performed here in addition to the standard CTRL and PLIO simulations. This procedure allows the slab model, and therefore the Planet Simulator, to react with a greater sensitivity to boundary conditions changes. In the additional runs, the temporal evolution of the oceanic boundary conditions are given by the heat transfer calculated by the Planet Simulator for a preindustrial climate, following the PMIP1 protocol. The preindustrial oceanic heat flux distribution was calculated from the CTRL experiment with fixed sea-surface temperatures and sea-ice cover. The differences between the sea surface temperatures calculated by the model and these prescribed determined the oceanic heat flux adjustments to apply to ocean grid-cells. The oceanic heat fluxes calculated for the additional preindustrial and Pliocene experiments are shown in Figure 5.3.

Vegetation cover

The surface boundary condition parameters controlled by the vegetation cover (surface albedo, roughness length and rooting depth) for the CTRL simulation have been derived from the BIOME4-based modern vegetation (SALZMANN et al., 2008). The modern biome distribution was interpolated onto the model grid. The surface albedo, roughness length and rooting depth

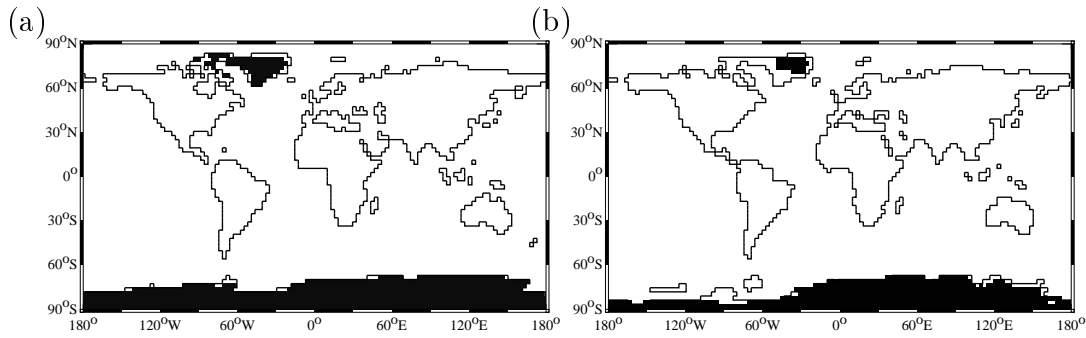


Figure 5.2: Ice-sheet mask for (a) the preindustrial and (b) the Pliocene configurations.

of the land grid-cells were calculated from the specific values of snow-free albedo, surface roughness length and rooting depth attributed to each biome of the BIOME4 classification with twenty-eight types (SALZMANN et al., 2008; HAYWOOD et al., 2010).

5.3.2 Middle Pliocene conditions

Orbital configuration and atmospheric CO₂

As the Middle Pliocene in this study spans about 320,000 years, and thus integrates several orbital cycles, a present-day orbital configuration is applied for the PLIO experiment (HAYWOOD et al., 2010). The concentration of the atmospheric CO₂ is set to 405 ppmv, as suggested by HAYWOOD et al. (2010). This CO₂ concentration is higher than the proxy-based CO₂ concentration estimates for the Middle Pliocene (between 360 and 380 ppmv following the estimations of KÜRSCHNER et al. (1996) and RAYMO et al. (1996)), in order to account for possible additional contributions of other greenhouse gases to the Pliocene warmth, such as methane, for which no Pliocene proxy record is available (HAYWOOD et al., 2010).

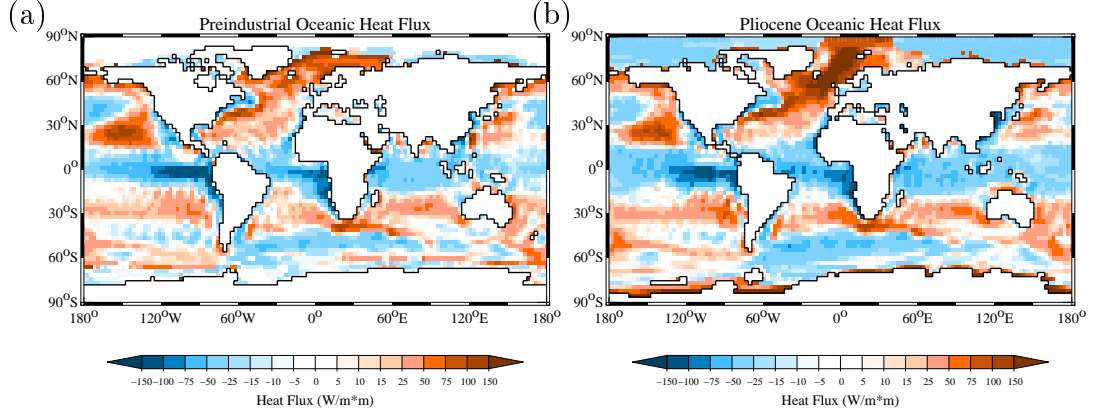


Figure 5.3: Oceanic surface heat transfer for (a) the CTRL configuration and (b) the PLIO configuration. Positive values indicate a net transfer of heat from the ocean to the atmosphere.

Land-sea distribution, topography and land ice

The Middle Pliocene land-sea distribution has been derived from the fractional PRISM3D 2° by 2° resolution land-sea mask reconstruction (HAYWOOD et al., 2010), considering that grid-cells covered by a land fraction greater than 50% are land grid-cells. The Pliocene land-sea distribution takes into account a 25 m sea-level rise, a closed Central American Seaway, open Bering Strait, Drake Passage, Tasman Gateway, Gibraltar Strait and Indonesian Gateway, a filled Hudson Bay and no West Antarctic ice-sheet (see Figure 5.1).

We reconstructed the Pliocene topography using the anomaly method suggested in the PlioMIP protocol (HAYWOOD et al., 2010). We therefore applied the following algorithm

$$Z_{PLIO} = Z_{MOD} + (Z_{PLIO}(PRISM3D) - Z_{MOD}(PRISM3D)). \quad (5.1)$$

In this equation, $Z_{PLIO}(PRISM3D)$ is the PRISM3D Pliocene topography and $Z_{MOD}(PRISM3D)$ is the modern PRISM3D topography. Z_{MOD} is the preindustrial topography we used for the CTRL experiment. The PRISM3D Pliocene topography has been derived from the reconstruction of SOHL et al. (2009). This reconstruction is based upon a 25 m sea-level rise and a filled Hudson Bay. High reliefs, such as the Rocky Mountains and the Andes, are approximatively at their current elevations. The PRISM3D modern topography has been derived from the ETOPO1 Global Relief Model Data (AMANTE

and EAKINS, 2008). It should be noticed that negative elevation values over the oceans (bathymetry) have been set equal to zero. Absolute Pliocene topography ($Z_{PLIO}(PRISM3D)$) has been used in regions where no modern data was given (see Figure 5.1).

The ice-sheet mask has been interpolated from the PRISM3D ice-sheet reconstruction based on simulation results of the British Antarctic Survey Ice Sheet Model (BASISM) for the Middle Pliocene (HILL et al., 2007; HAYWOOD et al., 2010). This ice-sheet reconstruction shows significant reduction of the Greenland and Antarctic ice-sheets. In agreement with the studies of NAISH et al. (2009) and DECONTO and POLLARD (2003), the West Antarctic ice-sheet has been removed for the warm Middle Pliocene (see Figure 5.2).

Sea surface temperatures and sea-ice

As boundary conditions over ocean grid-points for the PLIO experiment, we have prescribed fixed monthly mean Pliocene sea-surface temperature and sea-ice distributions derived from the PRISM3D dataset (HAYWOOD et al., 2010). The sea surface temperatures (SSTs) have been calculated by the anomaly method, using the following algorithm

$$SST_{PLIO} = SST_{MOD} + (SST_{PLIO}(PRISM3D) - SST_{MOD}(PRISM3D)). \quad (5.2)$$

In this equation, $SST_{PLIO}(PRISM3D)$ is the PRISM3D Pliocene sea surface temperature reconstruction, $SST_{MOD}(PRISM3D)$ the modern PRISM3D SST distribution, and SST_{MOD} the SST distribution which was used for the CTRL experiment. The $SST_{PLIO}(PRISM3D)$ reconstruction is a series of monthly SST fields, which is based on multiple temperature proxies (DOWSETT et al., 2009; ROBINSON et al., 2008; DOWSETT and ROBINSON, 2009). The $SST_{PLIO}(PRISM3D)$ reconstruction shows little warming in low latitudes relative to present-day and increased warming at higher latitudes. The North Atlantic and North Pacific especially show warm anomalies. Compared to present-day, the equator-to-pole gradient is significantly reduced. The modern PRISM3D SSTs are monthly data from the climatology of REYNOLDS and SMITH (1995), modified to match the PRISM3D land-sea distribution. The sea-ice extent for the Pliocene is determined by the PRISM3D SST reconstruction (HAYWOOD et al., 2010), and from available distribution of key diatom taxa in the Southern Hemisphere (DOWSETT et al., 1996), whereas there is no direct evidence for Middle Pliocene sea-ice extent in the Northern Hemisphere (HAYWOOD et al., 2010). The differences

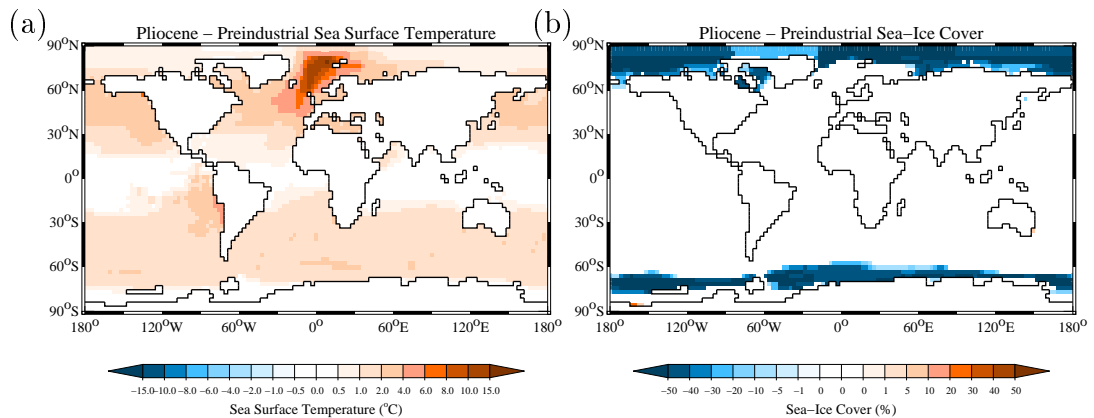


Figure 5.4: Differences between the Pliocene and preindustrial (a) sea surface temperatures and (b) sea-ice cover.

between the Pliocene and preindustrial sea surface temperatures and sea-ice cover are shown in Figure 5.4.

Using the same procedure as for the CTRL experiment, we prescribed an oceanic heat flux distribution for the additional PLIO experiments. The Middle Pliocene oceanic heat flux distribution was calculated from the PLIO experiment with fixed sea-surface temperatures and sea-ice cover. The Middle Pliocene oceanic heat fluxes we obtained are shown in Figure 5.3. The Pliocene distribution shows a strengthening of the surface heat transfer to the North Atlantic and the Arctic Ocean via the Gulf Stream current, and of the cold currents in the upwelling zones (see Figure 5.3).

Vegetation cover

The surface boundary condition parameters controlled by the vegetation cover have been derived from the BIOME4-based Pliocene vegetation reconstruction (SALZMANN et al., 2008), using the same procedure as for the CTRL experiment. The 28-type biome distribution for the Pliocene has been reconstructed from a biome reconstruction based upon paleobotanical data, and from predictions of the BIOME4 vegetation model, forced by a standard mid-Pliocene Hadley Center atmospheric model version 3 (HadAM3) GCM simulation (HAYWOOD and VALDES, 2006). In response to the warm and moist Middle Pliocene climate, the Middle Pliocene vegetation reconstruction shows a northward shift of the boreal forest at the expense of tundra, as

well as a northward expansion of temperate forests and grasslands. Desert areas are reduced, especially in Africa where tropical savannas and woodlands expand (SALZMANN et al., 2008; HAYWOOD et al., 2010). The differences between the Pliocene and preindustrial surface albedo, roughness length and rooting depth distributions derived respectively from the Pliocene and modern BIOME4 biome distributions are shown in Figure 5.5. Surface albedo, roughness length and rooting depth are affected by vegetation changes, but the albedo impact on surface temperature is dominant, because of its direct impact on the energy balance (HENROT et al., 2009). The expansion of temperate grasslands in North America and Siberia in the BIOME4-based Pliocene vegetation reconstruction induces a surface albedo increase and a decrease of roughness length and rooting depth over these regions. However, surface albedo decreases in some parts of Africa and Asia in response to the development of forests at the Middle Pliocene, whereas roughness length and rooting depth increase in North Africa and Arabia due to the replacement of desert areas by shrublands. Roughness length and rooting depth also increase at high latitudes due to the replacement of tundra by boreal forests.

5.3.3 Alternative vegetation cover: CARAIB setup

The CARAIB model was used to produce two vegetation distributions: a preindustrial one and a Middle Pliocene one. First, we performed an equilibrium run of CARAIB, forced with 280 ppmv of CO₂ in the atmosphere and the climatology of NEW et al. (2002). The NEW et al. (2002) climatology includes monthly mean observed climatic fields over the period 1961-1990, i.e., air temperature, precipitation, cloud cover, relative humidity and diurnal temperature amplitude.

The Middle Pliocene vegetation distribution was obtained from an equilibrium run of CARAIB forced with 405 ppmv of CO₂ in the atmosphere and the climate derived from the PLIO experiment. As climatic inputs for the Middle Pliocene CARAIB simulation, we used the anomalies of the GCM climatic fields between the Middle Pliocene (experiment PLIO) and the preindustrial (experiment CTRL), added to the climatology of New et al. (2002), following the approach described in OTTO et al. (2002).

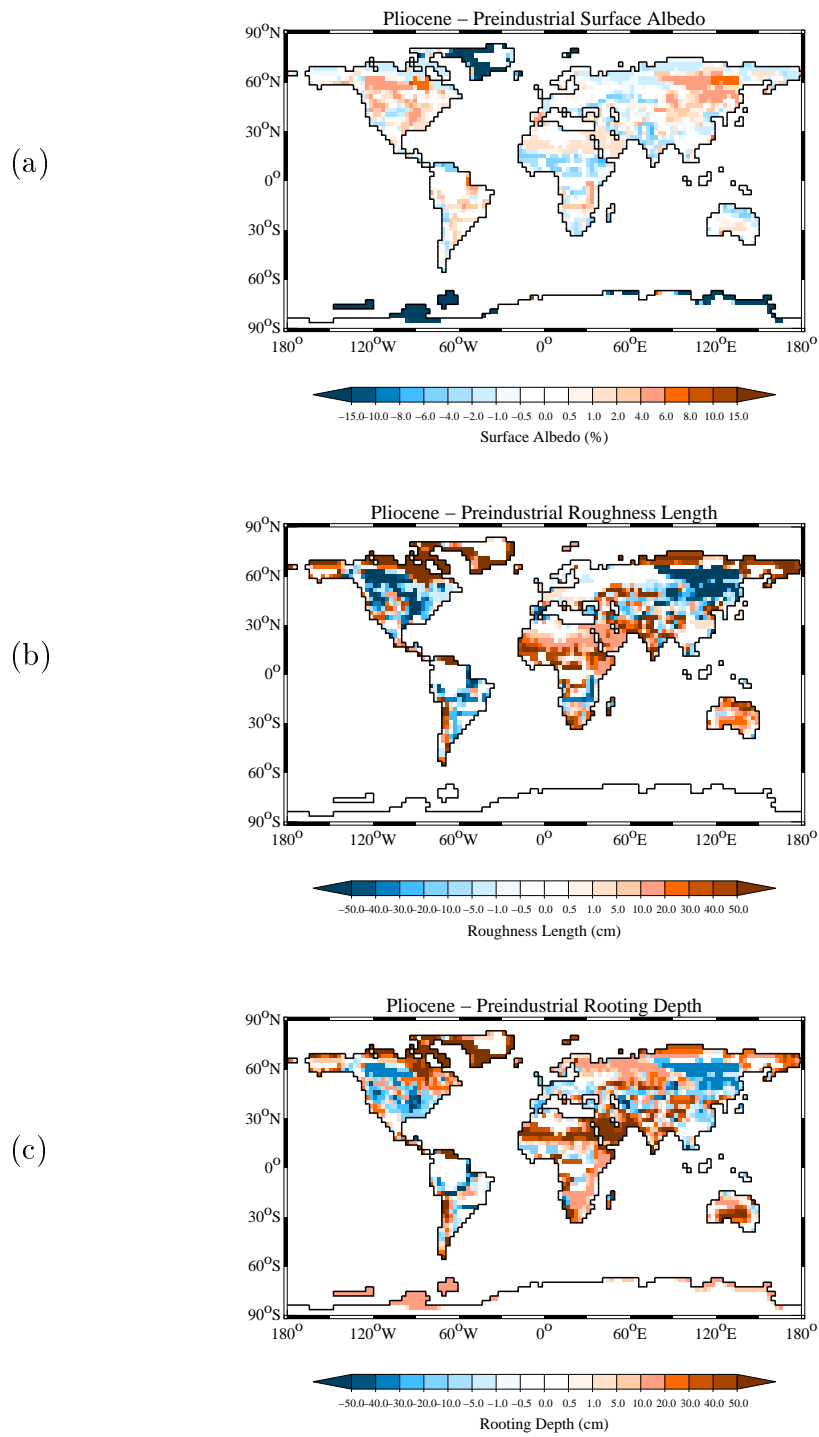


Figure 5.5: Differences between the Pliocene and preindustrial (a) surface albedo, (b) roughness length and (c) rooting depth distributions.

Table 5.2: Annual, DJF and JJA global mean, oceanic mean and continental mean surface air temperature T_{2m} ($^{\circ}\text{C}$) and precipitation (mm/day) anomalies for the Middle Pliocene simulation experiment. The continental mean includes the contribution from Antarctica. All results reported here are means over the last 50 years of 100-year simulations, allowing 50 years for the model to equilibrate. The absolute CTRL values are shown for comparison.

Variable	Global	Ocean	Continent
CTRL T_{2m} annual ($^{\circ}\text{C}$)	13.86	15.19	10.1
CTRL PRC annual (mm/day)	3.16	3.28	2.80
ΔT_{2m} annual ($^{\circ}\text{C}$)	+2.24	+1.83	+3.15
ΔT_{2m} DJF ($^{\circ}\text{C}$)	+2.19	+2.03	+2.56
ΔT_{2m} JJA ($^{\circ}\text{C}$)	+2.28	+2.33	+2.10
Δ PRC annual (mm/day)	+0.11	+0.05	+0.22
Δ PRC DJF (mm/day)	+0.11	+0.05	+0.26
Δ PRC JJA (mm/day)	+0.12	+0.06	+0.25

5.4 Middle Pliocene simulated climate

5.4.1 Global and zonal average temperature and precipitation

In the PLIO experiment, the global annual mean two-meter air temperature is 2.24°C higher and the global annual mean precipitation 0.11 mm/day higher than in the CTRL experiment (see Table 5.2). Both surface air temperature (SAT) and precipitation increase on the continents and the oceans, during both December, January, February (DJF) and June, July, August (JJA) periods.

The zonal mean surface air temperature (SAT) and precipitation distributions are shown in Figure 5.6. The global, continental and oceanic zonal mean temperature and precipitation anomalies (EXPERIMENT minus CTRL) are also shown in Figure 5.6 to allow a finer comparison. The zonal mean SAT averages indicate that the largest SAT increases occur at high latitudes, poleward of 60° in both hemispheres and particularly over the Antarctic Ocean, where the temperature increase reaches a maximum of $+23^{\circ}\text{C}$. Middle latitudes between 30 and 60° warm by less than 5°C , whereas the low-latitude regions experience little or no difference, or even slight cooling by 1 to 2°C on the continents. The total precipitation however slightly increases at high and middle latitudes but decreases in the tropics. The precipitation decreases in

the tropical regions are mainly due to precipitation decreases over the oceans, whereas large increases occur over the continents.

5.4.2 Regional climate responses

Surface air temperature

Figures 5.7 and 5.8 show the annual, the December, January, February (DJF) and the June, July, August (JJA) mean SAT and precipitation anomalies between experiment PLIO and the control run CTRL. As already pointed out in the zonal mean analysis, the largest increases of SAT occur at high latitudes in both hemispheres and mainly concern the oceans. The temperature increases are larger than 10°C over many areas of the Arctic and Antarctic oceans. Weaker warming, between 2 and 4°C , occur at middle latitudes, over the oceans and the continents, whereas some continental areas in the subtropics, e.g., North Africa, Amazonia, India and North Australia, experience temperature decreases between 1 and 4°C . At high latitudes, the largest magnitude of warming is obtained in the winter of the hemisphere over the ocean. During the JJA period, only Greenland and the region of the Norwegian Sea experience warming larger than 12°C , whereas the temperature increases by 2 to 4°C only over the Arctic Ocean. In JJA, the centre of the East Antarctic ice-sheet even experiences some cooling. In the subtropics, the cooling extends further north during the JJA period, especially across North Africa, India and Amazonia. SAT also decreases by 1 to 2°C in JJA over south- and western Europe, whereas it increases over central Eurasia.

Precipitation

In the Middle Pliocene experiment precipitation generally increases over the continents and the oceans (see Figure 5.7). Precipitation increases over the oceans mainly occur over areas that experience warmer sea surface temperatures in the PLIO experiment. In contrast to the SAT anomaly distribution, precipitation slightly increases in the high latitudes of both hemispheres, except over the North Atlantic, where precipitation increases larger than 2 mm/day occur during the whole year. The increase of precipitation over the North Atlantic induces a strong increase of precipitation over western Europe, especially during the JJA period. In the subtropics, precipitation decreases over the oceans, whereas an increase of more than 2 mm/day is observed across North Africa, Australia and India, explaining the cooling in

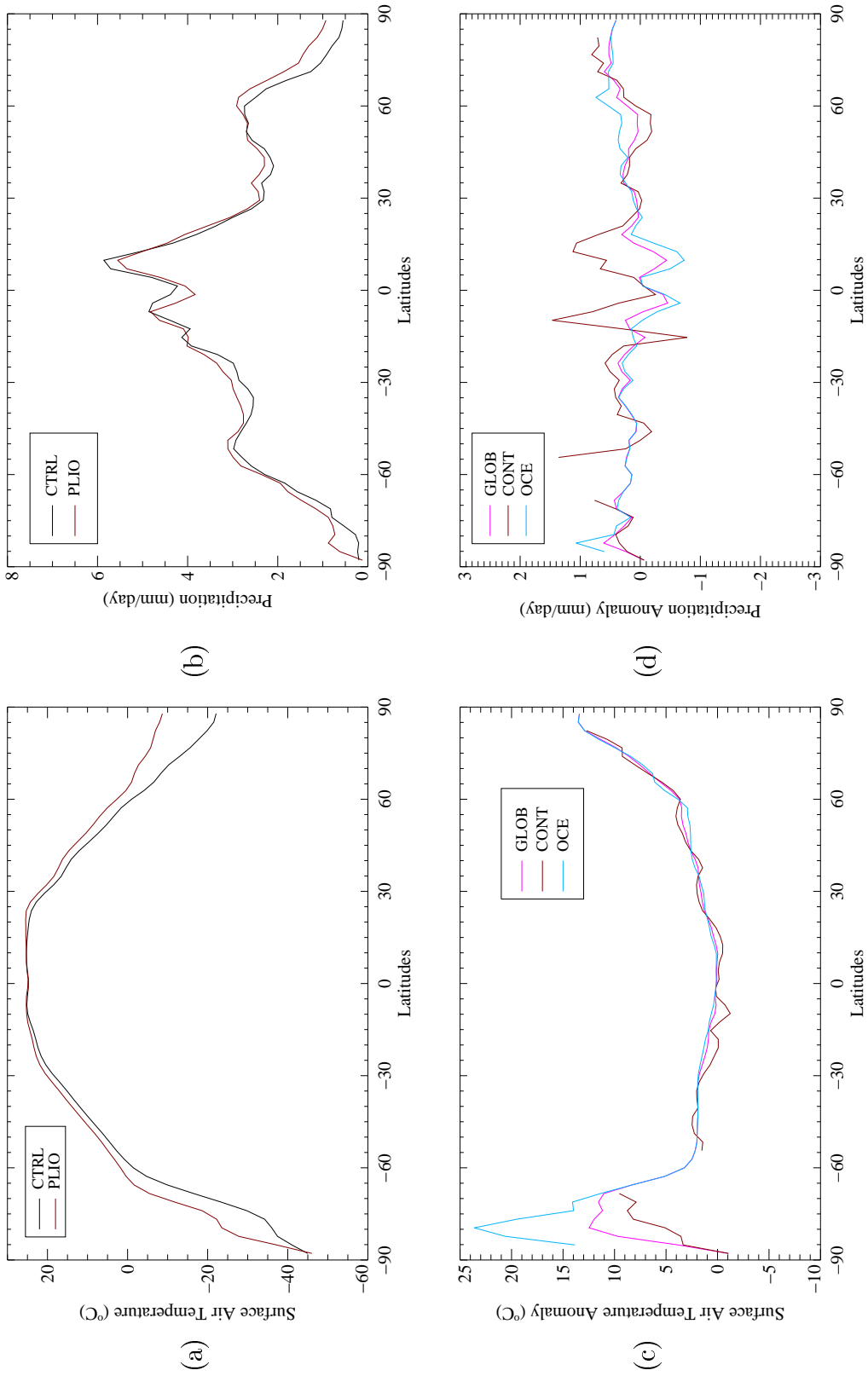


Figure 5.6: Zonal annual mean (a) surface air temperature ($^{\circ}\text{C}$) and (b) precipitation (mm/day) for CTRL and PLIO experiments. Global, land and ocean zonal annual mean (c) surface air temperature anomalies ($^{\circ}\text{C}$) and (d) precipitation anomalies (mm/day) between PLIO and CTRL experiments.

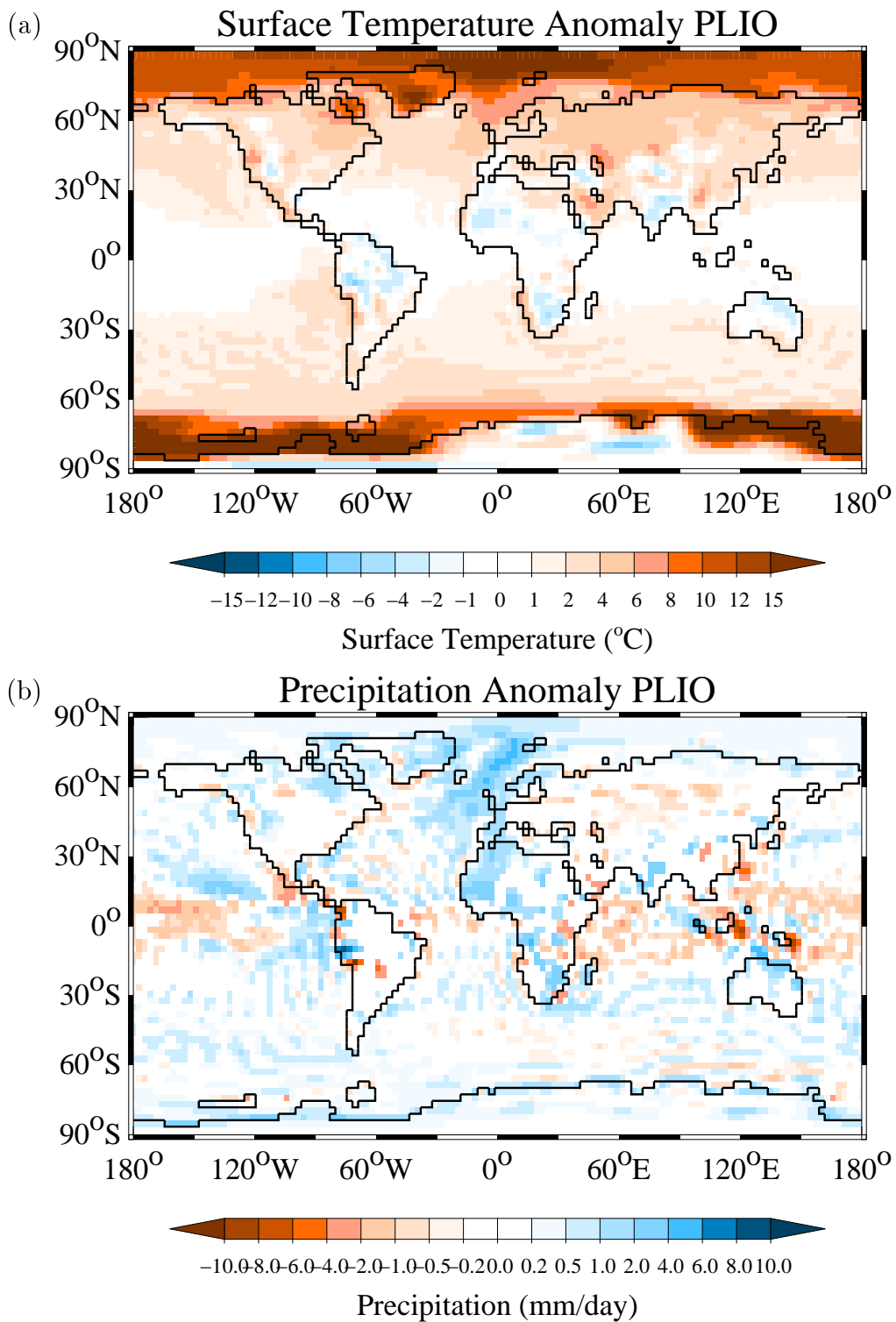


Figure 5.7: Annual mean (a) surface air temperature ($^{\circ}\text{C}$) and (b) precipitation (mm/day) anomalies between the PLIO and CTRL experiments.

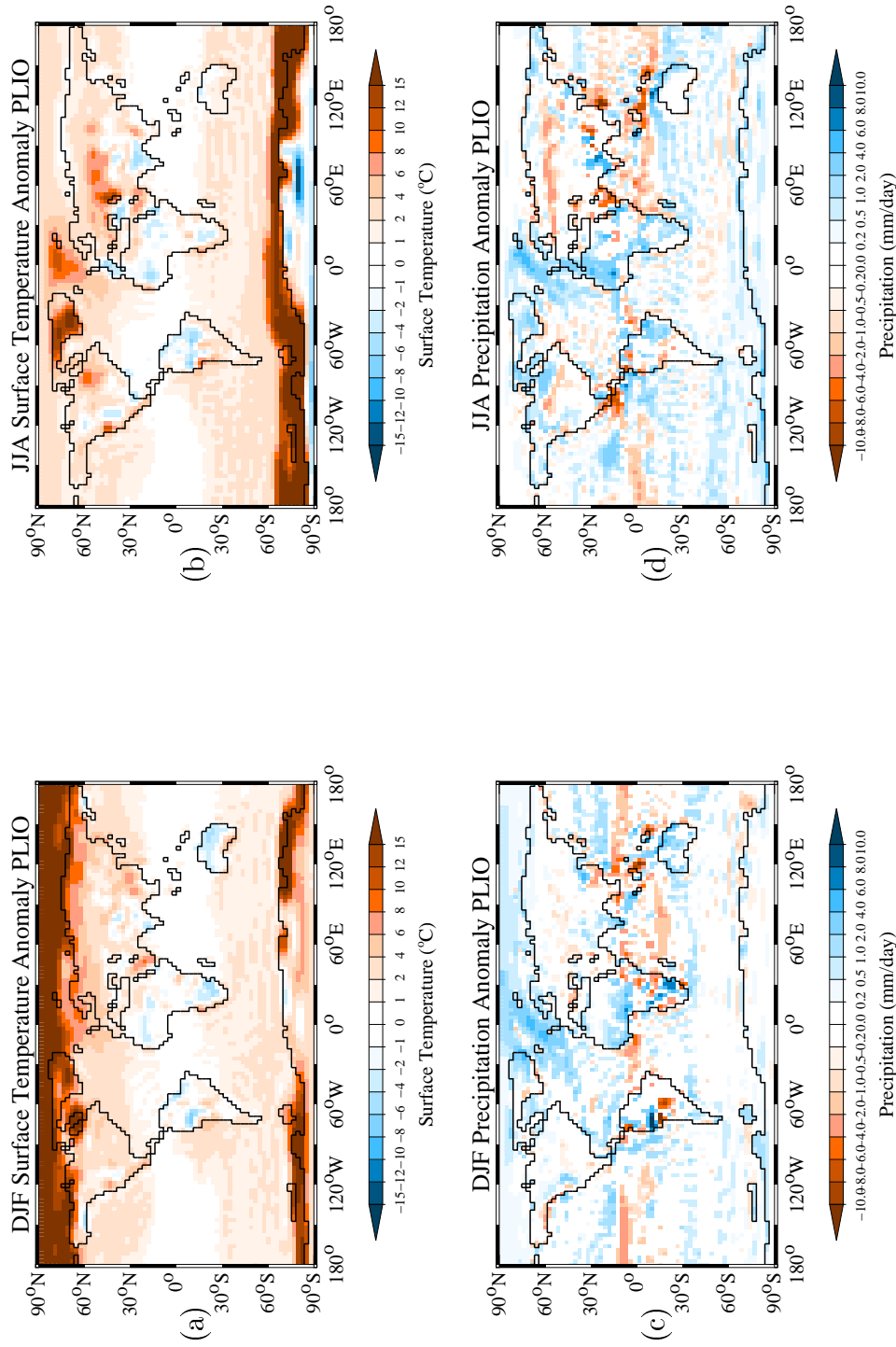


Figure 5.8: (a) DJF and (b) JJA surface air temperature anomalies ($^{\circ}\text{C}$), and (c) DJF and (d) JJA precipitation anomalies (mm/day) between the PLIO and CTRL experiments.

these regions. During the DJF period, precipitation mainly increases over the Arctic Ocean, the North Atlantic and Greenland, in response to the strong warming occurring in these regions. In JJA, Europe and North Africa experience wetter conditions, whereas precipitation decreases in central Eurasia and Arabia. In the subtropics, precipitation increases over some continental areas during the whole year. However, the maximum precipitation increases are displaced further north in JJA. The precipitation increases in JJA over summer monsoon regions (Africa and India) could also suggest an intensification of the monsoonal activity during the Middle Pliocene. However, precipitation decreases in southeastern Asia in JJA, which would rather point to a weakening of the monsoon in this region.

Total cloud cover and surface winds

Figure 5.9 shows the DJF and JJA mean total cloud cover anomalies between experiment PLIO and the control run CTRL. Total cloud cover increases over polar regions and particularly over the oceans during both DJF and JJA periods, but the increase is stronger during winter in each hemisphere, reaching 20% in some parts of the Arctic and the Antarctic ocean. Total cloud cover also increases over the subtropical land areas that experience precipitation increases, e.g. North Africa, India and Australia. However, it decreases by 5 to 10% over the oceans in the tropics, as well as over mid-latitude continental regions, e.g. Eurasia and North America, mainly during JJA.

The DJF and JJA mean surface wind speed for the PLIO and CTRL runs are shown in Figures 5.10 and 5.11. In general, the wind directions in the PLIO experiment are broadly similar to the wind directions in the CTRL experiment. Broad parts of the tropical oceans and also land areas at middle latitudes show reduced wind speeds for the Middle Pliocene. A decrease of wind speed, mainly in JJA, and a decrease of the anticyclonic activity are observed over Greenland. However, as a consequence of the warmer sea surface temperatures in the North Atlantic, wind speed strongly increases in this region and a cyclonic activity develops in DJF.

5.4.3 Vegetation effect on the Middle Pliocene climate

In order to isolate the vegetation change effect on the Pliocene climate, we performed an additional Pliocene experiment (PLIO-VEGP) where we kept

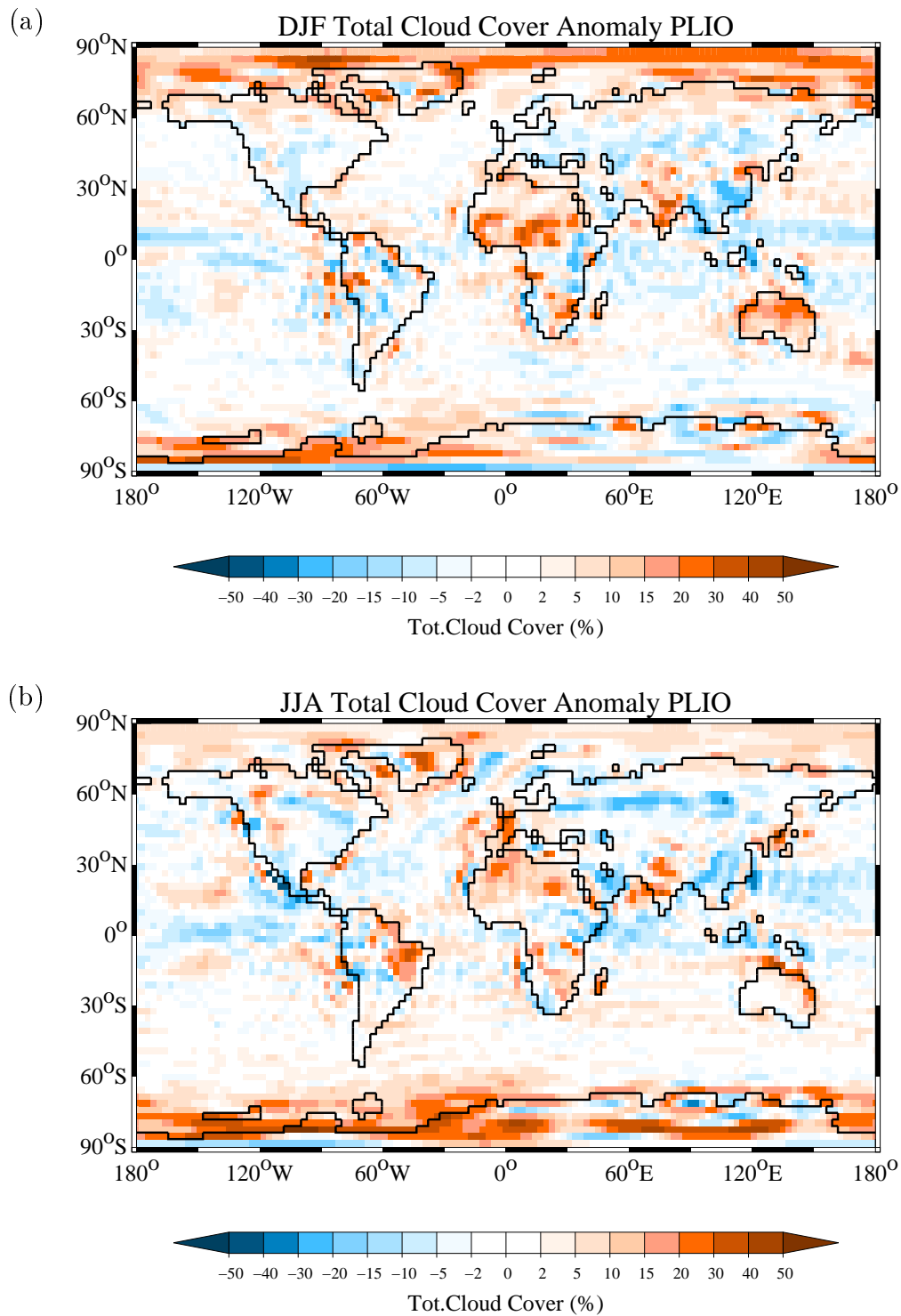


Figure 5.9: (a) DJF and (b) JJA total cloud cover anomalies (%) for the PLIO experiment.

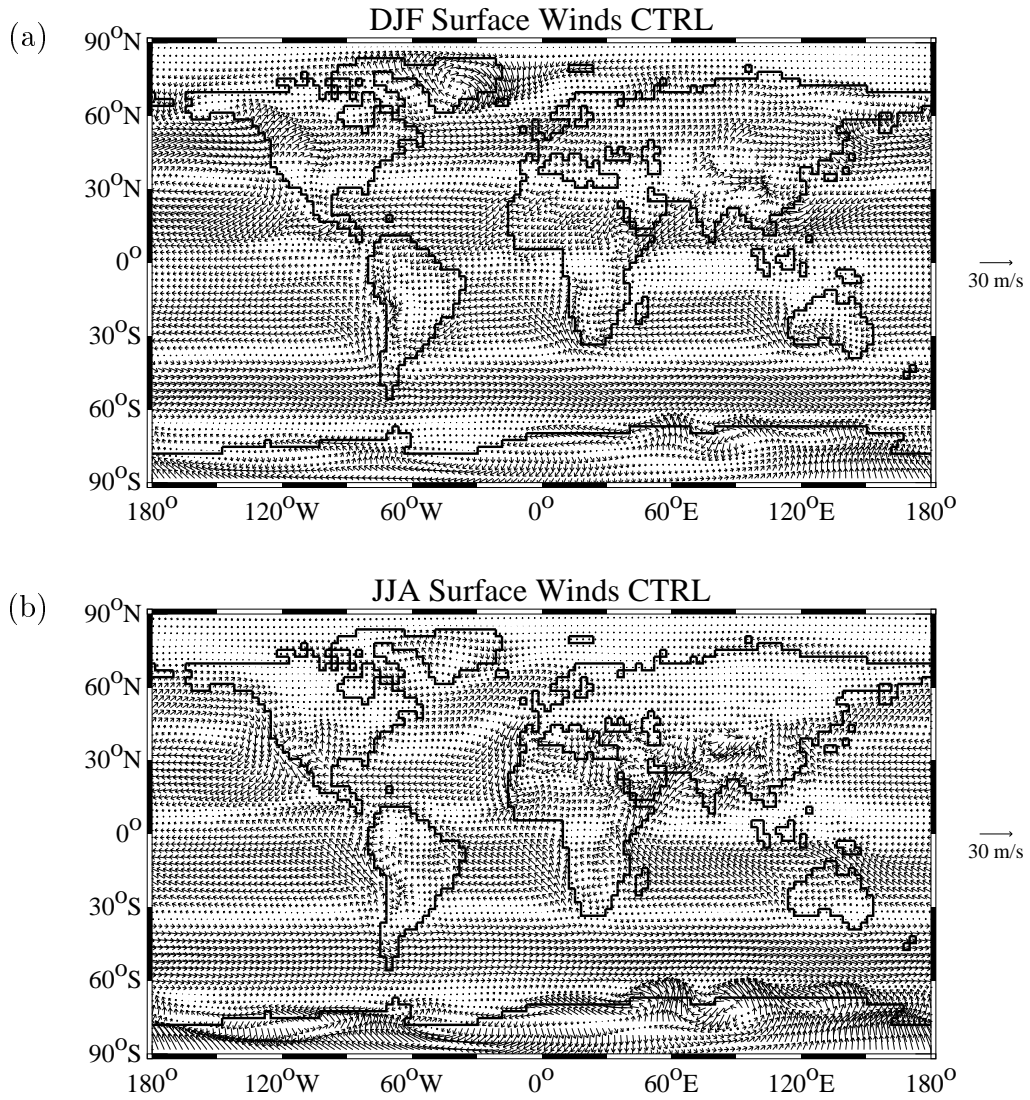


Figure 5.10: (a) DJF and (b) JJA surface winds for the CTRL experiment.

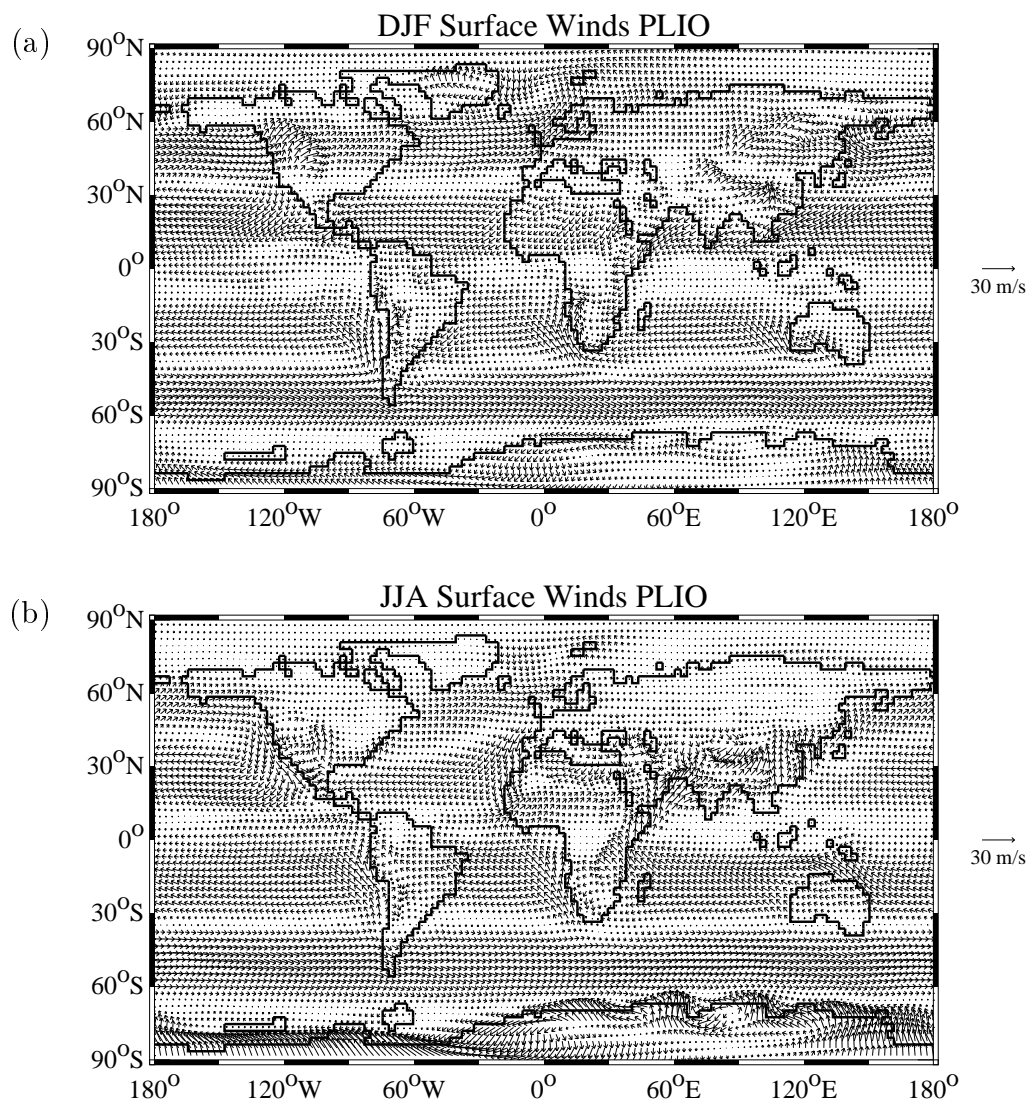


Figure 5.11: (a) DJF and (b) JJA surface winds for the PLIO experiment.

the preindustrial vegetation parameters used for the CTRL experiment (Section 5.3.1). The PLIO-VEGP experiment is compared to the PLIO experiment, which takes into account the Pliocene vegetation parameters. It should be noticed that we kept the other Pliocene boundary conditions and notably the Pliocene ice-sheet cover in the PLIO-VEGP experiment, in order to isolate the vegetation cover changes from the other effects.

The annual mean surface air temperature and precipitation differences between experiments PLIO and PLIO-VEGP (PLIO minus PLIO-VEGP) are shown in Figure 5.12. The use of Pliocene vegetation parameters in the PLIO experiment warms the global climate by 0.16°C (0.11°C over the oceans and 0.30°C over the continents), and increase the global precipitation by 0.005 mm/day (0.001 mm/day over the oceans and 0.02 mm/day over the continents) relative to the PLIO-VEGP experiment. Thus, the vegetation changes contribute to create slightly warmer and wetter conditions at the Middle Pliocene, especially over the continents. The relatively weak response of the oceans to the vegetation changes in comparison to the continental one may be partly explained by the direct and local effects of vegetation parameters on the continental climate (vegetation changes occur over the continents), but also by the use of fixed sea surface temperatures and sea-ice cover. Indeed, the prescription of fixed sea surface temperatures forces the slab model to stick to the imposed sea surface temperature and sea-ice cover distributions and prevent it to respond strongly to boundary condition changes. The same experiment repeated with prescribed heat transfer, instead of prescribed sea surface temperatures and sea-ice cover, yields a larger global warming of 0.39°C (0.4°C over the oceans and 0.32°C over the continents), and precipitation increase of 0.03 mm/day (0.02 mm/day over the oceans and 0.03 mm/day over the continents). In this additional experiment, most of the oceanic warming occur at high latitudes, over ice-covered areas. This warming may therefore be attributed to the melting of sea-ice in response to the warmer conditions generated by vegetation changes over continental regions at high latitudes (see below). Thus, the vegetation effect could reinforce the oceanic warming at high latitudes induced by the other boundary condition changes (Section 5.4.2).

Over the continents, most of the SAT differences can be linked to surface albedo changes. At high latitudes, the development of boreal forests decreases the surface albedo and warms the surface temperatures. This effect is stronger in winter due to the snow-albedo effect. Eurasia experiences a warming of about $+2^{\circ}\text{C}$ that is linked to surface albedo decrease due to the expansion of warm-mixed and temperate forests in this region. This effect is stronger in summer, and explains the surface temperature increase obtained

in the PLIO experiment (see Section 5.4.2). The reduction of desert areas in North Africa and Central Asia also leads to surface albedo decrease that in turn increases the SAT. However, the reduction of the roughness length in these regions reduces the surface heat fluxes. This effect increases the SAT, and therefore partly counterbalances the albedo effect. The development of grassland ecosystems in East Asia and north of North America induces an increase of the surface albedo that cools the SAT. This albedo effect is amplified in winter by the snow-albedo feedback.

The rooting depth changes mainly affect the hydrological cycle through surface evaporation. However, precipitation is weakly affected by the vegetation changes (see Figure 5.12). Precipitation increases over the southern border of the Sahara Desert in response to an increase of rooting depth. Precipitation also increases in southwestern Greenland due to the development of boreal forests. Precipitation slightly decreases in Siberia and North America due to the development of grasslands with smaller rooting depth. Larger precipitation decreases also occur over North Europe. This effect may be linked to the reduction of the soil water and thus of the surface evaporation, due to the development of warm mixed forests. This leads to a surface temperature increase in the region.

5.5 Comparison to previous climate modelling studies

It is of interest to compare the Planet Simulator results with results obtained with other models in order to examine the common and different responses of the climate models to the imposed Pliocene boundary conditions. Besides the differences in the models, we also have to take into account the differences in the versions of the PRISM data set used as boundary conditions in the mentioned studies.

In response to the higher atmospheric CO₂ concentration, warmer sea surface temperatures (in particular at high latitudes) and reduced ice cover on land and sea, the Middle Pliocene simulation yields a global surface air temperature increase of 2.24°C relative to the control simulation in our experiments. This warming is consistent with the global temperature increases produced in previous Middle Pliocene modelling studies, using atmospheric GCMs or coupled atmosphere-ocean GCMs and different version of the PRISM data set (see Table 5.3). The differences between the results could therefore be attributed to differences in the model configurations as well

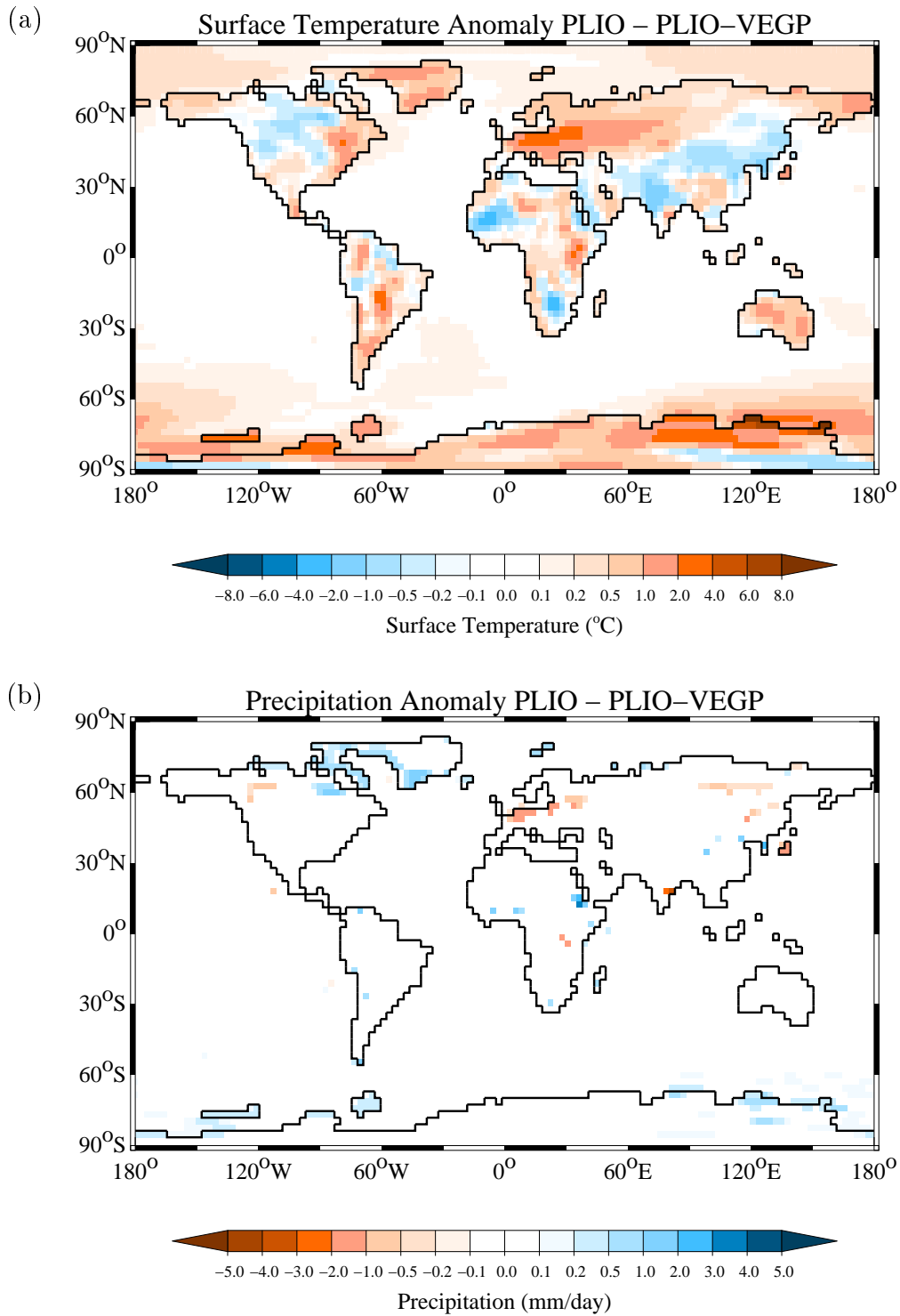


Figure 5.12: Annual mean (a) surface air temperature and (b) precipitation differences (mm/day) between the PLIO and PLIO-VEGP experiments.

Table 5.3: Global warming and precipitation increase produced in Middle Pliocene modelling experiments.

Study	PRISM version	ΔT ($^{\circ}\text{C}$)	ΔPRC
SLOAN et al. (1996)	PRISM1	+3.6	+5%
HAYWOOD et al. (2000b)	PRISM2	+1.9	+6%
HAYWOOD and VALDES (2004)	PRISM2	+3.09	+4%
JIANG et al. (2005)	PRISM2	+2.6	+4%
this study	PRISM3D	+2.24	+3.5%

as in the boundary conditions. Notably, as mentioned in HAYWOOD et al. (2000b), the large warming obtained by SLOAN et al. (1996) can partly be attributed to the strong response of high latitudes to the prescribed PRISM1 Antarctic ice-sheet. Our global warming is closer to the one obtained by HAYWOOD et al. (2000b) and JIANG et al. (2005). The difference could be linked to the refinement of the PRISM3D data set, but also to the different responses of the climate models to boundary condition changes. However, the global temperature increase produced here is lower than the one obtained by HAYWOOD and VALDES (2004) with the UKMO AOGCM. This difference could be partly linked to the use of fixed sea surface temperatures in our experiments.

Regional SAT anomalies, and notably the reduction of the equator-to-pole gradient, agree fairly well in terms of distribution and magnitude with the results of HAYWOOD et al. (2000b) and of HAYWOOD et al. (2009a), who compared the Middle Pliocene climate simulated by the atmospheric GCMAM3 and HadAM3 GCMs, using the PRISM2 data set. Three zones of temperature changes can be clearly identified: (1) high-latitude regions poleward of 60°N and S where warming is largest; (2) mid-latitude regions between 30° and 50° in each hemisphere where warming is moderate and (3) the tropical regions where very little warming occurs over the oceans or even slight cooling occurs over some land areas.

Our PLIO experiment produces an annual mean global precipitation increase of 3.5 % that is lower than the 6 % increase of precipitation obtained by HAYWOOD et al. (2000b) and closer to the 4 % increase obtained by HAYWOOD and VALDES (2004) and JIANG et al. (2005). Patterns of the precipitation anomaly distribution compare well with the results of HAYWOOD et al. (2000b,a); HAYWOOD and VALDES (2004) and JIANG et al. (2005). In most models, precipitation increases over the ocean are associated with warmer sea-surface temperature (HAYWOOD et al., 2009a).

As already observed by HAYWOOD et al. (2000b), the large SAT increases over the Arctic and Antarctic oceans occurring mainly in winter of the hemisphere can be attributed to the reduction of the terrestrial and oceanic ice cover and the warmer sea surface temperatures of the PRISM2 and PRISM3D data sets in these regions. These conditions allow a greater evaporation that, in turn, increases the cloud cover, generally acting to warm the climate at high latitudes.

The small changes in sea surface temperature, together with precipitation decreases over the tropical oceans can also partly be explained by the very small changes or even slight cooling in the tropical PRISM2 and PRISM3D sea surface temperatures for the Middle Pliocene. However, temperature decreases over some subtropical land areas are linked to large precipitation increases. These precipitation increases are due to the broadening of the Hadley Cell, as a result of the reduced equator-to-pole gradient (HAYWOOD et al., 2000b). In agreement with HAYWOOD et al. (2000b, 2009a) and JIANG et al. (2005), our results also indicate an enhancement of the African and Indian summer monsoon, but a weakening of the Asian summer monsoon, in response to a slightly colder and drier Tropical Pacific. However, the reduction of precipitation we obtain over Arabia in summer is not produced in HAYWOOD et al. (2009a). This reduction of precipitation in our results can be attributed to the change of direction and magnitude of the surface winds coming from East Africa in the PLIO experiment instead of the Arabian Sea in the CTRL experiment, which bring less humidity to the Arabian Peninsula. We also note that most of the precipitation anomalies we produced here in subtropical areas disagree with the AOGCM results used in HAYWOOD and VALDES (2004). This may be linked to the differences between the sea surface temperatures simulated by the AOGCM and the the PRISM2/PRISM3D reconstructions. In HAYWOOD and VALDES (2004), the AOGCM notably simulated an increase of sea surface temperatures over the tropical oceans, whereas the PRISM3D reconstruction rather indicate a slight cooling of the sea-surface temperatures in the tropics (DOWSETT et al., 2009).

At middle latitudes, and particularly over the North Atlantic and western Europe, the model produces warmer and wetter conditions, in response to warmer sea-surface temperature and enhanced atmospheric heat transfer and moisture. These results agree fairly well with the model results of HAYWOOD et al. (2000a) and JOST et al. (2009), who focused on the Middle Pliocene European and Mediterranean climate. As in HAYWOOD et al. (2000a) and JOST et al. (2009), warming occurs mainly in winter, whereas no warming or even cooler conditions prevail in summer in western Europe, as a consequence of the large increases of precipitation over the region in summer.

The change in the oceanic heat transport inducing sea surface temperatures anomalies and the reduction of the land and sea ice cover strongly influence the Middle Pliocene climate, by reducing the equator-to-pole gradient and affecting the precipitation distribution. The higher atmospheric CO₂ concentration is responsible for warming at the global scale and the increase of precipitation produced in the Middle Pliocene simulation. However, it is not sufficient by itself to explain the regional changes in surface air temperature and precipitation (HAYWOOD et al., 2009b). In comparison to the previous versions of the PRISM topography, the PRISM3D topography is closer to the modern one and the topographic forcing is therefore not a primary driver of the Middle Pliocene climate in our experiment. Vegetation cover changes in response to warmer conditions of the Middle Pliocene also contribute to explain the local Middle Pliocene climate anomalies. HAYWOOD and VALDES (2006) suggest that the principal impact of vegetation cover changes at the Middle Pliocene is to reduce temperature extremes, thus reducing the seasonality of temperature over wide regions. Here, surface albedo changes over the continents contribute to significantly warm the Pliocene climate. In agreement with HAYWOOD and VALDES (2006), the decrease of the surface albedo at high latitudes in response to the development of boreal forests, reinforced by the snow-albedo effect in winter, notably contributes to warm the high latitudes, and reduces the seasonality of temperature in these regions. The decrease of surface albedo linked to the reduction of the desert areas or to the expansion of warm forests also produces additional warming in the concerned regions. However, some of the vegetation change effects are weaker than the CO₂ and oceanic effects and are counterbalanced by these effects.

5.6 Extra Middle Pliocene vegetation simulation with CARAIB

In addition to the experiments defined by the PlioMIP protocol, we called upon the dynamic vegetation model CARAIB to reconstruct the vegetation distribution in response to the warm Middle Pliocene climate we simulated. The CARAIB vegetation distribution is compared to previous Middle Pliocene vegetation reconstructions, and notably to the BIOME4-based Pliocene vegetation reconstruction that has been used to force the PLIO experiment (Section 5.7). Furthermore, the effect of the vegetation changes simulated by CARAIB are compared with the effects of the BIOME4 vegetation distribution on the Middle Pliocene climate simulated with Planet

Simulator (see Section 5.8).

The globally warmer and wetter than present-day Middle Pliocene climate induces an expansion of forest and grassland ecosystems at the expense of deserts. The Middle Pliocene biome distribution derived from the PFT assemblages obtained with CARAIB is shown in Figure 5.13 and compared to the preindustrial one. It should be noticed that the vegetation maps do not show Antarctica, because the NEW et al. (2002) climatology does not include any data for Antarctica.

In response to the strong warming that occurs at high latitudes in the Middle Pliocene simulation, significant changes occur in the vegetation cover northward of 50° . Boreal forests and cold temperate open woodlands expand at the expense of tundra, which is shifted further north, where it replaces polar desert. Boreal forests notably develop in the southern and western parts of Greenland. Furthermore, the needleleaved trees are more productive at higher latitudes in the Middle Pliocene simulation, as illustrated in Figure 5.14, where the net primary productivity (NPP) of the cold boreal/temperate trees (PFTs 3 and 11) is shown, in comparison to their preindustrial NPP. However, boreal forests are replaced by temperate broadleaved deciduous forests in northern Europe and particularly in Scandinavia, due to the warmer conditions that prevail in winter in those regions.

At mid to low latitudes, broadleaved temperate deciduous trees develop at the expense of cool temperate mixed forest and install further north. Grasslands and cool temperate coniferous forest prevail along the west coast of Europe, due to colder conditions in summer over this region. A second major change that occurs in the Middle Pliocene vegetation distribution is the reduction of desert areas at the benefit of grasslands and open woodlands, e.g., in Central Asia and particularly in North Africa. Tropical grasslands and warm open woodlands expand into the modern Sahara desert. This vegetation change is linked to the enhancement of the African monsoon in response to the migration of the ITCZ further north in the Pliocene experiment.

In the tropics and the subtropics, tropical forests expand from their modern geographical positions. They are also much more productive at the Middle Pliocene, as illustrated in Figure 5.15, which shows the NPP of the broadleaved evergreen tropical trees (PFTs 15) in comparison to preindustrial NPP. Tropical forests extend to the west in Equatorial Africa and to the south in South America, mainly due to increased precipitation rates in these regions. Subtropical biomes also develop along the east coast of Australia in comparison to the preindustrial state. However, the subtropical types are restricted to southeastern China in the Pliocene distribution, and replaced by

warm open woodlands in southeastern China, in response to the weakening of the East Asian monsoon.

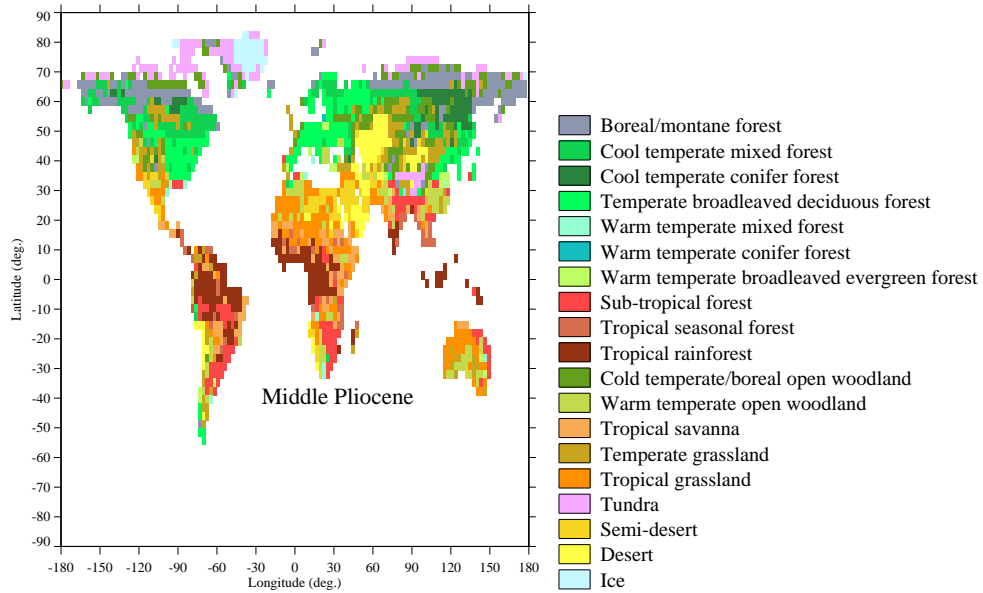
5.7 Comparison to previous Middle Pliocene vegetation reconstructions

At the global scale, the Middle Pliocene vegetation we produced with CARAIB compares well with previous vegetation reconstructions (THOMPSON and FLEMING, 1996; HAYWOOD and VALDES, 2006; SALZMANN et al., 2008; JOST et al., 2009). Some differences in the model-based vegetation reconstructions can possibly be attributed to the different classification schemes used in the various vegetation models. All the mentioned studies support a reduction of the desert areas at the Middle Pliocene and an expansion of forests, especially at high latitudes where boreal and cold forests replace tundra. Needleleaved trees therefore dominated at high latitudes, whereas broadleaved trees dominated in other regions during the Middle Pliocene (HAYWOOD and VALDES, 2006).

At high latitudes, the distribution of the boreal forest in the vegetation distribution simulated by CARAIB agrees well with the vegetation reconstruction of THOMPSON and FLEMING (1996), based on fossil pollen and plant megafossil data, which suggests that a boreal vegetation mainly composed of coniferous trees prevailed in Alaska, northeastern Canada and western Siberia. The northernmost limit of the temperate forest simulated by CARAIB is consistent with the limit of 60 to 70°N given by the vegetation reconstruction of SALZMANN et al. (2008), which combines vegetation reconstruction from paleobotanical data with a BIOME4 vegetation model simulation. However, CARAIB yields cold temperate forests in northeastern Russia, where the BIOME4 reconstruction predicted temperate grasslands (SALZMANN et al., 2008). Unfortunately, it is currently not possible to carry out a meaningful validation of the model results because of the poor data coverage in that region.

At middle latitudes, e.g., in North America and Europe, our results reproduce well the expansion of temperate broadleaved forests (THOMPSON and FLEMING, 1996; SALZMANN et al., 2008; JOST et al., 2009). In the CARAIB biome distribution broadleaved trees also dominate in eastern Europe, which disagrees with the results of the ORCHIDEE vegetation model, which suggest a dominance of needleleaved evergreen forests in this region (JOST et al., 2009). However, coniferous trees are well productive in eastern

(a) Biome Distribution



(b) Biome Distribution

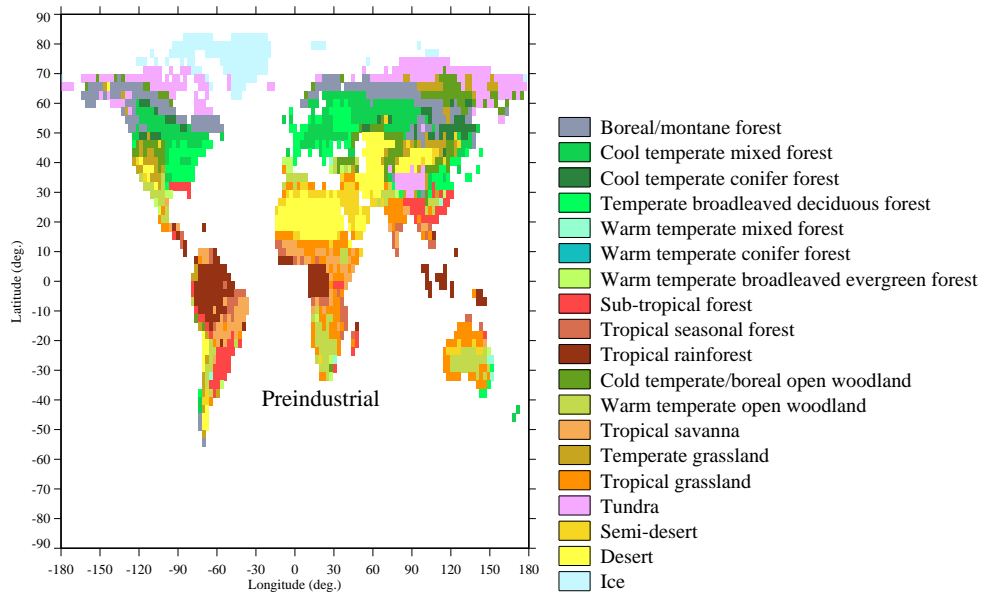


Figure 5.13: CARAIB biome distributions for (a) the Middle Pliocene and (b) the preindustrial period.

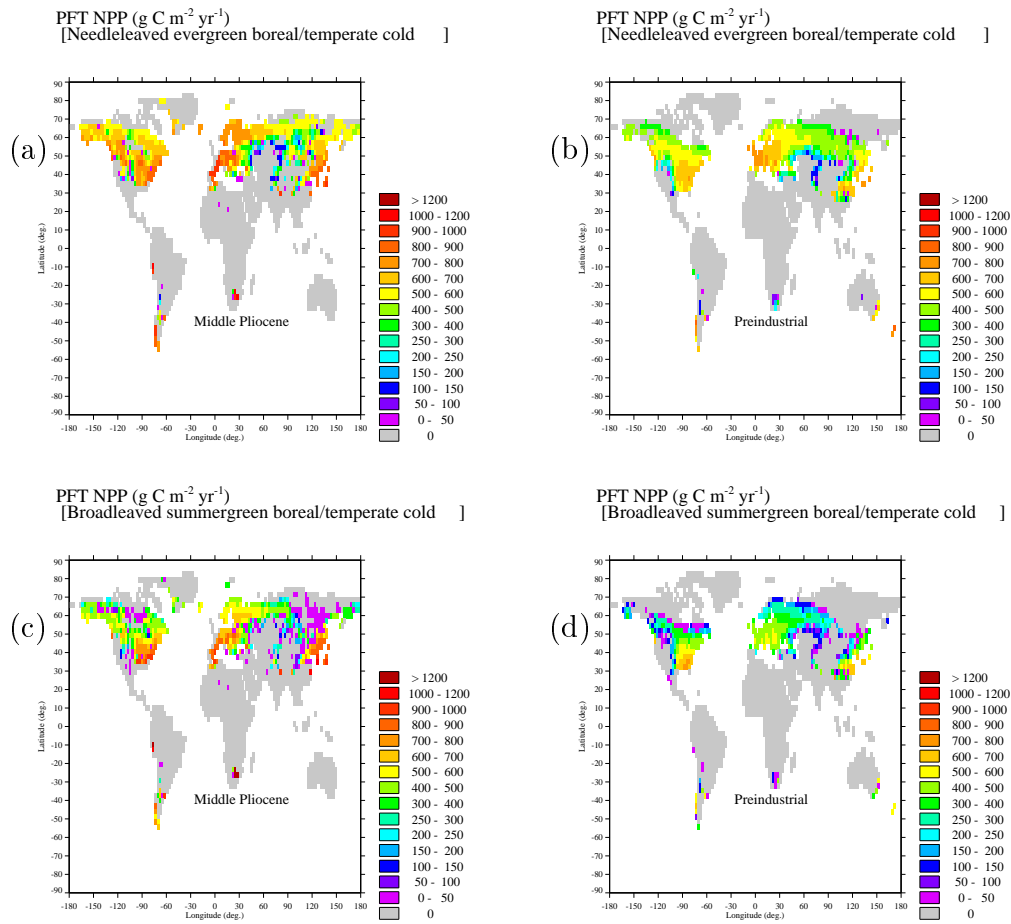
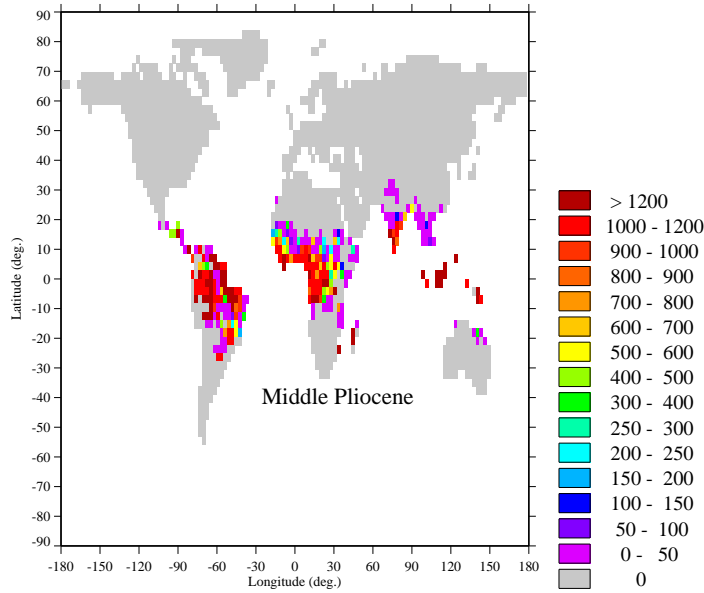


Figure 5.14: Net Primary Productivity of needleleaved evergreen boreal/temperate cold trees for (a) the Middle Pliocene and (b) the preindustrial vegetation distributions. Net Primary Productivity of broadleaved summergreen boreal/temperate cold trees for (c) the Middle Pliocene and (d) the preindustrial vegetation distributions.

(a) PFT NPP ($\text{g C m}^{-2} \text{yr}^{-1}$)
 [Broadleaved evergreen tropical]



(b) PFT NPP ($\text{g C m}^{-2} \text{yr}^{-1}$)
 [Broadleaved evergreen tropical]

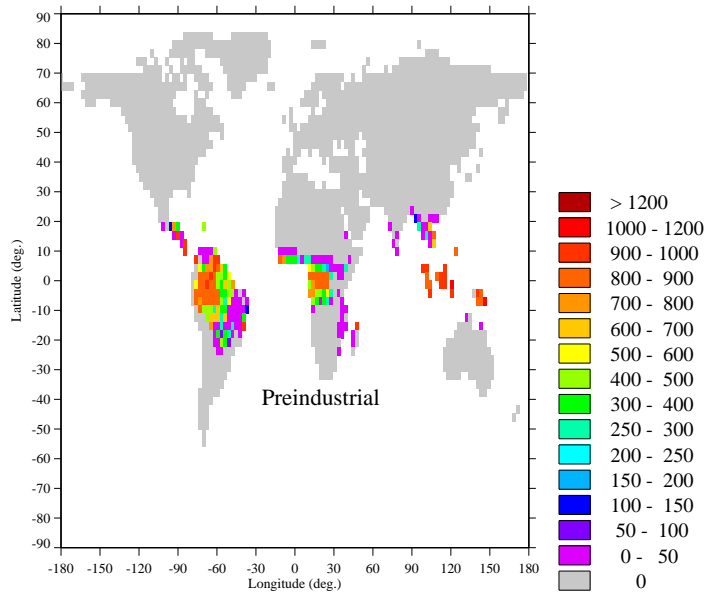


Figure 5.15: Net Primary Productivity of broadleaved evergreen tropical trees for (a) the Middle Pliocene and (b) the preindustrial vegetation distributions.

Europe, but not enough to show out on the biome distribution, which reflects the most productive plant type of each grid element (see Figure 5.14). In our results, the productivity of subtropical trees is very weak over Europe, which disagrees with data-based reconstructions suggesting that assemblages of thermophilous and temperate taxa prevailed in Europe (SALZMANN et al., 2008). Conversely, CARAIB reproduces well the development of warm mixed forests (including thermophilous taxa), and of conifer and temperate forests over the Black Sea region and eastern Mediterranean sector, as suggested by proxy reconstructions (THOMPSON and FLEMING, 1996; SALZMANN et al., 2008).

All the Pliocene vegetation reconstructions, including ours, indicate that desert areas were smaller at that time than today. In agreement with THOMPSON and FLEMING (1996) and SALZMANN et al. (2008), our results indicate that grasslands (C_4) were more prevalent than today in North Africa and particularly in northwestern Africa. However, previous vegetation modelling suggest that arid vegetation and deserts persisted in North Africa (SALZMANN et al., 2008; HAYWOOD and VALDES, 2006), whereas desert is almost completely replaced by tropical grasslands and warm open woodlands in the CARAIB reconstruction. Nevertheless, the productivities of trees and herbs remain weak in the Sahara and Arabian Peninsula. The presence of tropical savanna in East Africa in our results agrees well with palaeobotanical data (SALZMANN et al., 2008). Moreover, the presence of tropical forest in northwestern Africa in the CARAIB distribution is in good agreement with reconstructions based on marine core from northwestern Africa that indicate the presence of tropical forests and mangroves at the modern southern limit of the Sahara at 21°N (LEROY and DUPONT, 1994).

In the CARAIB reconstruction, tropical forests in Africa, South America and Asia are nearly at the same position as today, which is in good agreement with the palynological data (THOMPSON and FLEMING, 1996; SALZMANN et al., 2008). Subtropical and tropical forests slightly expand as previously found by HAYWOOD and VALDES (2006). Subtropical forests also develops along the east coast of Australia, which is consistent with the results of the BIOME4 model (SALZMANN et al., 2008).

5.8 CARAIB vegetation feedback on the Middle Pliocene climate

We performed an additional Pliocene experiment (PLIO-VEGC), where we prescribed the vegetation parameters derived from the Pliocene vegetation distribution obtained with the CARAIB model (see Section 5.6). It should be noticed that the PLIO-VEGC experiment has been forced with the set of boundary conditions used for the PLIO experiment (see Section 5.3.2), except for the surface parameters that have been derived from the CARAIB vegetation distribution. Experiment PLIO-VEGC and PLIO are compared in order to discuss the vegetation feedback on the Pliocene climate. The annual mean surface temperature and precipitation differences between experiments PLIO-VEGC and PLIO (PLIO-VEGC minus PLIO) are shown in Figure 5.16.

The replacement of the BIOME4 Pliocene vegetation distribution by the CARAIB one produces a global cooling of 0.25°C (0.07°C over the oceans and 0.73°C over the continents) and a global precipitation decrease of 0.03 mm/day ($+0.02\text{ mm/day}$ over the oceans and -0.19 mm/day over the continents). As a consequence of the forest expansion at high and middle latitudes and the reduction of desert areas (see Section 5.6), we rather expected a global warming effect of the vegetation. However, the global temperature and precipitation decreases we obtained here mostly reflect the differences in the vegetation parameters derived from the BIOME4 and CARAIB classifications, rather than the vegetation feedback to the Middle Pliocene warm climate, or the differences in the vegetation distributions simulated by the BIOME4 and CARAIB models. For comparison, the surface albedo and rooting depth differences derived from the CARAIB and BIOME4 vegetation distributions are shown in Figure 5.17. Indeed, the surface albedo values attributed to the PFTs used in the CARAIB model are on average greater than the ones attributed to the biomes of the 28-type biome classification used in the BIOME4 model. Therefore, replacing the BIOME4 Pliocene vegetation by the CARAIB one induces surface albedo increases that explain the surface temperature decreases we obtain here. Deserts and semi-deserts, e.g., in Africa, Arabia, Central Asia, and Australia, notably experience temperature decreases of more than 2°C , due to the greater albedo values attributed to grasslands and deserts in the CARAIB model (0.2 for grasslands and above 0.3 for deserts) relative to the values used for the BIOME4 biomes (below 0.2 for the grassland biomes and 0.25 for the desert biome). The decrease of surface albedo in northeastern Asia and North America is due to the replace-

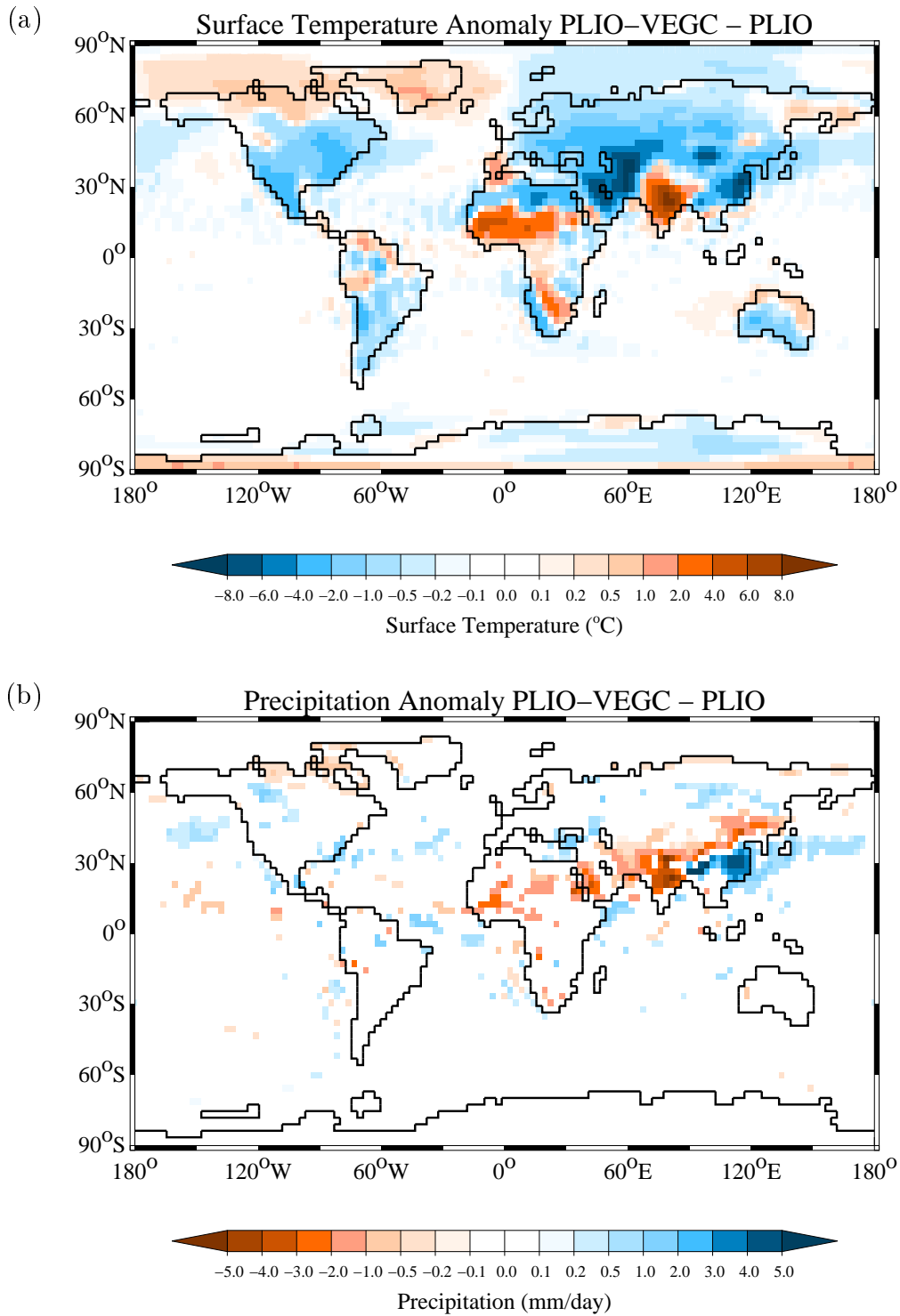


Figure 5.16: Annual mean (a) surface air temperature and (b) precipitation differences between the PLIO-VEGC and PLIO experiments.

ment of grasslands in the BIOME4 distribution by forests in the CARAIB distribution (see Figure 5.17). However, this surface albedo difference is not sufficient to explain all of the temperature differences in these regions. Nevertheless, some of the temperature and precipitation differences may be attributed to vegetation changes in response to the Pliocene simulated climate. The increases of surface temperature in Equatorial and South Africa and South America may notably be due to the decrease of surface albedo caused by the expansion of tropical and sub-tropical forests in the CARAIB vegetation distribution.

The differences in the vegetation distributions on land also slightly affect the temperature distributions over the oceans, especially at high latitudes over ice-covered ocean grid-cells. However, the oceanic response to vegetation changes is once more limited by the prescription of fixed sea surface temperature and sea-ice cover distributions. The prescription of oceanic heat transfer and the calculation by the model of the sea surface temperatures and sea ice cover in an additional experiment enhances the oceanic response. In this additional experiment, the replacement of the BIOME4 Pliocene vegetation distribution by the CARAIB one produces a global cooling of 0.98°C (0.81°C over the oceans and 1.35°C over the continents) and a global precipitation decrease of 0.09 mm/day (0.02 mm/day over the oceans and 0.20 mm/day over the continents). Most of the oceans even cool by about 1°C (see Figure 5.18). The response of precipitation over the oceans is also enhanced, particularly in the tropics (see Figure 5.18).

The vegetation changes strongly weaken the hydrological cycle in the tropics and disturb the precipitation distribution over the ITCZ (see Figure 5.16). North Africa and the Indian Peninsula experience strong precipitation decreases, whereas northeastern China experiences a strong increase of precipitation. These precipitation effects are even stronger than the precipitation differences between experiments PLIO and CTRL over these regions (see Section 5.4.2). Once more, the differences in the CARAIB and BIOME4 parameters may be responsible for these differences. Indeed, the soil water limit derived from the CARAIB model is the field capacity, calculated from the rooting depth and the soil texture. It is on average lower than the rooting depth calculated by CARAIB, which differs from the rooting depth derived from the BIOME4 biomes. This induces lower surface evaporation rates, and in turn surface temperature increases and precipitation decreases that could explain the disruption of the precipitation distribution in the tropics. Despite the expansion of boreal forests, precipitation is also reduced at high latitudes, in response to the decrease of the soil water capacity derived from the CARAIB vegetation distribution. However, northern Europe experiences

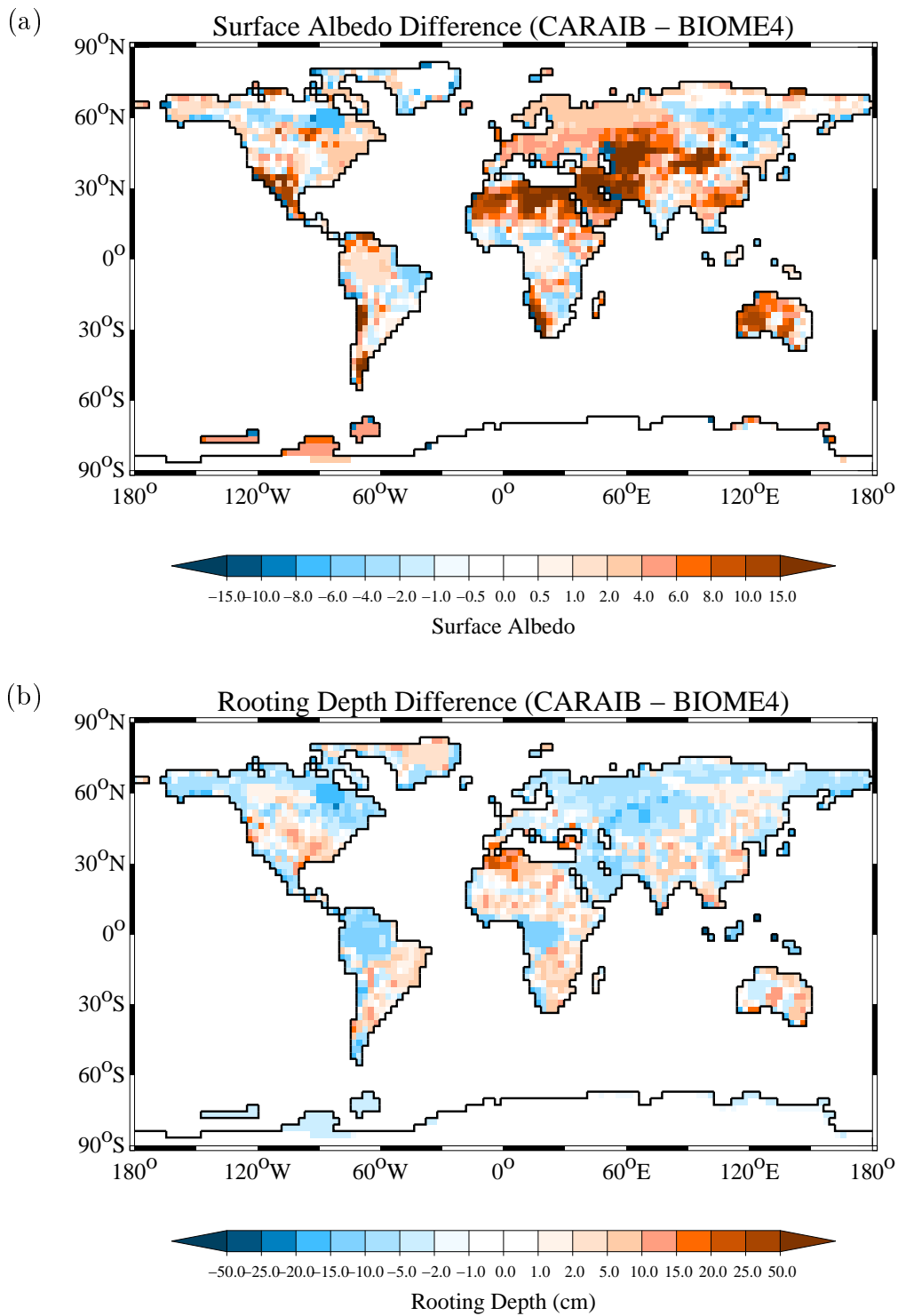


Figure 5.17: (a) Surface albedo and (b) rooting depth differences (CARAIB - BIOME4) derived from the CARAIB and BIOME4 vegetation distributions.

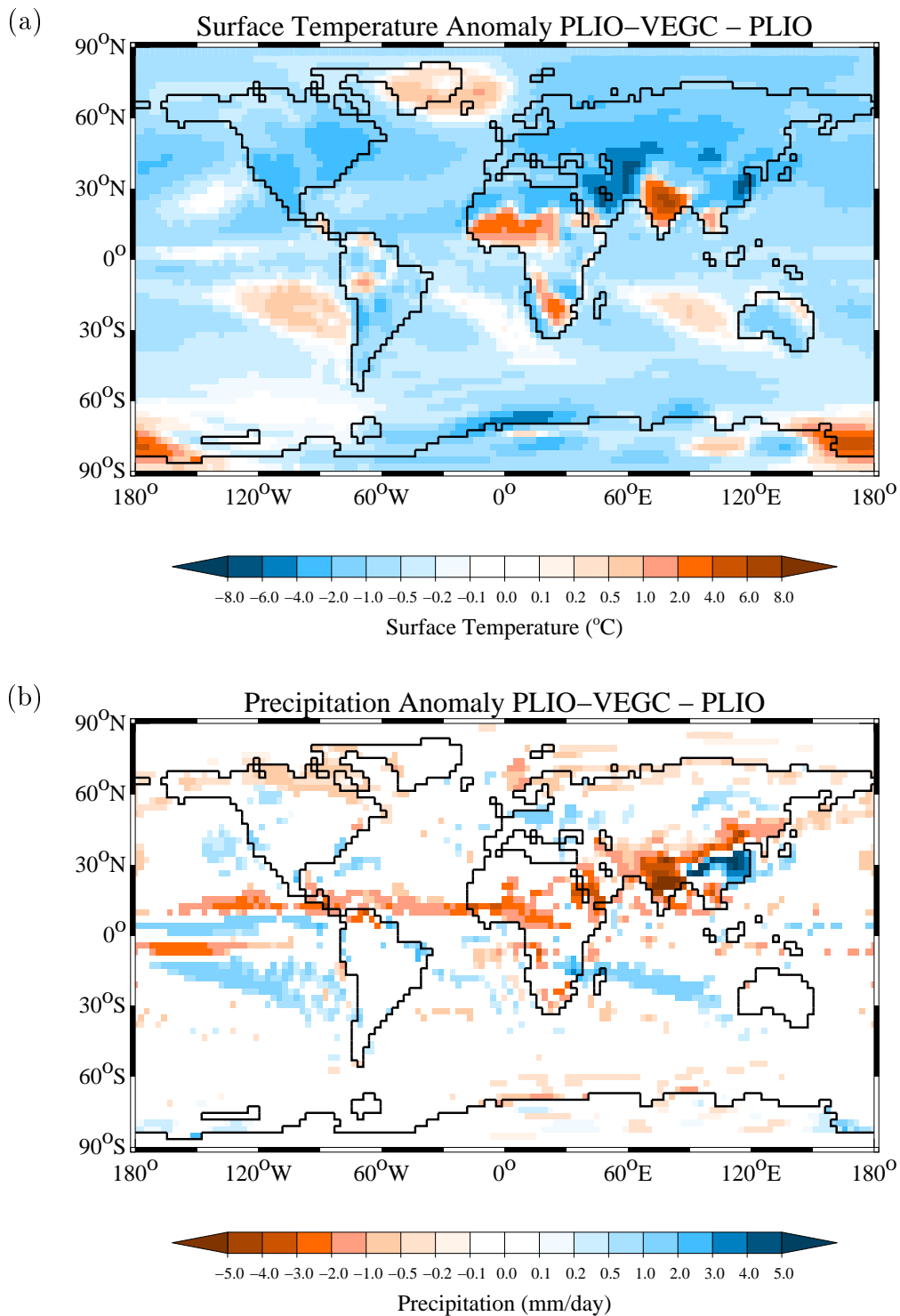


Figure 5.18: Annual mean (a) surface air temperature and (b) precipitation differences (mm/day) between the PLIO-VEGC and PLIO experiments with calculated sea surface temperatures and sea-ice cover.

an increase of precipitation of about 1 mm/day. This may be due to an increase of surface evaporation in response to a slight increase of roughness length (not shown), but also to the surface cooling induced by the increase of the surface albedo.

5.9 Conclusions

This study presents the results of a modelling experiment focusing on the Middle Pliocene climate and vegetation. We used the Planet Simulator, an Earth System model of intermediate complexity to simulate the Middle Pliocene climate following the Pliocene Model Intercomparison Project (PlioMIP) protocol (experiment 1, preferred conditions) (HAYWOOD et al., 2010), in order to enable a direct model-model comparison of the Pliocene results presented here. We therefore used the latest version of the PRISM3D data set (HAYWOOD et al., 2010), to prescribe initial and boundary conditions for the Planet Simulator. In addition to the requirements stated in the PlioMIP protocol, we furthermore realised a reconstruction of the vegetation distribution of the Middle Pliocene in response to the simulated climate, using the CARAIB dynamic vegetation model, and tested its effect on the Pliocene climate.

At the global scale, we produce a warmer and wetter than present-day climate for the Middle Pliocene. Most of the warming occurs over the oceans and the continents at high latitudes, whereas little changes occur at low latitudes. The equator-to-pole gradient in temperature and precipitation is thus reduced. These results broadly agree with previous modelling studies (HAYWOOD et al., 2000b; HAYWOOD and VALDES, 2004; JIANG et al., 2005; HAYWOOD et al., 2009a; JOST et al., 2009), despite the differences in the versions of the PRISM data set that were used as boundary conditions. Consistently with previous modelling studies, the simulated patterns of climate change at the Middle Pliocene, relative to the preindustrial control run, are associated with changes in the oceanic heat transport, inducing sea surface temperatures anomalies, and with the reduction of the land and sea ice cover. The higher atmospheric CO₂ concentration is also responsible for the global warming and increase of precipitation. However, regional changes in surface air temperature and precipitation can also be attributed to topography reduction or vegetation cover changes.

The Middle Pliocene vegetation we produced with CARAIB is consistent with previous data- and model-based vegetation reconstructions (THOMPSON and FLEMING, 1996; HAYWOOD and VALDES, 2006; SALZMANN et al.,

2008; JOST et al., 2009). Some discrepancies in the model-based vegetation reconstructions can be attributed to the different classification scheme used in the vegetation models. In agreement with previous studies, the CARAIB vegetation distribution shows a reduction of the desert areas at the Middle Pliocene, and an expansion of forests, especially at high latitudes where boreal and cold forests replace tundra. However, besides the relative good agreement between the CARAIB vegetation distribution and the BIOME4 one, the vegetation changes simulated by CARAIB do not produce the expected feedback on the Pliocene climate. Indeed, the differences in the vegetation parameter values used in the CARAIB and BIOME4 models induce climate differences that do not reflect the vegetation change effect in response to the simulated climate, but the differences in the parameterisations used in both models. These results thus illustrate how the climate models may be influenced by the parameters derived from the vegetation models. Therefore, the vegetation effect on the climate simulated by climate models should be analysed with great care, taking into account the differences in the parameterisations of the vegetation models, which must therefore be clearly documented.

Future work will aim to evaluate the reliability of the Middle Pliocene climate we simulate here to similar Middle Pliocene experiments with other atmospheric GCMs or fully coupled ocean-atmosphere GCMs using of the same PRISM3D boundary conditions. Further work regarding the vegetation-climate interactions at the Middle Pliocene should better take into account the vegetation impact on climate, depending on the vegetation model. A more precise comparison to available proxy-data in terms of taxa (FRANÇOIS et al. (submitted)—see Appendix A) could also improve the comparison of the Middle Pliocene vegetation distributions.

Chapter 6

Middle Miocene climate and vegetation modelling

This chapter presents the results of Middle Miocene climate and vegetation modelling. The Middle Miocene is one of the last warm periods of the recent past, before the glacial and interglacial periods of the Pleistocene, that may provide potential guidance to improve our knowledge on the global warming in the near future. This period also starts to be well covered by marine and terrestrial proxy data, notably thanks to the NECLIME project (Neogene Climate Evolution in Eurasia), which aims to provide quantitative proxy-based reconstructions of the Neogene climate evolution (BRUCH et al., 2007). However, in contrast to the Last Glacial Maximum and Middle Pliocene periods, only a few climate model simulations have been performed for the Middle Miocene. Furthermore, the key mechanisms that may be responsible for the warm Middle Miocene climate have not been clearly identified yet. The role of the atmospheric CO₂ is notably debated, as the proxy-based CO₂ estimations vary from glacial levels to nearly twice the modern values.

In the first section of this chapter, we reproduce the complete text of HENROT et al. (2010). This paper examines the contribution of several boundary condition changes to the warm Middle Miocene climate and particularly focus on the contribution of the vegetation feedback.

In the second section, we present and compare to available proxy-based vegetation reconstructions Middle Miocene vegetation distributions simulated by CARAIB under high (500 ppmv) and low (280 ppmv) CO₂ levels. We also examine the vegetation feedback on the MMCO climate at high and low CO₂ levels, and continue the iterations between Plasim and CARAIB ap-

plying the equilibrium asynchronous coupling procedure in order to analyse the vegetation-climate interactions at Middle Miocene.

Effects of CO₂, continental distribution, topography and vegetation changes on the climate at the Middle Miocene: a model study.

A.-J. Henrot¹, L. François², E. Favre², M. Butzin³, M. Ouberdous² and G. Munhoven¹

¹ Laboratory of Atmospheric and Planetary Physics, University of Liège, Liège, Belgium

² Unité de Modélisation du Climat et des Cycles Biogéochimiques, University of Liège, Liège, Belgium

³ MARUM - Center for Marine Environmental Sciences, University of Bremen, Bremen, Germany

Abstract The Middle Miocene was one of the last warm periods of the Neogene, culminating with the Middle Miocene Climatic Optimum (MMCO, approximately 17-15 Ma). Several proxy-based reconstructions support warmer and more humid climate during the MMCO. The mechanisms responsible for the warmer climate at the MMCO and particularly the role of the atmospheric carbon dioxide are still highly debated. Here we carried out a series of sensitivity experiments with the model of intermediate complexity Planet Simulator, investigating the contributions of the absence of ice on the continents, the opening of the Central American and Eastern Tethys Seaways, the lowering of the topography on land, the effect of various atmospheric CO₂ concentrations and the vegetation feedback.

Our results show that a higher than present-day CO₂ concentration is necessary to generate a warmer climate at all latitudes at the Middle Miocene, in agreement with the terrestrial proxy reconstructions which suggest high atmospheric CO₂ concentrations at the MMCO. Nevertheless, the changes in sea-surface conditions, the lowering of the topography on land and the vegetation feedback also produce significant local warming that may, locally, even be stronger than the CO₂ induced temperature increases.

The lowering of the topography leads to a more zonal atmospheric circulation and allows the westerly flow to continue over the lowered Plateaus at middle latitudes. The reduced height of the Tibetan Plateau notably prevents the development of a monsoon-like circulation, whereas the reduction of elevations of the North American and European reliefs strongly increases precipitation from northwestern to eastern Europe.

The changes in vegetation cover contribute to maintain and even to intensify the warm and humid conditions produced by the other factors, suggesting that the vegetation-climate interactions could help to improve the model-data comparison.

Introduction

In a long-term climatic cooling trend, the Middle Miocene represents one of the last warm periods of the Neogene, culminating with the Middle Miocene Climatic Optimum, MMCO, that occurred at approximately 17-15 Ma (ZACHOS et al., 2001). Various proxy data support a warmer and more humid climate during the MMCO (ZACHOS et al., 2001; MOSBRUGGER et al., 2005; BRUCH et al., 2007). Proxy-based studies suggest a warming at middle latitudes of about +6°C (FLOWER and KENNETT, 1994) and a weak equator-to-pole latitudinal temperature gradient (BRUCH et al., 2007). However, the climate mechanisms responsible for the warmer climate at the MMCO and, in particular, the role of the atmospheric carbon dioxide, CO₂, are still highly debated. Frequently, elevated greenhouse gas concentrations are cited as primary contributors to past warm climates (SHELLITO et al., 2003). However, estimates for the concentration of CO₂ in the atmosphere at the MMCO range from levels that are typical for Pleistocene glaciations to nearly twice the modern value. PAGANI et al. (1999) calculated

CO₂ levels of 180 to 290 ppmv from marine $\delta^{13}\text{C}$ biological isotopic fractionation. Marine *pH* reconstructions from $\delta^{11}\text{B}$ also point towards a low CO₂ level between 140 and 300 ppmv (PEARSON and PALMER, 2000), supporting a decoupling between CO₂ and temperature during the Middle Miocene. However, the reconstructions of KÜRSCHNER et al. (2008) based on leaf stomatal indices indicate much higher MMCO CO₂ levels between 300 and 600 ppmv. Reconstructions based on paleosoil analysis indicate an even higher CO₂ concentration of 850 ppmv (RETALLACK, 2009). However, CO₂ concentrations reconstructed on the basis of planktonic foraminiferal $\delta^{18}\text{O}$ temperature reconstructions are possibly biased due to estimates of ice volume or diagenesis (PAGANI et al., 2010, suppl. mat.). Alkenone-based temperature reconstructions could possibly lead to higher CO₂ concentration estimates for the Miocene (PAGANI et al., 2010, suppl. mat.).

The reconfiguration of inter-oceanic passages which significantly influences the ocean circulation may also have contributed to the MMCO climate (BICE et al., 2000; VON DER HEYDT and DI-

JKSTRA, 2008). The Central American Seaway and Eastern Tethys Seaway were notably open during the Middle Miocene (HEROLD et al., 2008), leading to significantly different ocean circulation patterns (VON DER HEYDT and DIJKSTRA, 2006).

Geological processes such as mountain uplift may also affect the atmospheric circulation and precipitation patterns (GREGORY-WODZICKI, 2000; HARRIS, 2006). Although the positions of the continents were close to modern, most of the higher orogens got elevated during the Miocene, such as the Himalayas and the Tibetan Plateau (CURRIE et al., 2005; HARRIS, 2006), the Central Andes (GREGORY-WODZICKI, 2000) as well as the Alps (KUHLEMANN et al., 2006). Topography was therefore generally lower at the Middle Miocene than at present-day (HEROLD et al., 2008).

Finally it should also be noticed that the warm climate prevailing during the Middle Miocene led to vegetation changes. Broadleaved evergreen forests appear to have extended as far north as 45°N in North America and 52°N in Europe (UTESCHER et al., 2000). Such a change in the vegetation cover may have led to significant impacts on climate (DUTTON and BARRON, 1997).

Up to now, only a few climate model simulations have been performed for the Middle Miocene. VON DER HEYDT and DIJKSTRA (2006) used an AOGCM (Community Climate System Model (CCSM v.1.4)) to study the effect of ocean gateways on global ocean circulation patterns in the Late Oligocene to Early Miocene. Their results in-

dicated that the different configuration of the ocean gateways may have significantly affected the global thermohaline circulation in the Miocene. However, they did not assess any topographic nor vegetation effect. They prescribed a flat land with a constant elevation of 350 m and a zonally constant vegetation distribution. The ocean model that they used furthermore had a flat bottom ocean at 5000 m depth. More recent climate modelling sensitivity experiments have particularly focused on the sensitivity of the Miocene climate to various atmospheric CO₂ concentrations using atmospheric models (TONG et al., 2009; YOU et al., 2009). TONG et al. (2009) used the NCAR Community Atmosphere Model (CAM v.3.1) and Community Land Model (CLM v.3.0) coupled to a slab ocean to examine the sensitivity of the Middle Miocene climate to successive quasi-doubling of atmospheric CO₂ concentration (180, 355 and 700 ppmv). YOU et al. (2009) used the same NCAR models coupled to a slab model to analyse the sensitivity of the MMCO climate to varying ocean heat fluxes derived from palaeo sea surface temperatures and successive quasi-doubling of atmospheric CO₂ concentrations (180, 355 and 700 ppmv) and compared their global temperature estimations to available proxy data. Both studies required higher than present-day CO₂ concentrations to produce a warmer climate at the MMCO. However, TONG et al. (2009) and YOU et al. (2009) also found that the sole increase of CO₂ is not sufficient to produce the MMCO warming inferred from proxy-data. Finally, HEROLD et al. (2009) tested the impact of altered Andean and Tibetan

Plateau elevations on the MMCO climate again with the same NCAR models, and fixed sea surface temperatures. HEROLD et al. (2009) indicated that the reduction of the Tibetan Plateau and Andes elevations significantly affects local temperatures. However, they also concluded that topography alone could not be a significant factor in reconciling the warm MMCO climate and the CO₂ concentration estimates.

The objective of the present study is to examine the contribution of several boundary condition changes to the warm MMCO climate and particularly to discuss the contribution of the vegetation feedback as a potential alternative mechanism to the large increase of CO₂ required by the models to produce a warmer climate at the MMCO. Therefore, we performed a series of simulation experiments with the Planet Simulator, where we have assessed the effects of the absence of ice on the continents, the opening of the Central American and Eastern Tethys Seaways, the lowering of the topography on land and the effect of various atmospheric CO₂ concentrations. We reconstructed the vegetation distribution for the Middle Miocene in response to the MMCO boundary conditions previously cited, using the CARAIB dynamic vegetation model. We then forced the Planet Simulator with the reconstructed Middle Miocene vegetation distribution to assess the vegetation feedback in response to the Middle Miocene simulated climate. We first describe our model setup and examine the response of surface climate (temperature, precipitation and low level winds) to the different forcings. Finally, we discuss the contribution of the factors on

the Middle Miocene climate, focusing in particular on the contribution of vegetation cover changes.

Model and experimental design

The Planet Simulator (FRAEDRICH et al., 2005a,b) is an Earth system Model of Intermediate Complexity (EMIC). It has been used for present-day climate modelling studies (FRAEDRICH et al., 2005b; GROSFELD et al., 2007; JUNGE et al., 2005) as well as for various paleoclimatic studies focusing on different past periods (ROMANOVA et al., 2006; HENROT et al., 2009), notably the late Miocene (MICHEELS et al., 2009b). The model has proven usefulness in the comparison to proxy data (HENROT et al., 2009; MICHEELS et al., 2009a). The Planet Simulator present-day climate compares fairly well to ERA-40 reanalysis although it is affected by two major climatological biases: (1) a cold bias at high latitudes in winter of the hemisphere and (2) a global overestimation of the surface evaporation (HABERKORN et al., 2009). The central component of the Planet Simulator is PUMA-2, a spectral GCM with triangular truncation, based upon the Portable University Model of the Atmosphere, PUMA (FRAEDRICH et al., 1998). PUMA-2 solves the moist primitive equations, representing the conservation of momentum, mass and energy, on σ coordinates in the vertical. It also includes boundary layer, precipitation, interactive clouds and radiation parametrizations. For the present study, we configured it to use a T42 truncation and

ten vertical equally spaced σ levels. The model atmosphere is coupled to a 50 m deep mixed-layer ocean, a thermodynamic sea-ice and a land surface and soil model.

Sea surface temperatures are computed from the net atmospheric heat flux at the surface. The transport of heat by oceanic surface currents is represented by an additional distribution of heat sources and sinks that is prescribed within the mixed-layer and the sea-ice and that varies monthly and spatially. Their distributions for the preindustrial period and the Middle Miocene were determined from preindustrial and Miocene experiments respectively, where sea surface temperature and sea-ice distributions were obtained from simulations with an updated version of the Hamburg LSG circulation model (developed by MAIER-REIMER et al. (1993)) (BUTZIN et al., submitted). This procedure allows the model to respond with a larger sensitivity to boundary condition changes than with prescribed sea-surface temperatures.

The land surface and soil models calculate the surface temperatures from a linearized energy balance equation and predict soil moisture on the basis of a simple bucket model. The influence of vegetation is represented by background albedo, roughness length and rooting depth. Their annual distributions are prescribed, and albedo may only change in grid-cells where snow is present. The distributions of surface albedo, roughness length and rooting depth were obtained from a preindustrial run and a Middle Miocene run of the dynamic vegetation model CARAIB (CARbon

Assimilation In the Biosphere) (OTTO et al., 2002; FRANÇOIS et al., 2006; LAURENT et al., 2008). CARAIB calculates the carbon fluxes between the atmosphere and the terrestrial biosphere and deduces the evolution of carbon pools, together with the relative abundances of a series of plant functional types. Its different modules respectively focus on the hydrological cycle, photosynthesis and stomatal regulation, carbon allocation and biomass growth, heterotrophic respiration and litter and soil carbon, and the distribution of the model plant types, as a function of productivity. Here we use a classification including 15 Plant Functional Types (PFTs), described in UTESCHER et al. (2007) and GALY et al. (2008). Model derived PFT assemblages can be translated into biomes to produce vegetation maps. The inputs of the model are meteorological variables, taken from meteorological databases or GCM simulation experiments.

Experimental setup

In this work we examine the potential contribution of several boundary condition forcings to the MMCO. We therefore perform a series of five sensitivity experiments where we have assessed the effects of the absence of ice on the continents, the opening of the Central American and Eastern Tethys Seaways, the lowering of the topography on land, of various atmospheric CO₂ concentrations and the effect of vegetation cover changes on climate (through surface albedo, roughness length and rooting depth, i. e., bucket size) in response

Table 6.1: Description of the simulation experiments. *P* refers to preindustrial conditions and *M* refers to Miocene conditions. Each one of the five columns corresponds to each of the five modified boundary conditions: ocean heat transfer, ice-sheet cover, atmospheric CO₂ concentration (in ppmv), topography and vegetation cover

Simulation	Ocean	Ice	CO ₂	Topo	Veg
CTRL	<i>P</i>	<i>P</i>	280	<i>P</i>	<i>P</i>
MM1	<i>M</i>	<i>M</i>	280	<i>P</i>	<i>P</i>
MM2	<i>M</i>	<i>M</i>	280	<i>M</i>	<i>P</i>
MM3	<i>M</i>	<i>M</i>	200	<i>M</i>	<i>P</i>
MM4	<i>M</i>	<i>M</i>	500	<i>M</i>	<i>P</i>
MM4-veg	<i>M</i>	<i>M</i>	500	<i>M</i>	<i>M</i>

to the Middle Miocene simulated climate. Table 6.1 lists the boundary condition changes applied for the series of experiments. The control experiment (CTRL) does not consider any of the changes and corresponds to a preindustrial state. All experiments have been run for 50 years and the results shown in Section 6 are means over the last 20 years of simulation, allowing 30 years for the model to equilibrate.

Land ice

According to FLOWER and KENNETT (1994) who place the major growth of the East Antarctic Ice-Sheet around 14.8 to 12.9 Ma (i. e. later than the MMCO), and PEKAR and DECONTO (2006) who suggest that only a reduced East Antarctic Ice-Sheet was present during the Middle Miocene (17 to 16 Ma), we removed ice-sheets from Antarctica and Greenland in the whole series of Miocene experiments. This mainly affects the surface albedo on land. In the absence of ice-sheets in Greenland and Antarctica the surface albedo is set equal to the bare soil value (20%). The conti-

ental land-ice cover for the (preindustrial) control experiment has been derived from Peltier’s ICE-5G (PELTIER, 2004), considering that grid-cells covered by an ice fraction greater than 50% are completely covered by ice.

Ocean and sea-ice

There is currently no global proxy-based SST reconstruction available for the MMCO that could be directly used with GCMs. Furthermore several biases towards notably colder temperatures have been detected in the oxygen isotope palaeo SST estimates (PEARSON et al., 2007). WILLIAMS et al. (2005) also suggested that the Miocene tropical sea surface temperatures may be underestimated in the current reconstructions, due notably to diagenesis. We therefore preferred to use as initial conditions over ocean grid points sea-surface temperature and sea-ice distributions derived from simulations of the updated Hamburg LSG circulation model, which includes a simple atmospheric energy balance model permitting that the LSG SSTs freely adjust to ocean

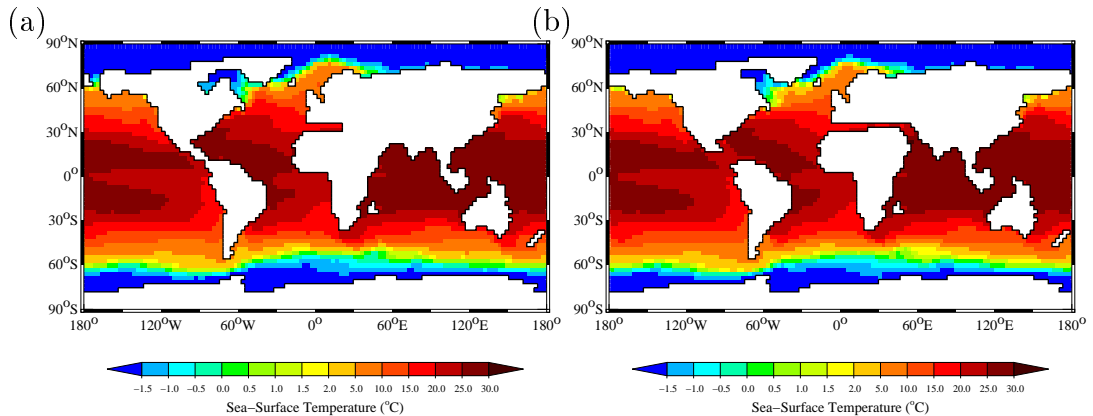


Figure 6.1: Initial sea-surface temperatures for (a) the CTRL experiment and (b) the Miocene experiments. Grid elements with a temperature below -1.5°C are covered by sea-ice.

circulation changes (BUTZIN et al., submitted). BUTZIN et al. (submitted) performed several simulation experiments to assess the sensitivity of benthic carbon isotope records to various seaway configurations and sea-ice scenarios. In this work, we use as initial oceanic conditions for all the Miocene simulation experiments the sea-surface temperature and sea-ice distributions from one LSG simulation featuring open Central American and Eastern Tethys Seaways, a filled Hudson Bay and a closed Bering Strait, according to GLADENKOV et al. (2002), a fixed atmospheric CO_2 concentration of 282 ppmv, and sea ice extent around 90% of the present-day value. Preindustrial LSG results were also used to derive the preindustrial sea-surface temperature and sea-ice distributions for the control run of our series. The LSG Miocene run's spinup is 10,000 years long and the LSG sea-surface temperatures and sea-ice cover used here as initial conditions are means

over the last 50 years of simulation. The LSG sea-surface temperature and sea-ice cover for the preindustrial and the Miocene are shown in Figure 6.1. In the Miocene LSG simulation, the opening of the Central American Seaway freshened the upper part of North Atlantic while salinities increased in the other oceans. The Meridional Overturning Circulation (MOC) in the Atlantic Ocean weakened. As a consequence, the upper North Atlantic got cooler and the South Atlantic warmer. The Eastern Tethys Seaway weakly impacted on Indian Ocean heat transport (BUTZIN et al., submitted). The impact of a closed Bering Strait is more convoluted (the Bering Strait first opened in the Late Miocene at about 5.4-5.3 Ma (GLADENKOV et al., 2002)). A closed Bering Strait may reinforce the impact of the open Central American Seaway. An open Bering Strait in a Late Miocene LSG sensitivity experiment mitigated the effect of the open Central American Seaway, be-

cause of a freshwater export from the Arctic Ocean into the North Pacific via the Bering Strait (unpublished results). The water flux through the open Bering Strait in the Miocene LSG experiment is opposite to the present-day water flux from the North Pacific to the Arctic Ocean, which is in line with results of fully coupled freshwater perturbation experiments under present-day conditions (OKUMURA et al., 2009).

The slab model included in the Planet Simulator precludes the interactive calculation of circulation changes. Therefore, we prescribed the oceanic heat flux distributions for the preindustrial (used for the CTRL experiment) and the Middle Miocene (used for the Miocene experiments). The preindustrial oceanic heat flux distribution was calculated from a preindustrial experiment forced with the same boundary conditions as the experiment CTRL, but fixed sea-surface temperatures and sea-ice cover derived from the LSG preindustrial experiment. The differences between the sea surface temperatures calculated by the model and the ones prescribed determined the oceanic heat flux adjustments to apply to ocean grid-cells in order to mimic the heat transport by ocean currents at preindustrial. The same procedure was applied under Miocene boundary conditions used for experiment MM1 to obtain the oceanic heat flux distribution for the Middle Miocene. The oceanic heat fluxes obtained are shown in Figure 6.2. The distribution of Miocene oceanic heat fluxes shows a weakening of the surface heat transfer to the North Atlantic due to the opening of the Central American Seaway, but an increase of the heat transfer

to the South Atlantic. However, besides the reorganization of heat transfer in the Atlantic Ocean, the distribution of the surface heat fluxes at the Miocene does not differ much from the preindustrial distribution.

Land-sea distribution and topography

The use of LSG sea-surface temperatures as initial oceanic conditions imposed us to stick to the land-sea distribution and corresponding topography prescribed in the LSG experiments (BUTZIN et al., submitted). The control experiment was therefore forced with the present-day LSG land-sea mask and topography, whereas the Miocene experiments were forced with the Miocene LSG land-sea mask which takes into account an open Central American Seaway, an open Eastern Tethys Seaway, a filled Hudson Bay and a closed Bering Strait as stated above (see Figure 6.3). However, the Miocene LSG simulations consider a present-day topography on land. It is thought that elevation on land was globally lower during the Miocene (RUDDIMAN, 1997; HARRIS, 2006; GREGORY-WODZICKI, 2000). We therefore applied the algorithm described in KUTZBACH et al. (1989) in order to reconstruct a topography approximatively at half-height of its modern elevation.

$$h = 400 \text{ m} + (h_0 - 400 \text{ m}) / 2$$

where $h_0 \geq 400 \text{ m}$

h_0 corresponds to the preindustrial topography and h to the Miocene lowered topography. That algorithm halves the elevation only above a base level of 400 m to approximate a geologic situation in which some continental relief

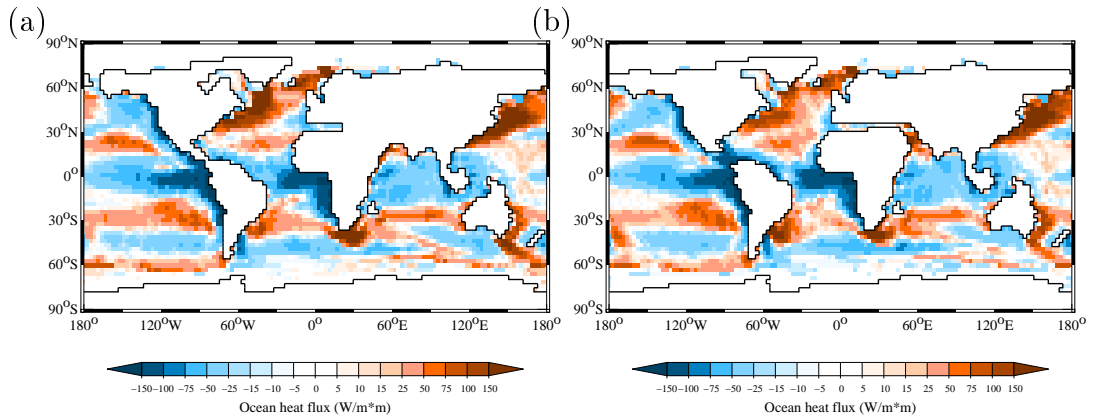


Figure 6.2: Oceanic surface heat transfer for (a) the CTRL configuration and (b) the Miocene configuration. Positive values indicate a net transfer of heat from the ocean to the atmosphere.

was present prior to geologically recent uplift (KUTZBACH et al., 1989). The present-day and Miocene land-sea mask and topography are shown on Figure 6.3. A more precise study would have used the recent Middle Miocene paleotopographic reconstruction by HEROLD et al. (2008), geographically constrained at 15 Ma. Unfortunately, the LSG land-sea distribution is incompatible with the paleogeography of HEROLD et al. (2008), especially regarding ocean gateways, which are central to the present study. Nevertheless, our Miocene adapted topography agrees fairly well with the reconstruction of HEROLD et al. (2008), given the model resolution. The elevations of the North American, European and African reliefs are comparable to the ones reported in HEROLD et al. (2008). However, the maximum elevation of the Tibetan Plateau is limited to 3500 m in our reconstruction, whereas HEROLD et al. (2008) constrained it to 4700 m. On the contrary, the Andes are around

500 m higher in our Miocene topography. Nevertheless, the differences between both topography reconstructions remain within the paleoelevation data errors for the Tibetan Plateau (CURRIE et al., 2005; WANG et al., 2006) and the Andes (GREGORY-WODZICKI, 2000).

Vegetation cover

Surface boundary condition parameters controlled by the vegetation cover (surface albedo, roughness length and rooting depth) have been derived from equilibrium runs of the CARAIB model. The surface albedo, roughness length and rooting depth of the land grid-cells are calculated from the PFT abundances and specific albedo, roughness length and rooting depth values attributed to each PFT. To obtain the preindustrial vegetation parameters, we performed an equilibrium run of CARAIB, forced with 280 ppmv of CO_2 and the climatology of NEW et al. (2002). All of the experiments were forced with the preindustrial

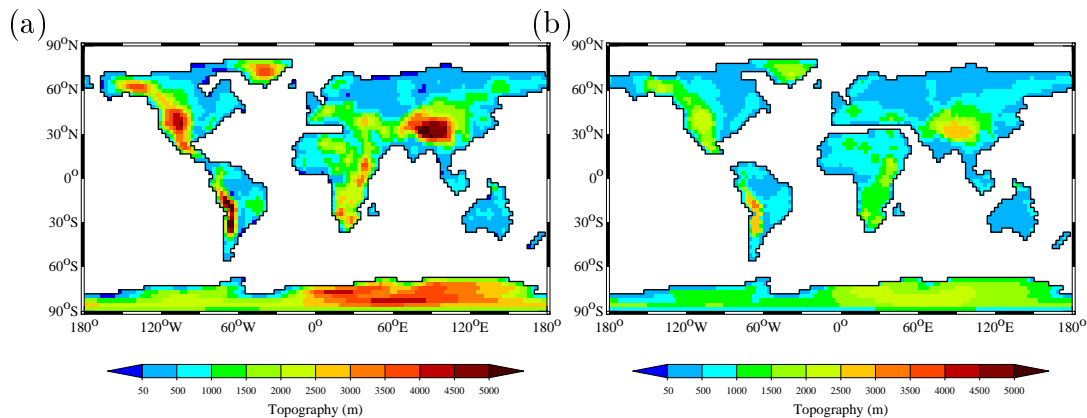


Figure 6.3: Land-sea mask and topography on land for (a) the CTRL configuration and (b) the Miocene configuration.

vegetation parameters except for experiment MM4-veg. In experiment MM4-veg, the vegetation parameters were replaced by their Middle Miocene distributions derived from an equilibrium run of CARAIB forced with 500 ppmv of CO_2 in the atmosphere and the climate from the experiment MM4, which is the warmest and most humid of the series and in best agreement with proxy-based climate reconstructions (see Section 6). We used the anomalies of the GCM climatic fields between the Middle Miocene (experiment MM4) and the preindustrial (experiment CTRL), added to the climatology of NEW et al. (2002), as climatic inputs for the Middle Miocene CARAIB simulation, following the approach described in OTTO et al. (2002). The vegetation parameters of the emerging land-points from the Miocene land-sea distribution were extrapolated from the vegetation parameters of the nearby land-points, using an inverse distance weighted average procedure.

Atmospheric CO_2 concentration

We forced our simulations with various atmospheric CO_2 concentrations. The control experiment, as well as the first Miocene simulation experiments MM1 and MM2 used a preindustrial CO_2 level of 280 ppmv. In experiment MM3 the CO_2 concentration was set to 200 ppmv. 200 ppmv is within the range given by marine isotopic reconstructions suggesting low and constant CO_2 levels throughout the Miocene (PAGANI et al., 1999; HENDERIKS and PAGANI, 1999; PAGANI, 2008; PEARSON and PALMER, 2000). For experiment MM4 we adopted a value of 500 ppmv to test the hypothesis of high CO_2 levels during the Miocene suggested by terrestrial proxies (KÜRSCHNER et al., 2008; RETALLACK, 2009).

Orbital configuration

As we refer for the MMCO to a time span of about two million years integrated over several orbital cycles, we applied a present-day orbital configuration

Table 6.2: Global, continental and oceanic annual mean near-surface temperature T_{2m} ($^{\circ}\text{C}$) and precipitation (mm/yr) anomalies for the five Middle Miocene simulation experiments. The continental mean excludes the contribution from Antarctica since strong warming can be attributed due to the absence of ice that is not representative of the other effects on the continents. All results reported here are global means over the last 20 years of 50-year simulations, allowing 30 years for the model to equilibrate. The CTRL absolute values are shown for reference.

	T_{2m} ($^{\circ}\text{C}$)			Prc (mm/yr)		
	<i>Global</i>	<i>Ocean</i>	<i>Continent</i>	<i>Global</i>	<i>Ocean</i>	<i>Continent</i>
CTRL	12.3	15.3	11.6	1022	1138	803
<i>Anomalies</i> (EXPERIMENT-CTRL)						
MM1	+0.6	+0.5	-0.2	-5	+6	-38
MM2	+0.3	-0.5	+0.8	+20	+8	+38
MM3	-1.5	-2.1	-1	-14	-36	+28
MM4	+2.9	+2	+3.7	+73	+70	+85
MM4-veg	+3.4	+2.4	+4.3	+92	+74	+143

(eccentricity 0.016724, obliquity 23.446° and longitude of perihelion 102.04°) and solar constant (1365 W/m²) for the whole series of experiments. To test the potential effect of such a warm orbital configuration on the MMCO climate we performed an additional experiment where we applied a cold LGM orbital configuration (eccentricity 0.018994°, obliquity 22.949°, longitude of perihelion 114.42° and present-day solar constant) under MMCO boundary conditions similar to those in experiment MM4. The "cold" orbital configuration induced a global temperature decrease of -0.1°C in comparison to the "warm" present-day one, and essentially affected the oceanic grid-cells at high latitudes, due to the response of sea-ice to the reduction of insolation in winter. Because of this low sensitivity of the model to orbital forcing, we kept the present-day orbital configuration for the whole series of experiments.

Results

Experiment MM1: surface ocean and ice-sheet boundary conditions

Experiment MM1 shows a global temperature increase of +0.6°C (see Table 6.2) that is mainly due to oceanic warming and Antarctic and Greenland warming in the absence of land-ice, whereas the temperatures and precipitation on other continents decrease. The zonal averages of surface air temperature (SAT) and precipitation are shown in Figure 6.4. The zonal average temperature and precipitation anomalies (MM1 -

CTRL) are also shown in Figure 6.5 to allow a finer comparison. The MM1 zonal temperature averages do not indicate large differences from the control experiment at any latitude, except at high latitudes of both hemispheres. The warming at high latitudes linked to an increase of precipitation is due to the absence of ice on land.

Figure 6.6 shows the annual mean surface air temperature (SAT) and precipitation anomalies between experiment MM1 and the control run CTRL. Large increases of the surface air temperature occur over Greenland and especially Antarctica. The absence of ice on Antarctica and Greenland strongly decreases the surface albedo that induces large warming and a decrease of the snow cover, leading to a positive albedo feedback during summer in each Hemisphere (not shown). However, in winter the influence of surrounding colder oceanic air masses induces a net cooling of about -1°C over Greenland. Large precipitation disruptions occur in the tropics and sub-tropics as well as over the North Atlantic Ocean.

Significant changes in surface air temperature as well as in precipitation are obtained especially over the oceans. These are a consequence of the sea surface temperature modification in response to ocean circulation changes in the Miocene LSG simulation. The reduction of the heat transfer to the North Atlantic leads to large decreases of SAT in that region. Colder and drier conditions are obtained along the south-west coast of North America but the strongest decrease of SAT, of up to -6°C, occurs in the North Atlantic, along the south

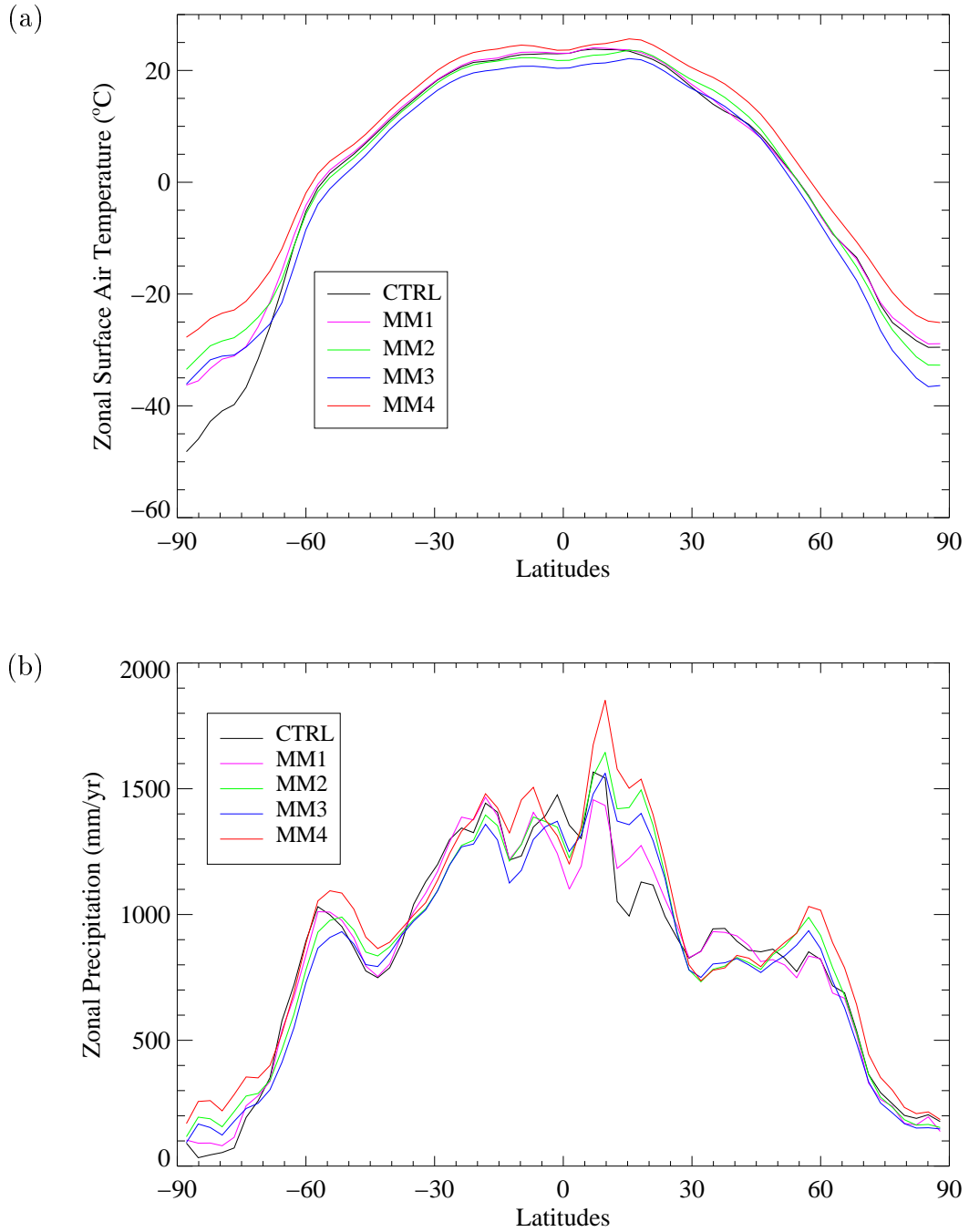


Figure 6.4: Zonal average (a) surface air temperature (°C) and (b) precipitation (mm/yr) for the series of simulation experiments MM1 to MM4.

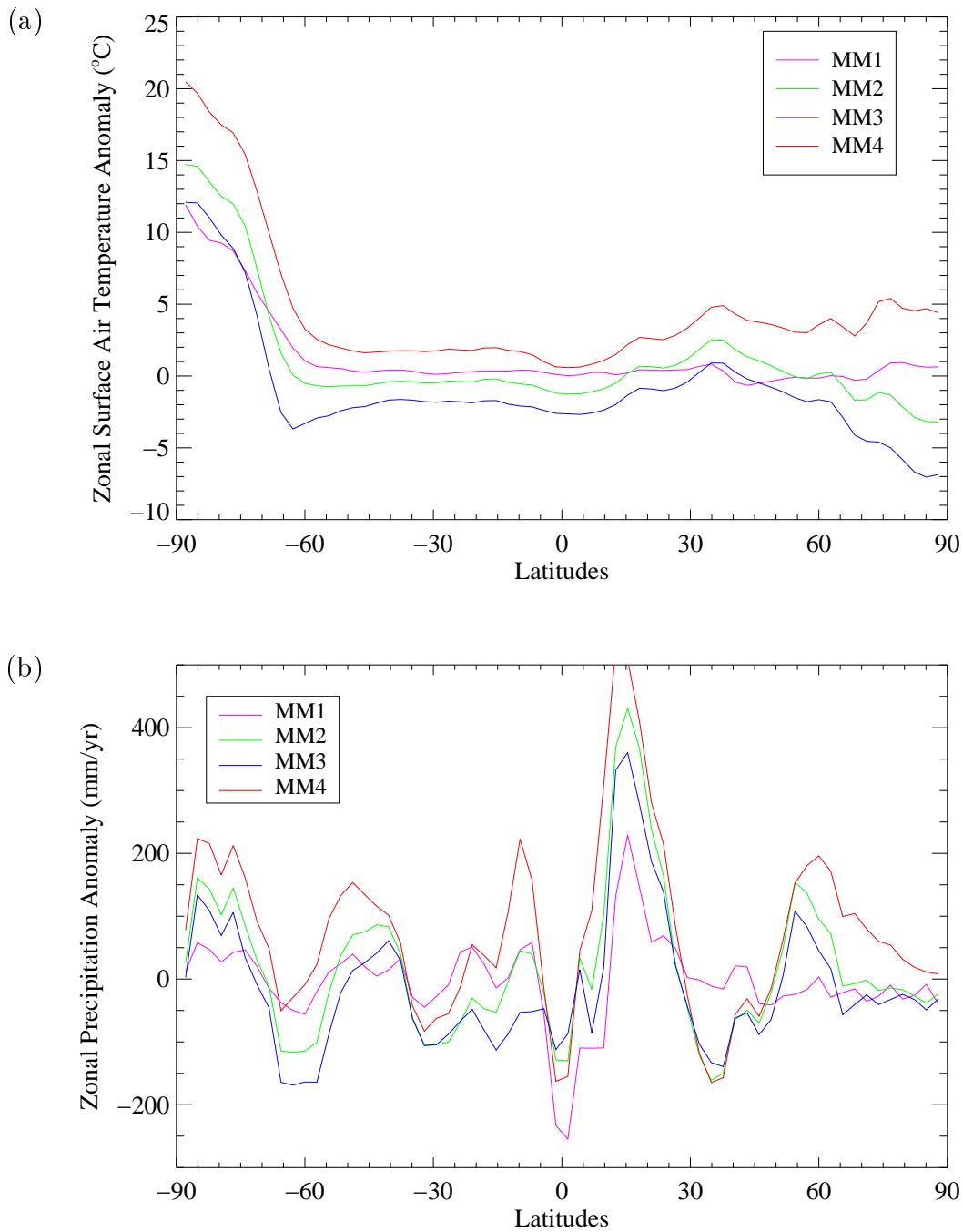


Figure 6.5: Zonal average (a) surface air temperature anomalies (°C) and (b) precipitation anomalies (mm/yr) for the series of Middle Miocene simulation experiments MM1 to MM4.

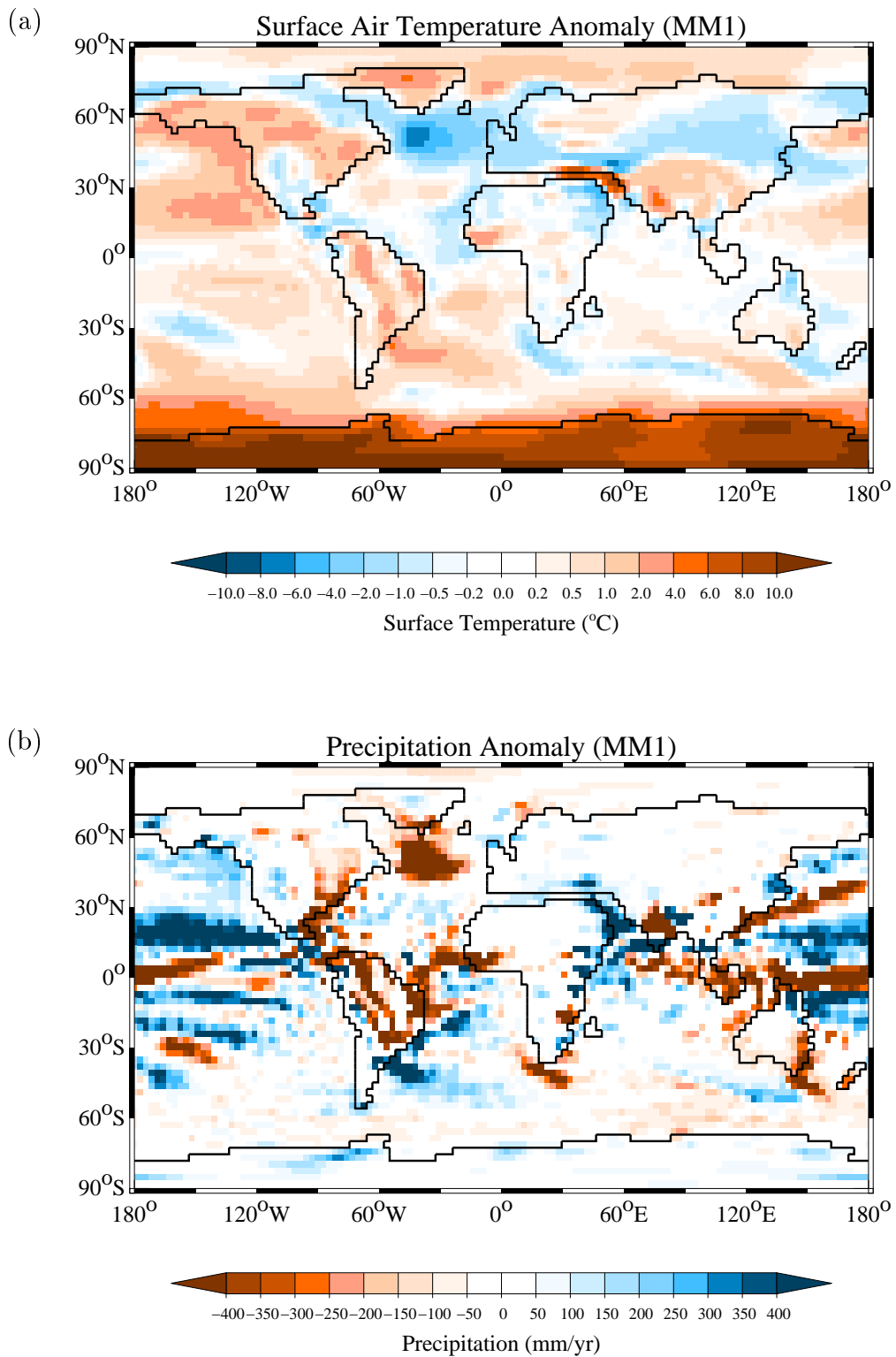


Figure 6.6: (a) Annual mean surface temperature and (b) precipitation anomalies (MM1-minus-CTRL) for experiment MM1. Only the precipitation anomalies greater than one standard deviation for the long-term annual mean over the last 20 simulation years are shown.

coast of Greenland. This region also experiences a large decrease of precipitation linked to the cooling of the air masses. The colder conditions over the North Atlantic induce continental temperature decreases together with precipitation increases, notably over north-western Europe and Africa in winter. However, the decrease of precipitation of about -400 mm/yr over the northern part of South America and the east coast of North America, linked to a decrease of surface evaporation, leads to a surface temperature increase of more than 1°C .

The opening of the Central American Seaway and the closure of the Bering Strait, which inhibits the influx of fresh and cold water from the Arctic Ocean into the Pacific induces warming in the North Pacific, reaching $+4^{\circ}\text{C}$ along the west coast of North America together with a precipitation increase. This brings warmer and more humid air masses from the west to the centre of North America and warmer air masses to the east after the passage of the high North American reliefs.

The opening of the Eastern Tethys Seaway influences the SAT in Central Asia and East Africa. A strong increase of SAT is obtained over the Tethys Seaway and is linked to the decrease of surface albedo and the large reduction of topography over the region due to the opening of the seaway. Precipitation is also strongly increased over the open seaway. As mentioned before, the opening of the Eastern Tethys Seaway weakly impacts on Indian Ocean heat transport. The western part of the Indian Ocean does not show any significant changes in

SAT when compared to the CTRL experiment. The land points surrounding the open seaway experience colder conditions, except in the Indian peninsula. The SAT decreases can be attributed to the more humid conditions that prevails in the presence of an open Tethys Seaway. However, since precipitation is strongly decreased in India during summer, the warming in this region can be linked to a reduced monsoon activity in presence of an open Eastern Tethys Seaway. Strong decreases of precipitation also occur in Indonesia and South-East China, suggesting a reduced monsoon activity in these regions too. Finally, the SAT cools by about -2°C in eastern Russia, extending the cooling trend over Europe to the east.

Experiment MM2: topography

The reduction of the topography in experiment MM2 generates the weakest effect in magnitude on global temperature in our series of experiments. It causes a global mean cooling of -0.3°C relative to experiment MM1, if we assume that the topographic and oceanic boundary conditions effects are independent of each other. However, the reduction of the topography significantly increases precipitation, especially on the continents (see Table 6.2). The lowering of the topography leads to a global decrease of temperature over the oceans whereas it leads to an increase of temperature over the continents. These opposite temperature effects over the oceans and continents can be explained by the conservation of the mass of the atmosphere in our model. The lowering

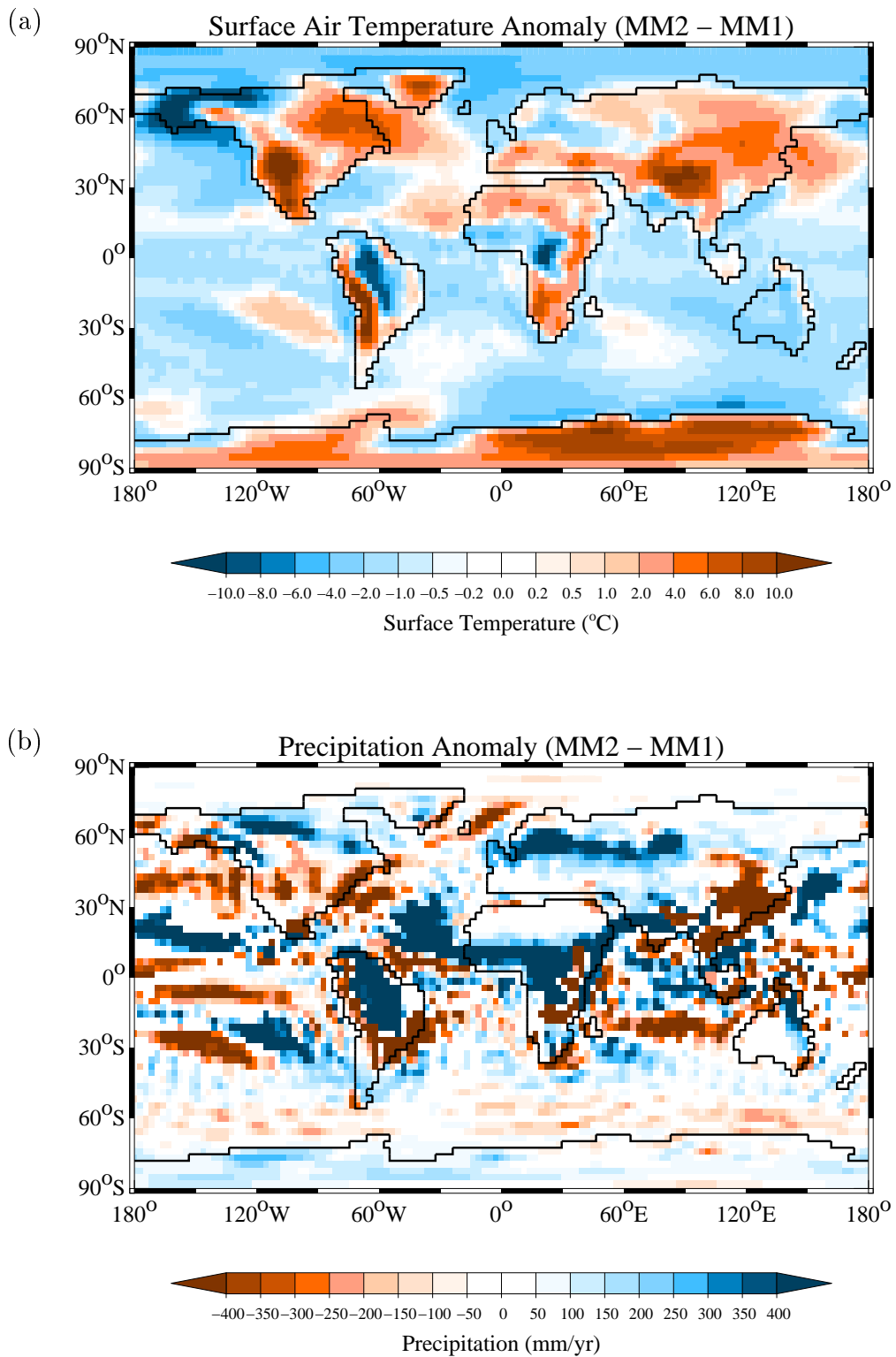


Figure 6.7: (a) Annual mean surface temperature and (b) precipitation anomalies between experiments MM2 and MM1. Only the precipitation anomalies greater than one standard deviation for the long-term annual mean over the last 20 simulation years are shown.

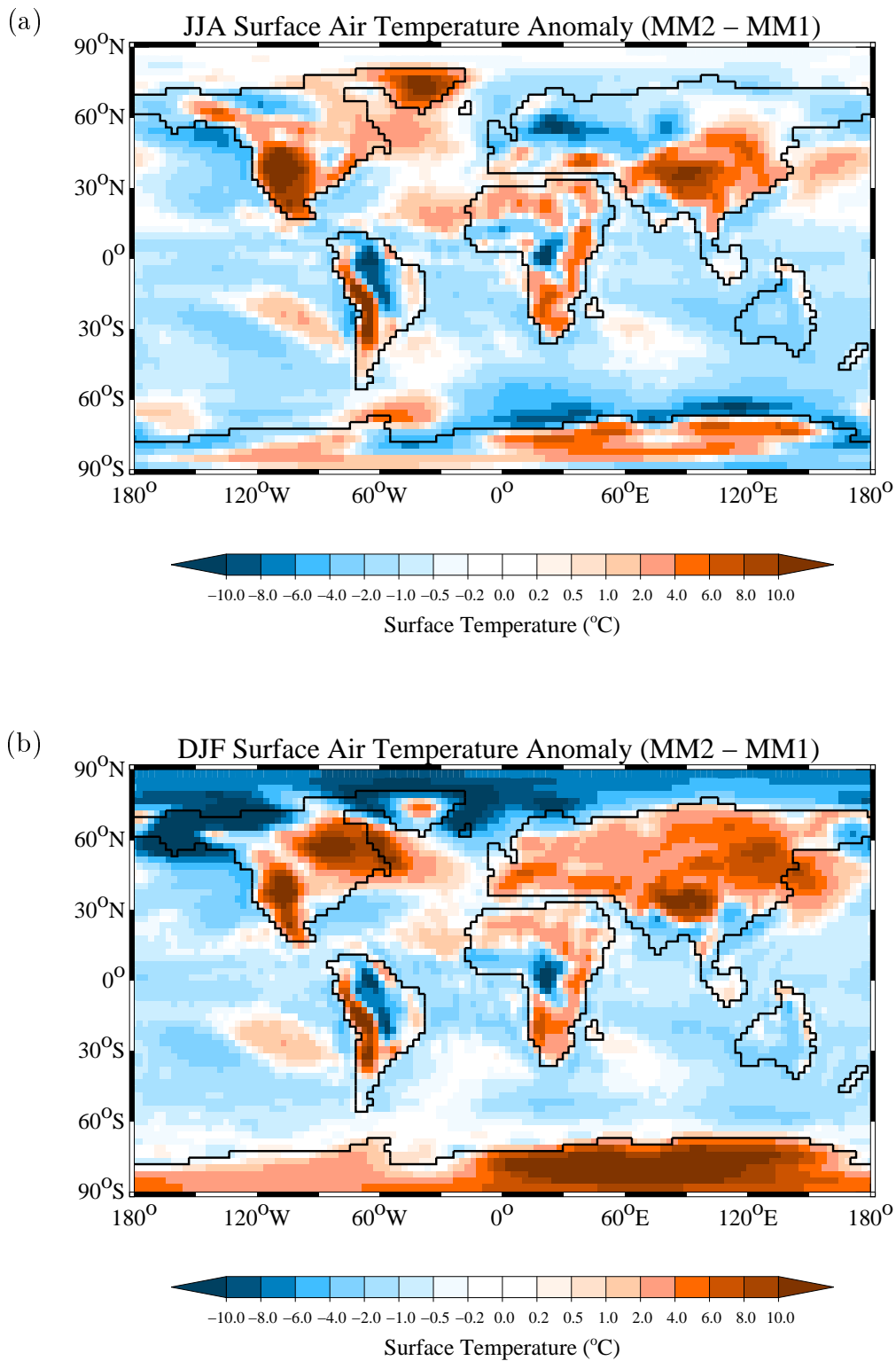


Figure 6.8: Surface air temperature anomalies in (a) Northern Hemisphere summer (JJA) and (b) Northern Hemisphere winter (DJF) between experiments MM2 and MM1.

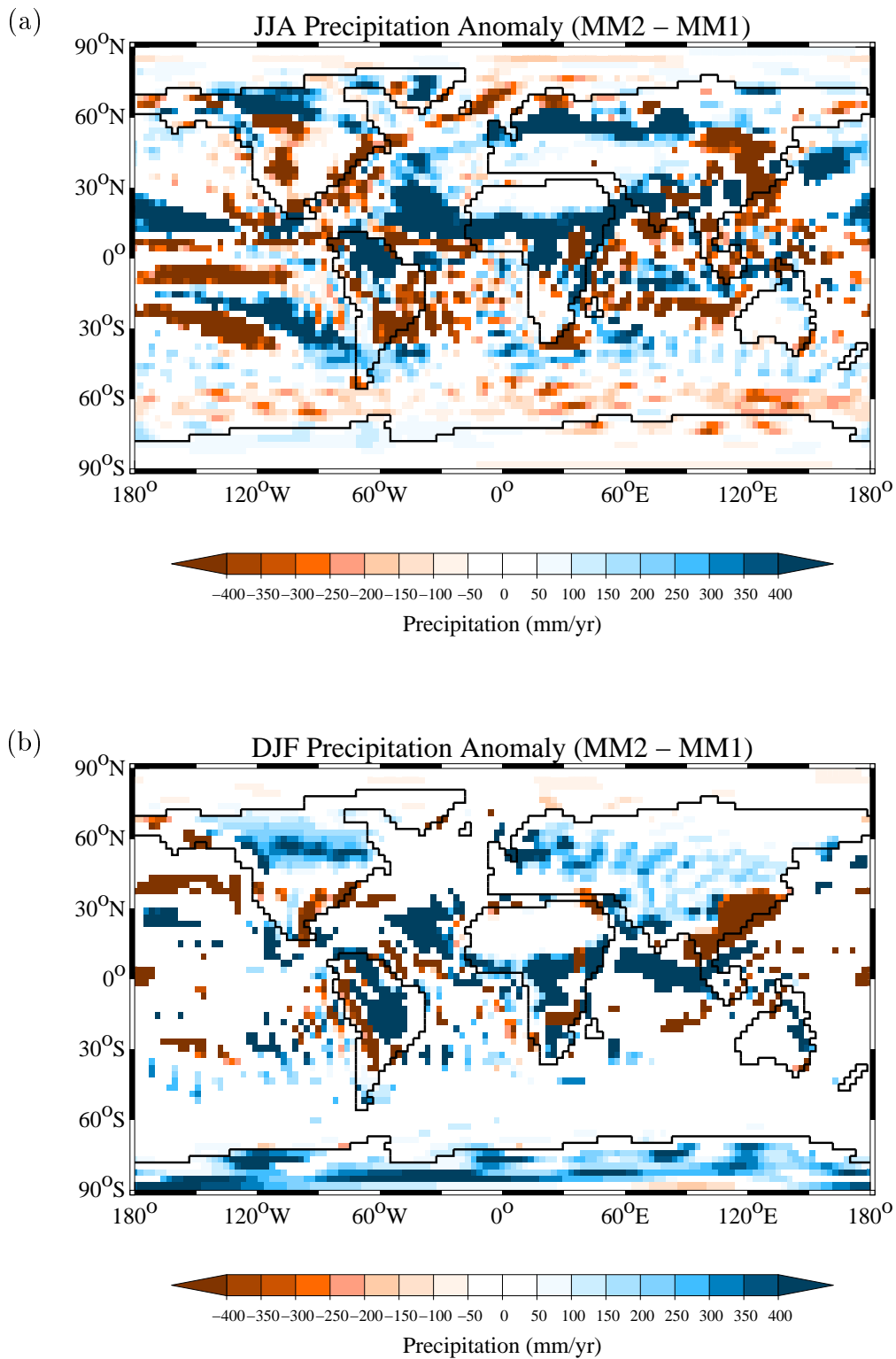


Figure 6.9: Precipitation anomalies in (a) Northern Hemisphere summer (JJA) and (b) Northern Hemisphere winter (DJF) between experiments MM2 and MM1.

of the topography induces a surface pressure increase on land that leads to a surface pressure decrease over the oceans that in turn cools the oceans. Nevertheless, local surface pressure changes occur due to the displacement of high/low pressure cells in response to topography reduction. The lowering of the topography also produces localized warming, notably over Antarctica and around 30°N over the lowered reliefs. However, it decreases the temperatures at latitudes higher than 60°N (see Figure 6.4). The lowering also decreases precipitation around 30°N but strongly increases precipitation especially in the tropics around the ITCZ (see Figure 6.5).

As shown in Figure 6.7, strong and localized warming occurs in the location of the present-day high reliefs that are directly affected by the largest topography reduction. Altitude reductions of more than 1000 m in some areas increase the annual mean SAT by more than +10°C, e.g., in some parts of the Tibetan Plateau, the Andes, the Rockies, Greenland and Antarctica. In contrast to the continental warming, the SAT decreases over the oceans. The topography reduction also strongly disturbs the annual precipitation anomaly distribution on the continents (see Figure 6.7). The anomalies show large differences when compared to the anomalies in experiment MM1. northern and western Europe experience a SAT decrease that extends to the east. The annual anomaly essentially reflects the colder conditions that affect Eurasia in summer, whereas warmer conditions prevail in winter (see Figure 6.8). Precipitation also strongly increases over northern Europe especially in summer (see Figure 6.9). As il-

lustrated in Figures 6.10 and 6.11, showing respectively the summer and winter low-level winds (850 hPa) for experiments CTRL and MM2, seasonal effects can be due to a more zonal atmospheric surface circulation in the presence of lower reliefs. Therefore stronger and more direct winds from the North Atlantic flow across Europe and penetrate deeper into the continent, bringing more humid and colder conditions in summer and more humid and warmer conditions in winter, weakening the seasonal contrast of temperature and precipitation over Europe. This strong effect of the lower reliefs on the precipitation distribution in northern Europe is discussed in more detail in section 6. Westerly winds coming from the North American continent instead of the Labrador Sea also flow over the North Atlantic, decreasing the activity of the Iceland low pressure cell. However, the southern part of Europe experiences an increase of SAT that is linked to the reduction of topography in the Alps and other reliefs, inducing local warming that dominates over the other effects. Furthermore, this warming can be reinforced in winter by a decrease of snowfall, resulting from the positive snow albedo feedback.

North America is affected by warming of more than +2°C that persists throughout the year. A precipitation increase in the North is induced by the direct contribution of humid air masses from the North Pacific especially in winter. In the absence of high reliefs, the winds flow directly to the west coast of North America and do not supply Alaska with humid air masses anymore. The isolation of the Alaska region leads to colder and drier conditions there in win-

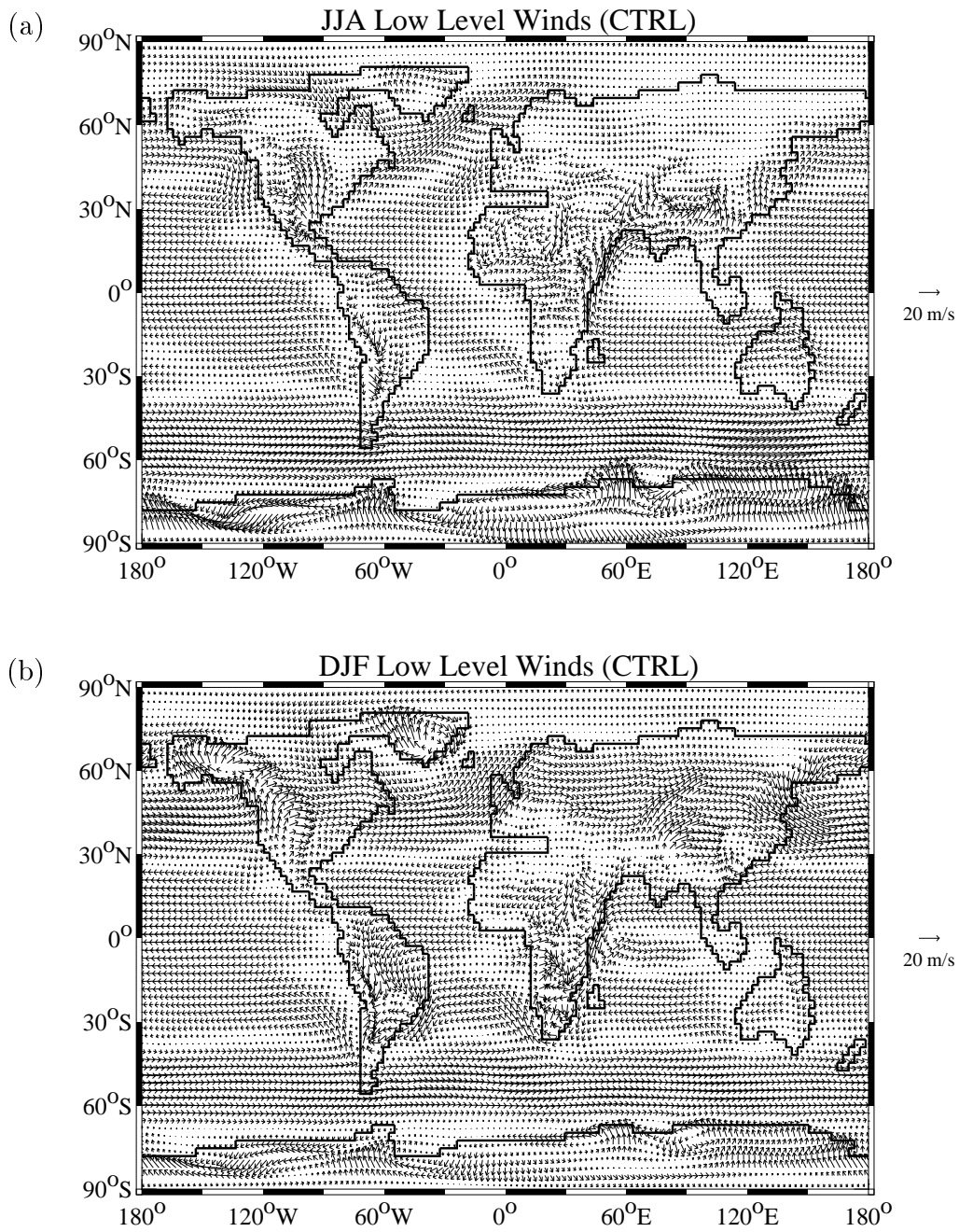


Figure 6.10: Low-level winds (850 hPa) for the CTRL experiment in (a) Northern Hemisphere summer and (b) Northern Hemisphere winter.

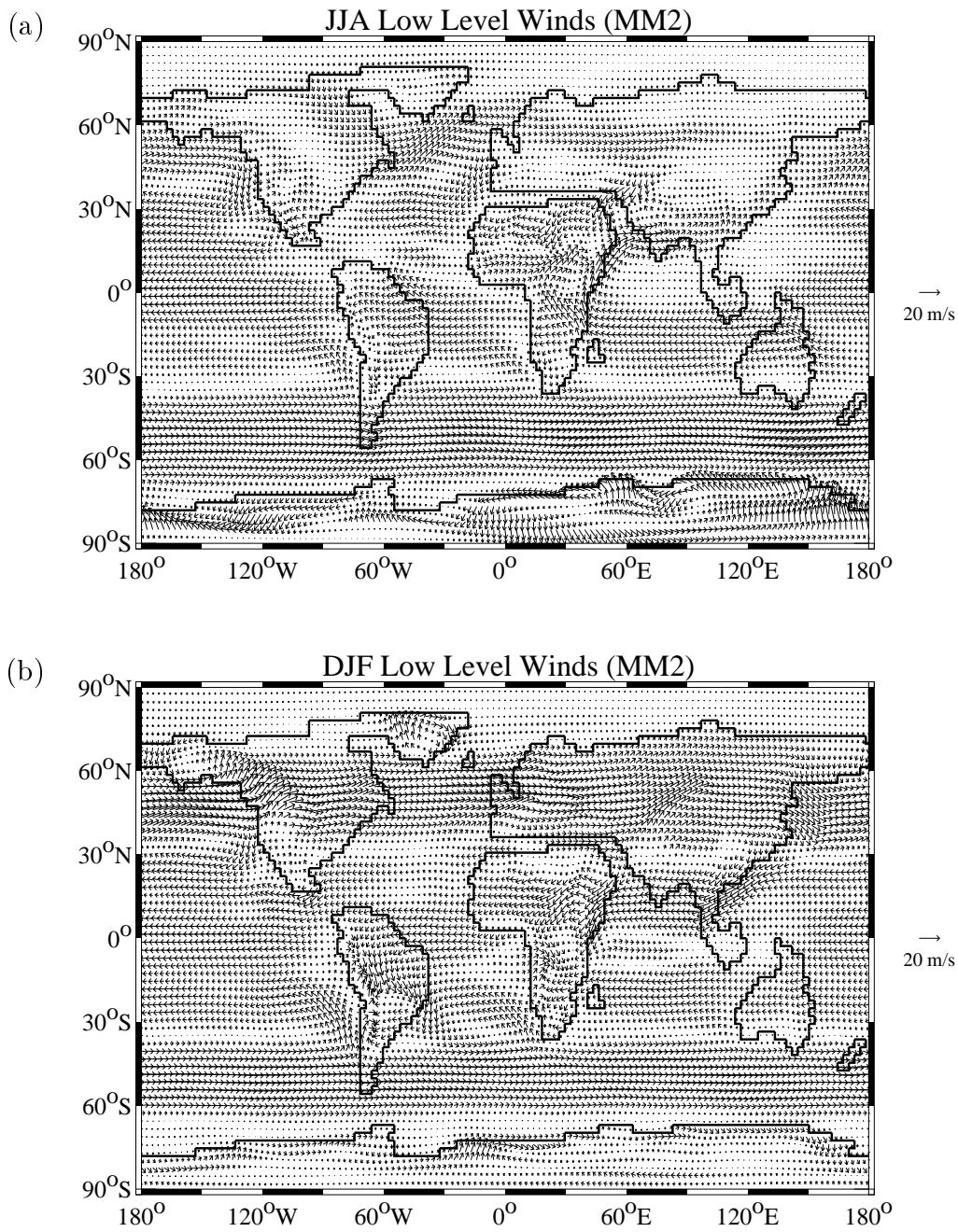


Figure 6.11: Low-level winds (850 hPa) for the MM2 experiment in (a) Northern Hemisphere summer and (b) Northern Hemisphere winter.

ter. The more zonal atmospheric surface circulation also contributes to isolate the Arctic Ocean that experiences strong winter cooling. In the Centre of North America, the lower Rockies also weaken the frontal zone activity in summer between air masses coming from the west and the east. This leads to a decrease of surface evaporation that decreases precipitation in summer and contributes to warm the region.

The decrease of the height of the Tibetan Plateau also produces large seasonal impacts. SAT increases for the whole year over China and eastern Russia, but decreases over India, Indonesia and Australia. As expected, a lower Tibetan Plateau contributes to weaken the Asian monsoon activity, which is characterized by a decrease of precipitation in summer. The summer precipitation also decreases in Indonesia and the eastern Equatorial Pacific, where the surface winds weaken. North-East China gets drier during the whole year, due to a strengthening of the continental winds coming from the north-east in winter, but a decrease of the south-east winds in summer, which bring less humidity.

Africa is affected by an increase of SAT that can be directly attributed to the topographic reduction in the north and the south-east. However, SAT decreases in West and Central Africa. This last effect comes together with a strong increase of precipitation, that can be attributed to the deeper penetration of westerly winds from the Atlantic together with a deeper penetration of north-easterly winds, which come from the moist region of the open Eastern Tethys Seaway. The northern part of

South America also experiences a decrease of SAT together with a strong increase of precipitation.

Effects of the topography on precipitation in Europe

The lowering of the high reliefs leads to a strong increase of precipitation together with a SAT decrease from north-western to northeastern Europe. This is essentially a summer effect and is linked to a modification of the summer surface wind strength and direction. In order to determine the single most important topography change responsible for the precipitation disruption in Europe, we carry out several variants of experiment MM2, lowering separately and together the North American and European reliefs. We run three additional sensitivity experiments, reducing the topography in Europe (between 15°W and 30°E and 25°N to 75°N—experiment MM2-E), in North America (between 165°W and 60°W and 15°N to 75°N—experiment MM2-A) and both together (experiment MM2-AE). We only lower the North American and European reliefs for this series of tests. The other reliefs are held at their respective present-day elevations.

The disruption of summer precipitation and the summer winds at 850 hPa in the absence of European reliefs are shown in Figure 6.12. The lower reliefs in North Europe allow stronger westerly winds that come more directly from the Atlantic Ocean to penetrate deeper into the continent, bringing more humid and cold oceanic air masses to northern Europe. Nevertheless, the lowering of the North European reliefs alone is not sufficient to form the wet tongue that we

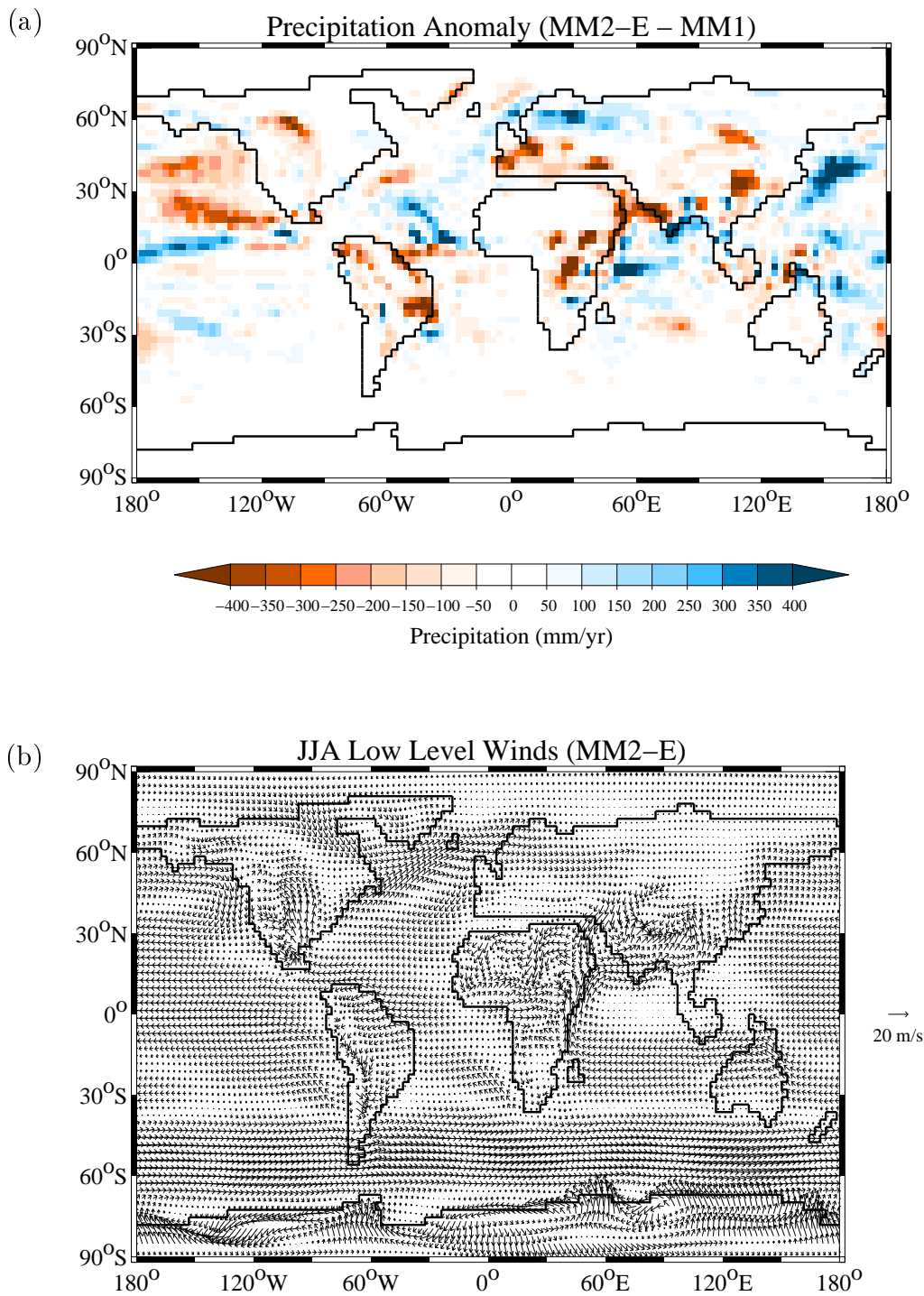


Figure 6.12: (a) Annual mean precipitation anomalies (MM2-E - MM1) and (b) Northern Hemisphere summer low-level winds (850 hPa) for experiment MM2-E that considers a reduced topography only in Europe.

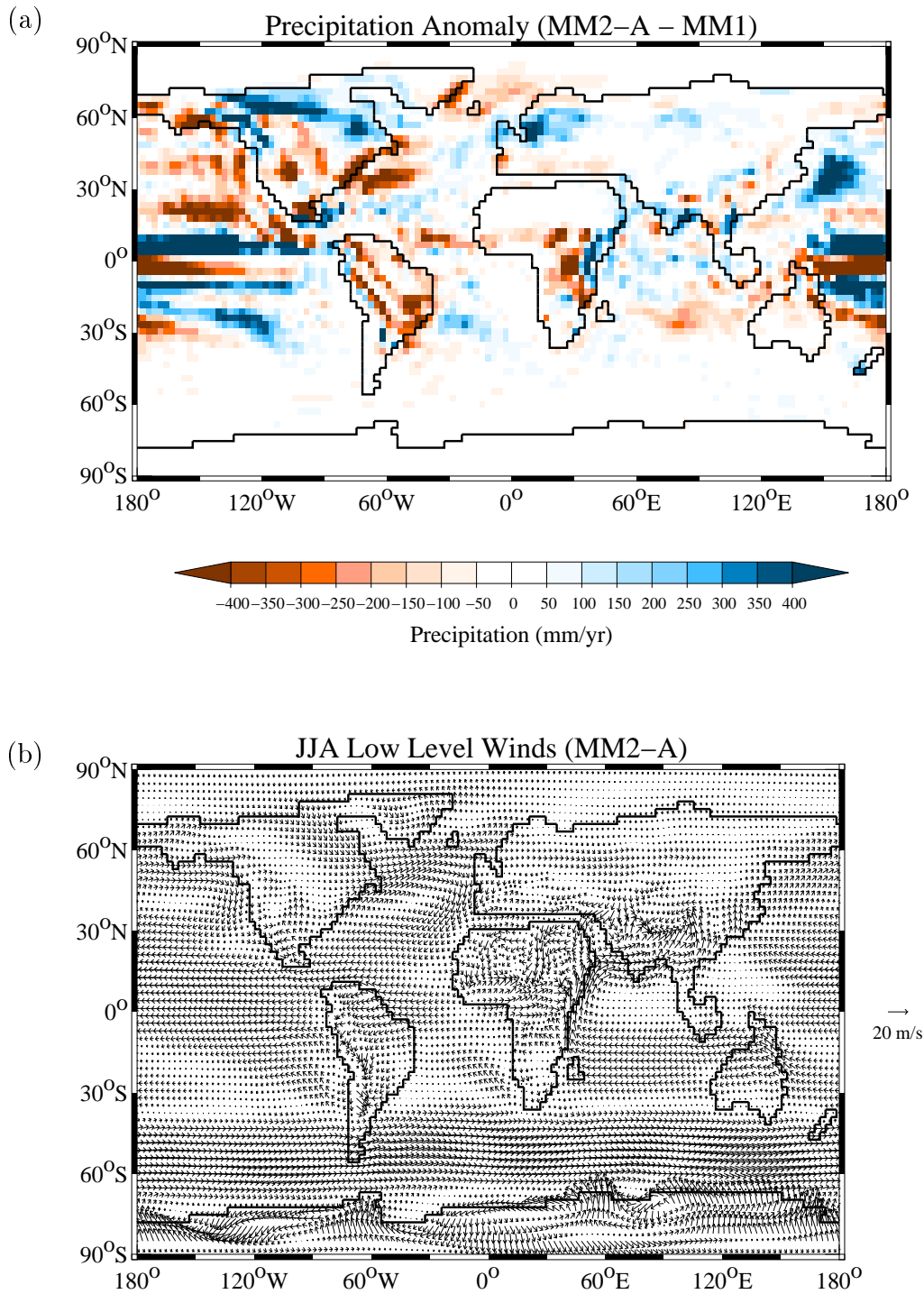


Figure 6.13: Same as Figure 6.12 for experiment MM2-A that considers a reduced topography only in North America.

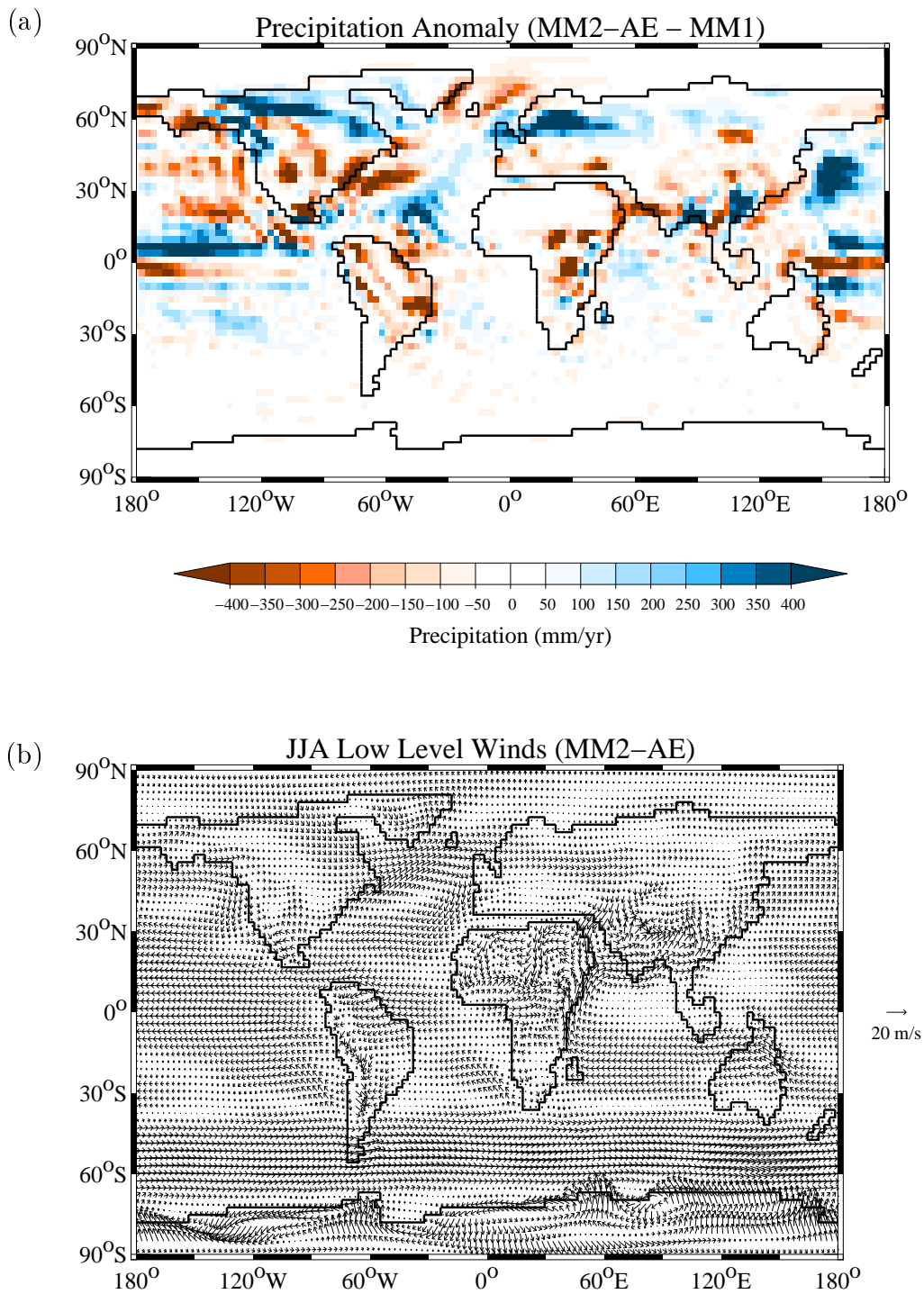


Figure 6.14: Same as Figure 6.12 for experiment MM2-AE that considers a reduced topography only in North America and in Europe.

obtained in experiment MM2. The lowering of the North American reliefs also produces stronger and more direct summer westerly winds in northwestern Europe, generating more precipitation in the region (see Figure 6.13). However the presence of the North European reliefs stops the wetter air masses coming from the west, and does not allow the wet tongue obtained in experiment MM2 to form neither. Precipitation increases in northwestern Europe similar in terms of magnitude to those found in experiment MM2 are only obtained when the effects of European and North American topography changes are combined (Figure 6.14). We also perform additional sensitivity experiments testing separately the effects of the lowering of the Tibetan Plateau, African reliefs and South American reliefs on the precipitation distribution in Europe. Effects on European precipitation and teleconnections found in these later experiments are rather weak (not shown). We conclude that the reduction of topography in North America and Europe is necessary to produce the colder and wetter conditions that prevail in North Europe in experiment MM2. However, the wet tongue does not extend to the east as far as it does in experiment MM2. We can therefore attribute the increase of precipitation in North West Asia to the reduction of the topography in Asia.

Experiment MM3: low CO₂

The lowering of the atmospheric CO₂ concentration in experiment MM3 produces a global cooling together with a precipitation reduction (see Table 6.2). The reduction of atmospheric CO₂ also

reinforces the general cooling trend and decreases the precipitation at all latitudes as compared to the results of experiment MM2 (see Figure 6.4). However, it does not disrupt the zonal profiles of SAT and precipitation. The surface air temperature and precipitation anomalies between experiments MM3 and MM2 are shown in Figure 6.15. The 80 ppmv lowering of the CO₂ concentration induces a rather uniform temperature cooling of about -2°C. The magnitude of the cooling is similar over continents and oceans, and in both Northern and Southern Hemispheres. Stronger cooling occurs at high latitudes, especially over the Arctic and Antarctic Oceans, due to sea-ice feedback. The decrease of the CO₂ concentration does not disrupt the precipitation distribution when compared to experiment MM2. It slightly decreases the precipitation over the tropical oceans.

Experiment MM4: high CO₂

The increase of the atmospheric CO₂ concentration to 500 ppmv in experiment MM4 has the strongest effect on temperature of the series. It warms the global climate by +2.6°C. The higher CO₂ level also reinforces the increase of precipitation caused by the reduction of the topography, producing the strongest effects of the four experiments on precipitation. The increase of atmospheric CO₂ reinforces the warming at high latitudes, reducing again the latitudinal temperature gradient (see Figure 6.4). This high-latitude warming can be attributed to the melting of sea-ice under warmer conditions. The CO₂

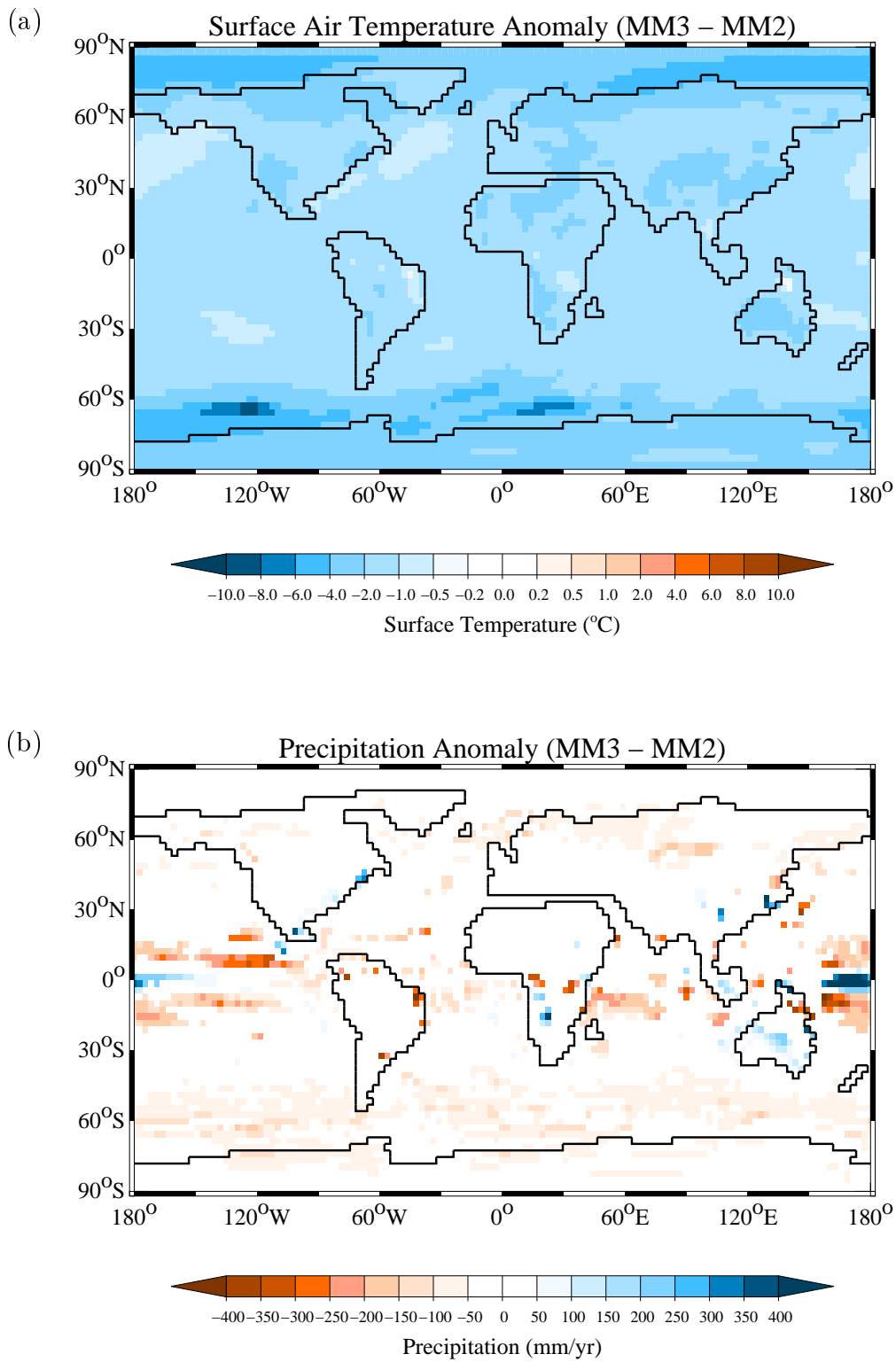


Figure 6.15: (a) Annual mean surface temperature and (b) precipitation anomalies between experiments MM3 and MM2.

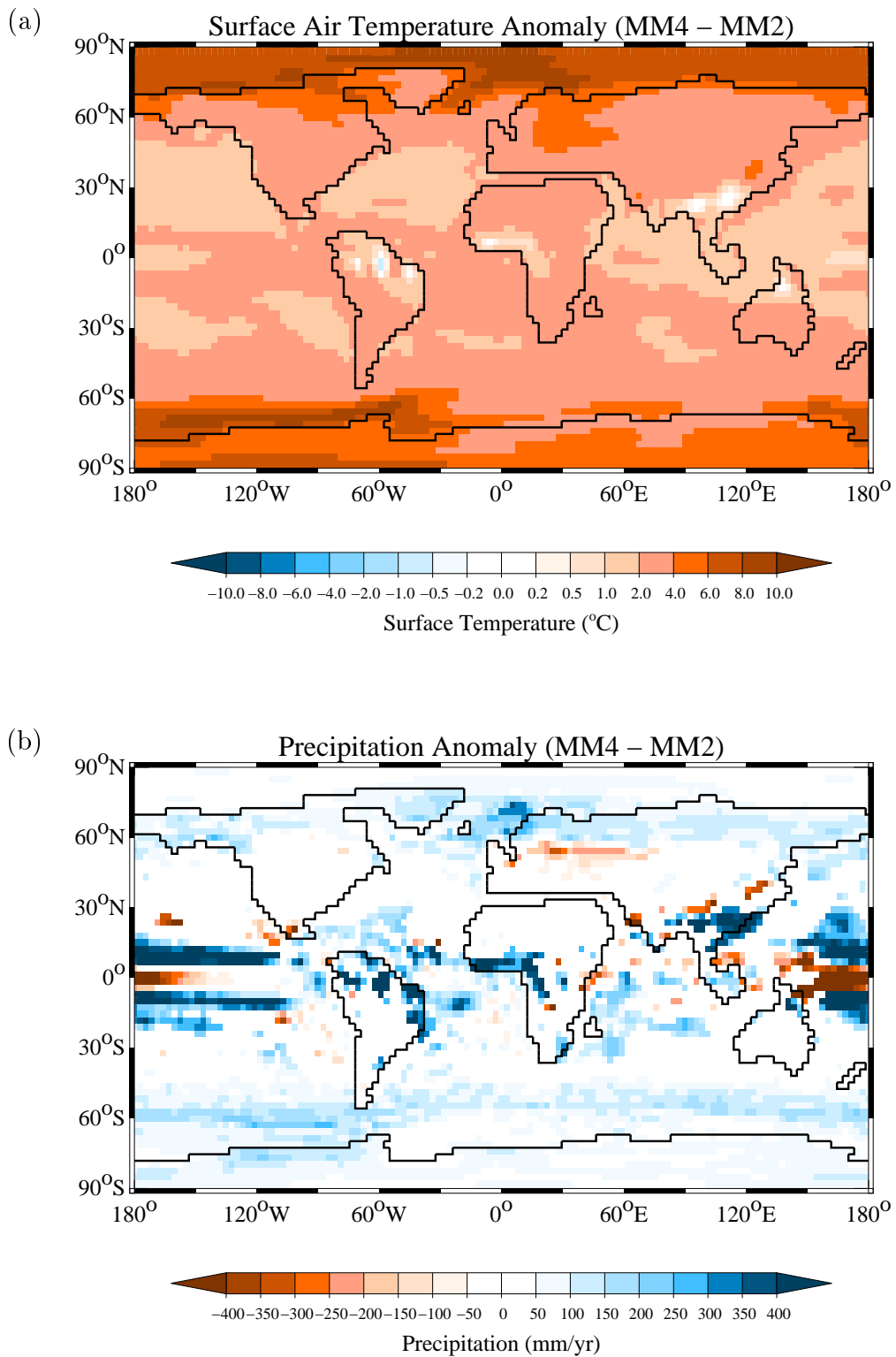


Figure 6.16: (a) Annual mean surface temperature and (b) precipitation anomalies between experiments MM4 and MM2.

induced warming also contributes to increase the precipitation rate at all latitudes. The difference in surface air temperature between experiments MM4 and MM3, equal to $+4.4^{\circ}\text{C}$, corresponds to the climate sensitivity of the model to a CO_2 increase of 300 ppmv under Middle Miocene conditions. Thus, the Miocene sensitivity to a doubling of CO_2 must be of the order of 3.3°C (using the temperature increase between experiment MM4 and MM3 as a reference), if we assume that the global mean temperature variation is proportional to the radiative forcing (FORSTER et al., 2007), and radiative forcing is proportional to the logarithm of pCO_2 ratios (MYHRE et al., 1998). In comparison, we obtained a climate sensitivity to a doubling of CO_2 from a preindustrial level of 280 ppmv to 560 ppmv of $+4.5^{\circ}\text{C}$ under a present-day configuration. The model climate sensitivity is thus significantly smaller under Middle Miocene conditions. That could be partially explained by the reduction of the sea-ice extent at Middle Miocene, which is very sensitive to CO_2 changes in our model.

The surface air temperature and precipitation anomalies between experiments MM4 and MM2 are shown in Figure 6.16. The increase of the atmospheric CO_2 concentration in experiment MM4 leads to uniform temperature increases on the continents and the oceans in both hemispheres. The effect of CO_2 is larger than the effect of the topography in some regions. Northwestern Europe notably experiences significant increases of temperature in experiment MM4, whereas the reduced topography alone induced a cooling in that region (see Section 6). The higher CO_2

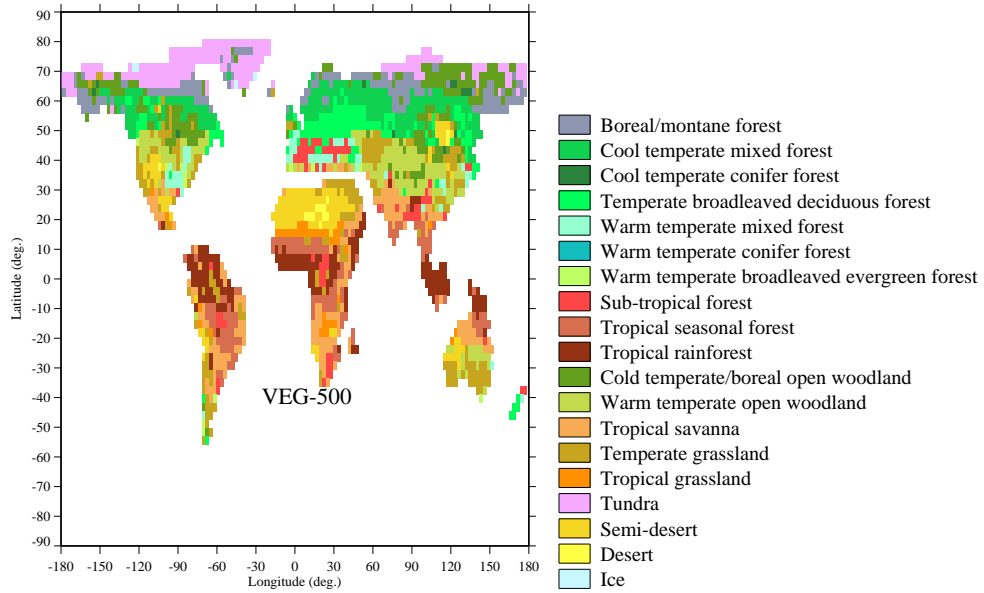
concentration also produces a stronger warming at high latitudes and especially over the Arctic and Southern Oceans due to the melting of sea-ice. However, the higher CO_2 concentration does not disturb the precipitation distribution induced by the reduction of the topography in experiment MM2. The distributions of the precipitation anomalies are quite similar in experiments MM2 and MM4. The CO_2 effect reinforces the precipitation increases especially in the tropics.

Experiment MM4-veg: vegetation

The warmer and more humid conditions prevailing in experiment MM4 could lead to significant vegetation cover modifications that could in turn affect the climate. Here, we analyse the results of experiment MM4-veg, taking into account the vegetation changes in response to the MM4 climate, in order to quantify the order of magnitude and the local impacts of vegetation changes on the MMCO climate.

The vegetation distribution obtained with CARAIB from the climate of experiment MM4 is shown in Figure 6.17 and compared to the preindustrial vegetation distribution used in the rest of the experiments. It should be noticed that the vegetation maps do not show Antarctica, because the NEW et al. (2002) climatology does not include any data point in Antarctica. Globally, in response to the warmer and more humid climate in experiment MM4, the simulated Miocene vegetation distribution demonstrates an expansion of for-

(a) Biome Distribution



(b) Biome Distribution

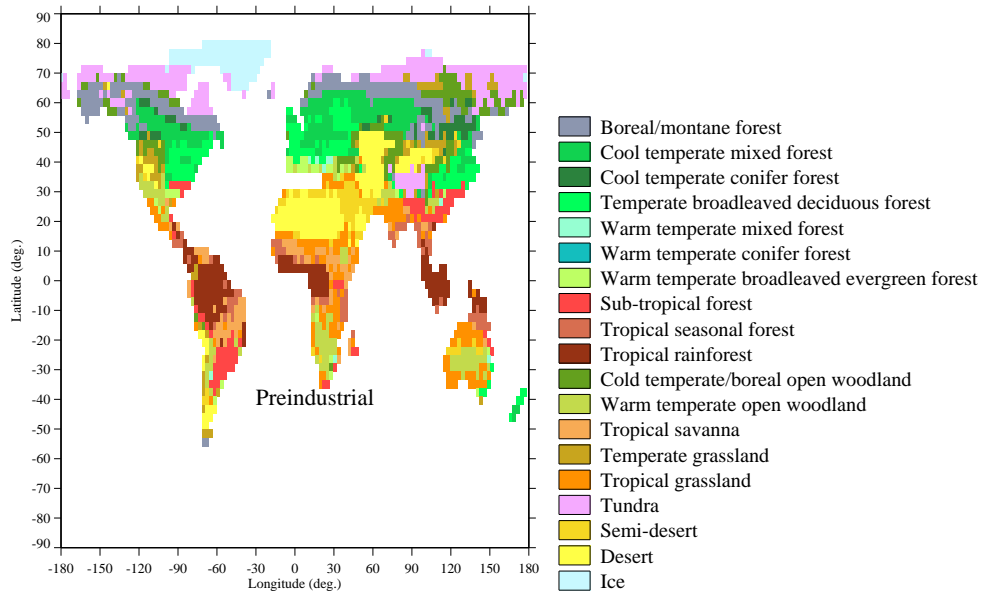


Figure 6.17: Biome distributions from CARAIB preindustrial and MMCO equilibrium runs.

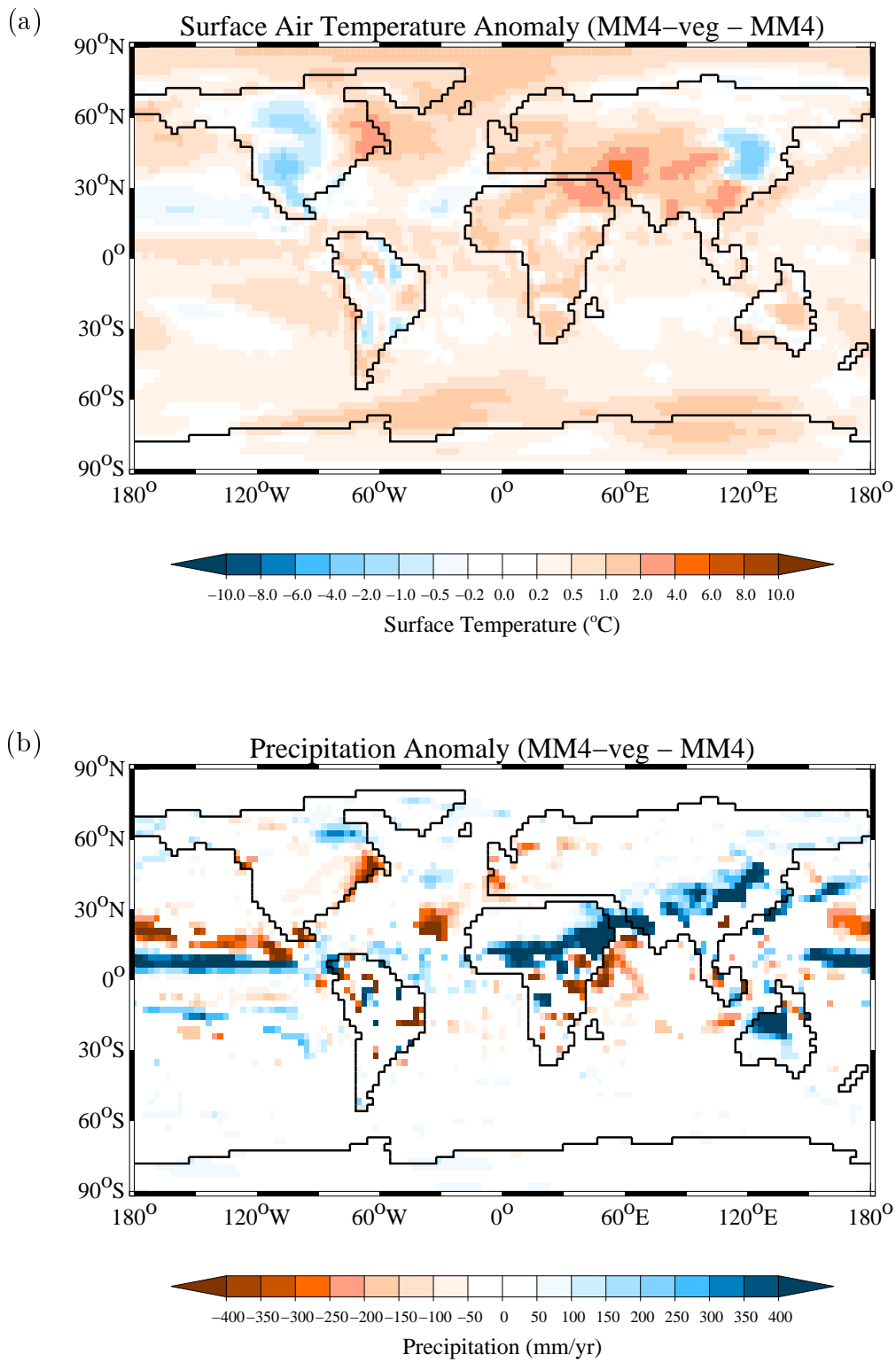


Figure 6.18: (a) Annual mean surface temperature and (b) precipitation anomalies between experiment MM4-veg and MM4.

est biomes at the expense of grasslands and deserts. Tundra and temperate forests expand at high latitudes mainly at the expense of polar deserts. Deserts and semi-deserts are strongly reduced and replaced by grasslands or warm and open woodlands, especially in Central Asia where deserts completely disappear. Thermophilous types included in the subtropical forest biome expand particularly in South and Central Europe, due to the warmer and wetter conditions prevailing in the region. This result seems to be consistent with the reconstruction of UTESCHER et al. (2007), which suggests the presence of warm mixed and broadleaved evergreen forests in South and Central Europe. However, the drier conditions at the east coast of North America and in southeastern China lead to the replacement of subtropical forests by warm and open woodlands.

The anomalies between experiments MM4-veg and MM4 are shown in Figure 6.18 in order to isolate the vegetation effects from the other forcings applied in experiment MM4. Globally, experiment MM4-veg shows the strongest global temperature and precipitation increases of the series of Miocene experiments (see Table 6.2), especially on the continents due to the vegetation change impact. In comparison with experiment MM4 the vegetation changes produce an additional global warming of $+0.5^{\circ}\text{C}$ ($+0.4^{\circ}\text{C}$ over the oceans and $+0.6^{\circ}\text{C}$ over the continents) and an increase of precipitation of $+19\text{ mm/yr}$ ($+4\text{ mm/yr}$ over the oceans and $+58\text{ mm/yr}$ over the continents). Locally, the vegetation contribution is only slightly lower in terms of magnitude than the contributions of

topography and high atmospheric CO_2 level. As described in Section 6, vegetation cover changes affect surface albedo and roughness length, but the albedo impact on surface temperature is dominant, because of its direct impact on the energy balance (HENROT, 2007). The changes in rooting depth mainly affect the water cycle and therefore precipitation. The differences between the surface albedo and rooting depth derived from the Miocene and the preindustrial vegetation distributions are shown in Figure 6.19.

Locally, the vegetation change effects on temperature are larger over the continents, than over the oceans (see Figure 6.18). Only the Arctic Ocean experiences a warming of the same order due to the melting of sea-ice induced by the warming of the surrounding continental grid points. Strong warming occurs around the Eastern Tethys Seaway. It is due to the decrease of surface albedo (see Figure 6.19) produced by the replacement of deserts and semi-deserts by open woodlands, which develop in the more humid conditions produced by the opening of the seaway. Central Asia also experiences a decrease of surface albedo linked to the replacement of deserts by forests. SAT increases in South and Central Europe due to the development of subtropical forests with a lower albedo. However, SAT decreases in the centre and south of North America as well as in northeastern China. This effect is linked to the increase of surface albedo induced by the opening of the landscape in response to the reduction of precipitation in these regions obtained in experiment MM4. Precipitation is essentially af-

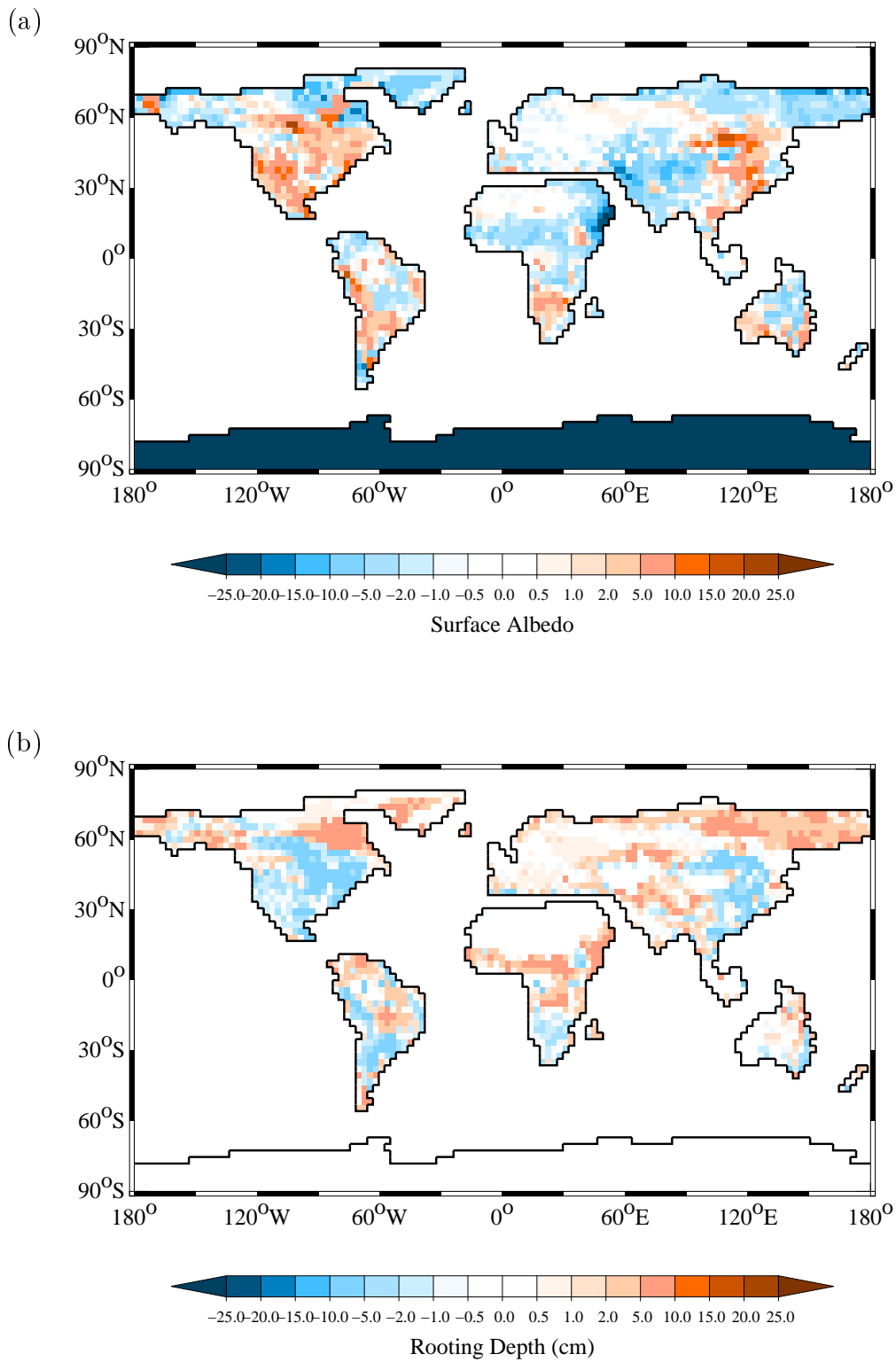


Figure 6.19: (a) Surface albedo difference and (b) rooting depth difference between experiment MM4-veg and CTRL.

ected by vegetation changes in the tropical regions. The development of forests around the Eastern Tethys Seaway increases the soil water content (see Figure 6.19) leading to an increase of evaporation and precipitation. The same effect occurs in central Asia. The precipitation increase in Equatorial Africa is due to the expansion of the tropical forests which enhances the hydrological cycle. The precipitation decrease along the west coast of Europe is due to the replacement of temperate forests by open woodlands, which decreases the soil water content.

Discussion

In our series, experiment MM1 assesses the climatic effects of the MMCO surface ocean heat flux distribution, derived from Miocene LSG model simulation (BUTZIN et al., submitted). These changes produce contrasted effects on surface air temperature and precipitation over the oceans that influence the climatic conditions on land. The reduction of the oceanic heat transfer to the North Atlantic due to the opening of the Central American Seaway brings colder conditions over the North Atlantic and northwestern Europe. This effect agrees with the majority of published modelling studies results indicating that the closure of the Central American Seaway was responsible for increased oceanic heat transport to the North Atlantic that brought warmer conditions and ultimately increased precipitation in the Northern Hemisphere (LUNT et al., 2008; SCHNEIDER and SCHMITTNER, 2006). The de-

crease of precipitation in South Asia, linked to SST changes, indicates a weakening of the Asian monsoon. According to TSCHUCK et al. (2004), the weakening of the Asian monsoon can be linked to the increase of sea surface temperatures in the Equatorial Indian Ocean and West Pacific Ocean. Therefore, the warmer conditions induced in the Pacific by the opening of the Central American Seaway may be contributing to the reduction of the precipitation in some parts of Asia.

Experiment MM2 allows us to discuss the climatic effects of the reduced topography on land. It also represents a Middle Miocene state with a preindustrial CO₂ concentration of 280 ppmv, since experiment MM2 includes all of the Middle Miocene boundary conditions considered in this study. As already demonstrated by KUTZBACH et al. (1989), the reduction of the topography allows a more zonal atmospheric circulation and the westerly flow to continue over the lowered Plateaus at middle latitudes, e.g., the Colorado Plateau, the Tibetan Plateau and European reliefs. Moreover, the reduced height of the Tibetan Plateau prevents the development of a monsoon-like circulation (KUTZBACH et al., 1989; HARRIS, 2006) that induces a strong decrease of precipitation in East Asia. Recently, HEROLD et al. (2009) focused on the effect of lowered Tibetan Plateau and Andes on the Middle Miocene climate using the NCAR model (CAM v.3.1) and Community Land Model (CLM v.3.0) coupled to a slab ocean model with fixed sea-surface temperatures. HEROLD et al. (2009) also obtained strong local warming and a significant disruption of the surface winds

due to the reduction of elevation over the Tibetan Plateau. However, the prescription of fixed sea-surface temperature in their experiment precluded a response of the ocean and therefore of the Asian monsoon system. Nevertheless, they also pointed out that the lowering of the Tibetan Plateau leads to a cooling linked to snow depth increase in Central Eurasia. In our experiment MM2, the reduction of the topography leads to slight warming in Eurasia, and does not significantly alter the snow depth in the region. Therefore, we can attribute the Eurasian warming in our results to the local increase of temperature induced by the reduction of reliefs higher than 400 m in the region. Unfortunately, our setup does not allow us to isolate the influence on Eurasia of the Tibetan Plateau elevation change. The lowering of North American and European reliefs produces wetter and colder conditions over northwestern Europe that are in disagreement with proxy-based reconstructions of the European Middle Miocene climate (MOSBRUGGER et al., 2005). However, the reduction of the seasonal gradient and the warming in South and Central Europe agree well with several reconstructions of the Middle Miocene climate based on pollen analysis (JIMENEZ-MORENO and SUC, 2007) and mega- or microfloral records (MOSBRUGGER et al., 2005; UTESCHER et al., 2007). Moreover, the reconstruction of UTESCHER et al. (2007) and other reconstructions based on the analysis of small mammals (VAN DAM, 2006) showed evidence for the persistence of a European wet zone during the Miocene, in agreement with our results. Nevertheless, the maximum increases of pre-

cipitation are located further north in Europe where no proxy reconstruction is available.

In the next two experiments (MM3 and MM4) we test the effect of various CO₂ concentrations on the middle Miocene climate. The CO₂ effect is rather uniform on the continents and the oceans of both hemispheres. However, the combination of the CO₂ and topographic effects in experiment MM4 generates a stronger warming over the continents than over the oceans, which is also seen in the results of TONG et al. (2009). The results of experiment MM4 over northwestern Europe show a slight increase of temperature, since the topography induced effect cooled that region. Both the topography reduction and increased CO₂ concentration contribute to wetter and warmer conditions in Europe, in better agreement with the proxies reconstructions (MOSBRUGGER et al., 2005; UTESCHER et al., 2007). As in TONG et al. (2009), the increase of the CO₂ concentration warms the high latitudes reducing the latitudinal gradient and also increases the precipitation. The increase of the CO₂ concentration furthermore enhances the hydrological cycle in the tropics, according to TONG et al. (2009). Nevertheless the activity of the monsoon system is still reduced in experiment MM4. This confirms the dominant effect of topography on the Asian monsoon system as compared to the CO₂ contribution (TONG et al., 2009).

Experiment MM4-veg finally allows us to investigate the vegetation feedback on climate in response to a warm and humid climate for the MMCO. The

simulated vegetation distribution forced with the climate of experiment MM4 mainly demonstrates a reduction of the desert and sub-desert areas in the benefit of grasslands and forests, as well as an expansion of warm forest types poleward of the subtropical zone. This fairly agrees with the Middle Miocene data-based vegetation reconstruction used as boundary condition in the study of TONG et al. (2009), despite the differences in plant type classifications. Our vegetation distribution also agrees over South and Central Europe with the reconstruction of UTESCHER et al. (2007), which suggested the presence of warm mixed and broadleaved evergreen forests in South and Central Europe. Consistently with the data from JIMENEZ-MORENO and SUC (2007), CARAIB also yields warm and open mixed forest in southwest Europe, whereas it leads to thermophilous and mesothermic elements in Central Europe. Such a change in the vegetation cover contributes to maintain and even to increase the warm and humid conditions that prevailed in experiment MM4.

In the series of sensitivity tests, several experiments result in an increase of the global surface air temperature. The increase of the atmospheric CO₂ concentration to 500 ppmv in experiment MM4 produces the strongest global warming of the series of four experiments, as compared to the warming produced by oceanic heat transport and ocean gateway changes (experiment MM1) or reduced topography (experiment MM2). A lower than preindustrial CO₂ concentration cools the global climate. A higher CO₂ concentration seems therefore necessary to generate a warmer cli-

mate in the Middle Miocene. The lower climate sensitivity of the climate model under Middle Miocene conditions may partly explain the requirement of the model for high CO₂ to produce significant temperature increases at the MMCO. However the warming we obtain is much lower than suggested by proxy data (MOSBRUGGER et al., 2005; ZACHOS et al., 2001), which witness temperatures at middle latitudes up to 6°C higher than at present (FLOWER and KENNETT, 1994). Nevertheless, our results agree fairly well with the results of previous modelling studies focusing on the Middle Miocene climate. TONG et al. (2009) tested the sensitivity of the Middle Miocene climate to various concentrations of atmospheric CO₂ using the NCAR model (CAM v.3.1) and Community Land Model (CLM v.3.0) coupled to a slab ocean model. They obtained a global warming of +0.6°C for an atmospheric CO₂ concentration of 355 ppmv and a global warming of +2.9°C for an atmospheric CO₂ concentration of 700 ppmv in comparison to a present-day control run with a reference CO₂ concentration equal to 379 ppmv. YOU et al. (2009) used the same models to test the effect of various CO₂ concentrations together with several sea surface temperature gradients. They obtained temperature increases of +2.3°C for an atmospheric CO₂ concentration of 350 ppmv and a high SST gradient and of +3.5°C for CO₂ at 700 ppmv and a medium SST gradient. MICHEELS et al. (2009a) used the Planet Simulator to test the sensitivity of the Late Miocene climate (Tortonian) to various CO₂ concentrations. They obtained global warming between +2.3°C

for 280 ppmv and $+3.7^{\circ}\text{C}$ for 460 ppmv in comparison to a preindustrial control run with a CO_2 concentration of 280 ppmv. In comparison to our results, MICHEELS et al. (2009a) found a greater warming under lower CO_2 concentration with the Planet Simulator. This effect could be due to the differences in the boundary conditions they used for the Late Miocene. They notably adopted a present-day ocean heat flux distribution, including a stronger Gulf Stream than used here and a lower topography on land in some regions. They also prescribed a vegetation distribution for the Late Miocene, where all the desert areas were replaced by forest or grassland ecosystems and the boreal forests shifted further North, whereas we did not consider any vegetation change in the MM1 to MM4 simulation experiments.

The model results consistently indicate that a higher than present-day CO_2 concentration is necessary to produce a warm Middle Miocene climate (YOU et al., 2009; TONG et al., 2009). In that sense, the model results support the terrestrial proxy reconstruction suggesting higher atmospheric CO_2 concentrations at the MMCO, between 300 and 850 ppmv (KÜRSCHNER et al., 2008; RETALLACK, 2009). Conversely modelling results do not support the low CO_2 concentration, between 140 and 300 ppmv, derived from marine isotopic records, that suggest a decoupling between CO_2 and temperature during the Middle Miocene (HENDERIKS and PAGANI, 2008; PEARSON and PALMER, 2000). Experiments using lower CO_2 concentrations generate colder climate than at present-day (experiment MM3 in this study, TONG et al. (2009) or YOU

et al. (2009)). However, as recently discussed by PAGANI et al. (2010, suppl. mat.) CO_2 concentrations during the Miocene could possibly have been higher than suggested by previous estimates based on planktonic foraminiferal $\delta^{18}\text{O}$ temperature reconstructions. Correcting for inherent biases could thus help to reconcile model results to proxy-based reconstruction. However, as emphasised by DIESTER-HAASS et al. (2009), a high CO_2 level at the Middle Miocene would be difficult to reconcile with the high $\delta^{13}\text{C}$ values of benthic foraminifera, which suggest large deposition rates of organic carbon tending to reduce atmospheric CO_2 levels. Therefore model results should be interpreted with care.

We indeed do not take into account all the possible effects that could contribute to the Middle Miocene warm climate. We notably miss the feedback of climate on ocean circulation at Middle Miocene, which could only be simulated with a fully coupled ocean-atmosphere model, since we used a slab ocean model as in previous studies (TONG et al., 2009; YOU et al., 2009). The opening of ocean gateways notably at low latitudes seems to have strongly contributed to modify the global ocean circulation in the Cenozoic in comparison to present-day (BICE et al., 2000; VON DER HEYDT and DIJKSTRA, 2008). We also only tested the effect of various CO_2 concentrations on climate given the large uncertainty in CO_2 estimations. We did not take into account a change in the concentrations of other atmospheric greenhouse gases such as methane. The potential role of such feedbacks is well illustrated by the results of our simulation experiment MM4-veg, which takes into

account the feedback on climate from the changing vegetation cover compared to the first four simulation experiments of our series.

Conclusions

In this study, we examine the potential contributions of several boundary condition changes to the warm climate of the Middle Miocene and particularly the Middle Miocene Climatic Optimum (MMCO). We used the Planet Simulator, an Earth System model of intermediate complexity to investigate the contributions of the absence of ice on the continents, the opening of the Central American and Eastern Tethys Seaways, the lowering of the topography on land and the effect of various atmospheric CO₂ concentrations on the Middle Miocene climate. We also investigated the feedback of vegetation on climate. Therefore, we prescribe vegetation cover changes derived from a MMCO vegetation distribution produced by the dynamic vegetation model CARAIB, forced with the climate of the warmest and most humid experiment of the series. The boundary condition changes generally produce global warming in the Middle Miocene that are in agreement with previous Middle Miocene sensitivity experiments (TONG et al., 2009; YOU et al., 2009). However, the increases of temperature that we obtained are lower than those supported by proxy data (ZACHOS et al., 2001; BRUCH et al., 2007).

The increase of the atmospheric CO₂ concentration to 500 ppmv produces the largest global warming of the series and

contributes to warm the climate at all latitudes, in agreement with the results of previous modelling studies (TONG et al., 2009; YOU et al., 2009). Therefore, a higher than present-day CO₂ concentration seems necessary to produce the warm climate of the MMCO inferred from proxy-data. This result supports the terrestrial proxy reconstruction suggesting higher atmospheric CO₂ concentrations at the MMCO (KÜRSCHNER et al., 2008; RETALLACK, 2009), but it does not support the decoupling between CO₂ and temperature during the Middle Miocene suggested by the marine isotopic CO₂ reconstructions (HENDERIKS and PAGANI, 2008; PEARSON and PALMER, 2000).

Nevertheless, increasing only the CO₂ concentration is not sufficient to produce the required warming at the MMCO suggested by proxy-based reconstructions. The lowered topography and the changes in oceanic heat transfer and in ocean gateways configuration also produce significant regional effects that have to be taken into account. The topographic and oceanic forcings applied here have a lower impact on the global temperature than the CO₂ forcing, due to a number of regional effects that partially cancel each other on global average. However, they significantly affect the temperature and precipitation distributions and their local effects can exceed the CO₂ effect. The lower topography allows a more zonal atmospheric circulation and the westerly flow to continue over the lowered Plateaus at middle latitudes. The reduced height of the Tibetan Plateau notably prevents the development of a monsoon-like circulation (KUTZBACH et al., 1989; HARRIS,

2006). Our results also highlight the effect of the reduction of elevations of the North American and European reliefs, which strongly increases precipitation but decreases surface air temperature from northwestern to eastern Europe. The temperatures obtained over northern Europe are too cold relative to proxy-based temperature reconstruction of the European Middle Miocene climate (MOSBRUGGER et al., 2005), but the reduction of the seasonal gradient and the wetter conditions agree well with several proxy-based reconstructions (JIMENEZ-MORENO and SUC, 2007; UTESCHER et al., 2007; MOSBRUGGER et al., 2005).

Unfortunately, we were not able to take into account all the possible mechanisms that could contribute to the Middle Miocene warm climate. We notably could not take into account the complete ocean-atmosphere feedback loop that could be simulated with a fully coupled ocean-atmosphere model. We furthermore did not take into account a change in the concentrations of other atmospheric greenhouse gases such as methane.

The vegetation feedback also plays an important role in the warm MMCO climate, as demonstrated by the last experiment where we investigated the vegetation cover change feedback. In response to warm and humid conditions, forests expand at the expense of deserts and warm forest types develop poleward of the subtropical zone. Such a change in the vegetation cover leads to stronger warming and increase of precipitation.

Moreover, the vegetation feedback on climate is of the same order of magnitude as the topographic or CO₂ effects, confirming the importance of the vegetation contribution to the MMCO climate. Therefore, vegetation-climate interactions could provide a complementary, if not an alternative mechanism, to the large increase of CO₂ required by the model to produce the estimated warming at the MMCO. This confirms the contribution of vegetation to the MMCO warm climate and emphasises the need for data-model comparison in order to estimate the reliability of climate model experiments and vegetation reconstructions.

Acknowledgements

We acknowledge the efforts of the Planet Simulator team (especially Klaus Fraedrich, Edilbert Kirk and Frank Lunkeit) for making available their model as Open Source Software and for the sustained development and help. We also thank the two anonymous reviewers for their constructive comments. A.-J. Henrot is a Research Fellow and G. Munhoven a Research Associate with the Belgian Fund for Scientific Research (F.R.S.-FNRS). We acknowledge support for this research from F.R.S.-FNRS under research grant "Crédit aux chercheurs" 1.5.179.07 F. This work is a contribution to the Deutsche Forschungsgemeinschaft project "Understanding Cenozoic Climate Cooling (UCCC)" (FOR 1070).

6.1 Middle Miocene climate and vegetation interactions under different levels of CO₂

In the present section, we describe more fully and compare to available proxy-based vegetation reconstructions the Middle Miocene vegetation distribution simulated by CARAIB in response to the warmest and most humid climate of the series of experiments presented in HENROT et al. (2010). As the mechanisms responsible for the warm climate at the MMCO and particularly the role of the atmospheric CO₂ are still highly debated, we discuss the potential impact of atmospheric carbon dioxide concentration on the vegetation by comparing the Middle Miocene vegetation distributions produced under high (500 ppmv) and low (280 ppmv) CO₂ level. The vegetation feedback on the MMCO climate at high and low CO₂ levels is then presented in order to discuss the potential role played by vegetation on the warm MMCO climate. Finally, we also present here the climatic and vegetation results of a series of iterations between Plasim and CARAIB (off-line coupling) to analyse the vegetation-climate interactions at Middle Miocene and under the two CO₂ levels considered here.

6.1.1 MMCO vegetation distribution at high CO₂ level

The Middle Miocene vegetation distribution at 500 ppmv (VEG-500) was obtained from an equilibrium run of CARAIB forced with the warmest and most humid climate of the series of simulation experiments carried out and described in the previously reproduced paper of HENROT et al. (2010), i.e. experiment MM4. The climate of the selected Middle Miocene experiment is globally warmer (+2.9°C) and wetter (+73 mm/yr) in comparison to the control experiment, and in best agreement with proxy-based climatic reconstructions (MOSBRUGGER et al., 2005; UTESCHER et al., 2007). The reduction of the topography on land and the higher CO₂ level contribute to warm the continents and notably to reduce the seasonal temperature gradient in Europe. Precipitation strongly increases from northwestern to eastern Europe, in response to the lowering of the North American and European reliefs, whereas the reduction of the Tibetan Plateau height prevents the development of a monsoon-like circulation. As a reminder, Figures 6.20 and 6.21 show the annual mean and winter/summer surface air temperature and precipitation anomalies between experiments MM4 and CTRL. A complete description and discussion of the experimental setup and climatic results has been presented in HENROT et al. (2010).

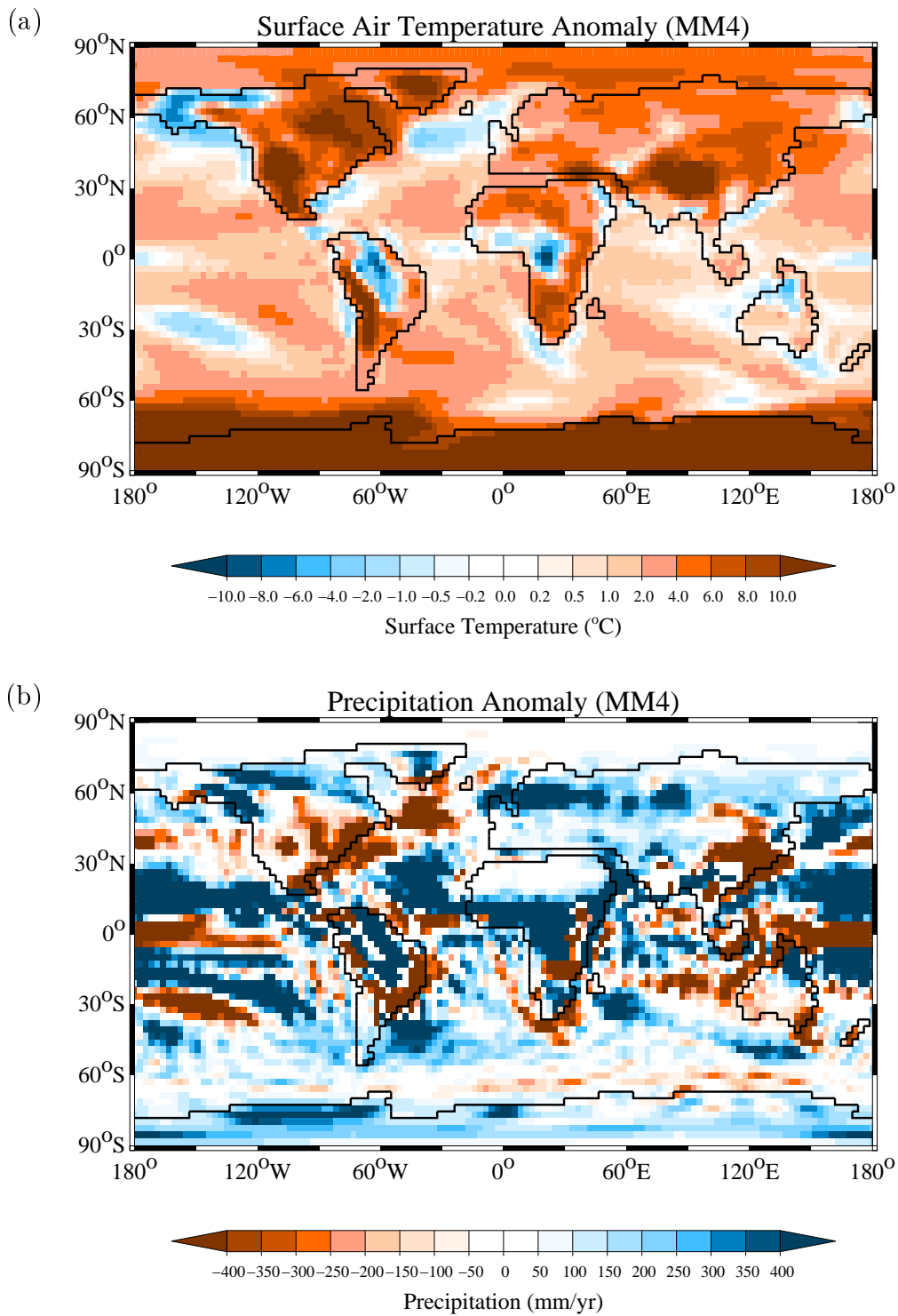


Figure 6.20: Annual (a) surface air temperature ($^{\circ}\text{C}$) and (b) precipitation (mm/yr) differences for the MM4 experiment (MM4 - CTRL).

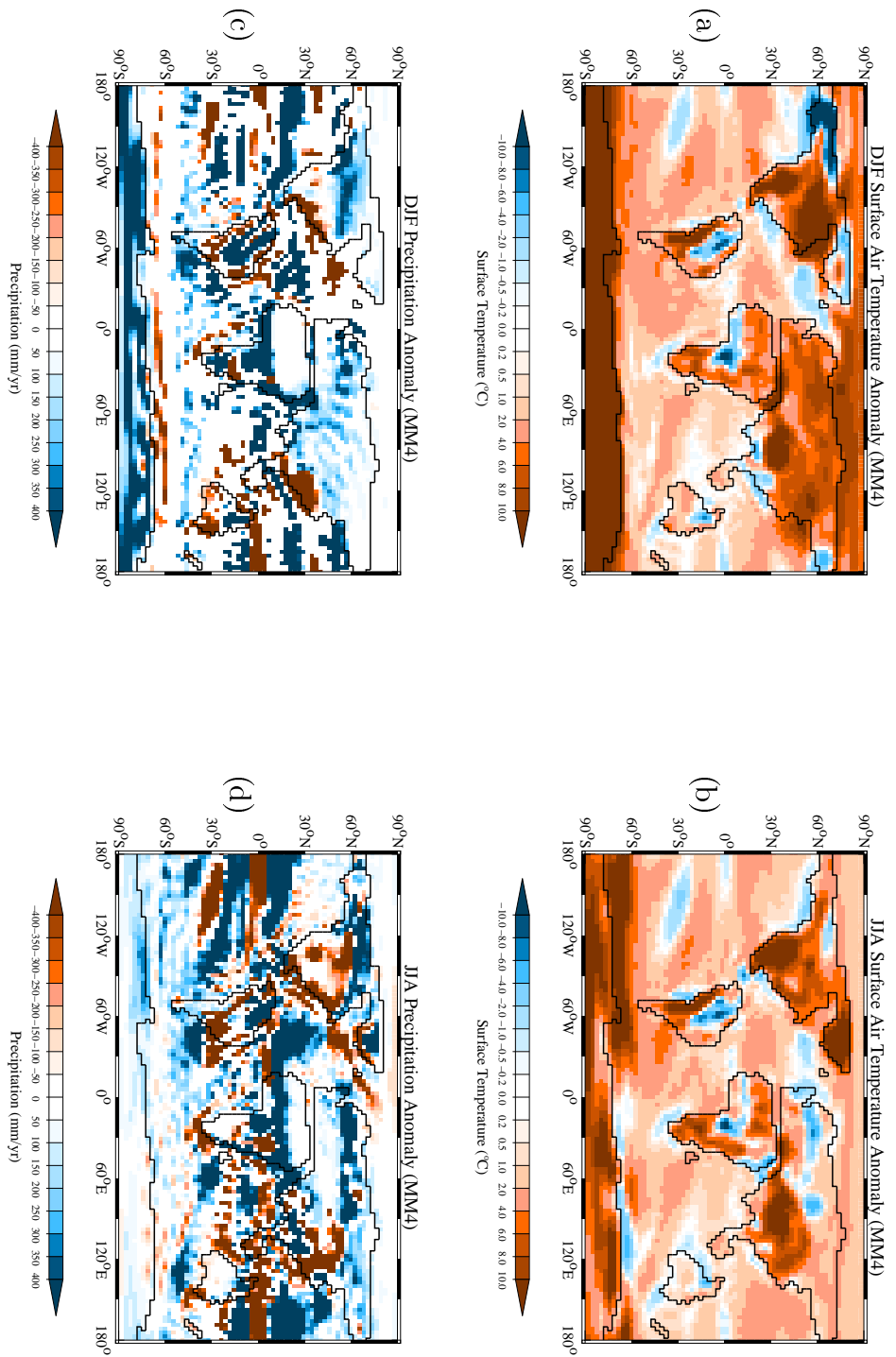


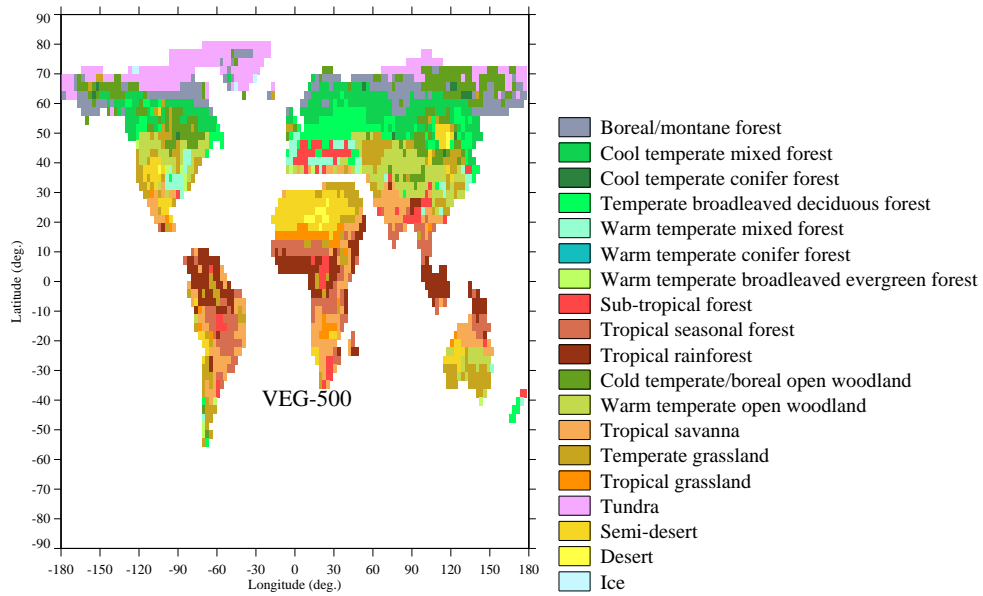
Figure 6.21: (a) DJF and (b) JJA surface air temperature anomalies ($^{\circ}\text{C}$), and (c) DJF and (d) JJA precipitation anomalies (mm/yr) for the MM4 experiment.

In response to the warmer and more humid climatic conditions, the simulated Middle Miocene vegetation distribution demonstrates an expansion of forest biomes at the expense of grasslands and deserts. The Middle Miocene and preindustrial biome distributions are shown in Figure 6.22. Poleward of 60°N, tundra replaces polar desert, and totally covers the ice-free Greenland. In response to high-latitude warming, especially in winter, boreal forests and boreal/temperate open woodlands expand further north, notably in Siberia, and are replaced at lower latitudes by warmer temperate forests. The needle-leaved trees are more productive at higher latitudes (northward of 50°N) in the Middle Miocene simulation as illustrated in Figure 6.24, showing the net primary productivity (NPP) of the cold boreal/temperate trees (PFTs 3 and 11) in comparison to preindustrial NPP of these PFTs. The development of boreal and temperate forests in Yukon and northwestern Canada is consistent with the pollen analysis performed by WHITE et al. (1997). However, the reconstruction of WHITE et al. (1997) suggests the presence of dense forests in these regions including also warmer taxa at the MMCO, such as *Fagus* and *Quercus*. The productivities of the cold boreal/temperate trees and temperate cool trees (PFT 12, not shown) we obtained here are too low to allow a dense boreal/temperate forest to develop, and suggest colder climatic conditions in our results than in the reconstructions of WHITE et al. (1997).

At mid to low latitudes (between 60 and 30°N), warmer and more humid conditions induce a reduction of deserts and semi-deserts at the benefit of grasslands (C3 steppes) or warm and open woodlands, especially in Central Asia where deserts completely disappear. This result fairly agree with the palaeoprecipitation reconstruction of LIU et al. (2009), based on hypsodonty of large herbivorous mammals, suggesting a general humid and uniform climate at the MMCO in East Asia, that could have lead to a reduction of desert areas. Our results are also consistent with the pollen analysis of SUN and ZHANG (2008), which suggest the presence of temperate and thermophilous broadleaved deciduous trees in northwestern China at the MMCO, supporting a warmer and more humid climate in the region.

Warm temperate mixed forests and subtropical biomes, including thermophilous and mesothermic elements, particularly develop in South and Central Europe. Figure 6.23 shows the NPPs of needleleaved and broadleaved evergreen temperate perhumid warm types (PFTs 6 and 10) for the Middle Miocene and the preindustrial period. In agreement with the pollen analysis of JIMENEZ-MORENO (2006), JIMENEZ-MORENO and SUC (2007) and JIMENEZ-MORENO et al. (2008) and the mega- and microfloras analysis of UTESCHER et al. (2007), which indicates that the vegetation in South and

(a) Biome Distribution



(b) Biome Distribution

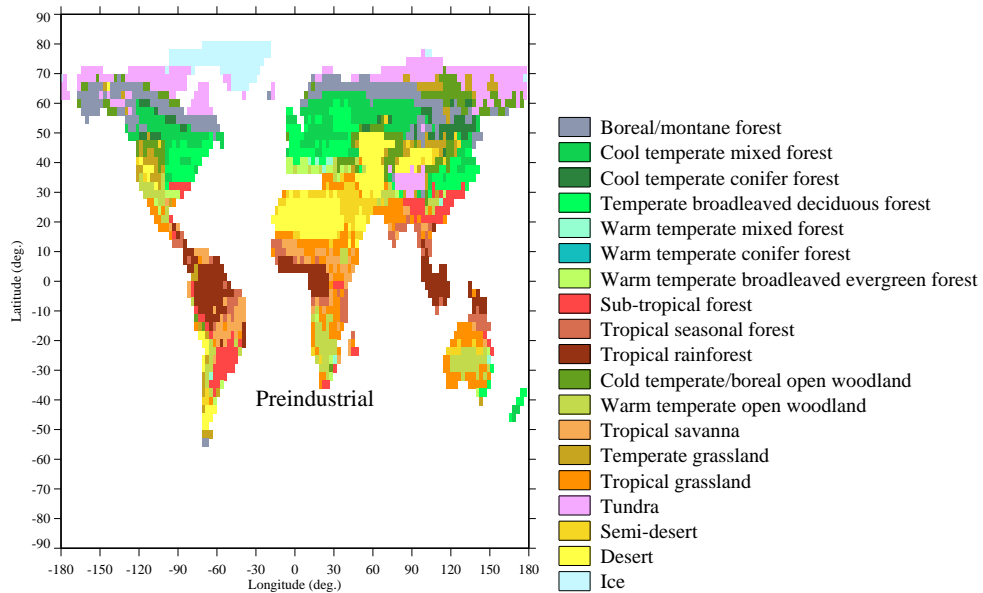


Figure 6.22: (a) VEG-500 and (b) preindustrial CARAIB biome distributions.

Central Europe was dominated by thermophilous elements rich in evergreen trees, our results demonstrate highly productive and well expanded warm evergreen forests in the region. According to UTESCHER et al. (2007), the expansion of thermophilous elements in the South of Europe restricts the deciduous vegetation to more northerly localities. However, evergreen trees are also highly productive at higher latitudes, which suggests that a very rich, mixed and dense flora prevailed in Europe at the MMCO (JIMENEZ-MORENO, 2006; JIMENEZ-MORENO et al., 2008). Moreover, despite the low model resolution and the land-sea distribution we adopted here, the simulated vegetation distribution well reproduces the vegetation gradient observed in the pollen assemblages (JIMENEZ-MORENO and SUC, 2007). Steppic environments prevailed in southwestern Europe (Spain), reflecting dry climate with marked seasonality, whereas dense forests of thermophilous elements, supporting a more humid climate with very weak seasonal temperature and precipitation gradients, prevailed in Central Europe (JIMENEZ-MORENO and SUC, 2007).

However, in response to drier conditions in southwestern North America and East China, the productivities of broadleaved evergreen trees decrease, whereas needleleaved evergreen trees subsist (see Figure 6.23). The presence of thermophilous types in North China agrees well with the reconstruction of SUN et al. (2002), indicating that the vegetation of the region was typical from warm and moist subtropical conditions at the MMCO. In North America, CARAIB yields warm and open woodlands or grasslands, reflecting an opening of the landscape due to the drier and warmer climate simulated there. This is consistent with the vegetation reconstructions of BOLICK et al. (2002), GABEL et al. (1998) and STRÖMBERG (2002), suggesting that savanna and C₃ grasslands were widespread in the Northern Great Plains during the Miocene.

The humid climatic conditions produced in the tropics here are sufficient to sustain the formation of tropical rainforest, notably in South America, as suggested by the fossil freshwater bivalves analysis by KAANDORP et al. (2005). The tropical rainforest is also well developed in Equatorial Africa and along the east coast of Africa. Elsewhere in Africa tropical savanna and grasslands dominate, in agreement with fossil plant and paleosol data of RETALLACK (1992) and the pollen analysis of BONNEFILLE (1984). Warm open woodlands and savanna are also prominent in Australia, where tropical forest is restricted to northerly localities, as suggested by MARTIN (2006).

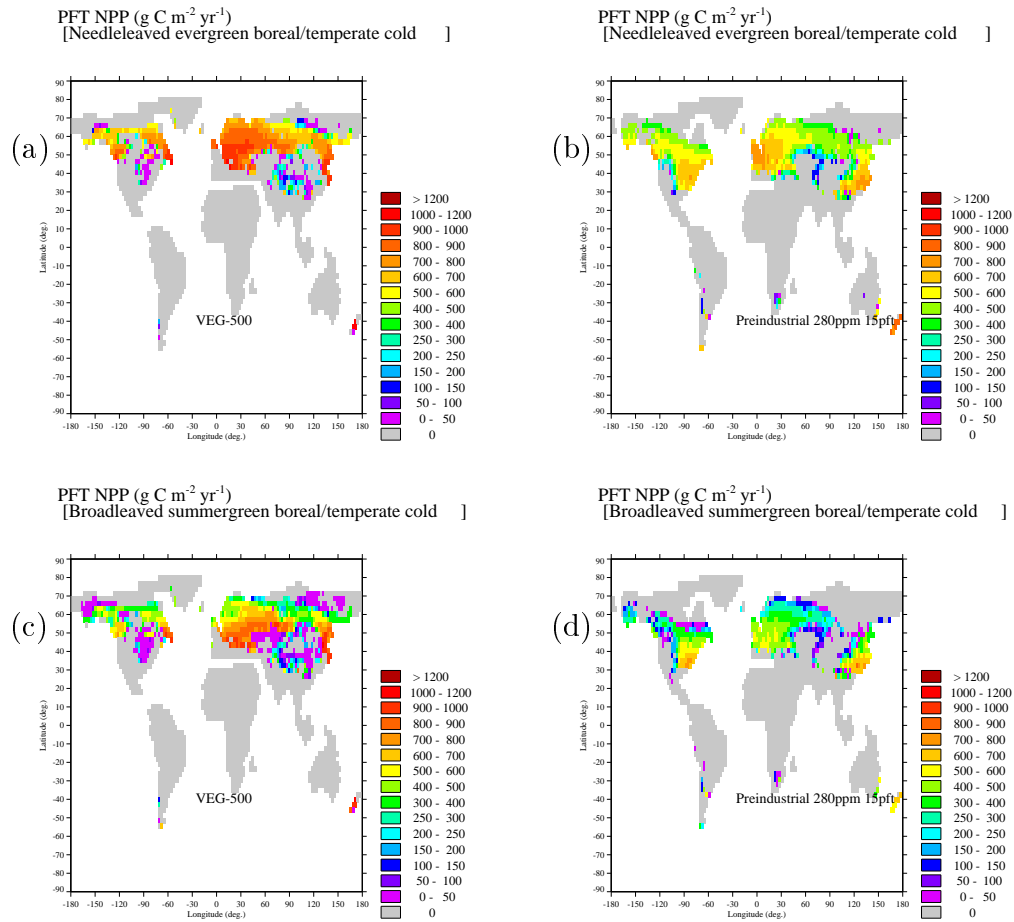


Figure 6.23: Net Primary Productivities of needleleaved evergreen boreal/temperate cold trees for (a) the VEG-500 and (b) the preindustrial vegetation distributions. Net Primary Productivities of broadleaved summergreen boreal/temperate cold trees for (c) the VEG-500 and (d) the preindustrial vegetation distributions.

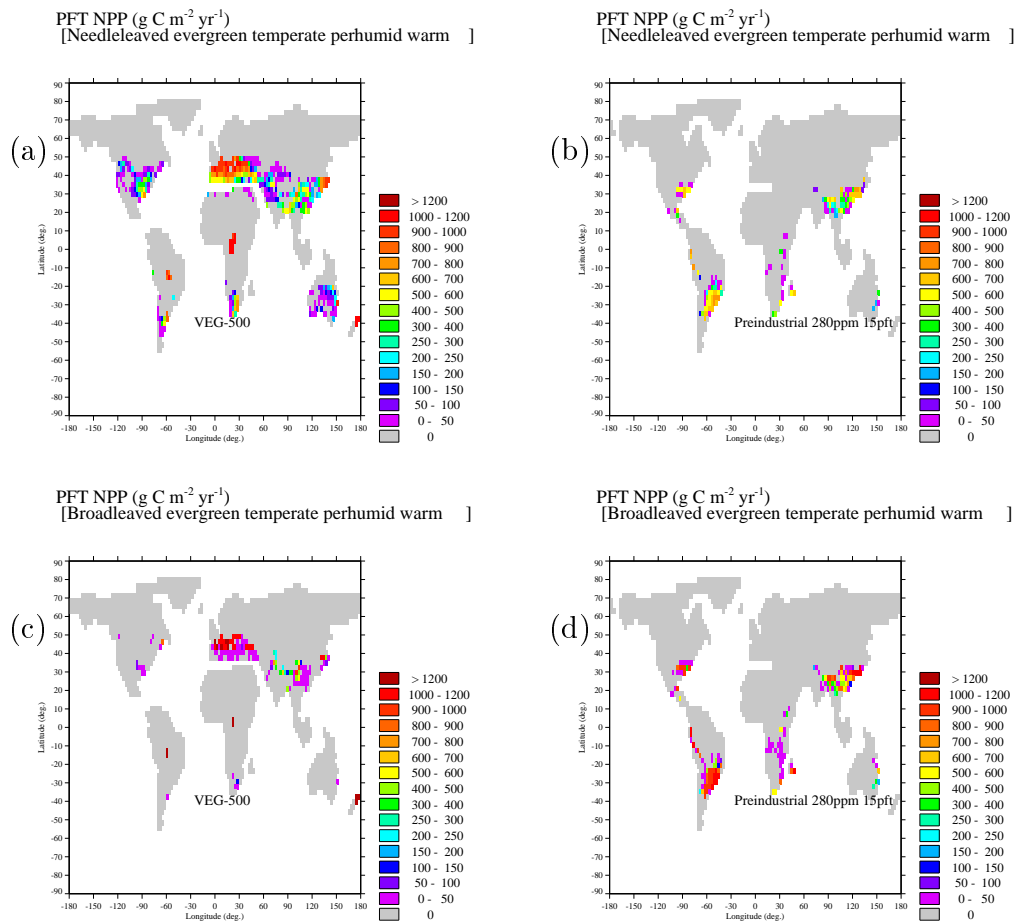


Figure 6.24: Net Primary Productivities of needleleaved evergreen temperate perhumid warm trees for (a) the VEG-500 and (b) the preindustrial vegetation distributions. Net Primary Productivities of broadleaved evergreen temperate perhumid warm trees for (c) the VEG-500 and (d) the preindustrial vegetation distributions.

6.1.2 MMCO vegetation distribution at low CO₂ level

We performed here an additional simulation with CARAIB using a preindustrial atmospheric CO₂ concentration (280 ppmv). With this experiment, we wanted to test whether the Middle Miocene surface boundary conditions are sufficient to produce an expansion of the warm forest types at middle latitudes in good agreement with the proxy-based vegetation reconstructions or whether atmospheric CO₂ is the main driver of vegetation changes. The vegetation distribution VEG-280 shown in Figure 6.26, in comparison to the preindustrial one, was obtained from an equilibrium run of CARAIB forced with 280 ppmv of CO₂ and the climate of experiment MM2 (fully described in HENROT et al. (2010)), which considers Miocene oceanic conditions and land-sea distribution, a lowered topography and a preindustrial CO₂ level of 280 ppmv. The annual mean temperature and precipitation anomalies resulting from experiment MM2 are shown in Figure 6.25.

At high latitudes, the warming produced in experiment MM2 is sufficient to allow tundra to replace polar desert. However, boreal forest and boreal/temperate open woodlands do not install as far north as in the vegetation distribution produced under a higher CO₂ level (see Section 6.1.1). It is remarkable that the NPPs of the cold boreal/temperate trees are weaker under a lower CO₂ concentration (see Figure 6.27). At middle latitudes, open woodlands and grasslands replace the desert and semi-desert areas. Nevertheless, some desert areas subsist in North Asia and North America. Colder open woodlands also develop in Central Asia, where warm temperate open woodlands prevailed in the VEG-500 vegetation distribution, indicating colder climatic conditions in the region under a lower CO₂ level.

In Europe the expansion of subtropical biomes is not strongly marked and only a few grid elements in southern Europe are covered by subtropical biomes. However, the NPPs of evergreen temperate perhumid warm trees indicate that the thermophilous types are well productive and more extended in Central Europe than suggested by the biome distribution (see Figure 6.27). This can be explained by the biome assemblage procedure that reflects the most productive PFTs of the grid element. Nevertheless, the VEG-280 vegetation distribution supports the presence of a warm mixed flora in Europe at the MMCO, including thermophilous types (JIMENEZ-MORENO, 2006; JIMENEZ-MORENO et al., 2008). The vegetation gradient from southwestern Europe (Spain) to Central Europe suggested by JIMENEZ-MORENO and SUC (2007) is also well reproduced here. However, the colder and drier climatic conditions obtained under a lower CO₂ restrict the thermophilous types to some isolated areas in eastern Asia and southeastern North America. In

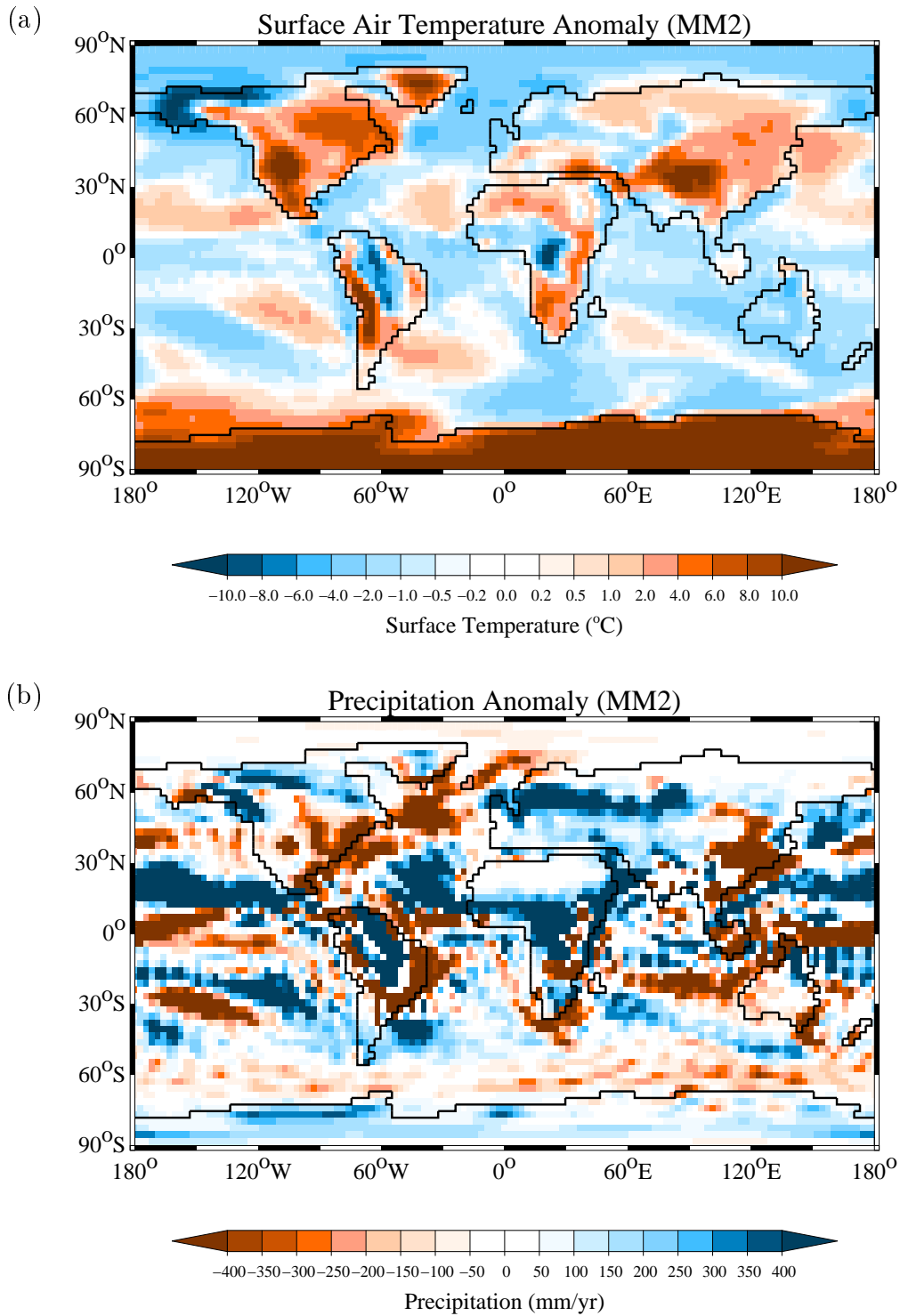
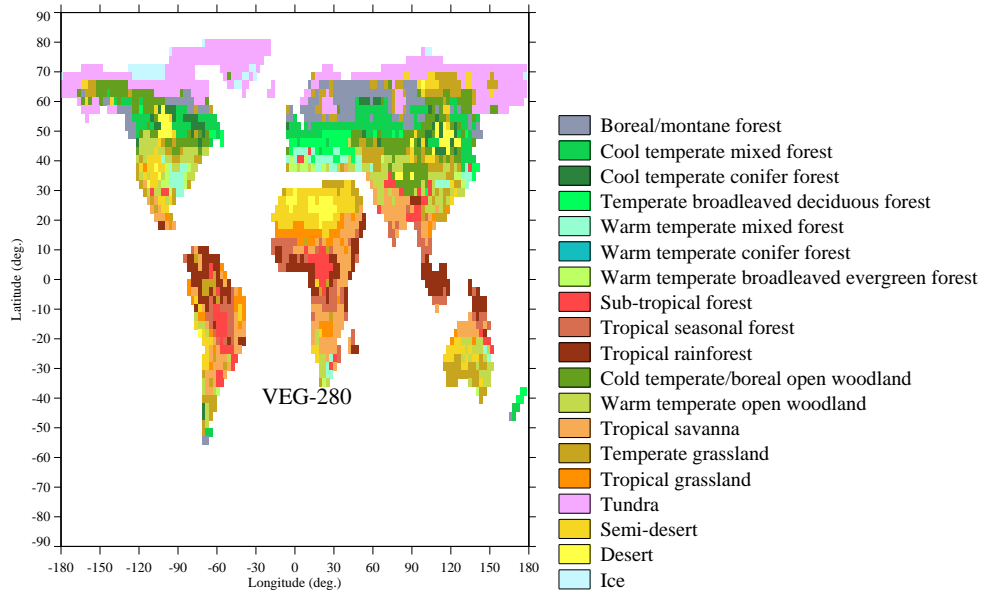


Figure 6.25: Annual (a) surface air temperature ($^{\circ}\text{C}$) and (b) precipitation (mm/yr) differences for the MM2 experiment (MM2 - CTRL).

(a) Biome Distribution



(b) Biome Distribution

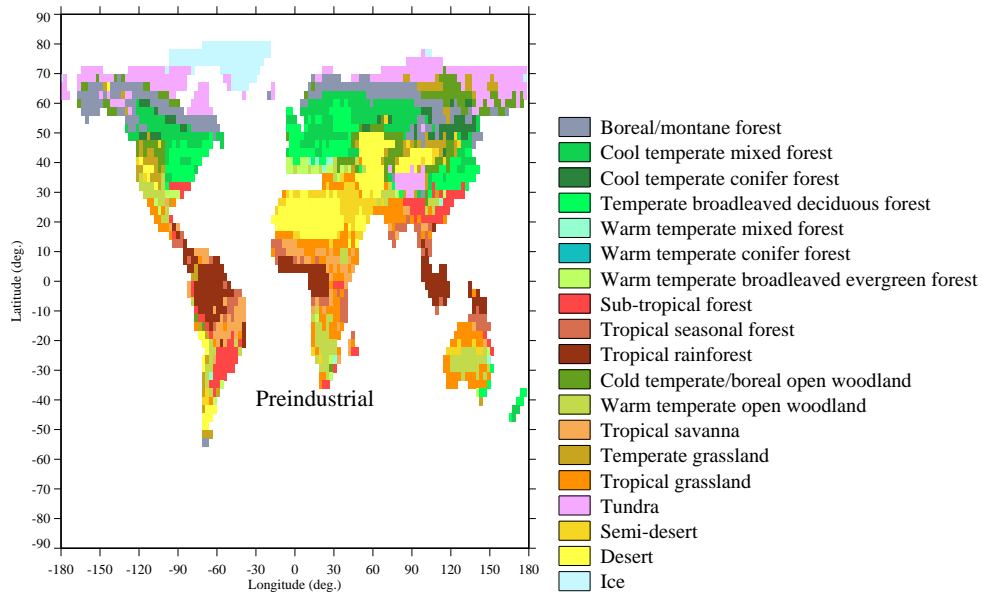


Figure 6.26: (a) VEG-280 and (b) preindustrial CARAIB biome distributions.

the tropics and subtropics, the VEG-500 and VEG-280 vegetation distributions are quite similar. The tropical forests are well developed, except in Equatorial Africa where subtropical biomes dominate, due to slightly colder conditions in the region under 280 ppmv of CO₂.

The CARAIB results discussed here suggest that the VEG-500 vegetation distribution produced under a higher CO₂ level is in better agreement with the available proxy-based reconstructions for the MMCO than VEG-280. Nevertheless, a more precise model-data comparison based on the presence/absence of taxa as performed by FRANÇOIS et al. (submitted) for the Late Miocene could improve the comparison to data and better highlight the differences between both vegetation distributions presented here (see Appendix A). The vegetation results also support the climatic results discussed in HENROT et al. (2010), suggesting that higher than preindustrial concentrations of CO₂ are most likely required to reconcile Miocene climate simulations with appropriate climatic reconstructions. Here the increase of the atmospheric CO₂ concentration to higher than preindustrial concentration contributes to generate a warmer and more humid climate that allows the warm forest types to expand poleward and reduces the desert and semi-desert areas. Moreover, the CO₂ concentration increase also impacts on the biosphere through its fertilization effect and benefits the forest and grassland ecosystems at the expense of desert. Nevertheless, the VEG-280 vegetation distribution suggests that the warming and weakening of the seasonal temperature gradient as well as the wetter conditions that prevail in Europe in response to a lower topography are sufficient to allow the thermophilous trees types to install in Europe at the MMCO. However, due to the lower productivities of the thermophilous types in Europe, the VEG-280 vegetation distribution rather suggests the presence in the region of warm mixed forests, including deciduous temperate and thermophilous trees, in agreement with JIMENEZ-MORENO (2006) and JIMENEZ-MORENO et al. (2008).

CO₂ fertilisation effect

The differences between the VEG-500 and VEG-280 vegetation distributions may be attributed to the CO₂ effects on the biosphere. However, carbon dioxide may affect the biosphere indirectly through its impact on climate and directly through its fertilisation effect. In order to isolate the climatic effect of CO₂ on the vegetation distribution from the fertilisation effect, we performed a supplementary simulation with CARAIB. We forced the model with the climate of the experiment MM4 (including a high CO₂ concentration) and lowered the atmospheric CO₂ concentration seen by the CARAIB model to

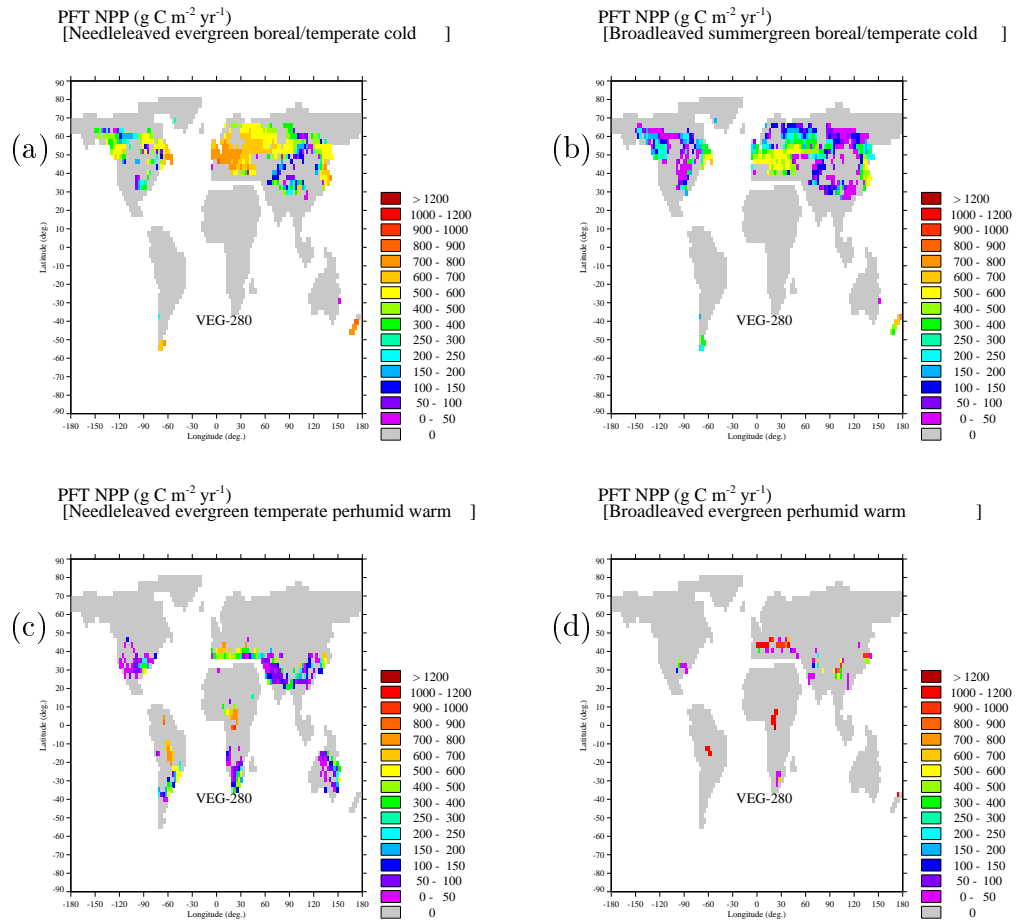


Figure 6.27: Net Primary Productivities of (a) needleleaved evergreen boreal/temperate cold trees for, (b) broadleaved summergreen boreal/temperate cold trees, (c) needleleaved evergreen temperate perhumid warm trees and (d) broadleaved evergreen temperate perhumid warm trees for the VEG-280 vegetation distribution.

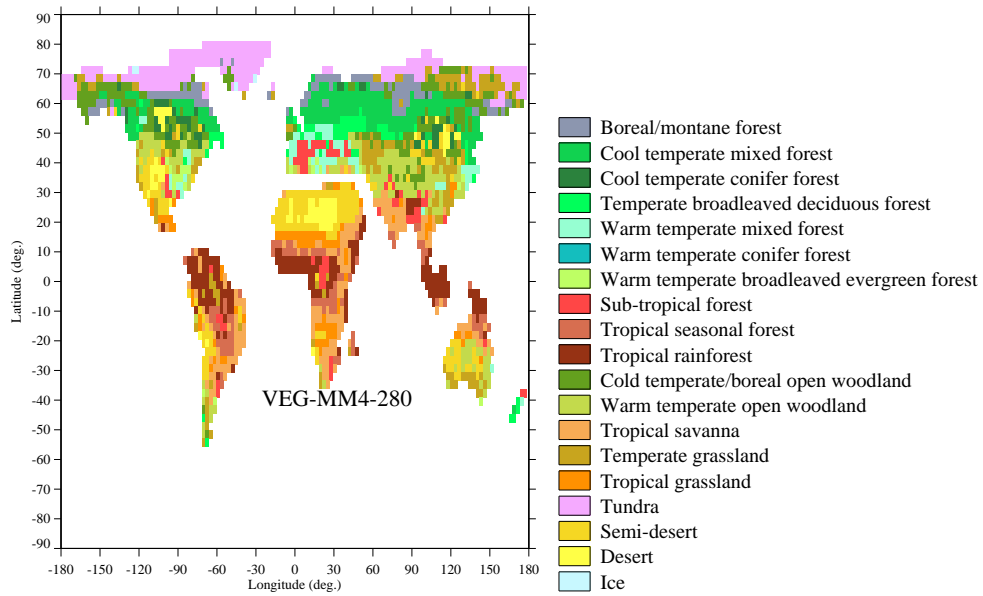
280 ppmv. The biome distribution of this new simulation (VEG-MM4-280) is compared to the biome distribution VEG-500 in Figure 6.28.

At the global scale, the carbon stocks in vegetation and soils strongly decrease in response to the lowering of the atmospheric CO₂ concentration. The total biospheric carbon stock varies from 1321 Gt C at 500 ppmv to 800 Gt C at 280ppmv. This high sensitivity of carbon storage to the atmospheric CO₂ concentration is notably due to the absence of nutrient cycle in the model (FRANÇOIS et al., 2006). The decrease of the CO₂ concentration also affects the net primary productivity, as a direct consequence of the fertilisation effect. The global NPP varies from 86 Gt C/yr at 500 ppmv to 50 Gt C/yr at 280ppmv. All the PFTs are affected by a decrease of NPP. Thus, the atmospheric CO₂ concentration occurs as an important factor for considering the existence of a denser vegetation at the MMCO.

At regional scale, the area of deserts and semi-deserts strongly depends on the CO₂ concentration. In response to the lower CO₂ concentration, the desert and semi-desert areas increase in desertic and peri-desertic regions, e. g. in the Sahara, northeastern China, some parts of Australia and North America. The extent of tropical seasonal forest is also very sensitive to CO₂ effect. At 280 ppmv, the tropical seasonal forests are replaced by tropical savannas and grasslands, e. g. in Indonesia, India and South America. This results can be attributed to the increased sensitivity of the tropical seasonal forest to water stress at lower CO₂ levels due to stomatal opening, giving to forest a disadvantage with respect to grasses in water deficient environments (FRANÇOIS et al., 2006). However, the extent of tropical forest is not significantly modified at lower CO₂ level, and seems to be mainly governed by the precipitation distribution in the MM4 climate experiment.

At middle latitudes, the most striking feature is the replacement of temperate and broadleaved deciduous forests by cool and conifer forests at lower CO₂ level. In Europe, northward of 50°N, the temperate broadleaved deciduous forest biome is notably replaced by cool temperate mixed forest biome. Both broadleaved and needleleaved NPPs are reduced under lower CO₂ level, but needleleaved trees become dominant due to the weaker productivity of broadleaved trees at high latitudes. However, the tundra/boreal forest limit is not modified by the reduction of the CO₂ concentration. Thus, the development of boreal forest at high latitudes can be attributed to the response of the vegetation to the warmer climatic conditions that are induced under a higher atmospheric CO₂ concentration. The sub-tropical forests also remain well present in southern Europe in the VEG-MM4-280 vegetation distribution. The presence of warm forest types in Europe seems therefore linked to

(a) Biome Distribution



(b) Biome Distribution

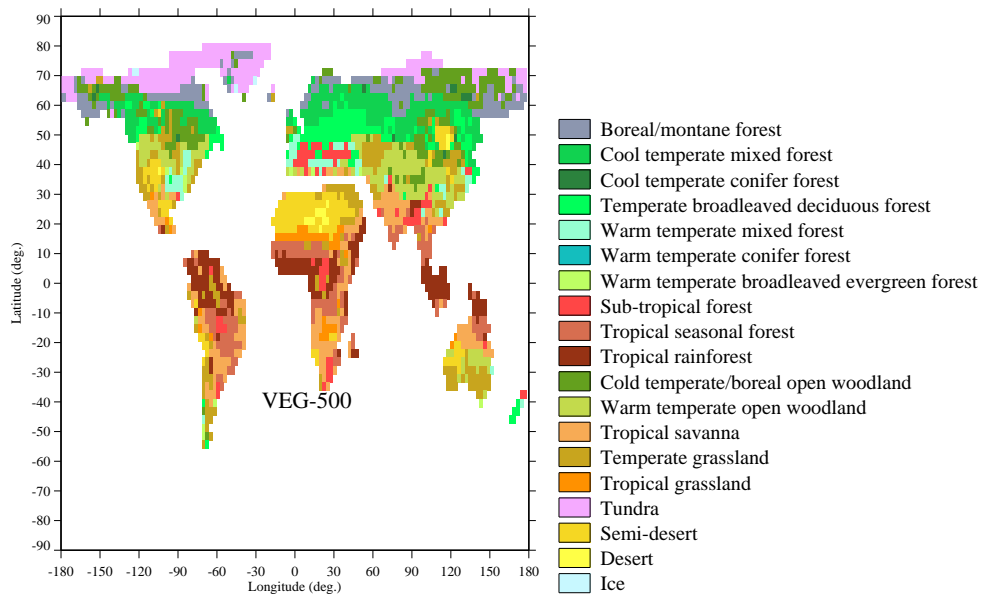


Figure 6.28: (a) VEG-MM4-280 and (b) VEG-500 CARAIB biome distributions.

climate patterns under high CO₂ level and MMCO boundary conditions.

6.1.3 Vegetation feedback on the MMCO climate

The vegetation changes in response to the warmer and wetter MMCO climate could in turn affect the climate. Here, we discuss the vegetation feedback on the MMCO climate at a higher (500 ppmv) and lower (280 ppmv) than present-day atmospheric CO₂ concentration. The surface parameters (surface albedo, roughness length and field capacity) used to force the model have been respectively derived from the two vegetation distributions discussed above (VEG-500 in section 6.1.1 and VEG-280 in section 6.1.2).

The impact of the VEG-500 vegetation distribution on the climate of the MMCO at 500 ppmv of CO₂ has already been discussed in HENROT et al. (2010) (experiment MM4-veg). Here we will only briefly sum up the main vegetation change effects obtained in this experiment. Figure 6.29 shows the annual vegetation feedback on temperature and precipitation of the VEG-500 distribution (differences between experiments MM4-veg and MM4) and of the VEG-280 distribution (differences between experiment MM2-veg and MM2).

Globally, the vegetation cover changes produce an additional warming of +0.5°C and increase the global precipitation by 19 mm/yr in comparison to the MMCO experiment forced with a preindustrial vegetation cover (experiment MM4). The development of denser forests and the replacement of desert and semi-desert by grassland and forest ecosystems decrease the surface albedo on land, which leads to a warming in some regions, notably around the open Tethys Seaway and in Central Asia. However, the opening of the landscape in North America and East Asia increases the surface albedo which induces some cooling in these regions. The expansion of forests, and notably of tropical forest in Africa, increases the rooting depth, which leads to a stronger evaporation and more precipitation over the concerned regions.

The vegetation changes obtained in the VEG-280 vegetation distribution produce a global warming of +0.4°C (+0.3°C on the oceans and +0.6°C on the continents) and an increase of precipitation of +16 mm/yr (+3 mm/yr on the oceans and +43 mm/yr on the continents) compared with experiment MM2. Interestingly, the vegetation feedback at 280 ppmv is of the same sign and magnitude than the vegetation effect at 500 ppmv (see Figure 6.29). Locally, the vegetation change effects in experiment MM2-veg are comparable in distribution and magnitude to the vegetation effects in experiment MM4-veg. The development of forests induces albedo decreases, leading to regional

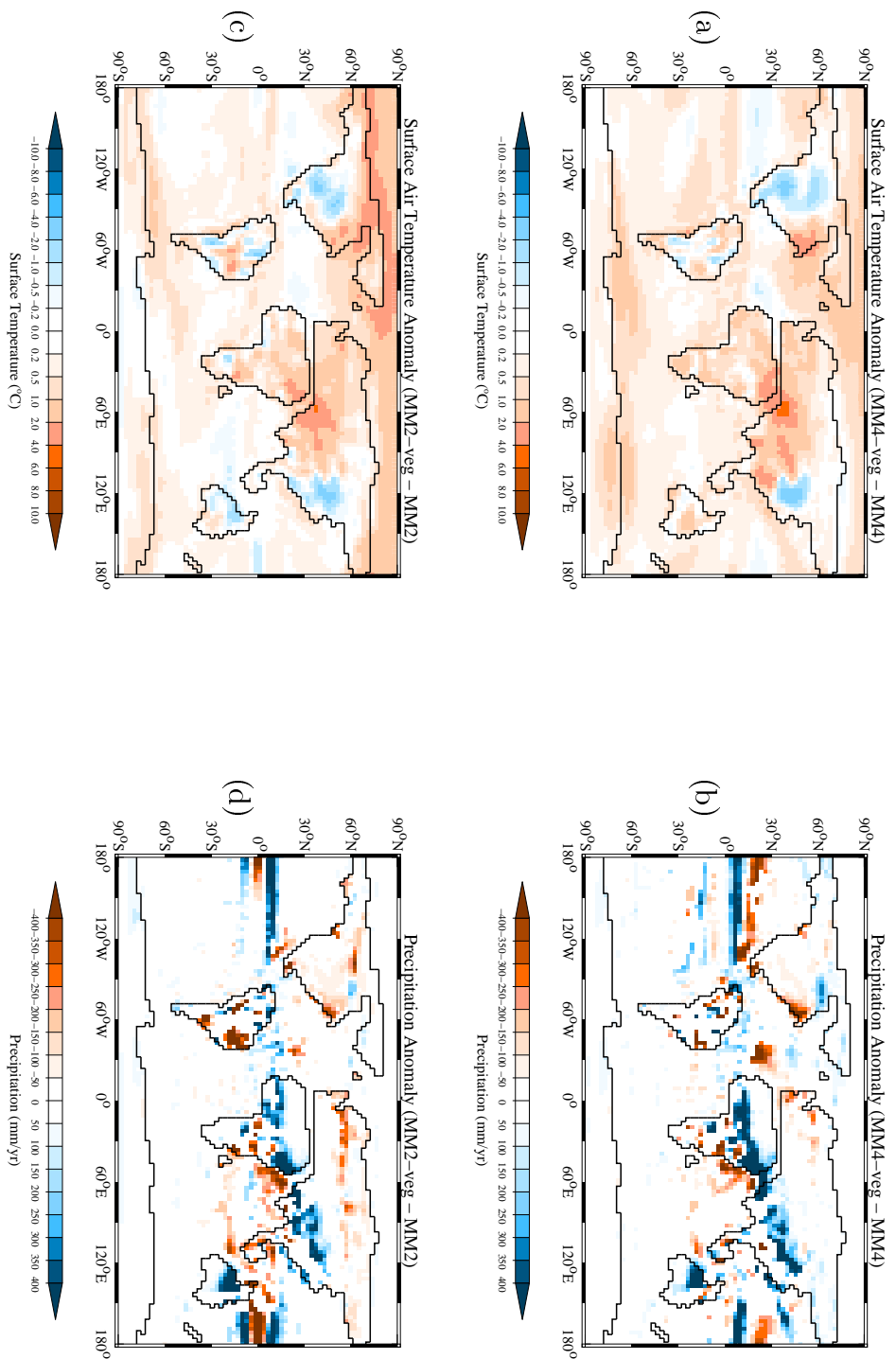


Figure 6.29: Annual mean (a) surface air temperature and (b) precipitation differences between experiments MM4-veg and MM4. Annual mean (c) surface air temperature and (d) precipitation differences between experiments MM2-veg and MM2.

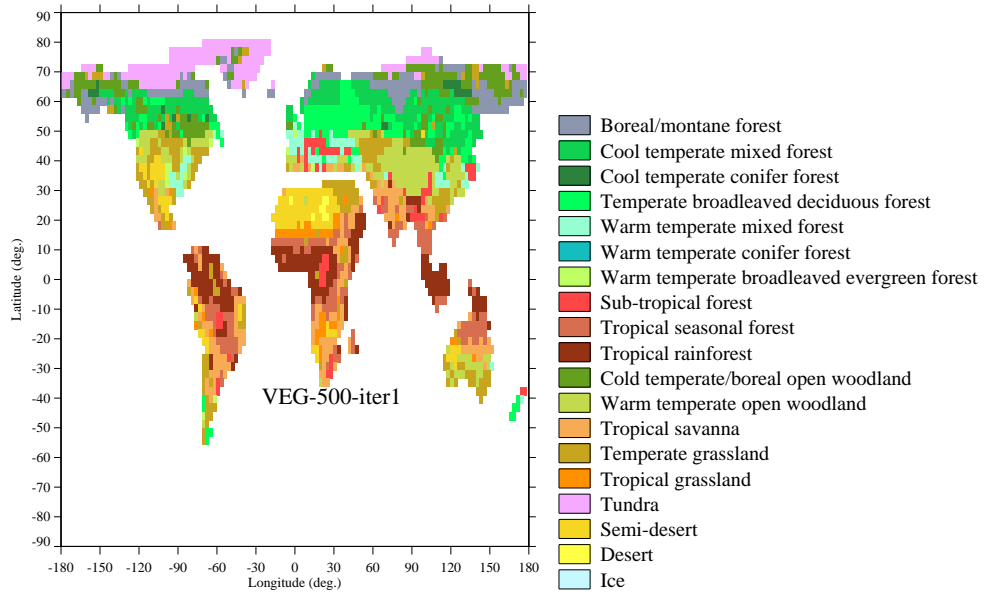
warming, e.g., around the Eastern Tethys Seaway and in Central Asia. The expansion of forest types also increases the soil water content, which causes greater evaporation and precipitation increases, notably in Equatorial and East Africa. However, the vegetation change impacts on land in MM4-veg are slightly stronger than in MM2-veg, due to the more marked expansion of forests in the VEG-500 vegetation distribution, in response to the warmer climate and to the fertilization effect under a high CO₂ concentration. However, the Arctic Ocean experiences a stronger warming in the MM2-veg experiment in comparison to the MM4-veg experiment. This can be explained by the presence of a larger sea-ice cover under colder climatic conditions that responds to vegetation changes at high latitudes with a larger sensitivity.

6.1.4 Climate-vegetation iterations at Middle Miocene

In order to check whether the vegetation feedback on climate could lead to vegetation changes and in turn climate changes, we carried out a series of iterations with Plasim and CARAIB, following the equilibrium asynchronous coupling procedure (see Section 3.3). We performed two series of three iterations starting respectively from experiment MM4-veg and MM2-veg as the initial vegetation states. Then, the Planet Simulator was forced with the vegetation parameters derived from respectively the MM4-veg and MM2-veg vegetation distribution to complete the initial state. The results of the initial vegetation and climate states have been discussed in the previous sections (Sections 6.1.1, 6.1.2 and 6.1.3). They are referred here as ITER 0.

The vegetation distributions VEG-500-iter1 and VEG-280-iter1, obtained at the first vegetation iteration, using respectively the climates of experiments MM4-veg and MM2-veg are shown in Figure 6.30. Both VEG-500-iter1 and VEG-280-iter1 vegetation distributions differ only slightly from the initial vegetation distributions produced before, i.e. VEG-500 and VEG-280. In the VEG-500-iter1 distribution, boreal forests and cold temperate open woodlands continue to expand to the north at high latitudes, in response to the vegetation-induced warming in climate experiment MM4-veg (see section 6.1.3). In the VEG-280-iter1 distribution, the tundra still dominates the high latitudes vegetation and also expand further north in response to high latitudes warming in climate experiment MM2-veg. At middle latitudes, in both VEG-500-iter1 and VEG-280-iter1 distributions, temperate broadleaved forests develop at the expense of colder conifer forests, and extend to higher latitudes. In Europe, subtropical biomes remain well productive and warm temperate mixed forest extend to the north. The thermophilous elements

(a) Biome Distribution



(b) Biome Distribution

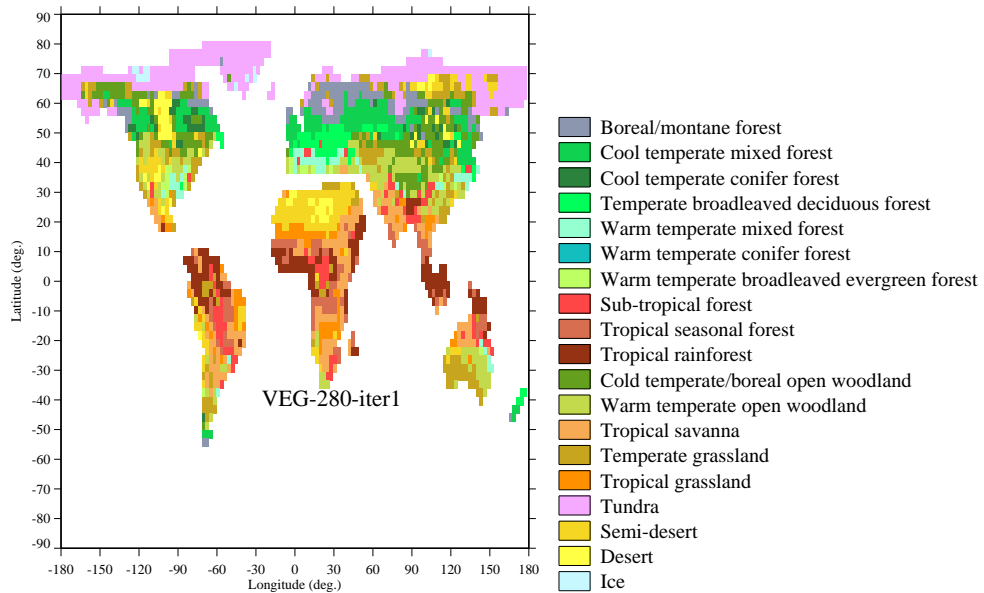


Figure 6.30: (a) VEG-500-iter1 and (b) VEG-280-iter1 CARAIB biome distributions.

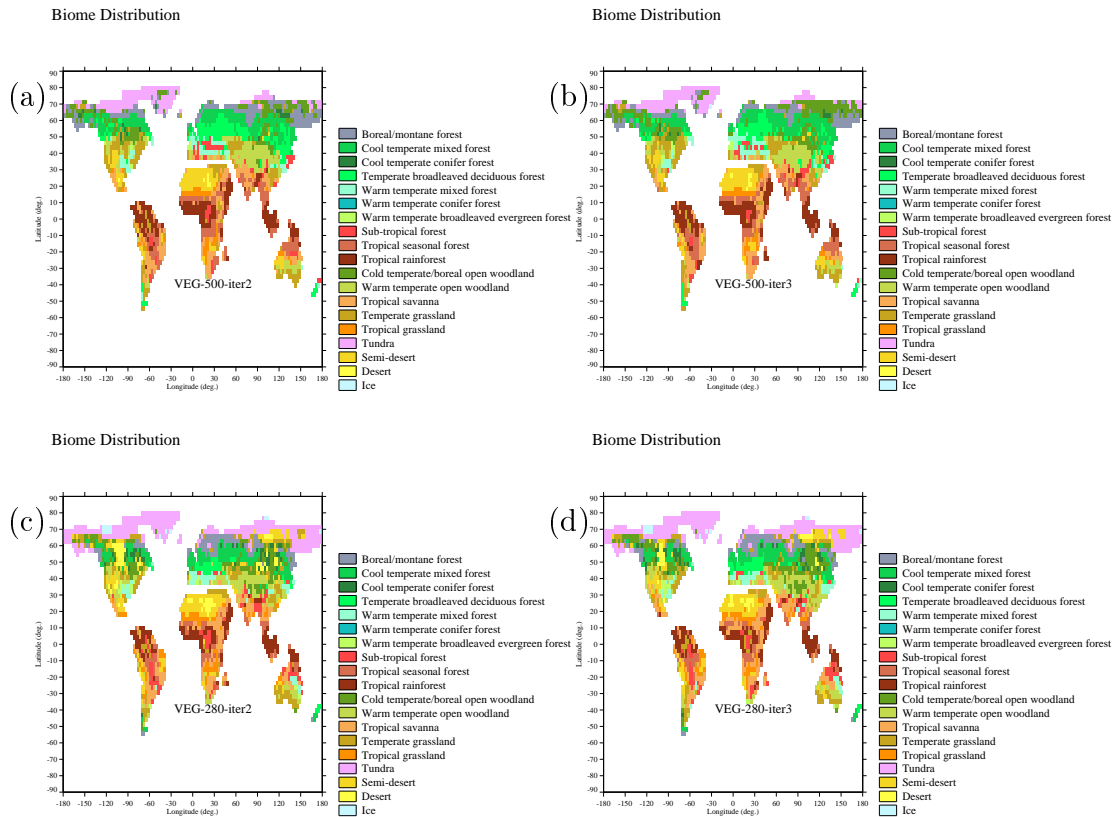


Figure 6.31: (a) VEG-500-iter2, (b) VEG-500-iter3, (c) VEG-280-iter2 and (d) VEG-280-iter3 CARAIB biome distributions.

also reappear in East and Central Asia. Tropical forest also expand in East Africa. However, in the VEG-280-iter1 distribution, desert areas develop in North America in response to the cooling in the experiment MM2-veg, induced by an increase of the surface albedo in response to the opening of the landscape in the VEG-280 vegetation distribution (response to positive vegetation feedback).

The vegetation distributions produced at the next two iterations (respectively VEG-500-iter2, VEG-280-iter2 and VEG-500-iter3, VEG-280-iter3) show very little changes in comparison to the vegetation distributions produced at the first iteration (see Figure 6.31). Boreal forests or tundra continue to expand at high latitudes, and temperate forest to extend at middle latitudes. The desert areas formed in North America in VEG-280-iter1 slightly extend in the following vegetation distributions. In the vegetation distributions produced at the third iteration the biome differences in compar-

ison to the biome distributions produced at the second iteration concern only a few isolated grid elements and most of the differences can be attributed to the biome classification procedure, using thresholds to determine the biomes that can be easily crossed especially at the relatively low resolution of the experiments.

The successive temperature and precipitation anomalies in response to the respective vegetation changes are shown in Figure 6.32, for the first climate iteration and both 500 and 280 ppmv CO₂ levels, and in Figure 6.33, for the second iteration and both CO₂ levels. The anomalies of the third iteration are not shown since they are very weak and non significant. Due to the small changes occurring in the vegetation cover at both CO₂ levels, the climate anomalies are very weak and only concern a few regions. East Africa notably experiences a slight warming linked to the expansion of tropical forest. In North China the development of temperate forest also leads to a slight temperature increase. However, the opening of the landscape and development of desert in North America induces slight decreases of the temperature.

Considering the slight changes obtained in the series of vegetation distributions and climate anomalies, we stopped the iteration procedure after 3 iterations and considered that the vegetation and climate we simulated here have both reached an equilibrium state. The equilibrium vegetation and climate state obtained here only slightly differ from the initial ones. However, in the series of iterations, the forest biomes continue to expand at middle and high latitudes, especially under a high CO₂ level, which in turn slightly amplifies the warm and humid conditions over the continents. Thus, this confirms that the consideration of climate and vegetation interactions at the MMCO helps to improve the climate and vegetation modelling results.

6.1.5 Conclusions

First, the CARAIB results discussed here suggest that the VEG-500 vegetation distribution produced under a higher CO₂ level is in better agreement with the available proxy-based reconstructions for the MMCO than VEG-280. The vegetation results also support the climatic results discussed in HENROT et al. (2010), suggesting that higher than preindustrial concentrations of CO₂ are most likely required to reconcile Miocene climate simulations with appropriate climatic reconstructions. Here the increase of the atmospheric CO₂ concentration to higher than preindustrial concentration contributes to generate a warmer and more humid climate that allows the

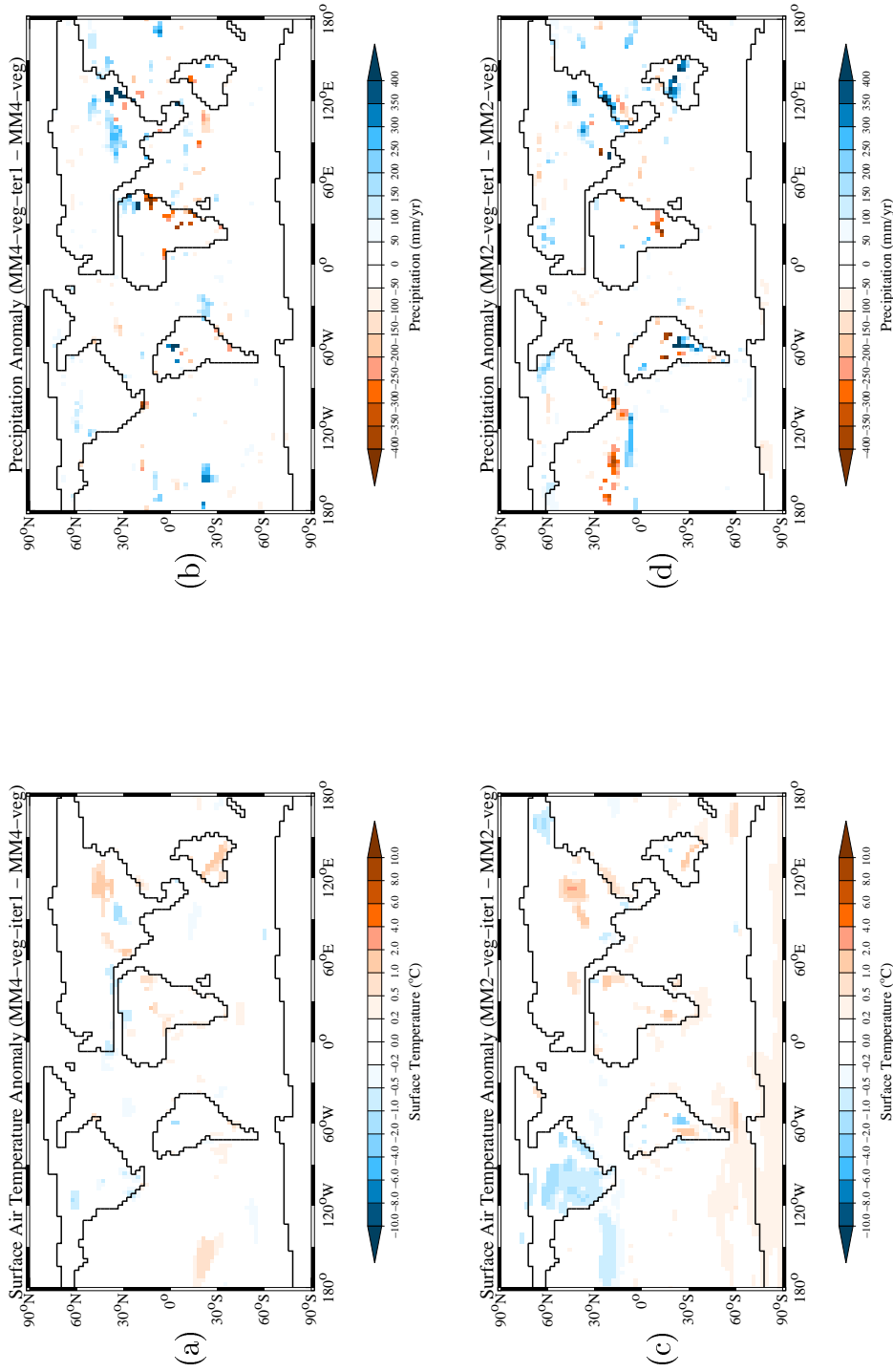


Figure 6.32: Annual mean (a) surface air temperature differences and (b) precipitation differences between experiments MM4-veg-iter1 and MM4-veg. Annual mean (c) surface air temperature differences and (d) precipitation differences between experiments MM2-veg-iter1 and MM2-veg.

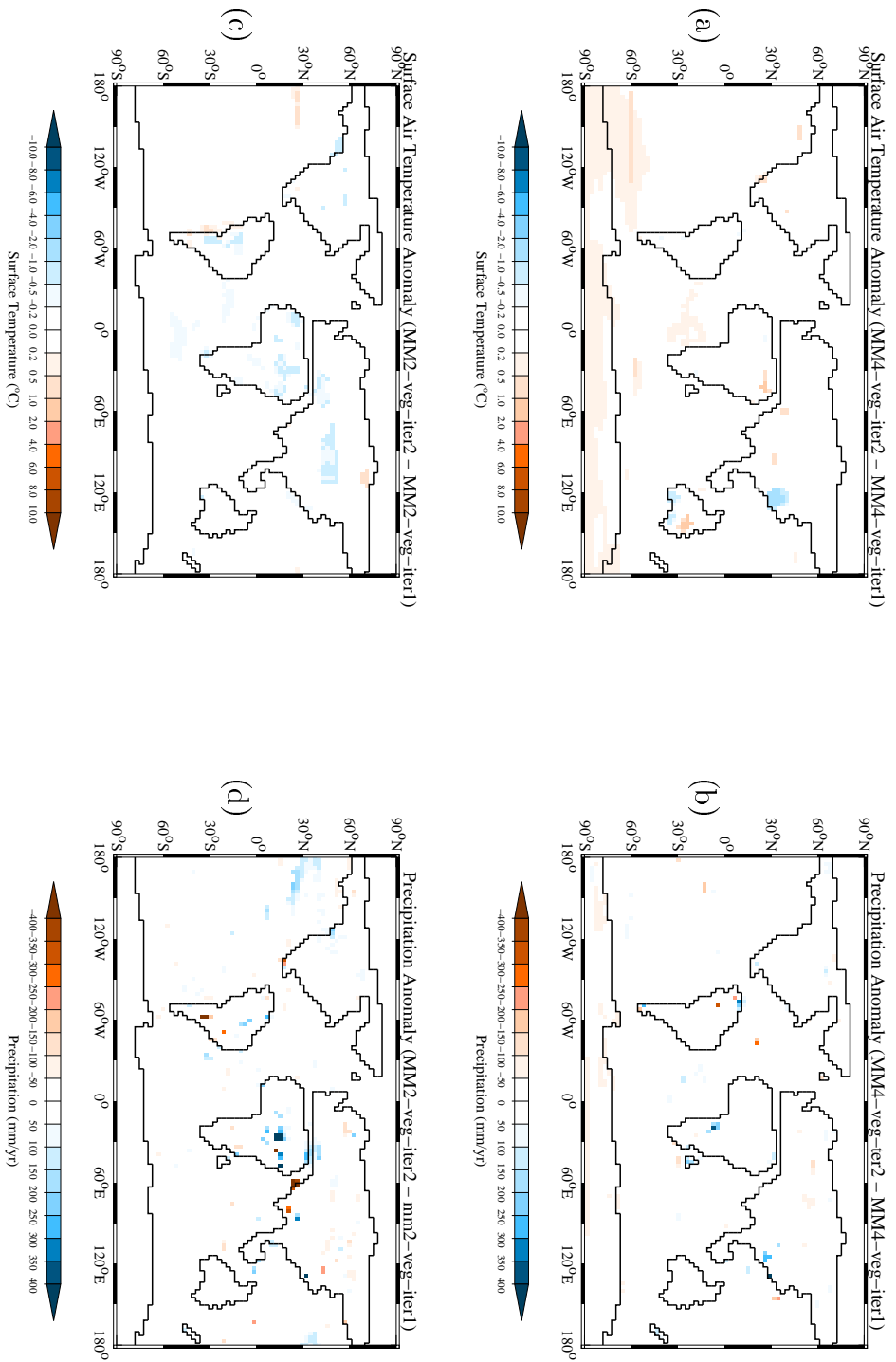


Figure 6.33: Annual mean (a) surface air temperature differences and (b) precipitation differences between experiments MM4-veg-iter2 and MM4-veg-iter1. Annual mean (c) surface air temperature differences and (d) precipitation differences between experiments MM2-veg-iter2 and MM2-veg-iter1.

warm forest types to expand poleward and reduces the desert and semi-desert areas. Moreover, the CO₂ concentration increase also impacts on the biosphere through its fertilization effect and benefits the forest and grassland ecosystems at the expense of desert. Nevertheless, the VEG-280 vegetation distribution suggests that the warming and weakening of the seasonal temperature gradient as well as the wetter conditions that prevail in Europe in response to a lower topography are sufficient to allow the thermophilous trees types to install in Europe at the MMCO. However, due to the lower productivities of the thermophilous types in Europe, the VEG-280 vegetation distribution rather suggests the presence in the region of warm mixed forests, including deciduous temperate and thermophilous trees, in agreement with JIMENEZ-MORENO (2006) and JIMENEZ-MORENO et al. (2008).

Furthermore, the vegetation changes produced under a lower or a higher CO₂ concentration than the present-day one contribute to increase the temperature and precipitation especially on the continents. Therefore, the vegetation feedback amplifies the warmer and wetter climatic conditions produced by Middle Miocene boundary conditions, particularly the lowering of the topography, even in the case of a low CO₂ concentration (see MM2-veg results). Moreover, the vegetation feedbacks at 500 ppmv and 280 ppmv are comparable in terms of magnitude, which suggests that a high CO₂ concentration is not entirely necessary to produce vegetation changes that significantly impact on climate.

In conclusion, the results presented here suggest that vegetation changes could have played a significant role on the MMCO climate, since the vegetation feedbacks discussed here contribute to maintain and even amplify the warm and humid conditions produced in the Miocene climate experiments, even under a low preindustrial atmospheric CO₂ concentration. The vegetation-climate interactions could also provide a complementary, if not an alternative mechanism, to the large increase of CO₂ required by the models to produce the estimated warming at the MMCO (YOU et al., 2009; TONG et al., 2009; HENROT et al., 2010). They could help to reconcile the proxy-based MMCO climate reconstructions suggesting large warming at the MMCO (FLOWER and KENNETT, 1994; ZACHOS et al., 2001; MOSBRUGGER et al., 2005; UTESCHER et al., 2007) and model-based climate reconstructions.

The climate and vegetation produced at high CO₂ concentration (500 ppmv) are in best agreement with proxy-based climate and vegetation reconstructions (MOSBRUGGER et al., 2005; UTESCHER et al., 2007; JIMENEZ-MORENO et al., 2008). Nevertheless, a more precise comparison

to proxy-data in terms of taxa could improve the comparison of the vegetation distributions at different CO₂ concentrations (FRANÇOIS et al. (submitted)—see Appendix A). The vegetation results presented here are also highly dependent on the vegetation classification used in CARAIB. Recent results using an extended classification including 26 PFTs show that some extended thermophilous types can be well productive notably in Europe under a preindustrial CO₂ level, which better agrees with the pollen analysis (JIMENEZ-MORENO, 2006; JIMENEZ-MORENO et al., 2008), and that tropical types can also install in southern Europe at atmospheric CO₂ concentrations below 500 ppmv (FAVRE et al., 2010).

Conclusions

In the framework of this study, we have examined climate-vegetation interactions with (1) the dynamic global vegetation model CARAIB, and (2) the Earth system model of intermediate complexity Planet Simulator. Both models have been made to interact through an equilibrium asynchronous coupling procedure. This procedure consists of a series of iterations where the climate resulting from an equilibrium run of the climate model is used to drive changes in the equilibrium distribution of vegetation types, which in turn are fed back into the land surface scheme of the climate model through surface albedo, roughness length and field capacity. The coupled system has been applied to study the joint evolutions of climate and vegetation during three relatively well documented geological periods that have experienced large scale climate and vegetation changes: the Last Glacial Maximum, the Middle Pliocene and the Middle Miocene.

At a first stage, we used the Planet Simulator to investigate the implications of land surface cover change on the Last Glacial Maximum climate. We carried out a series of sensitivity experiments, investigating the contributions of the ice sheet expansion and elevation, the lowering of the atmospheric CO₂ and of the vegetation cover change on the LGM climate. We applied the factor separation method of STEIN and ALPERT (1993), in order to rigorously determine the different contributions of the boundary condition modifications, and to isolate the pure contribution of the vegetation cover change. Our results highlight the dominant cooling and drying effect of the ice sheet expansion on the global LGM climate. The expansion of ice sheet contributes to cool the global temperature by 2.6°C. The next most important factors are the lower CO₂ concentration in the atmosphere, which cools the global climate by 2°C, and the vegetation cover change. Our results suggest that the isolated vegetation contribution may have played a significant role in maintaining cold and dry climatic conditions at the LGM, which is in good agreement with the results of previous modelling studies (GANOPOLSKI, 2003; JAHN et al., 2005; SCHNEIDER VON DEIMLING et al., 2006). The

expansion of desert and grassland ecosystems, in response to cold and dry climatic conditions, leads to surface albedo increases that induce an additional global cooling by 0.9°C and an additional precipitation decrease of 10 mm/yr , when the vegetation changes are combined with the other boundary conditions changes at LGM. Vegetation changes at the LGM notably induce strong cooling over the continents of the Northern Hemisphere that further affect the tropical precipitation and reinforce the southward shift of the ITCZ, when combined with the ice forcing. Furthermore, the inclusion of the vegetation feedback in the climate model improves the comparison between the LGM simulated climate and climatic reconstructions over Eurasia (WU et al., 2007).

In a second stage, we used the climate and vegetation models to study the warm climate and corresponding vegetation changes at the Middle Pliocene. We simulated the Middle Pliocene climate by following the protocol set up for the Pliocene Model Intercomparison Project (HAYWOOD et al., 2010) and using the latest version of the PRISM3D data set (HAYWOOD et al., 2010) to prescribe initial and boundary conditions for the Planet Simulator. In addition to the simulation experiments required by that protocol, we also reconstructed the vegetation distribution of the Middle Pliocene in response to the simulated climate, using CARAIB, to assess the effect of vegetation cover changes on the Pliocene climate. Our Middle Pliocene climate simulation results in a globally warmer ($+2.2^{\circ}\text{C}$) and wetter ($+3.5\%$) climate relative to present-day climate, with a reduced equator-to-pole gradient in temperature and precipitation. As a consequence, the CARAIB vegetation distribution shows a reduction of the desert areas at the Middle Pliocene, and an expansion of forests, especially at high latitudes where boreal and cold forests replace tundra. These results are in good agreement with previous climate and vegetation modelling results (HAYWOOD et al., 2009a; JOST et al., 2009; SALZMANN et al., 2008). However, the comparison of the vegetation feedbacks on the Middle Pliocene climate, derived from the BIOME4 and CARAIB vegetation models, highlights again the influence on climatic results of the vegetation parameterisations used in vegetation models. The differences in the vegetation feedbacks calculated from the two vegetation models mainly reflect the differences in the vegetation parameter values used in the CARAIB and BIOME4 models rather than vegetation change effects in response to the simulated climate.

Finally, we also applied the climate and vegetation models to study the Middle Miocene climate and vegetation. We first performed several sensitivity experiments in order to evaluate the vegetation feedback on the Middle Miocene climate against the effects of land-sea configuration, oceanic heat

transfer, topography and atmospheric CO₂ concentration changes. Furthermore, we compared the Middle Miocene vegetation distributions simulated by CARAIB under various CO₂ levels with available proxy-based vegetation reconstructions, and also compared their potential feedback on climate at different CO₂ levels. Our results show that a higher than present-day CO₂ concentration is necessary to generate a warmer climate at all latitudes at the Middle Miocene. The increase of the atmospheric CO₂ concentration from 280 to 500 ppmv warms the global surface temperature by 2.6°C. Nevertheless, the changes in sea-surface conditions, the lowering of the topography on land and the vegetation feedback also produce temperature increases that may, locally, even be stronger than the CO₂ induced temperature increases. The expansion of forest ecosystems, in response to warm and humid climatic conditions, leads to an additional warming of the global climate by 0.5°C and an additional precipitation increase of 19 mm/yr. Our results show that the vegetation feedback on climate may have contributed to maintain and even to intensify the warm and humid conditions produced by the other factors, suggesting that vegetation-climate interactions could help to improve the model-data comparison for this period. The expansion of warm forest types poleward and the reduction of the desert and semi-desert areas that we simulate are in good agreement with proxy-based reconstructions (MOSBRUGGER et al., 2005; UTESCHER et al., 2007). It is, however, the climate and vegetation produced at high CO₂ concentration (500 ppmv) that are in best agreement with the proxy-based climate and vegetation reconstructions, suggesting that significantly higher than preindustrial concentrations of CO₂ are most likely required to reconcile Miocene climate simulations with appropriate climatic reconstructions.

In a general way, the results of this thesis highlight the importance of taking into account the interactions between climate and vegetation in paleoclimate modelling. The changes in the surface parameters (surface albedo, roughness length and rooting depth) in response to the vegetation changes that occurred during the past periods studied here are sufficient to affect the biophysical processes included in the climate model parameterisation, and thus to significantly impact on climate. Moreover, our results also illustrate that considering the vegetation feedback on climate helps to improve the comparison of climate modelling results to proxy-based reconstructions for the studied periods.

Thus, it would be interesting to apply the vegetation and climate models to other periods of the more recent or ancient geological past for which climate models so far failed to reproduce the climatic patterns inferred from proxy data analysis, such as high-latitude warming inducing the develop-

ment of dense forests at high latitudes, weakening of the equator-to-pole temperature gradient, or large scale precipitation changes. For example, the CARAIB and Planet Simulator models could be used to study the warm climate of the Paleocene-Eocene Thermal Maximum (PETM, around 55 Ma BP) that is characterised by an abrupt increase of global temperature coincident with a massive release of carbon to the oceans and the atmosphere, and the development of dense and warm (even tropical) forests over the continents (BOWEN et al., 2006; SLUIJS et al., 2007). On the other hand, the models could also be applied to the study of more recent climatic events, such as the case of the *green Sahara* during the Holocene climatic optimum some 9000 to 6000 years ago, for which previous modelling studies demonstrated the important role of climate and vegetation interactions (GANOPOLSKI et al., 1998; BROVKIN et al., 2002).

Nevertheless, the coupling technique that we applied here does not enable a complete representation of the climate-vegetation interactions, notably of the biogeochemical processes that are important to understand long term climate changes. The equilibrium asynchronous procedure has also shown several limitations in its application. As notably mentioned by FOLEY et al. (1998, 2000), this procedure is unable to simulate transient changes in vegetation and climate and to address the time-dependent nature of the atmosphere-biosphere response to climate variability. Moreover, the surface energy and water balances are calculated differently in the climate and vegetation models. In consequence, the behaviour of the coupled climate-vegetation model does not guarantee that water and energy are properly conserved.

Thus, the first important topic to be envisaged for future research would be the improvement of the coupling between the Planet Simulator and the CARAIB models. To provide a more direct linkage between the atmospheric and ecological processes, the CARAIB model should be fully incorporated within the Planet Simulator, replacing the terrestrial component of this latter. The climate and vegetation could therefore interact through an on-line coupling. Such a completely coupled climate-vegetation model could notably be used to study the transient evolution of climate and vegetation in response to boundary conditions changes during the Holocene (11.8 kyr B.P. to present-day), for which abundant and well-dated pollen records exist. Additional developments to produce a fully-coupled PlanetSimulator-CARAIB model have been done in parallel to the work presented in this study, and will be the subject of a technical report.

The simulation of realistic transient climate-vegetation evolutions in the

past, or in the near-future in the framework of global warming scenarios, would benefit of several improvements in the CARAIB model. The introduction of a dispersal module into CARAIB should allow to study more accurately the potential shift and survival of plant species under climate changes. It would also be interesting to apply CARAIB at the species level to analyse the response of a selected set of plant species to climate change, since individual species are probably more vulnerable to climate change than PFTs (DURY et al., submitted). The introduction of a fire module, in order to take into account the impact of wild- and human-induced fires on the plant distribution and mortality, may improve the simulation of future vegetation distribution (DURY et al., submitted).

Furthermore, a good representation of the climate system mechanisms is also crucial to model realistic vegetation distributions for past, present and future periods. The Planet Simulator notably shows some limitations, regarding for example the representation of the oceanic circulation and oceanic processes, and the atmospheric trace gases which may also significantly affect climate and vegetation (e. g., methane (CH_4), nitrous oxide (N_2O), aerosols). Ongoing efforts are made at the Hamburg University to couple the Planet Simulator to the LSG oceanic general circulation model (MAIER-REIMER et al., 1993), thus opening long-term perspectives, not only from a climatic point of view but also from a biogeochemical point of view (carbon cycle). Switching to a more complex climate model, such as the atmospheric GCM ECHAM5 (ROECKNER et al., 2003), which is coupled to the oceanic general circulation model MPI-OM in the COSMOS framework (JUNGCCLAUS et al., 2006; WETZEL et al., 2006), could also be a possibility to improve the representation of climate mechanisms, and thus the representation of climate-vegetation interactions.

Finally, the comparison of climate and vegetation modelling results over past periods against proxy-based reconstructions are also important to validate the models results, and in the case of mismatch to better understand the behaviour of the models. Here, the vegetation results have notably been compared to terrestrial proxy-based reconstructions on the basis of biomes or plant functional types. It will be interesting to pursue this comparison in applying a rigorous and more systematic methodology based on precise criteria, such as the one developed in FRANÇOIS et al. (submitted) (see Appendix A).

Appendix A

Modelling Late Miocene vegetation in Europe: results of the CARAIB model and comparison with palaeovegetation data

In this appendix chapter the complete text of FRANÇOIS et al. (submitted) is reproduced. This paper presents the results of the Late Miocene (Tortonian) vegetation simulation with CARAIB and describes a new methodology for comparing vegetation results to palaeo-vegetation and pollen data on the basis of presence/absence of plant functional types.

**Modelling Late Miocene vegetation in Europe: results of the CARAIB model
and comparison with palaeovegetation data**

L. François^{a,*}, T. Utescher^b, E. Favre^a, A.-J. Henrot^c, P. Warnant^a, A. Micheels^d, B. Erdei^c
, J.-P. Suc^f, R. Cheddadi^g, V. Mosbrugger^d

^a *Unité de Modélisation du Climat et des Cycles Biogéochimiques (UMCCB), Université de Liège, Bât. B5c, Allée du Six Août 17, B-4000 Liège (Belgium)*

^b *Steinmann Institute, University of Bonn, Nussallee 8, D-53115 Bonn (Germany)*

^c *Laboratoire de Physique Atmosphérique et Planétaire (LPAP), Université de Liège, Bât. B5c, Allée du Six Août 17, B-4000 Liège (Belgium)*

^d *Senckenberg Research Institute und Nature Museum, LOEWE - Biodiversity and Climate Research Centre (LOEWE BiK-F), Senckenberganlage 25 D-60325 Frankfurt am Main, (Germany)*

^e *Botanical Department, Hungarian Natural History Museum, H-1476, POB222 (Hungary)*

^f *Institut des Sciences de la Terre de Paris (UMR 7193 CNRS), Université Pierre et Marie Curie, 4 place Jussieu, case 117, 75252 Paris Cedex 05 (France)*

^g *Institut des Sciences de l'Evolution, CNRS UMR 5554, Université de Montpellier II, Case Postale 061, Place Eugène Bataillon, F-34095 Montpellier (France)*

Abstract

The CARAIB (CARbon Assimilation In the Biosphere) model is used to study the vegetation distribution during the Late Miocene (Tortonian). In this version, the plant classification is specifically adapted to best represent Miocene European vegetation. Compared to other plant classifications used in global models, this adapted classification is finer, since it is specifically developed for European vegetation and it involves various thermophilous tree types, which were present in Europe during the Miocene. The corresponding climatic tolerance parameters are based on the study of Laurent et al. (2004) for the tree types currently present in Europe and on the distribution of analogue species in southeastern Asia and North/Central America for the thermophilous (sub-tropical) trees. The same classification is used to characterize the palaeoflora at the available Late Miocene localities, allowing a model-data comparison at the plant functional type

* Corresponding author: Tel. +32-4-3669776 ; Fax +32-4-3669711 ; e-mail: louis.francois@ulg.ac.be

level, rather than at the biome level. The climatic inputs to CARAIB are obtained from the COSMOS atmosphere-ocean general circulation model. The climatic anomalies (Tortonian minus Present) derived from COSMOS are interpolated to a higher spatial resolution before being used in the vegetation model. These anomalies are combined with a modern climatology to produce climatic fields with high spatial resolution ($10' \times 10'$). This procedure has the advantage of making apparent relief features smaller than the grid cells of the climate model and, hence, makes easier the comparison with local vegetation data, although it does not really improve the quality of the Tortonian climate reconstruction. The new version of CARAIB was run over Europe at this higher spatial resolution. It calculates the potential distribution of 13 different classes of trees (including cold/cool/warm-temperate, sub-tropical and tropical types), together with their cover fractions, net primary productivities and biomasses. The resulting model vegetation distribution reconstructed for the Tortonian is compared to available palaeo-vegetation and pollen data. Before performing this comparison, the tree taxa present at the various data sites are assigned to one or several model classes, depending on the identification level of the taxa. If several classes are possible for a taxon, only those that can co-exist with the other tree classes identified at the site are retained. This methodology is similar to the co-existence approach used in palaeoclimatic reconstructions based on vegetation data. It narrows the range of tree types present at the various sites, by suppressing in the data the extreme types, such as the cold boreal/temperate and tropical trees. The method allows a comparison with the model simulation on a presence/absence basis. This comparison provides an overall agreement of 53% between the model and the data, when all sites and tree types are considered. The agreement is high (> 85 %) for needle-leaved summergreen boreal/temperate cold trees (*Larix* sp.) and for tropical trees, intermediate (> 40 %) for other boreal/temperate cold trees and for needle-leaved evergreen temperate cool trees, broadleaved summergreen temperate cool trees and broadleaved evergreen warm-temperate trees, and poor (< 40 %) for most temperate perhumid warm trees. In many cases, the model is shown to be better at predicting the absence than the presence, as observed for tropical trees. The modelled distributions of cold boreal/temperate trees tend to extend too much towards the south compared to the data. By contrast, model sub-tropical trees (temperate perhumid warm and needle-leaf summergreen temperate warm trees) appear to be restricted to some limited areas in southern Europe, while they are present in the data from central Europe up to at least 50°N. Consequently, modelled Late Miocene climate appears to remain too cold to produce assemblages of trees consistent with the data. The predicted modelled trends from the past to the present are in the good direction, but the amplitude remains too small. For the simulations to be in a better agreement with the data, higher CO₂ levels may be necessary in the climate simulations, or possibly other oceanic boundary conditions may be required, such as different bathymetry in the Panama seaway.

Keywords : Miocene, Europe, vegetation, model, palaeovegetation data, plant functional types, biomes

1. Introduction

The CARAIB model is used to study the vegetation in Europe simulated for the Tortonian (11.61 - 7.25 Ma). Although the time-span studied coincides with the Late Miocene cooling (Zachos et al., 2001) and the first presence of sea ice in the Northern High Latitudes (e.g., Darby, 2008) there is evidence from various proxy data that climate still was all over warmer and more humid than today, especially in the mid- and the higher latitudes. Also latitudinal and longitudinal climate gradients were shallower than at present (e.g., Bruch et al, 2007; Fauquette et al., 2007). In the continental realm various proxy data, such as the plant and mammal fossil records and systematics-based climate reconstructions allow to quantify continental climates and provide an insight into spatial patterns and amplitudes of change in time series all over Europe (e.g., Akkiraz et al., this volume; Boehme et al., this volume; Bruch et al. 2007; this volume; Utescher et al., 2009; this volume). Using proxy data it is inferred that in Central Europe mean annual temperatures were higher by ca. 5°C than today (e.g., Mosbrugger et al., 2005), the study of Utescher et al. (this volume) shows strong positive temperature anomalies for both, the cold and the warm season for the mid-latitudes of Central and Eastern Europe in the 5 °C at a minimum. According to palaeobotanical proxies temperature were only slightly raised in the lower latitudes of Europe when compared to present (e.g., Utescher et al., this volume) but conditions were all over more humid, a Mediterranean type climate did not yet exist (e.g., Bertini, 2003).

Consistently Tortonian phytocoenoses should display a distinctly warmer and/or more humid aspect, in dependence of its geographical position, when compared to modern potential vegetation.

There exist numerous qualitative descriptions of the vegetation types recorded in the European Tortonian (e.g., Mai, 1995; Eder-Kovar et al., 1996). In more recent times, semi-quantitative and quantitative studies were carried out on well dated late Miocene floras focussing on diversity patterns of plant functional types (Utescher et al., 2007a; Eder-Kovar et al., 2008). According to these studies deciduous forest was the dominant zonal vegetation type all over Central Europe, extending over the former Western Paratethys (Molasse Basin, Styrian Basin, and Vienna Basin)

along the north coast of Lake Pannon to the Transcarpathian realm and Ukraine. Depending on the region this vegetation may contain a minor proportion of broadleaved evergreen elements (e.g., Erdei et al., 2007; Utescher et al., 2007a; Ivanov et al., this volume). Towards the lower latitudes, all over Spain, in the southern Pannonian realm, and in the Eastern Paratethys, Mixed Mesophytic Forests existed. This forest type is characterized by a higher account of broadleaved evergreen trees, partly thermophilous conifers are important as well.

In the Southwest of the study area and along the south coast of the Eastern Paratethys the presence of sclerophyllous broadleaved trees points to the presence of a drier season (Utescher et al., 2007a,b). In the East and the Southeast partly open woodlands existed in the earlier part of the time-span studied (e.g., Ivanov et al., this volume)

The Tortonian was characterized by all over warmer climate conditions with respect to the present and is thus an example of a warmer world that may help understand future climate, although it cannot be considered as direct analogue for the future. Indeed, atmospheric CO₂ contents and palaeogeography differ from the present-day situation and prognosticated evolution, as well as the rate of warming. In the Tortonian mainly the southern part of the study area did undergo considerable palaeogeographic shifts, such as orogenic uplift (e.g., Carpathians), subsidence (e.g., Pannonian basin), and volcanism. A large brackish water body, the Lake Pannon, formed as a result of plate reorganisation in the Central Paratethys and was filled in by sediment discharge of huge river delta systems (e.g., Magyar et al., 1999). In the Tethyan realm the Western Mediterranean Basin was opened, except for the Tyrrhenian Sea. Our palaeogeographic maps consider the classical connection between the Mediterranean and the Eastern Paratethys through the Bosphorus area (Popov et al., 2004, 2006), a concept which has been recently severely questioned (Melinte-Dobrinescu et al., 2009) in favour of a long and narrow marine gateway through the Balkans, particularly through the areas of Skopje and Niš where the connection between the Pannonian and Dacic basins took also place (Popescu et al., 2009). It is clear that these specific settings had an impact on regional climate and vegetation hampering a direct comparison with modern or near future condition. There is, however, no doubt that on a continent-wide scale, the Tortonian example is useful to assess future scenarios.

Also, palaeoclimatic and palaeovegetation simulations have been performed for this period (Steppuhn et al., 2006, 2007; François et al., 2006; Micheels et al., 2007; Gladstone et al., 2007; Micheels et al., 2009). New climatic simulations have been performed for the Tortonian with

COSMOS (Eronen et al., 2009; Micheels et al., this volume), i.e., the coupled atmosphere-ocean general circulation model (AOGCM) ECHAM5-MPIOM which allows to better integrate the oceanic contributions (e.g., opening of oceanic pathways) in the climatic simulation and to produce the inputs for the CARAIB dynamic vegetation model.

The aim of this study is to develop a methodology to validate climate and vegetation model runs for some Neogene time slices on the basis of available palaeoflora. We will apply this method to the validation of the CARAIB dynamic vegetation model forced with ECHAM5-MPIOM Tortonian climatology in Europe. The simulation results will be compared to available palaeo-vegetation data of several localities in Europe. This is the reason why the classification of the CARAIB vegetation model is specially adapted to the vegetation which was present in Europe during the Miocene, with many warm-temperate taxa recorded in the available palaeobotanical records. For the vegetation simulation, 15 plant functional types (PFTs) are defined and 13 among them are allocated to different classes of trees from arctic to tropical conditions. More precisely, the tree types used in the classification can be subdivided into three groups with broadleaved or needle-leaved characteristic: temperate cold/cool, temperate warm and tropical PFTs.

2. The CARAIB model

General description

The CARAIB model (Warnant, 1999; Otto et al., 2002; Laurent et al., 2008) is a global vegetation model, originally designed to study the role of vegetation in the global carbon cycle at present (Warnant et al., 1994; Nemry et al., 1996; Gérard et al., 1999) or in the past (François et al., 1998, 1999, 2006; Galy et al., 2008). It is composed of five modules describing respectively (1) the hydrological budget, (2) canopy photosynthesis and stomatal regulation, (3) carbon allocation and plant growth, (4) heterotrophic respiration and litter/soil carbon dynamics, and (5) plant competition and biogeography. The model contains a given set of herbaceous and tree plant functional types (PFTs), which can share the same grid cell. For each of these PFTs, the model calculates the temporal evolution of 2 carbon reservoirs in the plant (metabolic and structural carbon) and 3 in the soil (metabolic and structural litter, soil organic carbon). By contrast, the evolution of the soil water content in the root zone is calculated for all PFTs together by the soil hydrological module, assuming that all PFTs share the same soil water reserve. The same module also evaluates any possible amount of snow present on the grid cell. The model time step is 1 day for updating all water and carbon reservoirs, but photosynthesis and plant respiration are calculated every two hours

and, hence, take into account non-linear effects associated with the variation of photosynthetic/respiration fluxes over the day. Vegetation cover is updated once a month for herbs and once a year for trees. Herbs are assumed to grow below trees, except if environmental conditions are such that no tree can survive on the grid cell. Consequently, herb photosynthesis is limited by the amount of light transmitted through the tree canopy. The input climatic fields which are necessary to run the model are: (1) the diurnal mean air temperature ($T_d = 0.5(T_{max} + T_{min})$), (2) the diurnal amplitude of air temperature change between day and night ($\Delta T = T_{max} - T_{min}$), (3) precipitation (P), (4) air relative humidity (RH), (5) percentage of sunshine hours (SH) and (6) wind speed (v). Daily values of all these variables are needed. They are derived from monthly mean values by using a stochastic generator (Hubert et al., 1998).

The *hydrological module* (Hubert et al., 1998; François et al., 2006) evaluates the average soil water content in the root zone, the snow cover and all related water fluxes. Daily precipitation P is the only prescribed water flux. It is separated into its rain and snow components according to the value of minimum T_{min} and maximum T_{max} temperature over the day. Snow is stored in a single reservoir assumed to cover indifferently the soil and the vegetation. The fraction of the grid cell covered by snow is parameterized as a square root function of the content of this reservoir (snow depth). Over this fraction, snow evaporates at the potential evapotranspiration rate (PET). Snowmelt occurs if T_{max} exceeds 0°C , at a rate proportional to the value of this temperature in $^\circ\text{C}$. The fraction of precipitation intercepted by the foliage and re-evaporated is parameterized as a function of the canopy leaf area index (LAI) and of the ratio P/PET. This parameterization was developed on the basis of a reservoir model for leaf surface water using a 1-minute time step and assuming a statistical distribution of the precipitations during the day. Potential evapotranspiration *PET* is calculated according to Penman's equation (e.g., Mintz and Walker, 1993). Surface soil evaporation and vegetation transpiration are represented as a single flux in the model, evaluated as the minimum between a supply and a demand function. The supply function depends on the soil water content, while the demand function is equal to $PET - E_{snow} - E_{int}$, where E_{snow} and E_{int} are the evaporation of snow and intercepted water respectively. Vertical drainage at the bottom of the soil layer is calculated as a free drainage flux corresponding to the current soil conductivity, which is evaluated as a function of soil water content and soil texture (Saxton et al., 1986). When the soil layer reaches saturation, the excess water is evacuated as surface runoff, but this is relatively rare in the model. Soil water stress impacts the photosynthesis of each PFT through a decrease of the stomatal conductance, a reduction of the leaf area index and, under most severe stress conditions, an enhanced plant mortality rate.

The *canopy photosynthesis and stomatal regulation module* is based on Farquhar et al.'s (1980) model for C3 and Collatz et al. (1992) for C4 plants. Stomatal conductance is related to net assimilation using the parameterization developed by Ball et al. (1987) and modified to take into account the effect of soil water in a similar way to Van Wijk et al. (2000). The canopy is divided into 16 layers of equal thickness ($\Delta\text{LAI}=0.5$) in terms of leaf area. The top layers are filled with the tree leaves, while the bottom layers are filled with the herb leaves. Transfer in the canopy of solar direct and diffuse radiation follows the model of Goudriaan and van Laar (1994). Photosynthesis is first evaluated for the trees present on the grid cell, filling from the top the model layers separately for each tree PFT. The number of filled layers is such that the LAI of each tree PFT corresponds to its amount C_{leaf} of leaf carbon calculated in the plant growth module, through the relationship $\text{LAI} = \text{SLA} \cdot C_{\text{leaf}}$, where SLA is the specific leaf area (i.e., leaf area per gram of leaf carbon) of the PFT. Then, the average LAI of the tree canopy is calculated weighting each individual LAI by the cover fraction of each tree. The photosynthesis of the herbs is calculated by filling towards the bottom the remaining canopy layers, starting at the level corresponding to this average tree LAI (i.e., a level where solar radiation has been attenuated by the average tree canopy). Again, the number of filled layers corresponds to the current amount of leaf carbon calculated for each herb PFT. Note that herbs are assumed to have slightly higher SLA values compared to trees, consistently with our assumption that herbs grow under trees and that acclimation of species to shade conditions tends to increase SLA (Chabot et al., 1979; Meziane and Shipley, 2001; Simioni et al., 2004). This canopy model provides an implicit scheme of competition for light between trees and herbs.

The *carbon allocation and plant growth module* allocates photosynthetic products to the metabolic (leaves and fine roots) and structural (wood and coarse roots) carbon reservoirs. This module also evaluates the autotrophic respiration and litter production fluxes. Autotrophic respiration is divided into maintenance and growth respiration. The former is proportional to the carbon content of the pool and varies exponentially with temperature, while the latter is proportional to the biomass increase. Only part of the structural pool (sapwood) is subject to respiration. Litter is produced by the mortality of metabolic and structural tissues, through: (1) seasonal leaf fall and fine root turnover of deciduous species, (2) plant death due to natural regeneration of the canopy, and (3) plant death due to unfavourable climatic conditions (Otto et al., 2002). The growth rate of each plant carbon reservoir (metabolic or structural) is obtained as the difference between the carbon allocated to the reservoir and the respiration and litter production fluxes.

The *heterotrophic respiration and litter/soil carbon module* calculates heterotrophic respiration rates, as well as the time evolution of metabolic litter, structural litter and soil carbon reservoirs.

Heterotrophic respiration is a function of temperature, soil moisture and depends linearly on the reservoir content (Nemry et al., 1996). This module is not directly useful in the present study.

The *plant competition and biogeography* module evaluates the cover fractions of all tree and herb PFTs on each grid cell of the studied geographical area. Seed production, as well as their dispersal and germination is not explicitly described in the current version of CARAIB. As a result, a priori PFT-dependent climatic requirements must be fulfilled prior to the installation of PFTs on a grid cell. The first requirement is that the yearly sum of daily temperatures above 5°C (growing degree-days GDD5) exceeds a given threshold $GDD5_{min}$. The second requirement is the necessity of some cold period during the winter for non-tropical PFTs, i.e., that the coldest monthly mean night temperature (T_{cm}) is lower than a given threshold T_{max} . Similarly dry PFTs are assumed to require at least one dry month for germination to be possible, i.e., the minimum monthly soil water content (SW) calculated by the hydrological model must be below a threshold SW_{max} . Other parameters having a strong impact on the geographical distribution of PFTs are the air temperature threshold (T_{mins}) below which temperature stress occurs, and similarly the soil water threshold (SW_{mins}) below which water stress occurs. When such extreme temperature or soil water conditions are reached, plant mortality is enhanced which is translated through a strong increase of the litter production rate with respect to the baseline rate. The values of these parameters controlling PFT germination and stress conditions are derived from a statistical analysis of the modern distribution of the PFTs (see below). In each vegetation storey (trees or herbs), the cover fraction of each PFT is assumed to be proportional to its net primary productivity (NPP) multiplied by a factor ξ representing the germination probability of the PFT. In the current version of the model, this weighting factor is set to 0 if climatic requirements for germination are not met, and to 0.4 for coniferous trees and 1 for other PFTs if the climatic conditions are favourable to germination. The lower germination probability of coniferous trees is assumed to reflect the more primitive mode of reproduction of gymnosperms compared to angiosperms, with less efficient pollination and probably less competitive growth of seedlings under favourable climatic conditions. The cover fractions are updated annually in the over-storey and monthly in the under-storey.

PFT classification and assignment of PFT-dependent parameters

In the current version of the model, we have adapted the original PFT classification (Otto et al., 2002) to the study of the European vegetation in the Miocene. This new classification, first proposed by Utescher et al. (2007a), is presented in table 1. It has been obtained by grouping several plant types (“bioclimatic affinity groups”, BAGs) of the classification developed by Laurent

et al. (2004) for modern European trees (PFTs 3, 4, 5, 7, 9, 11, 12 and 13), by adding some new classes corresponding to warm-temperate trees (PFTs 6, 8 and 10) and by keeping the classes of the original CARAIB classification (Otto et al., 2002) for tropical trees (PFTs 14, 15) and herbs (PFTs 1 and 2).

Laurent et al. (2004) have defined a new classification of modern European vegetation. They compared the observed geographical ranges of 320 taxa to the climate distribution in Europe using a discriminant analysis. From this analysis, they calculated the potential geographical ranges of all these taxa and then applied a hierarchical clustering using these potential ranges to define the bioclimatic affinity groups of European plants. Thirteen BAGs were defined for the trees. For each of these, the above-mentioned parameters controlling plant stress and germination in CARAIB were derived by selecting 5% or 95% thresholds in the climatic potential distribution of the BAG (Laurent et al., 2008). More precisely, a one-year series of daily temperature series was produced over Europe using CARAIB weather stochastic generator (Hubert et al., 1998). This stochastic series is renormalized in such a way that the monthly mean temperature is equal to the monthly climatological value in New et al.'s (2002) database (average climate for 1961-1990 period). From this series, a map of the distribution of GDD5 was produced over Europe and put in correspondence with the potential geographical range of each BAG. The parameter $GDD5_{\text{min}}$ was then set to the 5% quantile in the GDD5 distribution of the BAG. Similarly, T_{min} was obtained as the 5% quantile in the BAG's distribution of the temperature of the coldest day in the simulated year. The other parameters were obtained from monthly values. T_{max} was taken as the 95% quantile in the distribution of the coldest monthly mean night temperature T_{cm} . In the current study, temperate tree PFTs were obtained by merging together several BAGs: PFT 3 corresponds to BAGs 4, 5 and 6 of Laurent et al. (2004), PFT 4 to BAG 2, PFT 5 to BAG 1, PFT 7 to BAG 7, PFT 9 to BAG 8, PFT 11 to BAGs 12 and 13, PFT 12 to BAGs 10 and 11, and PFT 13 to BAG 9. The parameters controlling germination and stress for the PFT were obtained by retaining the most extreme value among those of all BAGs belonging to the same PFT. They are listed in table 2.

PFTs 6, 8 and 10 correspond to warm-temperate trees that are at present distributed in the Southeast of Northern America and Southeastern China where they grow under Cfa (warm-temperate, fully humid with hot summers) climate conditions (Kottek et al., 2006). These PFTs are almost absent from the natural vegetation of Europe today. These PFTs were present in Europe during the Miocene. They disappeared from the region with the development of the Pleistocene glaciations but are good analogues for the European Miocene warm-temperate tree flora. Digitized maps of these species have been used to produce present gridded distribution maps of PFTs 6, 8 and 10 in these

regions. These distribution maps have been put in correspondence with the gridded climatology of New et al. (2002) to derive the values of CARAIB germination and stress parameters for each of these PFTs (table 2), using the same method as for the BAGs.

The PFT classes corresponding to herbaceous species (PFTs 1 and 2) and to tropical trees (PFTs 14 and 15) are taken from the earlier version of CARAIB (Otto et al., 2002). Because of the absence of precise distribution maps for these PFTs, the germination and stress parameters were adjusted to roughly reproduce their large scale distribution in global vegetation maps.

Other PFT-dependent parameters apart from those controlling germination and stress are used in CARAIB, such as those related to photosynthesis, stomatal regulation, phenology, etc. In general, these parameters were set to their corresponding value in the earlier version of CARAIB, depending on the different characteristics of the PFT: vegetation storey (tree or herb), photosynthetic scheme (C3 or C4), leaf type (broadleaved or needle-leaved) and phenology (evergreen, summergreen or raingreen) (Warnant, 1999).

Biome assignment scheme

CARAIB produces as outputs the cover fractions of all PFTs on every grid cell of the studied region. However, it is useful to transform this information on the abundance of plant type into a biome type characterizing each grid cell. Such a biome assignment scheme is useful essentially for the visualizing the model results, but should not be used for comparing these results with the data. Indeed, the biome limits are rather imprecise and the biome classification generally varies from one author to the other. For this paper, we have adapted the biome assignment scheme of CARAIB. This biome assignment scheme is presented in table 3. It will be used to provide synthetic maps illustrating the overall vegetation distribution in the model. Comparison with the data (section 5) will be performed at the PFT level. The scheme contains a set of threshold conditions on GDD5, total NPP (NPP_{tot}) and LAI (LAI_{tot}) of the grid cell, the ratio R of herbaceous NPP to tree NPP, the LAI of trees (LAI_{tree}), the fraction of C4 herbs (f_{C4}) in the under-storey, the fraction of different types of trees and the dominant tree NPP. Most important thresholds are: permanent ice or polar desert is assumed to occur for $GDD5 < 50$, (extreme) desert for $NPP_{tot} = 0$, tundra for $50 \leq GDD5 \leq 500$ and $LAI_{tree} < 0.8$, semi-desert for $NPP_{tot} \neq 0$ and $LAI_{tot} < 0.3$; grasslands occur for $R > 0.8$ and $LAI_{tree} < 0.8$, open woodlands for $R > 0.8$ and $LAI_{tree} \geq 0.8$; forests occur for $R \leq 0.8$, their types being determined by the relative abundances of the different tree PFTs present in the over-storey.

3. Design of the simulations

The climatic inputs for the CARAIB vegetation model are derived from the COSMOS atmosphere-ocean general circulation model (AOGCM) (e.g., Jungclaus et al., 2006; Roeckner et al., 2003, 2006). The atmospheric component of the model is ECHAM5 (Roeckner et al., 2003) at a resolution of T31 (i.e., a resolution of $3.75^{\circ} \times 3.75^{\circ}$ in longitude-latitude). The oceanic component is MPIOM (Marsland et al., 2003). This fully coupled AOGCM allows taking into account the impacts of palaeogeographical changes on ocean circulation and climate, considering possible ocean-atmosphere dynamical feedbacks. We use the ECHAM5-MPIOM simulation performed by Eronen et al. (2009) and Micheels et al. (this volume) for the Tortonian. Most important palaeogeographic changes in this Tortonian climate simulation with respect to the present-day control include the opening of the Panama seaway, a southward shift of Australia and the inclusion of the Paratethys and the Pannonian Lake in Europe. Orography was also changed with generally lower mountain elevations in the Tortonian, including a reduction by 70 % of the mean elevation of the Tibetan Plateau and the Alps and the removal of the Greenland ice sheet. Finally, another important change is the use of a proxy-based Tortonian palaeovegetation map as boundary conditions in the ECHAM5 atmospheric model, with more forests and less desert areas than today. More detail on the COSMOS model and the design of the Tortonian climate simulation can be found in the two publications mentioned above.

We interpolated to $10' \times 10'$ resolution over Europe the anomalies between this Tortonian simulation and the present control simulation and then combined these interpolated fields with the present-day climatology of New et al. (2002), using a method similar to François et al. (2006). All necessary monthly input fields for the CARAIB model, mean temperature, diurnal temperature amplitude, precipitation, percentage of sunshine hours (derived from cloudiness), relative humidity and wind speed were prepared in that way. Note that the model climatic anomalies between the Tortonian and Present implicitly contain climate changes associated with the elevation reduction in the Alps and other mountain ranges, which was considered in the climate simulation. Consequently, the interpolated fields take these orographic changes into account, at least at coarse resolution. In view of the very poor knowledge of palaeorography, no attempt was made to integrate the elevation reduction at finer resolution in the interpolation method. Daily mean fields of climate variables were then obtained from the weather generator implemented in CARAIB (Hubert et al., 1998) for mean and diurnal amplitude of air temperature, as well as for precipitation, using renormalization to ensure that the monthly value is not altered. For the percentage of sunshine and air relative humidity, stochastic generation was not used, but two different values are defined for wet and dry

days in each month, again chosen so that the monthly value is matched. For wind speed, the daily value is just linearly interpolated between months.

For this study, a palaeogeographic map for the late Miocene is used (Popov et al., 2004) representing the time span from 8.5 to 7.0 Ma. As discussed in the Introduction, this palaeogeographic reconstruction is based on the classical connection between the Mediterranean and the Eastern Paratethys through the Bosphorus area (Popov et al., 2004, 2006). No attempt was made to incorporate in our high resolution maps at $10^{\circ}\times 10^{\circ}$ the new concept of a long and narrow marine gateway through the Balkans, as proposed by Melinte-Dobrinescu et al. (2009). Indeed, the palaeogeography of the Paratethys in the climate model simulations was based on the reconstruction of Popov et al. (2004) and, moreover, the Balkan gateway is a rather small-scale feature that cannot be captured at the coarse resolution of the climate model, preventing any meaningful sensitivity test. In order to have a plane projection, the palaeogeographic map in polar projection has been deformed. This transformation explains the curved boundary in the northern part of Scandinavia (figure 1). This boundary is actually the northern border of the map in the conic projection used by Popov et al. (2004). Similarly, the straight line cutting the western part of North Africa between approximately 28°N and 34°N is not a shoreline, but the western limit of the original palaeogeographic map. Moreover, compared to the maps for the present day, the Tortonian one extends further to the East and less to the North. The palaeocontinents are digitized at the $10^{\circ}\times 10^{\circ}$ resolution used in the CARAIB model.

Some continental grid cells of the Tortonian correspond to marine cells in the present-day distribution. In the anomaly method explained above, the modern climatology for these points is needed. These climatic data are not available in New et al. (2002)'s (continental) dataset. Present-day marine climatological data could be used, but this may generate artificial discontinuities in the palaeoclimatic reconstruction, due to the present-day climatic gradient existing between marine and continental areas, but also to possible inconsistencies (e.g., different resolutions) between available marine data and New et al. (2002)'s climatology. In order to avoid such discontinuities, New et al. (2002)'s climatology has been extrapolated on all palaeocontinental grid cells that are currently marine grid cells, using an inverse distance weighted mean on most proximal present-day continental cells (i.e., in a circle of prescribed radius that can be progressively increased if no continental grid cell is found).

Finally, no change in CO_2 is assumed between the present and the Tortonian in the vegetation model (thus, the model assumes no change in CO_2 fertilisation). A pre-industrial value of 280 ppmv is

adopted in both simulations, because the present-day distribution of potential vegetation (unperturbed vegetation) in the CARAIB model has been calibrated with a pre-industrial CO₂ level, despite the fact that the 1961-1990 climate fields of New et al. (2002) were used. This CO₂ level “seen by the vegetation” is slightly lower than the value of 360 ppmv (Micheels et al., this volume) used in the COSMOS climatic simulation (also not changed between present and Tortonian). In any case both values fall in the range of proxy-based CO₂ levels reconstructed for the Late Miocene (e.g., Pagani et al., 2005; Demicco et al., 2003). Moreover the fertilisation effect which would result from increasing CO₂ from 280 to 360 ppmv (to be consistent with the value used in the climate model) would non negligibly impact the absolute values of net primary productivities and biomasses of the PFTs, but not their relative values, implying only small changes on the PFT distribution. This is particularly true of the tree distribution, which is analysed here and compared to palaeovegetation data. This comparison, which mainly focuses on the presence and absence of the tree PFTs and not on their absolute productivity, is probably not very sensitive to atmospheric CO₂, as far as only the fertilisation effect is concerned (i.e., without any effect of CO₂ on the climate system).

4. Simulation results

Figure 1 shows the distribution of modelled air temperature and precipitation anomalies (Tortonian minus Present) interpolated over Europe and northern Africa palaeogeographic maps, for average winter and summer climatic conditions. In general, the Tortonian appears warmer than the present in southern Europe and the Mediterranean region, with a reduced seasonal amplitude, while in western and northern Europe, modelled Tortonian climate tends to be cooler than today. In winter, the air temperature anomaly is up to +4°C in North Africa and around the Paratethys. In summer, a similar warming trend is observed in northern Africa, as well as over the western Paratethys and Turkey, but with a slightly reduced magnitude. Over the rest of Europe a cooling is observed. This cooling is particularly strong around the eastern Paratethys (-4°C) and over the British Isles (-2 to -3°C).

As discussed by Micheels et al. (this volume), the Miocene simulation is globally warmer than the present-day control, mostly as a result of land cover (albedo) change: removal of ice sheets in the high latitudes and expansion of forests at the expense of deserts and steppes in lower latitudes. Moreover, in mountainous areas, the reduction of elevation also contributes to warming. In Northern Africa, the warming is particularly strong, as a result of the replacement of the Sahara desert by grassland and savannah vegetation. The warming in Southern Europe is also presumably

the result of this regional change in climate, with some possible effect of elevation reduction in the Alps and neighbouring mountain ranges. In high latitudes, warming is generally observed as a result of the ice albedo feedback, except in Northern Atlantic and Northern Europe where a cooling is observed. This cooling results from the opening of the Central American Isthmus, which results in a weaker northward heat transport in the Atlantic Ocean.

Concerning precipitations, the conditions are generally more humid except around the Mediterranean Sea during winter and in the western part of the Paratethys and on the Atlantic side in summer. The strong precipitation increase in mid-latitude Europe between 50°N and 60°N, especially marked in the winter season, is linked to an increased moisture flux with the westerlies in the Tortonian simulation (Micheels et al., this volume).

The monthly minimum soil water calculated by the CARAIB vegetation model is shown in figure 2. This parameter is an indication of water stress undergone by plants in the model. This minimum can be expected to occur in the summer months, but the exact month may vary from one grid cell to the other. Thus, the Tortonian field results directly from the combination of the summer temperature and precipitation changes discussed above. In a general way, the water stress in the Tortonian is more severe in the southern part of the study area and less pronounced in the northern part, consistently with the summer warming and/or reduced precipitation observed in the south and the summer cooling with increased precipitation in the north. The most significant drying occurs in Anatolia, northern Africa, central Spain, western France and on the northern shoreline of western Paratethys. No significant change occurs in Greece and the Balkans, as well as in Italy. Wettening occurs around the eastern Paratethys, especially on the northern and eastern shorelines, in central Russia and over the British Isles.

In term of biomes illustrated in figure 3, even if most of Europe is covered by cool-temperate mixed and temperate broadleaved deciduous forests as for the present day, the results for the Tortonian simulation shows the presence of warmer vegetation types like the warm-temperate mixed forest growing under fully humid Cfa climate conditions around the Adriatic Sea and in the north of Turkey. Warm-temperate mixed forests (which include Mediterranean-type trees, PFT 5 and 9) colonize the area surrounding the western part of the Paratethys and an extension of the tropical grassland around the Mediterranean Sea can be observed. In the high latitudes, the boreal/mountain forest type seems more widespread compared to the present, but this is partly an artefact due to the deformation of the geographic projection. On the other hand, some tundra type appears on the Lesser Caucasus and on the Greater Caucasus in the Eastern part of the Paratethys area. This can be

explained by the air temperature anomaly mentioned about -4°C in summer for this area.

5. Comparison with palaeovegetation data

Data

Palaeovegetation data for the Late Miocene of Europe are derived from published palaeobotanical records from a total of 58 floras. References, geographical coordinates, and available stratigraphical information are summarized in Appendix A. The time interval represented by the floras (earlier part of the Tortonian, 11.61–7.25 Ma) is about contemporaneous with the EEDEN high resolution interval HR2 and also has been intensely studied in the NECLIME program (cf. Bruch et al., 2007). As criteria for selecting the floras, high diversity of the record, and exactness of stratigraphical dating are crucial. The floras cover a region extending from Spain in the West to Armenia in the East and Morocco in the South. The spatial distribution of the data points is shown in figure 4. For many of the Miocene localities, palaeotemperature and precipitation data are available (Mosbrugger and Utescher, 1997; Utescher et al., 2000; Ivanov et al., 2002; Bruch et al., 2004; Mosbrugger et al., 2005; Bruch et al., 2006; Fauquette et al., 2006; Utescher et al., 2007a).

Methodology

The resulting model vegetation distribution reconstructed for the Tortonian is compared to palaeovegetation data as derived from diversities of plant functional types in micro- and megaflores. This comparison is allowed by the assignment of tree taxa present at the various data sites to one or several model classes, depending on the identification level of the taxa. Since mega- and microfloras with a variety of different taphonomic conditions are analysed in an integrative approach diversity of fossil taxa is regarded, not their frequency. Thus, the bias caused by taphonomic effects is reduced. The method allows a comparison with the model simulation on the basis of presence/absence (Fig. 5).

All arboreal taxa present in the floral record are classified according to the model PFT classes (Table 1). The allocation of a fossil taxon to one single, or to several model classes is based on the interpretation of the Nearest Living Relative(s) (NLRs). The accuracy of identification thus depends on the taxonomic level of identification on NLRs. Consequently, a fossil taxon may contribute to several classes especially when analysing microfloras where NLRs in many cases are only identified on the family level. To allocate taxa to single PFTs that are defined by climatic

thresholds, i.e. to separate between boreal, cool- and warm-temperate PFTs (e.g. PFTs 11 to 13) temperature ranges for the Northern Hemisphere vegetation as proposed by Wolfe (1979) are employed. The corresponding climate ranges for extant tree species are available in the PALAEOFLORA database (Utescher and Mosbrugger, 1990–2010).

If several classes are possible for a taxon, only those that can co-exist with the other tree classes identified at the site are retained. This methodology is similar to the coexistence approach used in palaeoclimate reconstructions from the palaeobotanical record. It narrows the range of tree types present at the various sites by suppressing in the data the extreme end members, such as the cold boreal/temperate and tropical PFTs. These can be indicated by taxa representing a variety of different PFTs but can be in conflict with a taxon representing one single, incompatible PFT.

To eliminate PFTs in conflict with such taxa, a PFT co-existence table was constructed (table 4). This co-existence table was not obtained directly from data, but from the overlapping between PFTs in a CARAIB simulation over Europe and Southeastern Asia. The use of the model was necessary, because an excessively large amount of data on species distribution would be required to evaluate geographic overlapping of PFTs. With the already significant number of data that we assembled in this study, it is likely that the overlapping would have been less reliable when estimated directly from the data without using the model, than when derived from a model simulation over a relatively large domain. Moreover, the overlapping is probably significantly modified by present-day land use (crops, forest plantations, etc), meaning that potential rather than actual PFT distribution should be used. The model somehow transforms the geographical distribution of PFTs into a corresponding distribution in the climatic space, so that the model distribution is actually a potential distribution, which is exactly what is needed to assess PFT affinity. The accuracy of the method to establish overlapping of PFTs thus depends mostly on the amount and accuracy of the species distribution data that have been used to estimate the parameters controlling PFT distribution in the model (i.e., mainly the parameters listed in table 2).

The co-existence table is used to evaluate the likelihood for the presence of each PFT at each site, according to the six following categories: *absent*, *inconsistent*, *unlikely*, *likely*, *very likely*, *present*. A programme was written for this purpose. First, all PFTs to which at least one taxon has been unequivocally assigned are considered as present. Similarly, all PFTs that have not been allocated any taxa are considered as absent. Then, all remaining PFTs are tested for consistency with all other present or potentially present PFTs, using the co-existence table, as illustrated in table 5 for PFT 11 at Vilella site in Spain. This procedure results in the tested PFT to be classified in one of the

remaining categories, inconsistent, unlikely, likely or very likely. For PFT 11 at Vilella, for instance, the resulting category is unlikely. The same procedure repeated for all tree PFTs provides the following results for Vilella:

Absent: 7, 8, 14

Inconsistent: 15

Unlikely: 3, 11, 12

Likely: 4

Very likely: 5, 6, 10, 13

Present: 9

The presence/absence status of the PFTs can then be decided from these likelihood levels, by setting for instance the threshold for the presence between *unlikely* and *likely*, i.e., by retaining the last three categories for the presence and the first three for the absence (table 6). By setting the threshold at this level, we eliminate PFTs 15, 3, 11 and 12. Consequently, the method has eliminated the most extreme PFTs among those that were identified as potentially present, i.e., the cold boreal/temperate tree PFTs (3, 11), a cool-temperate one (12) and the tropical one (15) were eliminated. Setting a stricter threshold for the presence between *likely* and *very likely* would have also eliminated the other cool-temperate PFT (4). In that case, only warm-temperate types would have been kept. Conversely, a softer threshold placed between *inconsistent* and *unlikely* would only eliminate the tropical PFT. So, it looks quite probable that tropical trees were absent from this site, but it is less certain that cold boreal/temperate trees were also absent. This hierarchy in the level of certainty may be taken into account when comparing the model results with the data in terms of presence or absence.

In order to compare model results with data not only on a presence/absence basis, but also on an abundance basis (fig. 5), we calculate a biodiversity fraction for each PFT at each data locality. This biodiversity fraction (f_{bio}) is reported in table 6 for the Vilella site as an example. It is evaluated by calculating the proportion of the taxa, which were assigned to the relevant PFT. In this calculation, when more than one PFT is attributed to a given taxon, a double weight is given to the most likely PFT. Table 7 illustrates this calculation in the case of Vilella. This biodiversity fraction is a measure of the diversity of the PFT in the palaeoflora. It is likely, however, that the biodiversity fraction will be higher when the PFT abundance is higher. Under this hypothesis, it is possible to compare model and data on the abundance level. The hypothesis may not be true, but the biodiversity fraction is probably the most reliable indicator of abundance, in the case of macrofloras. Indeed, the relative

abundance of macroremains in the flora is probably a poor indicator of the actual abundance of the taxa or PFTs. In the case of pollen sites, the PFT abundances may be estimated from pollen abundances, which is a more reliable indicator. This would not change the model-data comparison methodology presented here. However, the use of the biodiversity fraction allows to use the same methodology for macro- and micro-floras and thus to combine both types of localities in the same study.

Results

The PFT distribution maps including the agreement level with the data are shown in figure 6 for cold/cool-temperate PFTs, in figure 7 for warm-temperate PFTs and in figure 8 for tropical PFTs. For each PFT, the cover fraction in the over-storey is plotted and the comparison with palaeovegetation is indicated at the different sites by a circle in case of agreement between data and model for the presence/absence status of the PFT, and by a diamond in case of discrepancy. In the model, the agreement is tested over the 10'x10' grid cell containing the site. The color inside the circle or the diamond at each site indicates the biodiversity fraction of the PFT derived from the analysis of the data (tables 6 and 7).

Among the temperate cold/cool PFTs (Fig. 6), except for the needle-leaved evergreen temperate cool trees, most agreements result from the absence of the PFTs in the simulations, in particular for the needle-leaved summergreen boreal/temperate cold trees. However, the number of agreements is quite small for cold/cool PFTs. For many sites, these PFTs are simulated in the vegetation model, but they are absent from the palaeovegetation data. Moreover, when the PFT is both present in the simulation and in the data, as is often the case for needle-leaved evergreen temperate cool trees (PFT 4), the biodiversity fraction of the PFT in the data is usually lower than the cover fraction in the model, suggesting that the PFT is less well-represented in the palaeoflora than in the model. In term of palaeoclimate, these results clearly indicate that the model appears significantly colder than what the data suggest.

Concerning the warm-temperate PFTs (Fig. 7), when the classes are simulated in the localities, this often leads to an agreement. It is the opposite than for the temperate cold/cool PFTs: disagreements arise from the too small number of simulated presence in the vegetation model. This conclusion is particularly obvious for the needle-leaved evergreen temperate perhumid warm, needle-leaved summergreen temperate warm and the broadleaved evergreen temperate perhumid warm PFTs.

For tropical PFTs (Fig. 8), model and data agree at most sites, because these PFTs are generally not present in the data, while the model does not simulate them. This conclusion must be taken with caution, because at many sites as illustrated for Vilella in Spain, the tropical PFTs have been eliminated from the list of present PFTs, since they resulted from multiple allocation of taxa and they were not considered as most likely PFT for any of these taxa.

6. Discussion and conclusion

As stated above the Tortonian is characterized by warmer conditions than today, especially in the mid- and higher latitudes. This is quite obvious when regarding the available palaeovegetation data, where the presence of warm-temperate PFTs in the arboreal vegetation is indicated for most sites over Europe, even up to 55° northern latitude (fig. 7). As shown by the biome distribution in the control run (fig. 3) cold boreal/temperate and cool-temperate vegetation types and corresponding PFTs today are present in the latitudinal range between 45° and 55° N, except for coastal areas of Western France and the northern coast of the Black Sea where a warm-temperate biome is modelled. Using PFT coexistence table and likelihood analysis tropical PFTs (PFTs 14;15) in the primary data obtained from the flora lists (cf. Utescher et al., 2007a) are now excluded for most of the sites being considered as incompatible or unlikely (fig. 8). The presence of PFT 14 in two sites of the Eastern Paratethys (Emetovka, Valea Neagra) refers to the record of legume-type taxa (*Acacia* sp.). In Central and Northeastern Spain representatives of the Bombacaceae, Olacaceae families and the *Cassia* genus point to a very warm climatic aspect of the vegetation.

According to this study broadleaved summergreen cold- to cool-temperate arboreal PFTs (PFTs 11, 12) are absent from almost all fossil sites located in the study area (fig. 6). All boreal cold and most cool-temperate PFTs are excluded by likelihood analysis (see above) while the primary data of the fossil record do not provide an unequivocal solution because many conifer and broadleaved summergreen arboreal genera cover the climatic range from cool- to warm-temperate (Utescher et al., 2007a). However, implications on a complete absence of cold- and cool-temperate PFTs has to

be treated with caution because not all of floral remains have been embedded near their habitat. In many cases a provenance of such components from higher altitudes is probable (e.g., pollen grains belonging to the *Abies*, *Picea*, *Tsuga* genera; cf. e.g., Jiménez-Moreno 2005; Syabryaj et al., 2007; Ivanov et al., this volume) or cannot be excluded (pollen grains of many deciduous trees presently common in the mid-altitudes of mountain areas). In these cases PFTs would have been present that are excluded using the present methodological approach. Consequently, tests using softer thresholds have to be performed to study this problem.

The taxonomic composition of the assemblages recorded at the different localities and the PFT table obtained from likelihood considerations can also be directly translated in terms of large biome classes, using a classification scheme similar to, but simpler than the one used in the model (table 3). As shown in Figure 4 warm-temperate forest types result for the parts of the study area where palaeobotanical data are available. A mainly deciduous forest with PFT 13 as dominant component is mainly distributed over the Central Paratethys and in the Northwest (Juteland). Most of the sites south of 45° N and in the Eastern Paratethys indicate a “mesophytic” forest vegetation characterized by a high proportion of trees requiring humid and warm conditions (PFTs 6; 10) in the over-storey cover fraction (Fig. 5). Even up to latitudes higher than 50°N sites are allocated to this vegetation type. However, both sites in this region (Klettwitz, Zukunft fruit and seed floras) both dating from the earliest part of the time slice grew under specific edaphic conditions (peat bog) and do not represent zonal vegetation. It is known that edaphic conditions may lead to erroneous results when the attempt is made to reconstruct zonal vegetation (e.g., Eder-Kovar et al., 2008). In peat bog communities evergreen and in many cases also thermophilous elements tend to be overrepresented (e.g. Utescher et al., 2000) while alluvial wetland vegetation has a “deciduous bias” (e.g., Eder-Kovar and Kvaček, 2003). It is known that most of the localities of the Central Paratethys presently studied represent the latter type (Erdei et al., 2007). As is the case for stratigraphical uncertainties the present approach does not allow access to this problem because most plants are present in azonal communities and zonal as well (e.g., Utescher et al., 2007a)

Unlike the direct reconstruction from proxy data modelling provides area-wide data.

Figure 9 illustrates the model-data comparison in terms of warm tree PFTs fractions (“warm” = warm-temperate + tropical types). The interpretation of the results is clear, the abundance of warm PFTs is significantly higher in the data than in the model. This has to be expected when regarding temperature anomalies obtained for the Tortonian model run with respect to the control run (fig. 1) where especially the western part of Central Europe, in addition summer temperatures in the East

show no change or even cooling with respect to present-day conditions. Correspondingly, cooler vegetation types such as cool-temperate mixed forest and temperate deciduous forest result from the CARAIB run for those areas. Warm-temperate, “mesophytic” forest, so common in proxy data-based reconstructions are suggested by the model only for the coastline of Adriatic Sea, and along the south coast of the Black Sea (Fig. 3) where the simulation of the atmosphere shows a strong positive anomaly (fig. 1). Other regions in the lower latitudes are too dry (cf. Negative anomalies in fig. 1) in the model for the existence of a fully humid vegetation type. Consequently the biome model shows open woodlands.

The quality of the model-based reconstruction can also be tested by kappa statistics (table 8). For each tree PFT, number and proportion of localities are listed where presence (p) or absence (a) of the group is compared between the data (first index) and the model simulation (second index), the “kappa” for absence and for presence and the percentages of agreement. It appears that several PFTs show a better agreement due to the absence in the simulation than on the basis of the presence. This is especially true for the tropical PFTs 14 and 15. These tropical types are present in a total of 4 localities, but never are simulated by the CARAIB vegetation model.

The overall percentage of localities where there is agreement between model and data (%Agr) remains very small (< 30 %) in the case of the warm-temperate PFTs 6, 8 and 10. These PFTs are present in the data at most localities, while they are absent in the model at all localities, except at one of them where PFT 6 is simulated. Other warm-temperate PFTs (5, 9 and 13) have intermediate percentage of agreement, ranging between 43 and 52 %. Cold- and cool-temperate PFTs 3, 4, 11 and 12 have also intermediate levels of agreement, since these PFTs are usually absent from the data and present in the model. The agreement is, however, slightly larger for cool PFTs than for cold ones. An exception is PFT 7 (corresponding to *Larix* species), for which the agreement is high, since the data indicate its presence at only one locality and the model simulates this PFT only in northern and north-eastern Europe where there are no localities. The tropical PFTs also show high percentages of agreement for essentially the same reason (absence in the model and also in the data after the likelihood test), as already discussed above. These results may be dependent on the threshold in likelihood levels used to separate absence and presence in the data. The sensitivity of the model-data comparison to this threshold is explored in table 9. Lowering the threshold significantly increases the agreement for cold boreal/temperate PFTs 3 and 11. Raising the threshold increases the agreement for needle-leaved cool-temperate PFT 4 and for warm-temperate PFTs 6, 8 and 10. This result indicates that the presence of PFTs 6, 8 and 10 in the data is not certain at some

localities. Overall, the percentages of agreement are on average larger for the higher threshold.

Summarizing up the discussion it can be stated that the temperatures presently used as forcing for the CARAIB model run as obtained from the coupled ocean-atmosphere modelling study of a Tortonian time slice (Micheels et al., this volume) are higher for Europe than in previous published simulations. However, comparing the vegetation modelled on the basis of these climatic fields using the new method developed here, the warm PFTs are still much less abundant in the model reconstruction than in the data. The reason might be linked to a too strong reduction of the northward Atlantic ocean heat flux in the Tortonian climate simulation, in response to the opening of the Central American Isthmus. The intensity of this reduction, and hence the reconstructed climate for Europe, may depend on the bathymetry and the exact land-sea configuration within and around the Isthmus, which are not known precisely and/or cannot be represented accurately in the model due to the limited resolution. Another possible reason of the model-data mismatch may be related to the atmospheric CO₂ level used in the model. Large uncertainties remain on Neogene atmospheric CO₂ and higher values than those used here cannot be excluded. Finally, another important limitation of the simulations is that the vegetation model is not coupled to the climate model, so that climate cannot respond to the modelled vegetation changes. For the Middle Miocene, Henrot et al. (submitted) have shown that the impact of vegetation changes is to warm many parts of the continents, including Europe. Thus, the absence of vegetation feedbacks may also be at the origin of the too cold European climate simulated here by the COSMOS model for the Tortonian. However, the effect is probably limited, since the COSMOS model was forced with a vegetation reconstructed specifically for the Tortonian and not with present-day vegetation.

The new approach that we have developed in this paper looks to be a powerful tool to check the reliability of palaeoclimate modelling by independent data. It allows a comparison of the modelled vegetation with the flora recorded at the various localities, at the plant functional type level in a way fully consistent between model and data. Contrary to most previous model-data comparisons, this new approach does not rest on the biome concept, which is not a directly observable feature of vegetation and whose classification may vary from one author to the other and involves the use of many ecosystem parameters that are not accessible in the palaeoflora. This is especially important for Miocene floras for which the information is sparser and less precise than for Pleistocene and Holocene plant assemblages. Biomes are reconstructed only to provide a synthetic view of the model results and the data, but they are not used in the comparison. Moreover, the method is

applicable both to macro-flora and pollen data. It allows for a locality-wise adjustment of proxy data-based vegetation reconstruction and quality of modelled data.

In the moment work is in progress to refine the approach. Additional, non-arboreal PFTs are included to better represent Neogene vegetation. Further efforts are made to improve the climatic definition of the PFTs and the classification of the Neogene floral record. This last point is particularly important, since the modelled PFT distribution in the vegetation model is quite sensitive to the values of the thresholds (table 2) chosen for cold/drought stress and germination parameters. The climatic definition of the PFTs and the Neogene floral record depends on: (1) an appropriate choice of NLR species for each fossil taxa, (2) the availability of precise (high resolution) distribution ranges of these NLR species for present-day, and (3) the way these NLRs species are assembled into PFT classes.

None of these steps is obvious and each of them can add significant uncertainties to the palaeovegetation reconstruction and the model-data comparison. Future work should focus on improving these steps and reducing the associated uncertainties, in order to achieve a strong and reliable method to test climate/vegetation model simulations for Neogene time slices.

Acknowledgments

We are grateful to all colleagues who provided data for the present study. This work benefited from discussions within NECLIME and databases made available through this research network. A.-J. Henrot is research fellow at F.R.S.-FNRS. We acknowledge support for this research from F.R.S.-FNRS under research grant “Crédit aux chercheurs” 1.5.179.07 F. This work was also supported by the DFG within the project FOR 1070 and the federal state Hessen (Germany) within the LOEWE initiative. We thank the reviewers for their constructive comments that help to improve this manuscript.

References

- Akkiraz, M.S., Akgün, F., Utescher, T., Bruch, A.A., Mosbrugger, V., Wilde, V., this volume. Miocene precipitation gradients in western and central Turkey as quantified from pollen data.
- Agusti, J., Sanz de Siria, A., Garces, M., 2003. Explaining the end of the hominid experiment in

- Europe. *J. Hum. Evol.*, 45, 145-153.
- Bachiri Taoufiq, N., 2000. Les environnements marins et continentaux du corridor rifain au Miocène supérieur d'après la palynologie. Thèse, Univ. Casablanca, Casablanca, 206 pp.
- Ball, J.T., Woodrow, I.E., Berry, J.A., 1987. A model predicting stomatal conductance and its contribution to the control of photosynthesis under different environmental conditions. In: Biggins, J. (ed.): *Progress in Photosynthesis Research*. Vol. 4. 221-224. Martinus Nijhoff Publishers, Dordrecht-Boston-Lancaster.
- Barron, E., 1999. Estudio paleobotánico del afloramiento vallesiense (Neogeno) del torrente del vilella (La Cerdania, Lerida, España). Aspectos tafonómicos y paleoecológicos. *Bot. R. Soc. Esp. Hist. Nat., Sec. Geol.* 94, 41-61.
- Bessais, E., Cravatte, J., 1988. Les écosystèmes végétaux pliocènes de Catalogne méridionale, Variations latitudinales dans le domaine nord-ouest méditerranéen. *Geobios* 21, 49-63.
- Berger, W., 1952. Die altpliozäne Flora der Congerien-Schichten von Brunn-Vösendorf bei Wien. *Palaeontographica*, Abt. B 92, 79-121.
- Berger, W., 1955: Die Altpliozäne Flora des Laaerberges in Wien. *Palaeontographica* B97, 81-113.
- Bertini, A., 2003. Palynological evidence of the upper Neogene environments in Italy. In: Z. Kvaček, Editor, *Neogene Vegetation and Climate Reconstructions*. *Acta Univ. Carol., Geol.* vol. 46, 4 (2003), 15-25.
- Bessedik M., 1985. Reconstitution des environnements miocènes des régions nord-ouest méditerranéennes à partir de la palynologie. Thèse, Univ. Montpellier 2, 161 pp.
- Böhme, M., Winklhofer, M., Ilg, A., this volume. Middle and late Miocene precipitation in Spain and Central Europe: temporal trends and spatial gradients.
- Bruch, A.A., Utescher, T., Alcalde Olivares, C., Dolakova, N., Mosbrugger, V., 2004. Middle and Late Miocene spatial temperature patterns and gradients in Central Europe - preliminary results based on palaeobotanical climate reconstructions. *Courier Forschungsinstitut Senckenberg* 249, 15-27.
- Bruch, A.A., Utescher, T., Mosbrugger, V., Gabrielyan, I., Ivanov, D.A., 2006. Late Miocene climate in the circum-Alpine realm - a quantitative analysis of terrestrial palaeofloras. *Palaeogeography, Palaeoclimatology, Palaeoecology* 238, 270-280.
- Bruch, A., Uhl, D., Mosbrugger, V., 2007. Miocene climate in Europe - patterns and evolution: a first synthesis of NECLIME, *Palaeogeography, Palaeoclimatology, Palaeoecology* 253, 1-7.
- Bruch, A.A., NECLIME members (www.neclime.de), this volume. Changes in precipitation patterns in the Miocene of Central Europe as a force for landscape opening.
- Chabot, B.F., Jurik, T.W., Chabot, J.F., 1979. Influence of instantaneous and integrated light-flux density on leaf anatomy and photosynthesis. *Am J. Bot.* 66, 940-945.

- Chryssanthi, I., Solounias, N., 1985. A radiometrically dated pollen flora from the Upper Miocene of Samos Island, Greece. *Revue de Micropaleontologie* 28, 197-204.
- Collatz, G.J., Ribas-Carbo, M., Berry, J.A., 1992. A coupled photosynthesis - stomatal conductance model for leaves of C4 plants. *Australian Journal of Plant Physiology* 19, 519-538.
- Darby, D.A., 2008. Arctic perennial ice cover over the last 14 million years. *Paleoceanography* 23, PA1S07, doi:10.1029/2007PA001479.
- Demico, R. V., Lowenstein, T. K., Hardie, L. A., 2003. Atmospheric pCO₂ since 60Ma from records of seawater pH, calcium, and primary carbonate mineralogy. *Geology*, 31, 793–796, doi:10.1130/G19727.1.
- Eder-Kovar, J., 1988. Obermiozäne Floren aus der Molassezone Österreichs. *Beitr. Paläont. Österr.* 14, 19-121.
- Eder-Kovar, J., Krainer, B., 1990. Faziesentwicklung und Florenabfolge des Aufschlusses Wörth bei Kirchberg/Raab (Pannon, Steirisches Becken). *Ann. Naturhist. Mus., Wien* 1991 A, 7-38.
- Eder-Kovar, J., Hably, L., Derek, T., 1995. Neuhaus-Klausenbach – eine miozäne (pannone) Pflanzenfundstelle aus dem südlichen Burgenland. *J. Geol. Bundesanstalt* 138(2), 321-347.
- Eder-Kovar, J., Kvaček, Z., Zastawniak, E., Givulescu, R., Hably, L., Mihajlovic, D., Teslenko, J., Walther, H., 1996. Floristic trends in the vegetation of the Paratethys surrounding areas during Neogene time. In: Bernor, R.L., Fahlbusch, V., Mittmann, H.-W. (Eds.), *The Evolution of Western Eurasian Neogene Mammal Faunas*. Columbia University Press, pp. 395–413.
- Eder-Kovar, J., Kvaček, Z., 2003. Towards vegetation mapping based on the fossil plant record: in Kvaček, Z., ed., *Neogene Vegetation and Climate Reconstructions*. Acta Universitatis Carolinae, Geologica 46, 7-13.
- Eder-Kovar, J., Jechorek, H., Kvaček, Z., Parashiv, V., 2008. The integrated plant record: An essential tool for reconstructing Neogene zonal vegetation in Europe. *Palaios* 23, 97-111.
- Erdei, B., Hably, L., Kázmér, M., Utescher, T., Bruch, A.A., 2007. Neogene vegetation development and dynamics in the Pannonian Basin. *Palaeogeography, Palaeoclimatology, Palaeoecology* 253, 113–138.
- Eronen, J.T., Mirzaie, M., Karne, A., Micheels, A., Bernor, R.L., Fortelius, M., 2009. Distribution history and climatic controls of the Late Miocene Pikermian chronofauna. *PNAS* 106(29), 11867-11871.
- Farjanel G., 1985. La flore et le climat du Néogène et du Pléistocène de Bresse (France) d'après l'analyse pollinique. Implications Chronostratigraphiques. Thèse, Univ. Dijon, 195 pp.
- Farquhar, G.D., von Caemmerer, S., Berry, J.A., 1980. A biochemical model of photosynthetic CO₂

- assimilation in leaves of C₃ species. *Planta* 149, 78-90.
- Fauquette, S., Suc, J.-P., Jiménez-Moreno, G., Micheels, A., Jost, A., Favre, E., Bachiri-Taoufiq, N., Bertini, A., Clet-Pellerin, M., Diniz, F., Farjanel, G., Feddi, N., Zheng, Z., 2007. Latitudinal climatic gradients in Western European and Mediterranean regions from the Mid-Miocene (c. 15 Ma) to the Mid-Pliocene (c. 3.5 Ma) as quantified from pollen data. In "Deep-Time Perspectives on Climate Change. Marrying the Signal from Computer Models and Biological Proxies", Williams M., Haywood A., Gregory J., Schmidt D.N. Edit., The Micropaleontological Society, The Geological Society, London, Special Publications, 481-502.
- François, L.M., Delire, C., Warnant, P., Munhoven, G., 1998. Modelling the glacial-interglacial changes in the continental biosphere. *Global Planet. Change* 16-17, 37-52.
- François, L. M., Goddérès, Y., Warnant, P., Ramstein, G., de Noblet, N., Lorenz, S. 1999. Carbon stocks and isotopic budgets of the terrestrial biosphere at mid-Holocene and last glacial maximum times. *Chem. Geol.* 159, 163-189.
- François, L., Ghislain, M., Otto, D., Micheels, A., 2006. Late Miocene vegetation reconstruction with the CARAIB model. *Palaeogeogr., Palaeoclim., Palaeoecol.* 238, 302-320.
- Galy, V., François, L., France-Lanord, C., Faure, P., Kudrass, H., Palhol, F., Singh, S.K., 2008. C₄ plants decline in the Himalayan basin since the Last Glacial Maximum. *Quaternary Sci. Rev.*, 27, 1396-1409.
- Gérard, J.-C., Nemry, B., François, L., Warnant, P., 1999. The interannual change of atmospheric CO₂: Contribution of subtropical ecosystems? *Geophys. Res. Lett.* 26, 342-246.
- Givulescu, R., 1962. Die fossile Flora von Valea Neagra, Bez. Crisana, Rumänien. *Palaeontographica B* 110, 128-187.
- Givulescu, R., 1975. Fossile Pflanzen aus dem Pannon von Delureni (Rumänien). *Palaeontographica, Abt. B* 153, 150-182.
- Givulescu, R., 1994. Quelques considérations sur la flore fossile du bassin d'Oas, département de Satu Mare. In: *The Miocene from the Transylvanian Basin, Romania*. Universitea Babeş-Bolyai, Cluj-Napoca, pp 29-34.
- Gladstone, G., Flecker, R., Valdes, P., Lunt, D., Markwick, P., 2007. The Mediterranean hydrologic budget from a Late Miocene global climate simulation, *Palaeogeogr. Palaeoclimatol. Palaeoecol.* 251, 254-267.
- Goudriaan, J., van Laar, H.H., 1994. Modelling potential crop growth processes Textbook with exercises, Kluwer Academic Publishers, Dordrecht, 238 pp.
- Henrot A.-J., François L., Favre E., Butzin M., Ouberdous M., Munhoven G., 2010. Effects of CO₂, continental distribution, topography and vegetation changes on the climate at the Middle

- Miocene: a model study. *Clim. Past*, submitted.
- Horváth, E., 1972. Beiträge zur Kenntnis der pliozänen Flora Westungarns, Savaria. *Vas megyei Múzeumok Értesítője* 5-6, 23-73.
- Hubert, B., François, L., Warnant, P., Strivay, D., 1998. Stochastic generation of meteorological variables and effects on global models of water and carbon cycles in vegetation and soils. *Journal of Hydrology* 212-213, 318-334.
- Ivanov, D.A., Ashraf, A.R., Mosbrugger, V., Palmarev, E., 2002. Palynological evidence for Miocene climate change in the Forecarpathian Basin (Central Paratethys, NW Bulgaria). *Palaeogeogr., Palaeoclim., Palaeoecol.* 178, 19–37.
- Ivanov, D., Utescher, T., Mosbrugger V., Syabryaj, S., Dordjevic-Milutinovic, D., this volume. Vegetation and climate dynamics in the Miocene of Southeast Europe.
- Jiménez-Moreno G., 2005. Utilización del análisis polínico para la reconstrucción de la vegetación, clima y estimación de paleoaltitudes a lo largo de arco alpino europeo durante el Mioceno (21-8 Ma). Thèse, Univ. Lyon 1 et Univ. Grenade, 312 pp.
- Jungclauss, J.H., Keenlyside, N., Botzet, M., Haak, H., Luo, J.-J., Latif, M., Marotzke, J., Mikolajewicz, U., Roeckner, E., 2006. Ocean Circulation and Tropical Variability in the Coupled Model ECHAM5/MPI-OM. *Journal of Climate - Special Section*, 19, 3952-3972.
- Knobloch, E., 1973. Die gegenseitigen Beziehungen der tschechoslowakischen und ungarischen Tertiärfloren. *Földt. Közl. Bull. Hung. geol. Soc.* 102(3-4), 246-269.
- Knobloch, E., 1978. Die Flora aus dem Pannon von Neusiedl/See (Burgenland, Österreich). *Paleont. Conf. 1977, Praha. Carlowa Univ.*, 157-168.
- Kottek, M., Grieser, J., Beck, C., Rudolf, B., Rubel, F., 2006. World Map of the Köppen-Geiger climate classification updated. *Meteorologische Zeitschrift* 15, 259-263
- Kretzoi, M., Krolopp, E., Lőrincz, H., Pálfalvy, I., 1976. Flora, Fauna und Stratigraphische Lage der Untenpannonischen Prähominiden-Fundstelle von Rudabánya, NO-Ungarn. *Annual Report of the Hungarian geological Institute* 1974, 365-394.
- Laurent, J.-M., Bar-Hen, A., François, L., Ghislain, M. et Cheddadi, R. 2004. Refining vegetation simulation models: from plant functional types to bioclimatic affinity groups of plants. *Journal of Vegetation Science* 15, 739-746.
- Laurent, J.-M., François, L., Bar-Hen, A., Bel, L., Cheddadi, R., 2008. European Bioclimatic Affinity Groups: data-model comparisons. *Global Planet. Change* 61, 28-40.
- László, J., 1992. Fossil plant remains from the lignite open mining at Bukkábrány. *Ann. Report Hungarian Geol. Inst. Budapest* 1990, 321-337.
- Magyar, I., Geary, D.H., Müller, P., 1999. Paleogeographic evolution of the Late Miocene Lake

- Pannon in Central Europe. *Palaeogeography, Palaeoclimatology, Palaeoecology* 147, 151–167.
- Mai, D.H., 1995. *Tertiäre Vegetationsgeschichte Europas*. Gustav Fischer, Jena, Stuttgart, New York.
- Mai, D.H., 2001. Die mittelmiozaenen und obermiozaenen Floren aus der Meuroer und Raunoer Folge in der Lausitz; Teil 2, Dicotyledonen. *Palaeontographica, Abteilung B* 257, 35-174.
- Manukyan, L.K., 1977. The Miocene flora and vegetation of the Hoktembryan depression on palaeopalynological data [in Russian]. *Akademia Nauk Armianskoy SSR. Biolog. Zhurnal Anneniy* 30(12), 9-15.
- Marsland, S.J. Haak, H., Jungclaus, J.H., Latif, M., Röske, F., 2003. The Max-Planck-Institute global ocean/sea ice model with orthogonal curvilinear coordinates. *Ocean Modell.*, 5, 91-127.
- Melinte-Dobrinescu, M.C., Suc, J.-P., Clauzon, G., Popescu, S.-M., Armijo, R., Meyer, B., Biltekin, D., Çağatay, M.N., Uçarkus, G., Jouannic, G., Fauquette, S., Çakir, Z., 2009. The Messinian Salinity Crisis in the Dardanelles region: Chronostratigraphic constraints. *Palaeogeography, Palaeoclimatology, Palaeoecology*, 278, 24-39.
- Menke B., 1975. *Vegetationsgeschichte und Florenstratigraphie Nordwestdeutschlands im Pliozän und Frühquartär. Mit einem Breitrag zur Biostratigraphie des Weichselfrühglazials*. *Geol. Jb.*, A26, 1-151.
- Meziane, D., Shipley, B., 2001. Direct and indirect relationships between specific leaf area, leaf nitrogen and leaf gas exchange. Effects of irradiance and nutrient supply. *Annals of Botany* 88, 915-927.
- Micheels, A., Bruch, A.A., Uhl, D., Utescher, T., and Mosbrugger, V., 2007. A Late Miocene climate model simulation with ECHAM4/ML and its quantitative validation with terrestrial proxy data. *Palaeogeography, Palaeoclimatology, Palaeoecology*, 253, 267-286.
- Micheels, A., Bruch, A.A., Mosbrugger, V., 2009. Miocene climate modelling sensitivity experiments for different CO₂ concentrations. *Palaeontologia Electronica*, 12, 6A, 20 pp.
- Micheels, A., Bruch, A.A., Eronen, J., Fortelius, M., Harzhauser, M., Utescher, T., Mosbrugger, V., this volume. Analysis of heat transport mechanisms from a Late Miocene model experiment with a fully-coupled atmosphere-ocean general circulation model.
- Mintz, Y., Walker, G.K., 1993. Global fields of soil moisture and land surface evapotranspiration derived from observed precipitation and surface air temperature. *J. Appl. Meteor.* 32, 1305-1334.
- Mosbrugger, V., Utescher, T., 1997. The coexistence approach - a method for quantitative reconstructions of Tertiary terrestrial palaeoclimate data using plant fossils, *Palaeogeogr.*

- Palaeoclim., Palaeoecol. 134, 61–86.
- Mosbrugger, V., Utescher, T., Dilcher, D.L., 2005. Cenozoic continental climatic evolution of Central Europe, PNAS 102, 14964-14969.
- Naud, G., Suc, J.-P., 1975. Contribution à l'étude paléofloristique des Coirons (Ardèche): premières analyses polliniques dans les alluvions sous-basaltiques et interbasaltiques de Mirabel (Miocène supérieur). Bull. Soc. Géol. France, sér. 7, 17, 5, 820-827.
- Nemry, B., François, L., Warnant, P., Robinet, F., Gérard, J.-C., 1996. The seasonality of the CO₂ exchange between the atmosphere and the land biosphere: a study with a global mechanistic vegetation model. J. Geophys. Res. 101, 7111-7125.
- New, M., Lister, D., Hulme, M., Makin, I., 2002. A high-resolution data set of surface climate over global land areas. Climate Research 21,1-25.
- Otto, D., Rasse, D., Kaplan, J., Warnant, P., François, L., 2002. Biospheric carbon stocks reconstructed at the Last Glacial Maximum: comparison between general circulation models using prescribed and computed sea surface temperatures. Global Planet. Change 33, 117-138.
- Pagani, M., Zachos, J.C., Freeman, K.H., Tipple, B., Bohaty, S., 2005. Marked decline in atmospheric carbon dioxide concentrations during the Paleogene. Science 309, 600-603.
- Pais, J., 1986. Evolution de la végétation et du climat pendant le Miocène au Portugal. Ciencias da Terra 8, 179-189.
- Palfalvy, I., 1952. Plantes fossils du Pliocène inférieur des environs de Rozsaszentmárton. Ann. Report Hungarian Geol. Inst. Budapest 1949, 63-66.
- Palfalvy, I., 1977. Pliozäne Pflanzenreste von Balatonszentgyörgy, SW-Ungarn. Ann. Report Hungarian Geol. Inst. Budapest 1975, 417-422.
- Palfalvy, I., Rakosi, L., 1979. Die Pflanzenreste des lignitflözführenden Komplexes von Visonta (N-Ungarn). Ann. Report Hungarian Geol. Inst. Budapest 1977, 47-66.
- Pantic, N., Mihajlovic, D., 1980. Neogene floras of "Balkan land" and their significance for paleoclimatology, paleobiogeography and biostratigraphy III. Ann. Géol. de la Péninsule Balkanique 43-44, 239-261.
- Popescu, S.-M., Dalesme, F., Jouannic, G., Escarguel, G., Head, M.J., Melinte-Dobrinescu, M.C., Sütő-Szentai, M., Bakrac, K., Clauzon, G., Suc, J.-P., 2009. *Galeacysta etrusca* complex, dinoflagellate cyst marker of Paratethyan influxes into the Mediterranean Sea before and after the peak of the Messinian Salinity Crisis. Palynology, 33, 2, 105-134.
- Popov, S.V., Rögl, F., Rozanov, A.Y., Steininger, F.F., Shcherba, I.G., Kovac, M. (Eds), 2004. Lithological-Paleogeographic maps of Paratethys. 10 maps Late Eocene to Pliocene. Courier

- Forschungsinstitut Senckenberg, 250, 1-46.
- Popov, S.V., Shcherba, I.G., Ilyina, L.B., Nevesskaya, L.A., Paramonova, N.P., Khondkarian, S.O., Magyar, I. 2006 Late Miocene to Pliocene palaeogeography of the Paratethys and its relation to the Mediterranean. *Palaeogeography, Palaeoclimatology, Palaeoecology*, 238, 1-4, 91-106.
- Rivas Carballo, M.R., 1986. Análisis palinológico del tramo superior de la sección de Torremormojón (Palencia). In: Civis Llovera, J., Valle Hernández, Ma. F. (Eds.), *Actas de Palinología. VI Simposio de Palinología (A.P.L.E.)*, Salamanca, 1986. Ediciones de la Universidad de Salamanca, pp. 338– 344.
- Rivas-Carballo M.R., 1991. The development of vegetation and climate during the Miocene in the south-eastern sector of the Duero Basin (Spain). *Rev. Palaeobot. Palynol.*, 67, 341-351.
- Rivas Carballo, M.R., Valle Hernández, M.F., 1987. Palinología de la cuenca del Duero Peñafiel (Valladolid). In : Civis Llovera, J., Valle Hernández, M.F. (eds.), *Actas de Palinología (Actas del VI Simposio de Palinología, A.P.L.E.)*, Universidad de Salamanca, Salamanca, pp. 345-350.
- Roeckner, E., Bäuml, G., Bonaventura, L., Brokopf, R., Esch, M., Giorgetta, M., Hagemann, S., Kirchner, I., Kornblueh, L., Manzini, E., Rhodin, A., Schlese, U., Schulzweida, U., Tompkins, A., 2003. The atmospheric general circulation model ECHAM5 Part 1 - Model description. Report 349, Max-Planck-Institut für Meteorologie, Hamburg.
- Roeckner, E., Brokopf, R., Esch, M., Giorgetta, M., Hagemann, S., Kornblueh, L., Manzini, E., Schlese, U., Schulzweida, U., 2006. Sensitivity of simulated climate to horizontal and vertical resolution in the ECHAM5 atmosphere model. *Journal of Climate*, 19, 3771-3791.
- Sanz de Siria, A., 1985. Datos para el conocimiento de las floras miocénicas de Cataluña. *Paleontol. Evol.* 19, 167– 177.
- Saxton, K.E., Rawls, W.J., Romberger, J.S., Papendick, R.I., 1986. Estimating generalized soil-water characteristics from texture. *Soil Sci. Soc. Am. J.* 50(4),1031-1036.
- Simioni, G., Gignoux, J., Le Roux, X., Appé, R., Benest, D., 2004. Spatial and temporal variations in leaf area index, specific leaf area and leaf nitrogen of two co-occurring savanna tree species. *Tree Physiology* 24, 205-216.
- Steppuhn, A., Micheels, A., Geiger, G., and Mosbrugger, V. 2006. Reconstructing the Late Miocene climate and oceanic heat flux using the AGCM ECHAM4 coupled to a mixed-layer ocean model with adjusted flux correction, *Palaeogeography, Palaeoclimatology, Palaeoecology*, 238, 399-423.
- Steppuhn, A., Micheels, A., Bruch, A.A., Uhl, D., Utescher, T., and Mosbrugger, V. 2007. The

- sensitivity of ECHAM4/ML to a double CO₂ scenario for the Late Miocene and the comparison to terrestrial proxy data. *Global and Planetary Change*, 57, 189-212.
- Suc J.-P., Legigan P., Diniz F., 1986. Analyse pollinique de lignites néogènes des Landes : Arjuzanx et Hostens (France). *Bull. Inst. Géol. Bassin Aquitaine*, 40, 53-65.
- Syabryaj, S., Utescher, T., Molchanov, S., 2007. Changes of climate and vegetation during the Miocene in the territory of Ukraine. *Palaeogeography, Palaeoclimatology, Palaeoecology* 253, 151–166.
- Utescher, T., Mosbrugger, V., Ashraf, A.R., 2000. Terrestrial climate evolution in Northwest Germany over the last 25 million years, *Palaios* 15, 430–449.
- Utescher, T., Erdei, B., François, L., Mosbrugger, V., 2007a. Tree diversity in the Miocene forests of Western Eurasia. *Palaeogeogr. Palaeoclim. Palaeoecol.*, 253, 226-250.
- Utescher, T., Djordjevic-Milutinovic, D., Bruch, B., Mosbrugger, V., 2007b. Climate and vegetation changes in Serbia during the last 30 Ma., *Palaeogeography, Palaeoclimatology, Palaeoecology* 253, 139–150.
- Utescher, T., Mosbrugger, V., 1990–2010. The Palaeoflora Database: <http://www.palaeoflora.de>.
- Utescher, T., Bruch, A.A., Micheels, A., Mosbrugger, V., this volume. Cenozoic climate gradients and regional anomalies in Eurasia and their potential for validating future climate change scenarios.
- Valle Hernández, M.F., Salvador de Luna, J.V., 1985a. Resultados palinológicos en el borde sur-occidental de la cuenca del Duero. *Estudios Geológicos* 41(1-2), 69-76.
- Valle Hernández, M.F., Salvador de Luna, J.V., 1985b. Palinología del Neógeno de la cuenca del Duero. *Castrillo del Val (Burgos). Estudios Geológicos* 41(3-4), 237-242.
- Van der Burgh, J., 1988. Some local floras from the Neogene of the Lower Rhenish Basin. *Journal of Tertiary Research* 9, 181-212.
- Van Wijk, M.T., Dekker, S.C., Bouten, W., Bosveld, F.C., Kohsiek, W., Kramer, K., Mohren, G.M.J., 2000. Modeling daily gas exchange of a Douglas-fir forest: comparison of three stomatal conductance models with and without a soil water stress function. *Tree Physiology* 20, 115-122.
- Warnant, P., François, L., Strivay, D., Gérard, J.C., 1994. CARAIB : A global model of terrestrial biological productivity. *Global biogeochemical cycles* 8, (3). 255-270.
- Warnant, P., 1999. Modélisation du cycle du carbone dans la biosphère continentale à l'échelle

globale. Université de Liège, 276 pp.

Wolfe, J.A., 1979. Temperature parameters of humid to mesic forests of Eastern Asia, Geological Survey Professional Papers 1106, 37 pp.

Zachos, J.C., Pegani, M., Stone, L., Thomas, E., Billups, K., 2001. Trends, rhythms, and aberrations in global climates 65 Ma to present. *Science* 292, 686-293.

Table 1. Classification of the model PFTs used in this paper: correspondence between main species or families and PFTs.

PFT name	Main species or families belonging to the PFT
1 C3 herbs	<i>all C3 herbaceous plants</i>
2 C4 herbs	<i>all C4 herbaceous plants</i>
3 Needle-leaved evergreen boreal/temperate cold trees	<i>Cupressaceae, Juniperus, Juniperus communis, Abies, Picea abies, Pinus, Pinus sylvestris</i>
4 Needle-leaved evergreen temperate cool trees	<i>Abies alba, Taxus, Chamaecyparis, Picea omorika, Pseudotsuga menziesii, Sequoia sempervirens, Thuja orientalis, Tsuga diversifolia</i>
5 Needle-leaved evergreen temperate dry warm trees	<i>Cedrus, Pinus halepensis, Pinus pinaster, Cupressus, Tetraclinis</i>
6 Needle-leaved evergreen temperate perhumid warm trees	<i>Sciadopitys, Cathaya, Keteleeria, Taiwania, Torreya, Athrotaxis</i>
7 Needle-leaved summergreen boreal/temperate cold trees	<i>Larix decidua</i>
8 Needle-leaved summergreen temperate warm trees	<i>Taxodium, Glyptostrobus</i>
9 Broadleaved evergreen temperate dry warm trees	<i>Olea europaea, Pistacia, Phillyrea, Quercus ilex, Quercus suber, Arbutus, Dalbergia, Ocotea, Quercus troyana</i>
10 Broadleaved evergreen temperate perhumid warm trees	<i>Alangium, Castanopsis, Fatsia japonica, Gordonia, Linderia, Magnolia virginiana, Neolitsea, Reevesia, Symplocos yunnanensis, Persea indica</i>
11 Broadleaved summergreen boreal/temperate cold trees	<i>Alnus, Alnus glutinosa, Corylus avellana, Quercus, , Populus, Tilia, Betula, Salix</i>
12 Broadleaved summergreen temperate cool trees	<i>Acer campestre, Carpinus betulus, Fagus sylvatica, Tilia platyphyllos, Acer, Fraxinus excelsior, Tilia cordata, Ulmus, Aesculus rubicunda, Populus cathayana, Quercus castaneaefolia, Quercus lobata, Tilia japonica, Ulmus davidiana, Quercus robur</i>
13 Broadleaved summergreen temperate warm trees	<i>Castanea, Juglans, Ostrya, Quercus pubescens, Craigia, Diospyros lotus, Halesia, Liquidambar formosana, Quercus benthamii, Sassafras,</i>
14 Broadleaved raingreen tropical trees	<i>Acacia, Bursera, Dendropanax, Gironniera</i>
15 Broadleaved evergreen tropical trees	<i>Annona, Bombax, Bursera, Cassine, Cupania, Monotes, Sterculia, Zenkerella</i>

Table 2. PFT-dependent parameters controlling plant stress and germination (see text). Soil water thresholds SW_{\min} and SW_{\max} refer to available soil water in relative units, i.e., in terms of the variable $(W-WP)/(FC-WC)$ where W , WP and FC are respectively the amount of soil water, the wilting point and the field capacity in mm.

PFT name	T_{\min} (°C)	SW_{\min}	T_{\max} (°C)	SW_{\max}	$GDD5_{\min}$ (°C day)	ξ
1 C3 herbs	-60.0	0.01	-	-	50	1
2 C4 herbs	0.0	0.01	-	-	3500	1
3 Needle-leaved evergreen boreal/temperate cold trees	-43.0	0.16	3.2	-	532	0.4
4 Needle-leaved evergreen temperate cool trees	-14.7	0.18	3.1	-	1186	0.4
5 Needle-leaved evergreen temperate dry warm trees	-7.4	0.09	6.1	0.38	2398	0.4
6 Needle-leaved evergreen temperate perhumid warm trees	-3.8	0.28	14.1	-	3383	0.4
7 Needle-leaved summergreen boreal/temperate cold trees	-60.0	0.25	-2.7	-	350	0.4
8 Needle-leaved summergreen temperate warm trees	-14.9	0.17	12.1	-	3671	0.4
9 Broadleaved evergreen temperate dry warm trees	-7.4	0.07	6.8	0.43	2442	1
10 Broadleaved evergreen temperate perhumid warm trees	-3.4	0.27	13.6	-	3546	1
11 Broadleaved summergreen boreal/temperate cold trees	-34.0	0.18	3.3	-	542	1
12 Broadleaved summergreen temperate cool trees	-23.9	0.16	2.9	-	1086	1
13 Broadleaved summergreen temperate warm trees	-12.6	0.15	4.1	-	1771	1
14 Broadleaved raingreen tropical trees	11.8	0.02	-	0.30	6250	1
15 Broadleaved evergreen tropical trees	11.8	0.18	-	-	6250	1

Table 3. Biome classification used in the model.

PFT name	GDD5 (°C day)	NPP _{tot}	LAI _{tot}	R	LAI _{tree}	f _{C4}	Other conditions	D
1 Ice/Polar Desert	< 50							
2 Desert	≥ 50	0						
3 Semi-desert	> 500	≠ 0	< 0.3					
4 Tundra	[50-500]	≠ 0			< 0.8			
5 Tropical grassland	> 500	≠ 0	≥ 0.3	> 0.8	< 0.8	> 0.5		
6 Temperate grassland	> 500	≠ 0	≥ 0.3	> 0.8	< 0.8	≤ 0.5		
7 Tropical savannah		≠ 0	≥ 0.3	> 0.8	≥ 0.8	> 0.5		
8 Warm-temperate open woodland		≠ 0	≥ 0.3	> 0.8	≥ 0.8	≤ 0.5	f _{med} +f _{strop} > 0.05	
9 Cold temperate/boreal open woodland		≠ 0	≥ 0.3	> 0.8	≥ 0.8	≤ 0.5	f _{med} +f _{strop} ≤ 0.05	
10 Tropical rainforest		≠ 0	≥ 0.3	≤ 0.8			f _{trop} > 0.67	15
11 Tropical seasonal forest		≠ 0	≥ 0.3	≤ 0.8			f _{trop} > 0.67	14
12 Warm-temperate mixed evergreen forest, fully humid		≠ 0	≥ 0.3	≤ 0.8			f _{strop} +f _{trop} > 0.67	6,8,10
13 Warm-temperate broadleaved evergreen forest / dry season		≠ 0	≥ 0.3	≤ 0.8			f ₉ > 0.67	
14 Warm-temperate conifer forest		≠ 0	≥ 0.3	≤ 0.8			f _{ndl} > 0.67	5
15 Warm-temperate mixed forest		≠ 0	≥ 0.3	≤ 0.8			f _{strop} +f _{trop} ≤ 0.67 f ₉ ≤ 0.67 f _{ndl} ≤ 0.67 f _{bdec} ≤ 0.67 f _{cold} ≤ 0.8	5,9
16 Temperate broadleaved deciduous forest		≠ 0	≥ 0.3	≤ 0.8			f _{bdec} > 0.67	
17 Cool-temperate conifer forest		≠ 0	≥ 0.3	≤ 0.8			f _{ndl} > 0.67	3,4,7
18 Cool-temperate mixed forest		≠ 0	≥ 0.3	≤ 0.8			f _{strop} +f _{trop} ≤ 0.67 f ₉ ≤ 0.67 f _{ndl} ≤ 0.67 f _{bdec} ≤ 0.67 f _{cold} ≤ 0.8	3,4,7, 11,12, 13
19 Boreal/montane forest		≠ 0	≥ 0.3	≤ 0.8			f _{cold} > 0.8	

GDD5 = growing-degree-days above 5°C cumulated over one year

NPP_{tot} = total NPP of the grid cell

LAI_{tot} = total leaf area index of the grid cell (herbs + trees)

LAI_{tree} = leaf area index of the over-storey (trees)

R = NPP(herbs)/NPP(trees) = ratio of herb NPP (PFTs 1-2) to tree NPP (PFTs 3-15)

f_{C4} = cover fraction of C4 herbs in the under-storey

f_i = cover fraction of tree PFT i in the over-storey

f_{cold} = f₃ + f₇ + f₁₁ = cover fraction of boreal/temperate cold trees in the over-storey

f_{bdec} = f₁₁ + f₁₂ + f₁₃ = cover fraction of broadleaved summergreen boreal/temperate trees in the over-storey

f_{ndl} = f₃ + f₄ + f₅ + f₇ = cover fraction of temperate needle-leaved trees in the over-storey

f_{med} = f₅ + f₉ = cover fraction of temperate dry warm trees (Mediterranean) in the over-storey

f_{strop} = f₆ + f₈ + f₁₀ = cover fraction of humid warm trees (from Cfa climates) in the over-storey

f_{trop} = f₁₄ + f₁₅ = cover fraction of tropical trees in the over-storey

D = dominant tree PFT

Table 4. Co-existence probability levels (or “affinity” levels) between tree PFTs under the classification defined in table 2. H = high affinity of PFTs, M = moderate affinity of PFTs, L = low affinity of PFTs, I = improbable co-existence of PFTs. These affinity levels have been determined from the overlapping of PFTs in a simulation of CARAIB over Europe and southeastern Asia. Let N_i (reported below) be the number of $10' \times 10'$ grid cells covered by PFT i in this simulation, and N_{ij} the number of grid cells covered both by PFT i and PFT j (i.e., intersection between i and j). The probability to find PFT j in the distribution area of PFT i is $p = N_{ij}/N_i$, while the probability to find PFT j at random over the studied area (Europe + southeastern Asia) is $p_0 = N_j/N_{\text{grid}}$, where $N_{\text{grid}}=114777$ is the total number of grid cells in the simulation. Affinity levels have been scaled according to $r = (p/p_0)-1$, a parameter (analogous to kappa statistics) that varies between -1 (no overlap between PFTs i and j) and +1 (perfect match between the areas of PFT i and j). $r = 0$ corresponds to random overlapping. In the current study, the affinity levels are defined here as follows: H ($r > 0.40$), M ($0.10 < r < 0.40$), L ($-0.60 < r < 0.10$), I ($r < -0.60$).

PFT	3	4	5	6	7	8	9	10	11	12	13	14	15	N_i
3	H	H	L	L	H	L	L	L	H	H	H	I	I	62876
4	H	H	H	M	H	M	H	M	H	H	H	I	I	31080
5	L	H	H	H	L	H	H	H	L	M	H	I	I	11271
6	L	M	H	H	I	H	H	H	L	L	H	H	H	13907
7	H	H	L	I	H	I	L	I	H	H	M	I	I	40643
8	L	M	H	H	I	H	H	H	L	L	H	H	H	15000
9	L	H	H	H	L	H	H	H	L	M	H	L	I	14902
10	L	M	H	H	I	H	H	H	L	L	H	H	H	14384
11	H	H	L	L	H	L	L	L	H	H	H	I	I	58239
12	H	H	M	L	H	L	M	L	H	H	H	I	I	46712
13	H	H	H	H	M	H	H	H	H	H	H	I	I	30028
14	I	I	I	H	I	H	L	H	I	I	I	H	H	3995
15	I	I	I	H	I	H	I	H	I	I	I	H	H	4029

Table 5. Determination of the likelihood level that a specified PFT was present at a given palaeovegetation data site. The case of PFT 11 (Broadleaved summergreen boreal/temperate cold trees) at Vilella site in northern Spain (EU_VILELLA, 42.3°N, 2.9°E) is illustrated. Each taxon observed in the database for this site is allocated to one or several PFTs. Then, the affinity level of all allocated PFTs with PFT 11 is derived from table 4 (H = high affinity, M = moderate affinity, L = low affinity, I = improbable co-existence). For each taxon, the highest affinity level is selected to provide the taxon affinity score with PFT 11. Finally, the smallest affinity score is selected among all taxa to get the global affinity score of PFT 11 at the site. A global affinity score of L is obtained, meaning that one or several taxa having at the best “low affinity” with PFT 11 are present at the site. Consequently, the presence of PFT 11 is considered as *unlikely*. Indeed, global affinity scores of L and I are considered to yield respectively likelihood levels of *unlikely* and *inconsistent*. Global affinity scores of H and M are normally considered to yield a likelihood level of *likely*, except if the PFT has been ranked as most likely PFTs for at least one taxon (in which case the PFT is assigned a likelihood level of *very likely*). The most likely PFT for each taxon is the one, among all possible PFTs for this taxon, that reaches the highest global affinity score expressed in term of the parameter $r = (p/p_0) - 1$ (see legend of table 4).

Observed fossil taxa (EU_VILELLA)	PFT allocation	Affinity levels with PFT 11	Taxon affinity score with PFT 11	Most likely PFT
<i>Abies sp.</i>	3, 4, 6	H, H, L	H	6
<i>Acer intergerrimum</i>	12, 13	H, H	H	13
<i>Acer pyrenaicum</i>	11, 12, 13	H, H, H	H	13
<i>Acer sp.</i>	11, 12, 13	H, H, H	H	13
<i>Alnus occidentalis</i>	11, 12, 13	H, H, H	H	13
<i>Cedrela sp.</i>	9, 10, 15	L, L, I	L	9
<i>Cryptomeria rhenana</i>	4, 6	H, L	H	6
<i>Fagus pristina</i>	12, 13	H, H	H	13
<i>Juglandaceae sp.</i>	11, 12, 13	H, H, H	H	13
<i>Lauraceae</i>	9, 10, 13, 15	L, L, H, I	H	9
<i>Ostrya sp.</i>	11, 12, 13	H, H, H	H	13
<i>Persea princeps</i>	9, 10, 15	L, L, I	L	9
<i>Pinus sp.</i>	4, 5, 6	H, L, L	H	5
<i>Quercus drymea</i>	10, 15	L, I	L	10
<i>Quercus hispanica</i>	9, 10, 11, 12, 13	L, L, H, H, H	H	9
<i>Quercus mediterranea</i>	9	L	L	9
<i>Tsuga moenana</i>	4, 6	H, L	H	6
<i>Zelkova zelkovaefolia</i>	12, 13	H, H	H	13
<i>Fagus gussonii</i>	12, 13	H, H	H	13
<i>Betula insignis</i>	11, 12, 13	H, H, H	H	13
<i>Populus tremulaefolia</i>	11, 12, 13	H, H, H	H	13
<i>Fraxinus numana</i>	11, 12, 13	H, H, H	H	13
Global affinity score of PFT 11 at EU_VILELLA			L	

Table 6. Global affinity scores, likelihood levels, presence/absence status and biodiversity ratios of tree PFTs in the palaeoflora observed at Vilella site in northern Spain (EU_VILELLA, 42.3°N, 2.9°E). Global affinity scores of a PFT with the other PFTs observed at the site are defined as follows: H = high affinity, M = moderate affinity, L = low affinity, I = improbable co-existence. A negative sign indicates that no taxa have been allocated to the PFT, a positive sign indicates that at least one taxon has been unequivocally allocated to the PFT. Likelihood levels are obtained as explained in the legend of table 5. The threshold between absence (A) and presence (P) status is placed between *unlikely* and *likely*. For all PFTs that are considered as present (P status), a biodiversity fraction is evaluated, by calculating the proportion of taxa in the palaeoflora that were allocated to that PFT, using weighting factors that are doubled when the PFT is the most likely one (see table 7).

PFT name	Global affinity scores	Likelihood levels	Presence/absence status	Biodiversity fraction
3 Needle-leaved evergreen boreal/temperate cold trees	L	unlikely	A	0.000
4 Needle-leaved evergreen temperate cool trees	M	likely	P	0.057
5 Needle-leaved evergreen temperate dry warm trees	H	very likely	P	0.023
6 Needle-leaved evergreen temperate perhumid warm trees	H	very likely	P	0.102
7 Needle-leaved summergreen boreal/temperate cold trees	-	absent	A	0.000
8 Needle-leaved summergreen temperate warm trees	-	absent	A	0.000
9 Broadleaved evergreen temperate dry warm trees	+	present	P	0.152
10 Broadleaved evergreen temperate perhumid warm trees	H	very likely	P	0.098
11 Broadleaved summergreen boreal/temperate cold trees	L	unlikely	A	0.000
12 Broadleaved summergreen temperate cool trees	L	unlikely	A	0.000
13 Broadleaved summergreen temperate warm trees	H	very likely	P	0.568
14 Broadleaved raingreen tropical trees	-	absent	A	0.000
15 Broadleaved evergreen tropical trees	I	inconsistent	A	0.000

Table 7. Calculation of the biodiversity fraction of PFTs. The case of the flora from Vilella site in northern Spain (EU_VILELLA, 42.3°N, 2.9°E) is illustrated. Allocated tree PFTs are listed for each taxon recorded in the flora, after elimination of the PFTs for which the status is *absent* (see table 6). The most likely PFT occurs first. The cumulated occurrence of each PFT is evaluated by counting the number of taxa to which the PFT has been allocated. In the calculation, a fractional amount (occurrence level) is assigned when several PFTs have been allocated to the same taxon, the most likely PFT being attributed a double weight. The cumulated occurrence is then divided by the total number of taxa (here 22) to obtain the biodiversity fraction.

Observed fossil taxa (EU_VILELLA)	Allocated PFTs (from most to less likely)	PFT occurrence level												
		3	4	5	6	7	8	9	10	11	12	13	14	15
<i>Abies sp.</i>	6, 4		0.33		0.67									
<i>Acer intergerrimum</i>	13											1		
<i>Acer pyrenaicum</i>	13											1		
<i>Acer sp.</i>	13											1		
<i>Alnus occidentalis</i>	13											1		
<i>Cedrela sp.</i>	9, 10							0.67	0.33					
<i>Cryptomeria rhenana</i>	6, 4		0.33		0.67									
<i>Fagus pristina</i>	13											1		
<i>Juglandaceae sp.</i>	13											1		
<i>Lauraceae</i>	9, 13, 10							0.50	0.25			0.25		
<i>Ostrya sp.</i>	13											1		
<i>Persea princeps</i>	9, 10							0.67	0.33					
<i>Pinus sp.</i>	5, 6, 4		0.25	0.50	0.25									
<i>Quercus drymea</i>	10									1				
<i>Quercus hispanica</i>	9, 13, 10							0.50	0.25			0.25		
<i>Quercus mediterranea</i>	9							1						
<i>Tsuga moenana</i>	6, 4		0.33		0.67									
<i>Zelkova zelkovaefolia</i>	13											1		
<i>Fagus gussonii</i>	13											1		
<i>Betula insignis</i>	13											1		
<i>Populus tremulaefolia</i>	13											1		
<i>Fraxinus numana</i>	13											1		
Cumulated occurrence		0	1.25	0.50	2.25	0	0	3.33	2.16	0	0	12.5	0	0
Biodiversity fraction		0	0.057	0.023	0.102	0	0	0.152	0.098	0	0	0.568	0	0

Table 8. Agreement percentages for the comparison between data and model for each PFTs. The first index is for the data and the second for the model simulation (n=number of sites, q=proportion of sites, a=absence and p=presence). K_a and K_p are the “kappa” parameters for absence and presence respectively:

$$K_a = 2 \left[\frac{n_{aa}}{n_{aa} + n_{ap}} - 0.5 \right] \quad K_p = 2 \left[\frac{n_{pp}}{n_{pp} + n_{pa}} - 0.5 \right]$$

%Agr is the percentage of agreement in term of presence/absence:

$$\% Agr = \frac{n_{pp} + n_{aa}}{n_{tot}}$$

PFT	n tot	n aa	n ap	n pa	n pp	q aa	q ap	q pa	q pp	K a	K p	% Agr
3	58	24	32	0	2	0.414	0.552	0	0.034	-0.143	1	44.8
4	58	7	6	19	26	0.121	0.103	0.328	0.448	0.077	0.156	56.9
5	58	8	9	24	17	0.138	0.155	0.414	0.293	-0.059	-0.171	43.1
6	58	15	0	42	1	0.259	0	0.724	0.017	1	-0.953	27.6
7	58	52	5	1	0	0.897	0.086	0.017	0	0.825	-1	89.7
8	58	13	0	45	0	0.224	0	0.776	0	1	-1	22.4
9	58	9	7	21	21	0.155	0.121	0.362	0.362	0.125	0	51.7
10	58	11	0	47	0	0.19	0	0.81	0	1	-1	19.0
11	58	26	30	0	2	0.448	0.517	0	0.034	-0.071	1	48.3
12	58	24	24	2	8	0.414	0.414	0.034	0.138	0	0.6	55.2
13	58	0	0	30	28	0	0	0.517	0.483	0	-0.034	48.3
14	58	53	0	5	0	0.914	0	0.086	0	1	-1	91.4
15	58	54	0	4	0	0.931	0	0.069	0	1	-1	93.1

Table 9. Sensitivity of the percentage of agreement (%Agr; see table 7) between model and data to the choice of the threshold in likelihood levels used to separate presence and absence in the data. %Agr_low corresponds to a threshold placed between *absent* and *unlikely*, %Agr to the standard threshold between *unlikely* and *likely* (as in table 7), and %Agr_high to a threshold between *likely* and *very likely*.

PFT	%Agr low	%Agr	%Agr high
3	56.9	44.8	44.8
4	56.9	56.9	65.5
5	43.1	43.1	43.1
6	20.7	27.6	37.9
7	89.7	89.7	89.7
8	22.4	22.4	48.3
9	53.4	51.7	50.0
10	17.2	19.0	29.3
11	56.9	48.3	46.6
12	56.9	55.2	55.2
13	48.3	48.3	46.6
14	91.4	91.4	91.4
15	93.1	93.1	93.1

FIGURE AND CAPTIONS

Fig. 1. Maps of air temperature and precipitation anomaly (Tortonian minus Present) over Europe for winter (DJF) and summer (JJA)

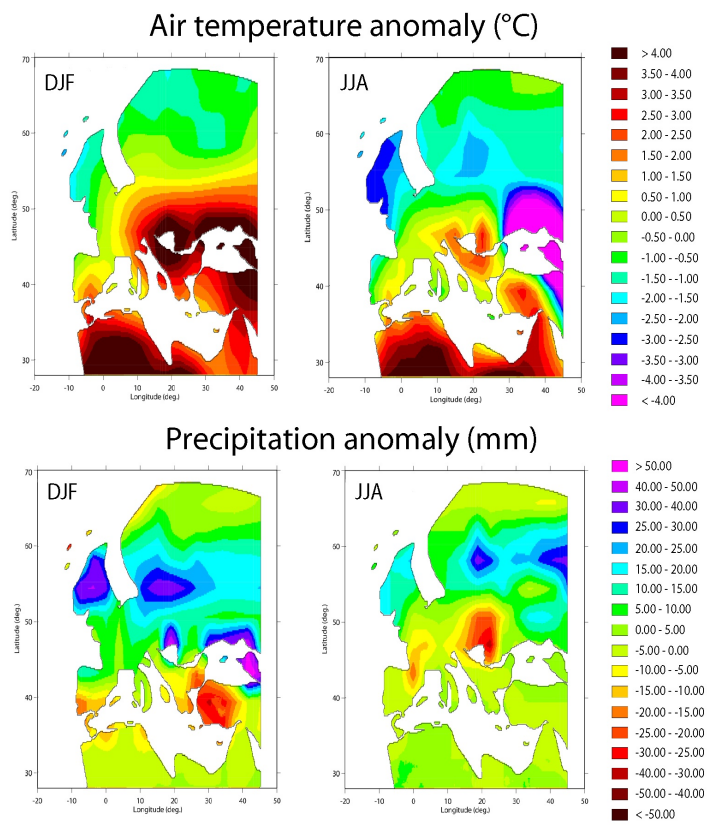


Fig. 2. Maps of the monthly minimum soil water for the Present and for the Tortonian

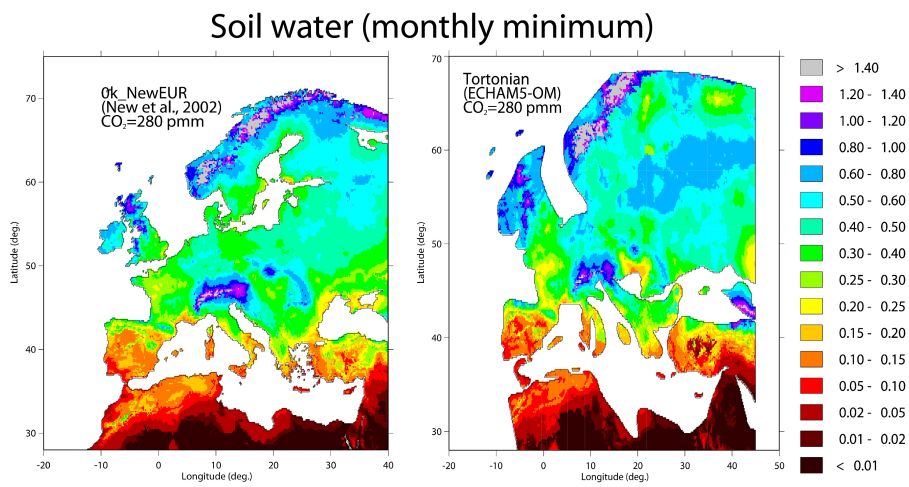


Fig. 3. Simulations of the potential vegetation biomes calculated with the CARAIB vegetation model for the Present and for the Tortonian. Biome classification is defined in Table 3.

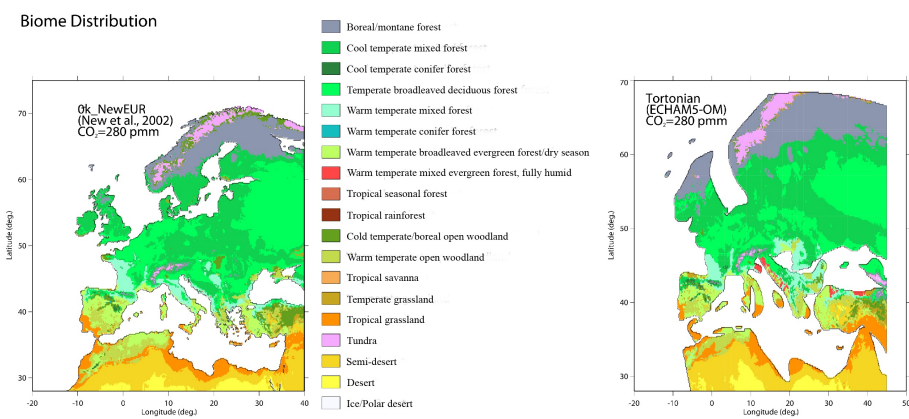


Fig. 4. Geographic distribution of the palaeovegetation data. The names of the localities and the coordinates are given in Appendix A. A biome type has been assigned to each locality on the basis of the observed palaeoflora, using a similar but simplified scheme with respect to the model.

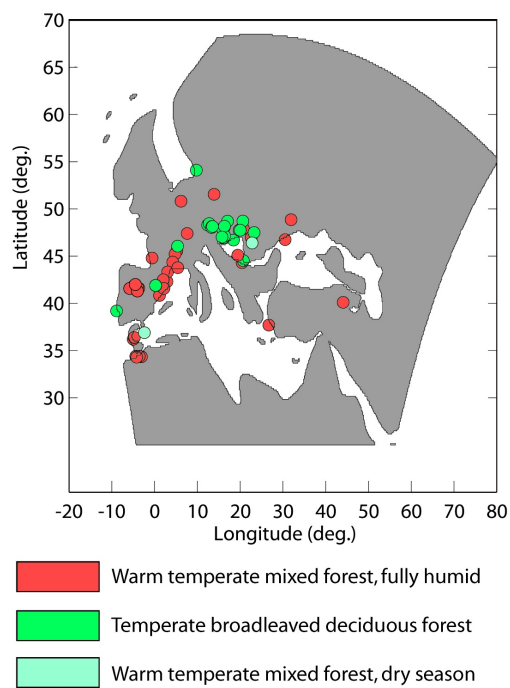


Fig. 5. Methodology of the comparison with the available data

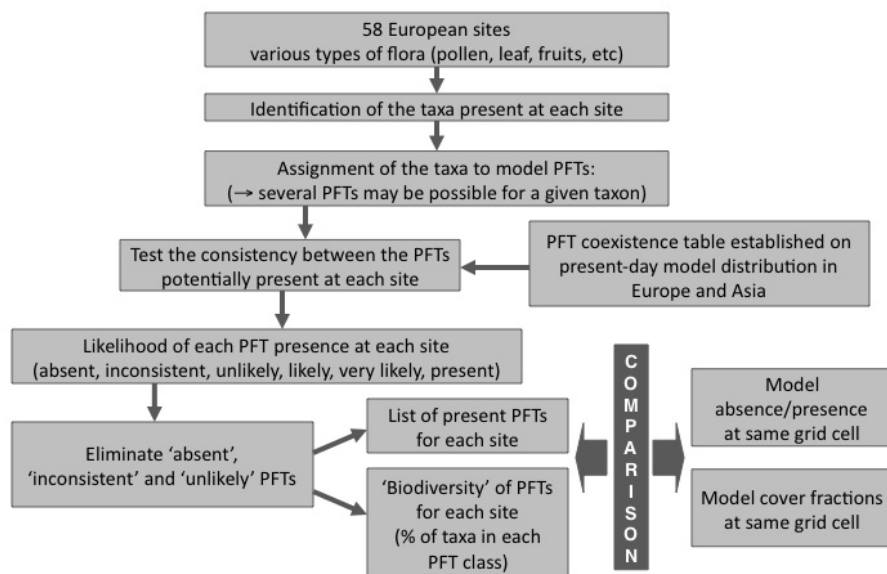


Fig. 6. Model-Data comparison in term of PFT presence and abundance for temperate cold/cool PFTs. The shape of the symbol at each locality refers to the agreement status between model and data: a circle corresponds to agreement in terms of presence/absence and a diamond to a discrepancy. The colour code corresponds to PFT cover fractions for the model results (overall distribution) and to PFT biodiversity fractions for the data (within each symbol).

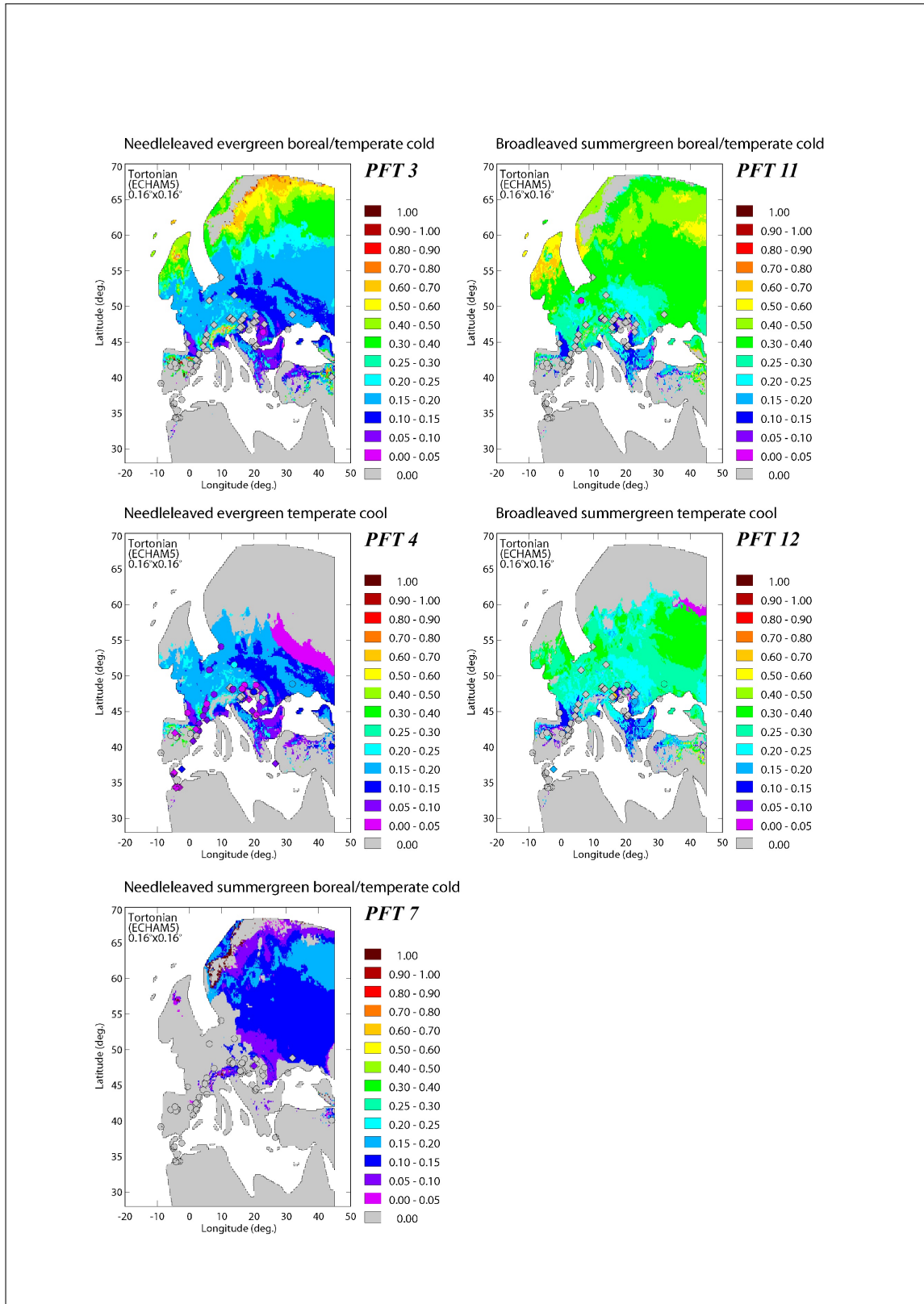


Fig. 7. Model-Data comparison in term of PFT presence and abundance for temperate warm PFTs. See legend of figure 6 for the definition of the symbols and colours.

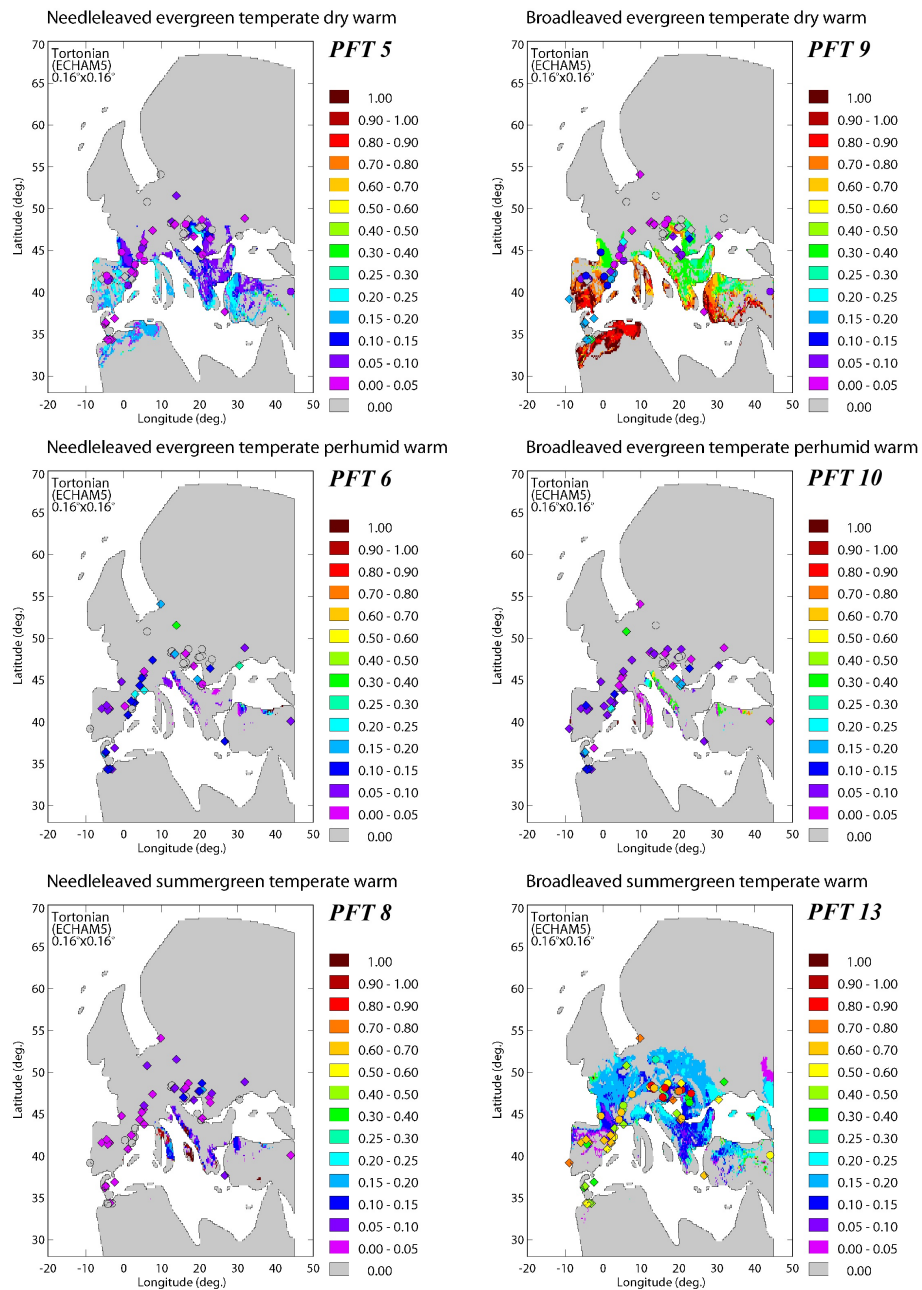


Fig. 8. Model-Data comparison in term of PFT presence and abundance for tropical PFTs. See legend of figure 6 for the definition of the symbols and colours.

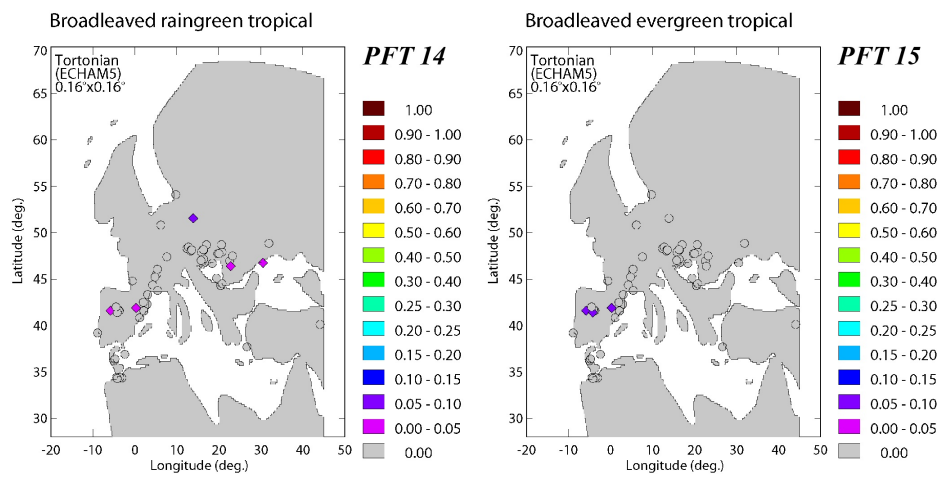
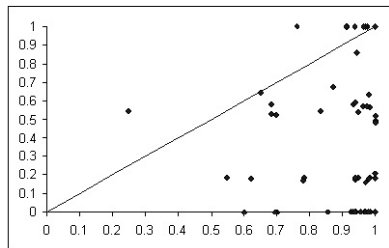


Fig. 9. Model-data comparison for the fraction of warm tree PFTs (“warm” means the sum of all warm-temperate and tropical types) at all available sites. Data biodiversity fractions are reported on the x-axis, while the model predicted cover fraction of these “warm” PFTs in the over-storey are reported on the y-axis. The straight line is a line with 1:1 slope on which the points would fall if there were a perfect agreement.



Appendix A

Diversities of plant functional types in the Late Miocene floras analysed. B: Leaf floras; F: Fruit and seed floras; M: Macrofloras; P: Palynofloras. N: Number of taxa; N PFT: Number of taxa contributing data (a single fossil taxon may contribute to several PFTs). Numbers 3 to 15 refer to PFT numbers in Table 1.

Miocene floras analyzed; diversity of trees

Locality name	Type	Lon	Lat	N	Npft	3	4	5	6	7	8	9	10	11	12	13	14	15
Euras_Hoktemberya	P	44.09	40.11	60	27	2	7	3	4	0	2	2	2	7	14	16	2	2
NEUSIEDL	B	15.83	47.92	17	17	0	3	0	2	0	1	0	0	3	12	12	1	0
SCHNEEGÄTTERN	B	13.32	48.04	12	12	0	1	1	1	0	1	0	0	3	10	10	0	0
WÖRTH	B	15.75	47.02	14	8	0	0	0	0	0	1	0	0	2	7	7	0	0
NEUHAUS	B	16.08	46.93	23	21	0	0	1	0	0	1	0	0	6	18	19	1	0
GROSSENREITH	B	13.36	48.16	16	14	0	1	1	1	0	1	0	0	2	12	12	0	0
LOHNSBURG	B	13.42	48.15	26	23	0	2	1	1	0	1	0	0	6	20	20	0	0
LAERBERG	B	16.27	48.17	35	33	0	2	1	2	0	2	1	2	9	25	25	0	2
VÖSENDORF	B	16.33	48.17	44	35	1	3	1	3	0	1	1	1	7	30	30	0	1
MORAVIAN BASIN	B	17.05	48.70	31	26	0	1	0	0	0	1	2	4	5	20	20	0	2
KLETTWITZ_FDP 12	F	13.90	51.55	53	15	3	8	2	7	0	1	0	0	2	4	4	0	0
ZUKUNFT 7A	F	6.17	50.82	48	21	0	2	1	1	0	2	0	8	1	9	10	0	6
EUR_Samos	P	26.70	37.70	29	17	1	4	1	4	0	2	1	2	6	11	11	0	1
BALATONSZENTGYÖRGY	B	18.45	46.70	20	12	0	1	1	1	0	1	2	2	5	9	10	0	1
BÜKKBRANY	B	20.75	47.92	22	13	0	0	0	0	0	2	0	0	5	11	11	0	0
ROZASZENTMARTON	B	19.75	47.75	27	22	1	2	0	0	0	2	1	2	5	15	16	1	2
RUDABANYA	B	20.63	48.71	40	29	0	2	1	1	0	3	0	2	9	20	21	1	1
SÉ	B	16.36	47.15	16	16	0	0	0	0	0	0	0	0	8	16	14	0	0
VISONTA	B	20.02	47.75	27	18	0	2	1	1	1	2	2	1	9	12	13	0	0
EURAS_POVOA_3	M	-8.90	39.20	16	14	0	0	0	0	0	0	3	2	5	10	11	0	3
DELURENI	B	22.58	46.97	22	22	3	6	3	5	0	1	4	3	2	6	9	2	4
OAS_BASIN	B	23.25	47.50	20	16	0	0	0	0	0	1	0	1	4	14	15	1	0
VALEA_NEAGRA	B	22.80	46.40	86	56	4	8	3	8	0	1	8	9	5	26	29	1	7
DUBONA_II	B	20.45	44.31	25	20	0	0	0	0	0	0	2	6	5	14	15	0	5
DURINCI	B	20.75	44.52	26	22	0	1	1	1	0	1	3	5	4	13	14	0	5
SREMSKA	B	19.45	45.10	11	9	0	2	2	3	0	0	1	2	1	4	4	0	1
EU_VILELLA	B	2.90	42.30	22	22	1	4	1	4	0	0	5	5	9	13	14	0	4
EUR_Abezames	P	-5.80	41.60	82	33	1	3	1	3	0	1	6	5	12	22	23	1	5
EUR_Burgos	P	-3.70	41.60	59	24	0	2	2	3	0	1	3	4	8	16	17	1	2
EUR_Penafiel	P	-4.20	41.40	52	21	0	2	2	2	0	1	2	3	8	13	12	0	4
EUR_Torrem 2	P	-4.50	42.00	38	14	0	2	1	2	0	1	3	3	8	9	10	1	2
EUR_Arjuzanx	P	-0.60	44.80	50	24	0	2	1	3	0	0	4	3	11	15	16	1	1
EURAS_SEO_DE_URGELL	M	0.30	41.90	64	52	0	1	1	1	0	0	11	9	19	35	38	2	12
EUR_Tarragona_E2	P	1.15	40.84	67	30	3	6	2	7	0	1	5	3	9	16	17	1	4
TERRASSA	B	2.16	41.58	26	25	0	0	0	0	0	0	7	11	13	18	20	0	4
EURAS_EMETOVKA	P	30.52	46.75	59	27	3	8	4	8	0	0	2	2	10	16	16	1	2
EURAS_W_Ukraina	P	31.91	48.86	108	36	4	8	2	7	0	3	0	1	12	23	21	0	1
Ain Mediouna	P	-4.40	34.40	59	20	0	1	1	2	0	0	5	4	9	11	12	1	4
Alboran A1	P	-5.00	36.20	42	15	1	4	1	5	0	2	4	4	4	5	6	1	2
Amberieu	P	5.21	45.57	33	21	2	4	2	4	0	1	2	2	8	14	15	1	0
Andalucia A1	P	-4.75	36.38	64	21	1	3	1	4	0	0	4	6	5	10	11	1	6
Andalucia G1	P	-4.75	36.40	43	16	0	2	1	3	0	1	4	4	5	7	8	1	3
Andance	P	4.78	45.23	33	32	2	5	2	6	0	1	3	2	11	18	19	1	0
Duero Basin	P	-4.00	41.70	80	30	0	3	2	3	0	2	4	5	14	20	21	0	4
Hennersdorf	P	16.36	48.11	46	44	3	6	2	7	0	2	1	2	8	16	17	1	1
Mirabel	P	4.23	44.37	63	31	3	6	2	7	0	1	2	1	11	21	22	1	0
Montredon	P	3.03	43.33	18	18	2	3	1	4	0	0	1	2	3	5	6	1	1
MSD 1	P	-3.08	34.35	49	16	0	1	1	2	0	0	6	3	5	7	8	1	3
Nebelberg	P	7.61	47.40	66	61	3	6	2	7	0	1	2	3	10	20	21	0	1
Oldenswort 9	P	9.75	54.10	36	27	3	5	0	6	0	1	1	2	12	20	20	0	1
Oued Msoun	P	-3.60	34.40	57	17	0	2	1	3	0	1	5	3	7	7	8	1	2
Sampsor	P	2.00	42.50	70	38	2	4	1	5	0	2	7	4	13	23	24	1	3
Sanavastre	P	2.00	42.50	72	33	2	5	1	6	0	3	3	4	12	21	22	1	3
Soblay	P	5.37	46.06	37	35	0	1	1	1	0	1	5	3	7	8	9	1	2
Strass 2	P	13.53	48.14	45	24	2	5	1	6	0	2	1	2	8	15	16	1	1
Taza mine	P	-4.20	34.30	40	12	0	1	1	2	0	0	3	3	6	6	7	1	1
Vaugines	P	5.42	43.78	30	29	3	5	1	6	0	1	2	2	4	8	9	1	2
Virgen Vittoria	P	-2.40	36.90	29	13	1	3	1	3	0	1	3	1	3	8	8	0	1

Miocene floras analyzed; references

locality name	reference
Euras_Hoktemberya	Manukyan, L.K., 1977.
NEUSIEDL	Knobloch, E., 1978.
SCHNEEGATTERN	Eder-Kovar, J., 1988.
WÖRTH	Eder-Kovar, J., Krainer, B., 1990.
NEUHAUS	Eder-Kovar, J., Hably, L., Derek, T., 1995.
GROSSENREITH	Eder-Kovar, J., 1988.
LOHNSBURG	Eder-Kovar, J., 1988.
LAAERBERG	Berger, W., 1955.
VÖSENDORF	Berger, W., 1952.
MORAVIAN_BASIN	Knobloch, E., 1973.
KLETTWITZ_FDP 12	Mai, D.H., 2001.
EUR_Samos	Chryssanthi, I., Solouniasd, N., 1985.
BALATONSZENTGYÖRGY	Pálfalvy, I., 1977.
BÜKKABRANY	Lászlo, J., 1992.
ROZSASZENTMARTON	Pálfalvy, I., 1952.
RUDABANYA	Kretzoi, M., Krolopp, E., Lőrincz, H., Pálfalvy, I., 1976.
SÉ	Horváth, E., 1972.
VISONTA	Pálfalvy, I., Rakosi, L., 1979.
ZUKUNFT 7A	van der Burgh, J., 1988.
EURAS_POVOA_3	Pais, J., 1986.
DELURENI	Givulescu, R., 1975.
OAS_BASIN	Givulescu, R., 1994.
VALEA_NEAGRA	Givulescu, R., 1962.
DUBONA_II	Pantic, N., Mihajlovic, D., 1980.
DURINCI	Pantic, N., and Mihajlovic, D., 1980.
SREMSKA	Pantic, N., and Mihajlovic, D., 1980.
EU_VILELLA	Barron, E., 1999.
EUR_Abezames	Valle Hernández, M.F., Salvador de Luna, J.V., 1985a.
EUR_Burgos	Valle Hernández, M.F., Salvador de Luna, J.V., 1985b.
EUR_Penafiel	Rivas Carballo, and Valle Hernández, M.F. 1987
EUR_Torrem 2	Rivas Carballo, M.R., 1986
EUR_Arjuzanx	Suc J.-P., Legigan P., Diniz F., 1986.
EURAS_SEO_DE_URGELL	Sanz de Siria, A., 1985
EUR_Tarragona_E2	Bessais, E., Cravatte, J., 1988
TERRASSA	Agusti, J., Sanz de Siria, A., Garces, M., 2003.
EURAS_EMETOVKA	Syabryaj et al., 2007.,
EURAS_W_Ukraina	Syabryaj et al., 2007.,
AIN MEDIOUNA	Bachiri Taoufiq, N., 2000.
ALBORAN A1	Jiménez-Moreno G., 2005.
AMBERIEU	Farjanel G., 1985.
ANDALUCIA A1	Jiménez-Moreno G., 2005.
ANDALUCIA G1	Jiménez-Moreno G., 2005.
ANDANCE	Bessedik M., 1985.
DUERO BASIN	Rivas-Carballo M.R., 1991.
HENNERSDORF	Jiménez-Moreno G., 2005.
MIRABEL	Naud G., Suc J.-P., 1975.
MONTREDON	Bessedik M., 1985.
MSD 1	Bachiri Taoufiq, N., 2000.
NEBELBERG	Jiménez-Moreno G., 2005.
OLDENSWORT 9	Menke B., 1975.
OUED MSOUN	Bachiri Taoufiq, N., 2000.
SAMPSOR	Bessedik M., 1985.
SANAVASTRE	Bessedik M., 1985.

SOBLAY	Jiménez-Moreno G., 2005.
STRASS 2	Jiménez-Moreno G., 2005.
TAZA MINE	Bachiri Taoufiq, N., 2000.
VAUGINES	Bessedik M., 1985.
VIRGEN VITTORIA	Suc, unpublished.

List of Figures

1.1	Schematic view of the climate system.	7
1.2	Map of major biome distributions.	8
1.3	Biophysical processes.	10
1.4	Biogeochemical processes.	14
2.1	Planet Simulator scheme.	20
2.2	Ocean heat fluxes for a preindustrial state.	24
2.3	Zonal annual mean (a) surface air temperature and (b) precipitation for the control simulations and the NCEP/NCAR reanalysis.	30
2.4	Zonal annual mean surface air temperature (a) over the continents and (b) over the oceans, and zonal annual mean precipitation (c) over the continents and (d) over the oceans for the control simulations and the NCEP/NCAR reanalysis.	31
2.5	Annual mean (a) surface air temperature and (b) precipitation for the control simulation in T21.	33
2.6	(a) JJA and (b) DJF surface air temperatures, and (c) JJA and (d) DJF precipitation for the control simulation in T21.	34
2.7	Annual mean (a) surface air temperature and (b) precipitation for the control simulation in T42.	35
2.8	(a) JJA and (b) DJF surface air temperatures, and (c) JJA and (d) DJF precipitation for the control simulation in T42.	36
2.9	CARAIB scheme.	38

3.1	CARAIB biome distributions using (a) the Cramer and Lee- mans and (b) the NEW et al. (2002) climate data sets.	50
3.2	Annual mean (a) surface albedo and (b) roughness length preindustrial distributions for the Planet Simulator.	55
3.3	Annual mean (a) rooting depth and (b) field capacity prein- dustrial distributions for the Planet Simulator.	58
3.4	Asynchronous equilibrium coupling of the Planet Simulator and CARAIB models.	59
3.5	CARAIB biome distributions for (a) the first vegetation itera- tion (ITER1) and (b) the second vegetation iteration (ITER2) for the preindustrial.	62
3.6	(a) Global Net Primary Productivity (Gt C/yr) for each veg- etation iteration, and (b) Total area in term of percentage of the land surface in which biomes differs from two successive vegetation iterations.	63
3.7	Continental annual mean surface albedo, roughness length and field capacity for each iteration.	64
3.8	Continental annual and seasonal (JJA and DJF) (a) mean surface air temperature and (b) precipitation for each iteration.	65
3.9	(a) Surface air temperature and (b) precipitation annual mean differences between the second and the first climate iterations (ITER2-ITER1).	67
3.10	(a) Surface air temperature and (b) precipitation annual mean differences between the third and the second climate iterations (ITER3-ITER2).	68
4.1	Land-sea mask and orography over the glacier mask for (a) the CTRL configuration and (b) the LGM configuration.	76
4.2	Biome distributions from CARAIB (a) preindustrial and (b) LGM equilibrium runs.	78
4.3	Control experiment (CTRL) results: (a) annual surface tem- perature; (b) precipitation.	79
4.4	Global surface temperature and precipitation anomalies (EXPERIMENT-minus-CTRL).	82

4.5	Comparison of the pure contributions with the effects of the interactions between the factors on the global, oceanic and continental annual (a) surface temperature and (b) precipitation.	84
4.6	Annual surface temperature anomalies (EXPERIMENT-minus-CTRL) for (a) experiment I; (b) experiment O; (c) experiment V; (d) experiment C.	85
4.7	Annual surface temperature anomalies (EXPERIMENT-minus-CTRL) for (a) experiment IV; (b) experiment IO; (c) experiment CIV; (d) experiment LGM.	87
4.8	Annual precipitation anomalies (EXPERIMENT-minus-CTRL) for (a) experiment I; (b) experiment O; (c) experiment V; (d) experiment C.	89
4.9	Annual precipitation anomalies (EXPERIMENT-minus-CTRL) for (a) experiment IV; (b) experiment IO; (c) experiment CIV; (d) experiment LGM.	91
4.10	Surface winter winds resulting for (a) experiment CTRL (b) experiment O	92
4.11	Effects of (a) interaction IV on surface temperature; (b) interaction IO on surface temperature; (c) interaction IV on precipitation; (d) interaction IO on precipitation.	94
4.12	Comparison between model results and data for the LGM-minus-PRESENT anomalies of the mean temperature of the coldest month (MTCO) and the mean temperature of the warmest month (MTWA), in the two sectors (20° W–20° E) and (20° E–60° E).	100
4.13	Comparison between model results and data for the LGM-minus-PRESENT anomalies in the mean annual temperature (MAT) and the mean annual precipitation (MAP).	101
4.14	CARAIB biome distributions for (a) the first vegetation iteration (LGM ITER1) and (b) the second vegetation iteration (LGM ITER2) for the LGM.	106
4.15	(a) Global Net Primary Productivity (Gt C/yr) for each vegetation iteration, and (b) Total area in term of percentage of the land surface in which biomes differs from two successive vegetation iterations.	108

4.16	Continental annual and seasonal (JJA and DJF) (a) mean surface air temperature ($^{\circ}\text{C}$) and (b) precipitation (mm/yr) for each iteration at the LGM.	110
4.17	(a) Surface air temperature and (b) precipitation annual mean differences between the first climate iteration and the experiment LGM (LGM ITER1-LGM).	111
5.1	Topography on land and land-sea distribution for (a) the preindustrial and (b) the Pliocene configurations.	120
5.2	Ice-sheet mask for (a) the preindustrial and (b) the Pliocene configurations.	121
5.3	Oceanic surface heat transfer for (a) the CTRL configuration and (b) the PLIO configuration	122
5.4	Differences between the Pliocene and preindustrial (a) sea surface temperatures and (b) sea-ice cover.	124
5.5	Differences between the Pliocene and preindustrial (a) surface albedo, (b) roughness length and (c) rooting depth distributions.	126
5.6	Zonal annual mean (a) surface air temperature ($^{\circ}\text{C}$) and (b) precipitation (mm/day) for CTRL and PLIO experiments. Global, land and ocean zonal annual mean (c) surface air temperature anomalies ($^{\circ}\text{C}$) and (d) precipitation anomalies (mm/day) between PLIO and CTRL experiments.	129
5.7	Annual mean (a) surface air temperature ($^{\circ}\text{C}$) and (b) precipitation (mm/day) anomalies between the PLIO and CTRL experiments.	130
5.8	(a) DJF and (b) JJA surface air temperature anomalies ($^{\circ}\text{C}$), and (c) DJF and (d) JJA precipitation anomalies (mm/day) between the PLIO and CTRL experiments.	131
5.9	(a) DJF and (b) JJA total cloud cover anomalies (%) for the PLIO experiment.	133
5.10	(a) DJF and (b) JJA surface winds for the CTRL experiment.	134
5.11	(a) DJF and (b) JJA surface winds for the PLIO experiment.	135
5.12	Annual mean (a) surface air temperature and (b) precipitation differences (mm/day) between the PLIO and PLIO-VEGP experiments.	138

5.13	CARAIB biome distributions for (a) the Middle Pliocene and (b) the preindustrial period.	144
5.14	Net Primary Productivity of needleleaved evergreen boreal/temperate cold trees for (a) the Middle Pliocene and (b) the preindustrial vegetation distributions. Net Primary Productivity of broadleaved summergreen boreal/temperate cold trees for (c) the Middle Pliocene and (d) the preindustrial vegetation distributions.	145
5.15	Net Primary Productivity of broadleaved evergreen tropical trees for (a) the Middle Pliocene and (b) the preindustrial vegetation distributions.	146
5.16	Annual mean (a) surface air temperature and (b) precipitation differences between the PLIO-VEGC and PLIO experiments.	149
5.17	(a) Surface albedo and (b) rooting depth differences (CARAIB - BIOME4) derived from the CARAIB and BIOME4 vegetation distributions.	151
5.18	Annual mean (a) surface air temperature and (b) precipitation differences (mm/day) between the PLIO-VEGC and PLIO experiments with calculated sea surface temperatures and sea-ice cover.	152
6.1	Initial sea-surface temperatures for (a) the CTRL experiment and (b) the Miocene experiments.	162
6.2	Oceanic surface heat transfer for (a) the CTRL configuration and (b) the Miocene configuration.	164
6.3	Land-sea mask and topography on land for (a) the CTRL configuration and (b) the Miocene configuration.	165
6.4	Zonal average (a) surface air temperature ($^{\circ}\text{C}$) and (b) precipitation (mm/yr) for the series of simulation experiments MM1 to MM4.	168
6.5	Zonal average (a) surface air temperature anomalies ($^{\circ}\text{C}$) and (b) precipitation anomalies (mm/yr) for the series of Middle Miocene simulation experiments MM1 to MM4.	169
6.6	(a) Annual mean surface temperature and (b) precipitation anomalies (MM1-minus-CTRL) for experiment MM1.	170

6.7	(a) Annual mean surface temperature and (b) precipitation anomalies between experiments MM2 and MM1.	172
6.8	Surface air temperature anomalies in (a) Northern Hemisphere summer (JJA) and (b) Northern Hemisphere winter (DJF) between experiments MM2 and MM1.	173
6.9	Precipitation anomalies in (a) Northern Hemisphere summer (JJA) and (b) Northern Hemisphere winter (DJF) between experiments MM2 and MM1.	174
6.10	Low-level winds (850 hPa) for the CTRL experiment in (a) Northern Hemisphere summer and (b) Northern Hemisphere winter.	176
6.11	Low-level winds (850 hPa) for the MM2 experiment in (a) Northern Hemisphere summer and (b) Northern Hemisphere winter.	177
6.12	(a) Annual mean precipitation anomalies (MM2-E - MM1) and (b) Northern Hemisphere summer low-level winds (850 hPa) for experiment MM2-E that considers a reduced topography only in Europe.	179
6.13	Same as Figure 6.12 for experiment MM2-A that considers a reduced topography only in North America.	180
6.14	Same as Figure 6.12 for experiment MM2-AE that considers a reduced topography only in North America and in Europe.	181
6.15	(a) Annual mean surface temperature and (b) precipitation anomalies between experiments MM3 and MM2.	183
6.16	(a) Annual mean surface temperature and (b) precipitation anomalies between experiments MM4 and MM2.	184
6.17	Biome distributions from CARAIB preindustrial and MMCO equilibrium runs.	186
6.18	(a) Annual mean surface temperature and (b) precipitation anomalies between experiment MM4-veg and MM4.	187
6.19	(a) Surface albedo difference and (b) rooting depth difference between experiment MM4-veg and CTRL.	189
6.20	Annual (a) surface air temperature ($^{\circ}\text{C}$) and (b) precipitation (mm/yr) differences for the MM4 experiment (MM4 - CTRL).	197

6.21	(a) DJF and (b) JJA surface air temperature anomalies ($^{\circ}\text{C}$), and (c) DJF and (d) JJA precipitation anomalies (mm/yr) for the MM4 experiment.	198
6.22	(a) VEG-500 and (b) preindustrial CARAIB biome distributions.	200
6.23	Net Primary Productivities of needleleaved evergreen boreal/temperate cold trees for (a) the VEG-500 and (b) the preindustrial vegetation distributions. Net Primary Productivities of broadleaved summergreen boreal/temperate cold trees for (c) the VEG-500 and (d) the preindustrial vegetation distributions.	202
6.24	Net Primary Productivities of needleleaved evergreen temperate perhumid warm trees for (a) the VEG-500 and (b) the preindustrial vegetation distributions. Net Primary Productivities of broadleaved evergreen temperate perhumid warm trees for (c) the VEG-500 and (d) the preindustrial vegetation distributions.	203
6.25	Annual (a) surface air temperature ($^{\circ}\text{C}$) and (b) precipitation (mm/yr) differences for the MM2 experiment (MM2 - CTRL).	205
6.26	(a) VEG-280 and (b) preindustrial CARAIB biome distributions.	206
6.27	Net Primary Productivities of (a) needleleaved evergreen boreal/temperate cold trees for, (b) broadleaved summergreen boreal/temperate cold trees, (c) needleleaved evergreen temperate perhumid warm trees and (d) broadleaved evergreen temperate perhumid warm trees for the VEG-280 vegetation distribution.	208
6.28	(a) VEG-MM4-280 and (b) VEG-500 CARAIB biome distributions.	210
6.29	Annual mean (a) surface air temperature and (b) precipitation differences between experiments MM4-veg and MM4. Annual mean (a) surface air temperature and (b) precipitation differences between experiments MM2-veg and MM2.	212
6.30	(a) VEG-500-iter1 and (b) VEG-280-iter1 CARAIB biome distributions.	214
6.31	(a) VEG-500-iter2, (b) VEG-500-iter3, (c) VEG-280-iter2 and (d) VEG-280-iter3 CARAIB biome distributions.	215

- 6.32 Annual mean (a) surface air temperature differences and (b) precipitation differences between experiments MM4-veg-iter1 and MM4-veg. Annual mean (c) surface air temperature differences and (d) precipitation differences between experiments MM2-veg-iter1 and MM2-veg. 217
- 6.33 Annual mean (a) surface air temperature differences and (b) precipitation differences between experiments MM4-veg-iter2 and MM4-veg-iter1. Annual mean (c) surface air temperature differences and (d) precipitation differences between experiments MM2-veg-iter2 and MM2-veg-iter1. 218

List of Tables

1.1	Albedos of various surface types.	11
1.2	Roughness lengths of various surface types.	12
1.3	Maximum rooting depths of various vegetation types.	13
2.1	Global, continental and oceanic annual mean near-surface temperature and precipitation for the T21, T42 simulations and NCEP/NCAR reanalysis.	29
2.2	Plant functional types of the 15-PFTs classification.	42
2.3	CARAIB biome assignment scheme.	44
3.1	Albedos and rooting depths attributed to the 15 PFTs.	54
4.1	Characteristics of the 16 simulation experiments.	75
4.2	Comparison of the pure contributions with the effects of the interactions between the factors on the global, oceanic and continental annual surface temperature (in °C).	80
4.3	Comparison of the pure contributions with the effects of the interactions between the factors on the global, oceanic and continental annual precipitation (in mm/yr).	81
5.1	Experimental design and boundary conditions for CTRL and PLIO experiments.	119
5.2	Annual, DJF and JJA global mean, oceanic mean and continental mean surface air temperature and precipitation anomalies for the Middle Pliocene simulation experiment.	127

5.3	Global warming and precipitation increase produced in Middle Pliocene modelling experiments.	139
6.1	Description of the Middle Miocene simulation experiments. . .	161
6.2	Global, continental and oceanic annual mean near-surface temperature and precipitation anomalies for the five Middle Miocene simulation experiments.	166

Bibliography

- J. ADAMS. *Vegetation-Climate Interaction*. Springer Praxis Books, New York, USA, 2nd edition, 2010.
- J. M. ADAMS, H. FAURE, L. FAURE-DENARD, J. M. MCGLADE, & F. I. WOODWARD. Increases in the terrestrial carbon storage from the Last Glacial Maximum to the present. *Nature*, 348:711–714, 1990.
- C. AMANTE & B. W. EAKINS. ETOPO1 1 Arc-Minute Global Relief Model: Procedures, Data Sources and Analysis. National Geophysical Data Center NESDIS, NOAA, U. S. Department of Commerce, Boulder, CO, 2008.
- AMIP2. The second phase of the Atmospheric Model Intercomparison Project (AMIP2). Workshop WCRP/WGNE, Météo France, Toulouse, France, 2004.
- V. ARORA. Modelling vegetation as a dynamic component in soil-vegetation-atmosphere transfer schemes and hydrological models. *Rev. Geophys.*, 40 (2):1006, 2002.
- R. ASSELIN. Frequency filter for time integrations. *Mon. Wea. Rev.*, 100: 487–490, 1972.
- J. T. BALL, I. E. WOODROW, & J. A. BERRY. A model predicting stomatal conductance and its contribution to the control of photosynthesis under different environmental conditions. *Progress in Photosynthesis Research*, 4:221, 1987.
- J. BARRON. Diatom constraints on the position of the Antarctic Polar Front in the middle part of the Pliocene. *Mar. Micropaleontol.*, 27:195–214, 1996.
- A. BERGER, A. DUTRIEUX, M.F. LOUTRE, & C. TRICOT. Paleoclimate sensitivity to CO₂ and insolation. Scientific Report 6, Institut d’Astronomie et de Géophysique Georges Lemaître, Louvain-la-Neuve, Belgium, 1996.

- R.A. BETTS, P.M. COX, S.E. LEE, & F.I. WOODWARD. Contrasting physiological and structural vegetation feedbacks in climate change simulations. *Nature*, 387:796–799, 1997.
- K. L. BICE, C. R. SCOTESE, D. SEIDOV, & E. J. BARRON. Quantifying the role of geographic changes in cenozoic ocean heat transport using uncoupled atmosphere and ocean models. *Earth Planet. Sci. Lett.*, 161:295–310, 2000.
- N. H. BIGELOW, L. B. BRUBAKER, M. E. EDWARDS, S. P. HARRISON, I. C. PRENTICE, P. M. ANDERSON, A. A. ANDREEV, P. J. BARTLEIN, T. R. CHRISTENSEN, W. CRAMER, J. O. KAPLAN, A. V. LOZHKIN, N. V. MATVEYEVA, D. V. MURRAY, A. D. MCGUIRE, V. Y. RAZZHIVIN, J. C. RITCHIE, B. SMITH, D. A. WALKER, K. GAJEWSKI, V. WOLF, B. H. HOLMQVIST, Y. IGARASHI, K. KREMENETSKII, A. PAUS, M. F. J. PISARIC, & V. S. VOKOVA. Climate change and Arctic ecosystems I. Vegetation changes north of 55° n between the Last Glacial Maximum, mid-Holocene and present. *J. Geophys. Res.*, 108:8170, 2003.
- M. R. BOLICK, R. G. CORNER, & M. R. VOORHIES. New pollen data from the Kilgore locality, Valentine Formation; additional evidence for savanna vegetation. *Society of America Program with Abstracts. North-Central Section, South-Central Section*, 27:A–41, 2002.
- G. B. BONAN. *Ecological climatology: concepts and applications*. Cambridge University Press, 2002.
- G. B. BONAN, D. POLLARD, & S. L. THOMPSON. Effects of boreal forest vegetation on global climate. *Nature*, 359:716–718, 1992.
- R. BONNEFILLE. Cenozoic vegetation and environments of early hominoids in East Africa. The Evolution of the East Asian Environment. *Palaeobotany, Palaeozoology, and Palaeoanthropology, Center for Asian Studies, University of Hong Kong, Hong Kong*, 2, 1984.
- G. J. BOWEN, T. J. BRALOWER, M. L. DELANEY, G. R. DICKENS, D. C. KELLY, P. L. KOCH, L. R. KUMP, J. MENG, L. C. SLOAN, E. THOMAS, S. L. WING, & J. C. ZACHOS. Eocene hyperthermal event offers insight into greenhouse warming. *EOS Trans. AGU*, 87:165–169, 2006.
- P. BRACONNOT, S. JOUSSAUME N. DE NOBLET, & G. RAMSTEIN. Mid-Holocene and Last Glacial Maximum African monsoon changes as simulated within the Paleoclimate Modelling Intercomparison Project. *Global Planet. Change*, 26(1-3):51–66, 2000.

- P. BRACONNOT, B. OTTO-BLIESNER, S. HARRISON, S. JOUSSAUME, J.-Y. PETERCHMITT, A. ABE-OUCHI, M. CRUCIFIX, E. DRIESSCHAERT, T. FICHEFET, C. D. HEWITT, M. KAGEYAMA, A. KITO, A. LAÎNÉ, M.-F. LOUTRE, O. MARTI, U. MERKEL, G. RAMSTEIN, P. VALDES, S. L. WEBER, Y. YU, & Y. ZHAO. Results of PMIP2 coupled simulations of the Mid-Holocene and Last Glacial Maximum—Part 1: experiments and large-scale features. *Climate of the Past*, 3(2):261–277, 2007a.
- P. BRACONNOT, B. OTTO-BLIESNER, S. HARRISON, S. JOUSSAUME, J.-Y. PETERCHMITT, A. ABE-OUCHI, M. CRUCIFIX, E. DRIESSCHAERT, T. FICHEFET, C. D. HEWITT, M. KAGEYAMA, A. KITO, M.-F. LOUTRE, O. MARTI, U. MERKEL, G. RAMSTEIN, P. VALDES, S. L. WEBER, Y. YU, & Y. ZHAO. Results of PMIP2 coupled simulations of the Mid-Holocene and Last Glacial Maximum—Part 2: feedbacks with emphasis on the location of the ITCZ and mid- and high latitudes heat budget. *Climate of the Past*, 3(2):279–296, 2007b.
- A. J. BROCCOLI, K. A. DAHL, & R. J. STOUFFER. The response of the ITCZ to Northern Hemisphere cooling. *Geophys. Res. Lett.*, 33:L01702, 2006.
- A. J. BROCCOLI & S. MANABE. The effects of the Laurentide ice sheet on north american climate during the Last Glacial Maximum. *Géographie physique et Quaternaire*, 41:291–299, 1987a.
- A. J. BROCCOLI & S. MANABE. The influence of continental ice, atmospheric CO_2 , and land albedo on the climate of the Last Glacial Maximum. *Climate Dyn.*, 1:87–99, 1987b.
- V. BROVKIN. Climate - vegetation interaction. *J. Phys. IV France*, 12:52–57, 2002.
- V. BROVKIN, J. BENDTSEN, M. CLAUSSEN, A. GANOPOLSKI, C. KUBATZKI, V. PETOUKHOV, & A. ANDREEV. Carbon cycle, Vegetation and Climate Dynamics in the Holocene: Experiments with the CLIMBER-2 Model. *Global Biogeochem. Cycles*, 16(4):1139, 2002.
- V. BROVKIN, A. GANOPOLSKI, & Y. SVIREZHEV. A continuous climate-vegetation classification for use in climate-biosphere studies. *Ecol. Model.*, 101:251–261, 1997.
- A. A. BRUCH, D. UHL, & V. MOSBRUGGER. Miocene climate in Europe. Patterns and evolution: A first synthesis of NECLIME. *Palaeogeogr., Palaeoclimatol., Palaeoecol.*, 253:1–7, 2007.

- M. I. BUDYKO. *Climate and Life*. Academic Press, 1974.
- M. BUTZIN, G. LOHMANN, & T. BICKERT. Miocene ocean circulation inferred from marine carbon cycle modeling combined with benthic isotope records. *Paleoceanography*, submitted.
- J. CANADELL, R. B. JACKSON, J. R. EHLERINGER, H. A. MOONEY, O. E. SALA, & E.-D. SCHULZE. Maximum rooting depth of vegetation types at the global scale. *Oecologia*, 108:583–595, 1996.
- R. CHEDDADI, G. VENDRAMIN, T. LITT, L. FRANÇOIS, M. KAGEYAMA, S. LORENTZ, JM. LAURENT, JL. DE BEAULIEU, L. SADORI, A. JOST, & D. LUNT. Imprints of glacial refugia in the modern genetic diversity of *pinus sylvestris*. *Global Ecology and Biogeography*, 15:271–282, 2006.
- J. C. H. CHIANG, M. BIASUTTI, & D. S. BATTISTI. Sensitivity of the Atlantic Intertropical Convergence Zone to Last Glacial Maximum boundary conditions. *Paleoceanography*, 18(4):1094, 2003.
- J. C. H. CHIANG & C. M. BITZ. Influence of high latitude ice cover on the marine Intertropical Convergence Zone. *Climate Dyn.*, 25(5):477–496, 2005.
- M. CLAUSSEN. On coupling global biome models with climate models. *Clim. Res.*, 4:203–221, 1994.
- M. CLAUSSEN. On multiple solutions of the atmosphere-vegetation system in present-day climate. *Global Change Biol.*, 4:549–559, 1998.
- M. CLAUSSEN, V. BROVKIN, & A. GANOPOLSKI. Biogeophysical versus biogeochemical feedbacks of large-scale land cover change. *Geophys. Res. Lett.*, 28(6):1011–1014, 2001.
- M. CLAUSSEN, V. BROVKIN, A. GANOPOLSKI, C. KUBATZKI, & V. PETHOUKOV. Modelling global terrestrial vegetation-climate interaction. *Phil. Trans. R. Soc. London Ser. B*, 353:53–63, 1998.
- M. CLAUSSEN, U. LOHMANN, E. ROECKNER, & U. SCHULZWEIDA. A global dataset of land surface parameters. Report 135, Max-Planck-Institute for Meteorology, Hamburg, Germany, 1994.
- M. CLAUSSEN, L. A. MYSAK, A. J. WEAVER, M. CRUCIFIX, T. FICHEFET, M.-F. LOUTRE, S. L. WEBER, J. ALCAMO, V. A. ALEXEEV, A. BERGER, R. CALOV, A. GANOPOLSKI, H. GOOSSE, G. LOHMANN,

- F. LUNKEIT, I. I. MOKHOV, V. PETOUKHOV, P. STONE, & Z. WANG. Earth system models of intermediate complexity : Closing the gap in the spectrum of climate system models. *Climate Dyn.*, 18(7):579–586, 2002.
- CLIMAP PROJECT MEMBERS. The surface of the ice-age Earth. *Science*, 191:1131–1137, 1976.
- J. G. COLLATZ, M. RIBAS-CARBO, & A. J. BERRY. Coupled photosynthesis-stomatal conductance model for leaves of C₄ plants. *J. Plant. Physiol.*, 19:519–538, 1992.
- M. H. COSTA & J. A. FOLEY. Combined effects of deforestation and doubled atmospheric CO₂ concentration on the climate of amazonia. *J. Climate*, 13:18–34, 2000.
- P. COX, R. BETTS, C. JONES, S. SPALL, & I. TOTTERDELL. Acceleration of global warming due to carbon-cycle feedbacks in a coupled climate model. *Nature*, 408:184–187, 2000.
- P. M. COX, R. A. BETTS, C. D. JONES, S. A. SPALL, & I. J. TOTTERDELL. Modelling vegetation and the carbon cycle as interactive elements of the climate system. In *Pearce R(ed) Meteorology at the millenium*, pages 259–279, New York, 2001. Academic.
- T. J. CROWLEY. Ice age terrestrial carbon changes revisited. *Global Biogeochem. Cycles*, 9(3):377–389, 1995.
- T. J. CROWLEY & S. K. BAUM. Effect of vegetation on an ice-age climate model simulation. *J. Geophys. Res.*, 102(14):443–480, 1997.
- M. CRUCIFIX, R. A. BETTS, & C. D. HEWITT. Pre-industrial-potential and Last Glacial Maximum global vegetation simulated with a coupled climate-biosphere model: Diagnosis of bioclimatic relationships. *Global Planet. Change*, 45:295–312, 2005.
- M. CRUCIFIX & C. D. HEWITT. Impact of vegetation changes on the dynamics of the atmosphere at the Last Glacial Maximum. *Climate Dyn.*, 25:447–459, 2005.
- M. CRUCIFIX & M. F. LOUTRE. Transient simulations over the last interglacial period (126-115 kyr bp): feedback and forcing analysis. *Climate Dyn.*, 19:419–433, 2002.

- U. CUBASCH, G. A. MEEHL, G. J. BOER, R. J. STOUFFER, M. DIX, A. NODA, C. A. SENIOR, S. RAPER, & K.S. YAP. Projection of Future Climate Change. In J. T. HOUGHTON, Y. DING, D. J. GRIGGS, M. NOGER, P. J. VAN DER LINDEN, X. DAI, K. MASKELL, & C. A. JOHNSON, editors, *Climate Change 2001. The Scientific Basis*, chapter 9, pages 527–582. Cambridge University Press, Cambridge, 2001.
- B. S. CURRIE, D. B. ROWLEY, & N. J. TABOR. Middle miocene paleoaltimetry of Southern Tibet: implications for the role of mantle thickening and delamination in the Himalayan orogen. *Geology*, 33(3):181–184, 2005.
- N. I. DE NOBLET, M. CLAUSSEN, & I. C. PRENTICE. Mid-Holocene greening of the Sahara: first results of the GAIM 6000 year BP Experiment with two asynchronously coupled atmosphere/biome models. *Climate Dyn.*, 16: 643–659, 2000.
- N. I. DE NOBLET, I. C. PRENTICE, S. JOUSSAUME, D. TEXIER, A. BOTTA, & A. HAXELTINE. Possible role of atmosphere-biosphere interactions in triggering the last glaciations. *Geophys. Res. Lett.*, 23(22):3191–3194, 1996.
- R. M. DECONTO & D. POLLARD. Rapid Cenozoic glaciation of Antarctica induced by declining atmospheric CO₂. *Nature*, 421:245–249, 2003.
- R. M. DECONTO, S. L. THOMPSON, & D. POLLARD. Recent advances in paleoclimate modelling: toward better simulations of warm paleoclimates. In B. T. HUBER, W. WING, & K. MACLEOD, editors, *Warm climates in Earth history*, pages 21–49, Cambridge, UK, 1999. Cambridge University Press.
- C. DELIRE, J. A. FOLEY, & S. THOMPSON. Evaluating the carbon cycle of a coupled atmosphere-biosphere model. *Global Biogeochem. Cycles*, 17(1): 1012, 2003.
- P. B. DEMENOCAL & D. RIND. Sensitivity of Asian and African Climate to Variations in Seasonal Insolation, Glacial Ice Cover, Sea Surface Temperature, and Asian Orography. *J. Geophys. Res.*, 98(4):7265–7287, 1993.
- K. L. DENMAN, G. BRASSEUR, A. CHIDTHAISONG, P. CIAIS, P. M. COX, R. E. DICKINSON, D. HAUGLUSTAINE, C. HEINZE, E. HOLLAND, D. JACOB, U. LOHMANN, S. RAMACHANDRAN, P. L. DA SILVA DIAS, S. C. WOFYSY, & X. ZHANG. Couplings Between Changes in the Climate System and Biogeochemistry. In S. SOLOMON, D. QIN, M. MANNING, Z. CHEN, M. MARQUIS, K. B. AVERYT, M. TIGNOR, & H. L. MILLER, editors, *Climate Change 2007. The Physical Science Basis. Contribution of Working*

- Group I to the Fourth Assessment Report of the Intergovernmental Panel on Climate Change*, chapter 7. Cambridge University Press, Cambridge, 2007.
- L. DIESTER-HAASS, K. BILLUPS, D. R. GRÖCKE, L. FRANÇOIS, V. LEFEBVRE, & K. C. EMEIS. Mid-Miocene paleoproductivity in the Atlantic Ocean and Implications for the Global Carbon Cycle. *Paleoceanography*, 24:PA1209, 2009.
- DKRZ. The ECHAM3 atmospheric general circulation model. Technical Report 6, Deutsches Klimarechenzentrum, Modellbetreuungsgruppe, Hamburg, 1993.
- H. J. DOWSETT. The PRISM palaeoclimate reconstruction and Pliocene sea-surface temperature. In M. WILLIAMS, A. M. HAYWOOD, J. GREGORY, & D. N. SCHMIDT, editors, *Deep-time perspectives on climate change: Marrying the signal from computer models and biological proxies*, pages 459–480, Geol. Soc. of London, London, UK, 2007. Micropalaeontological Soc., Spec. Pub.
- H. J. DOWSETT, J. BARRON, & H. R. POORE. Middle Pliocene sea surface temperature: a global reconstruction. *Mar. Micropaleontol.*, 27:13–25, 1996.
- H. J. DOWSETT, J. BARRON, R. POORE, R. THOMPSON, T. CRONIN, S. ISHMAN, & D. WILLARD. Middle Pliocene paleoenvironmental reconstructions: PRISM2. *US Geological Survey, open file report*, pages 99–535, 1999.
- H. J. DOWSETT & M. M. ROBINSON. Mid-Pliocene equatorial Pacific sea surface temperature reconstruction: a multi-proxy perspective. *Phil. Trans. R. Soc. London Ser. A*, 367(1886):109–126, 2009.
- H. J. DOWSETT, M. M. ROBINSON, & K. M. FOLEY. Pliocene three-dimensional global ocean temperature reconstruction. *Climate of the Past*, 5:769–783, 2009.
- H. J. DOWSETT, R. THOMPSON, J. BARRON, , T. CRONIN, R. FLEMING, S. ISHMAN, R. POORE, D. WILLARD, & T. HOLTZ. Joint investigations of the middle Pliocene climate I: PRISM paleoenvironmental reconstructions. *Global Planet. Change*, 9:169–195, 1994.
- M. DURY, A. HAMBUECKERS, P. WARNANT, A.-J. HENROT, E. FAVRE, M. OUBERDOUS, & L. FRANÇOIS. Response of the European forests

- to climate change: a modelling approach for the 21st century. *iForest*, submitted.
- J. F. DUTTON & E. J. BARRON. Miocene to present vegetation changes: A possible piece of the Cenozoic puzzle. *Geology*, 25(1):39–41, 1997.
- G. D. FARQUHAR, S. VON CAEMMERER, & J. A. BERRY. A biogeochemical model of photosynthetic CO₂ assimilation in leaves of C₃ species. *Planta*, 149:78–90, 1980.
- E. FAVRE, L. FRANÇOIS, F. FLUTEAU, R. CHEDDADI, L. THÉVENOD, & J.-P. SUC. Messinian vegetation maps of the Mediterranean region using models and interpollated pollen data. *Geobios*, 40:433–443, 2007.
- E. FAVRE, L. FRANÇOIS, T. UTESCHER, J.-P. SUC, A.-J. HENROT, K. HUANG, & R. CHEDDADI. Improving the classification of plant functional types in dynamic vegetation modelling for the Neogene. *Geophys. Res. Abstr.*, 12:EGU2010–3429–3, 2010.
- B. P. FLOWER & J. P. KENNETT. The Middle Miocene climatic transition: East Antarctic ice sheet development, deep ocean circulation and global carbon cycling. *Palaeogeogr., Palaeoclimatol., Palaeoecol.*, 108:537–555, 1994.
- J. A. FOLEY, M. H. COSTA, C. DELIRE, N. RAMANKUTTY, & P. SNYDER. Green surprise ? How terrestrial ecosystems could affect Earth's climate. *Front. Ecol. Environ.*, 1(1):38–44, 2003.
- J. A. FOLEY, S. LEVIS, M. H. COSTA, W. CRAMER, & D. POLLARD. Incorporating dynamic vegetation cover within global climate models. *Ecological Applications*, 10(6):1620–1632, 2000.
- J. A. FOLEY, S. LEVIS, I.C. PRENTICE, D. POLLARD, & S.L. THOMPSON. Coupling dynamic models of climate and vegetation. *Global Change Biol.*, 4:561–579, 1998.
- J. A. FOLEY, I.C. PRENTICE, N. RAMANKUTTY, S. LEVIS, D. POLLARD, S. SITCH, & A. HAXELTINE. An Integrated Biosphere Model of Land Surface Processes, Terrestrial Carbon Balance, and Vegetation Dynamics. *Global Biogeochem. Cycles*, 10:603–628, 1996.
- P. FORSTER, V. RAMASWAMY, P. ARTAXO, T. BERNTSEN, R. BETTS, D. W. FAHEY, J. HAYWOOD, J. LEAN, D. C. LOWE, G. MYHRE,

- J. NGANGA, R. PRINN, G. RAGA, M. SCHULZ, R., & VAN DORLAND. Changes in Atmospheric Constituents and in Radiative Forcing. In S. SOLOMON, D. QIN, M. MANNING, Z. CHEN, M. MARQUIS, K. B. AVERYT, M. TIGNOR, & H. L. MILLER, editors, *Climate Change 2007. The Physical Science Basis. Contribution of Working Group I to the Fourth Assessment Report of the Intergovernmental Panel on Climate Change*, chapter 2. Cambridge University Press, Cambridge, 2007.
- KLAUS FRAEDRICH, HEIKO JANSEN, EDILBERT KIRK, UTE LUKSCH, & FRANK LUNKEIT. The Planet Simulator : Towards a user friendly model. *Meteorol. Z.*, 14(3):299–304, 2005a.
- KLAUS FRAEDRICH, HEIKO JANSEN, EDILBERT KIRK, & FRANK LUNKEIT. The Planet Simulator : Green planet and desert world. *Meteorol. Z.*, 14(3):305–314, 2005b.
- KLAUS FRAEDRICH, EDILBERT KIRK, & FRANK LUNKEIT. PUMA Portable University Model of the Atmosphere. Technical Report 16, Meteorologisches Institut, Universität Hamburg, Hamburg, 1998.
- L. FRANÇOIS, C. DELIRE, P. WARNANT, & G. MUNHOVEN. Modelling the Glacial-Interglacial Changes in the Continental Biosphere. *Global Planet. Change*, 16-17(1-4):37–52, 1998.
- L. FRANÇOIS, H. FAURE, & J.-L. PROBST. The Global Carbon Cycle and its Changes over Glacial-Interglacial Cycles. *Global Planet. Change*, 33(2-3):vii–viii, 2002.
- L. FRANÇOIS, L. GHISLAIN, D. OTTO, & A. MICHEELS. Late Miocene vegetation reconstruction with the CARAIB model. *Palaeogeogr., Palaeoclimatol., Palaeoecol.*, 238:302–320, 2006.
- L. FRANÇOIS, Y. GODDÉRIS, P. WARNANT, G. RAMSTEIN, N. DE NOBLET, & S. LORENZ. Carbon stocks and isotopic budgets of the terrestrial biosphere at mid-Holocene and Last Glacial Maximum times. *Chem. Geol.*, 159(1-4):163–189, 1999.
- L. FRANÇOIS, S. LORENZ, M. GHISLAIN, R. CHEDDADI, & D. JOLLY. Impact of reduced tropical sea surface temperatures on the reconstruction of climate and land vegetation at the Last Glacial Maximum. *Proc. INQUA*, page 130, 2003.
- L. FRANÇOIS, T. UTESCHER, E. FAVRE, A.-J. HENROT, P. WARNANT, A. MICHEELS, B. ERDEI, J.-P. SUC, R. CHEDDADI, & V. MOSBRUGGER.

- Modelling Late Miocene vegetation in Europe: results of the CARAIB model and comparison with palaeovegetation data. *Palaeogeogr., Palaeoclimatol., Palaeoecol.*, submitted.
- M. L. GABEL, D. C. BACKLUND, & J. HAFFNER. The Miocene macroflora of the northern Ogallala Group, northern Nebraska and southern South Dakota. *J. Paleontol.*, 72:388–397, 1998.
- R. GALLIMORE, R. JACOB, & J. KUTZBACH. Coupled atmosphere-ocean-vegetation simulations for modern and mid-Holocene climates: Role of extratropical vegetation cover feedbacks. *Climate Dyn.*, 25:775–776, 2005.
- V. GALY, L. FRANÇOIS, C. FRANCE-LANORD, P. FAURE, H. KUDRASS, F. PALHOL, & S. K. SINGH. C₄ plants decline in the Himalayan basin since the Last Glacial Maximum. *Quat. Sci. Rev.*, 27:1396–1409, 2008.
- A. GANOPOLSKI. Glacial integrative modelling. *Phil. Trans. R. Soc. London Ser. A*, 361:1871–1884, 2003.
- A. GANOPOLSKI, C. KUBATZKI, M. CLAUSSEN, V. BROVKIN, & V. PETOUKHOV. The Influence of Vegetation-Atmosphere-Ocean Interaction on Climate During the Mid-Holocene. *Science*, 280:1916–1919, 1998.
- A. GANOPOLSKI, V. PETOUKHOV, S. RAHMSTORF, V. BROVKIN, M. CLAUSSEN, A. ELISEEV, & C. KUBATZKI. CLIMBER-2: a climate system model of intermediate complexity. II. model sensitivity. *Climate Dyn.*, 17:735–751, 2001.
- A. GANOPOLSKI & S. RAHMSTORF. Rapid changes of glacial climate simulated in a coupled climate model. *Nature*, 409:153–158, 2001.
- A. Y. GLADENKOV, A. E. OLEINIK, L. JR. MARINCOVICH, & K. B. BARI-NOV. A refined age for the earliest opening of the bering strait. *Palaeogeogr., Palaeoclimatol., Palaeoecol.*, 183:321–328, 2002.
- H. GOOSSE & T. FICHEFET. Importance of ice-ocean interactions for the global ocean circulation: a model study. *J. Geophys. Res.*, 104:23337–23355, 1999.
- J. GOUDRIAAN & H. H. VAN LAAR. Modelling potential crop growth processes, textbook with exercises. In *Current Issues in Production Ecology*, volume 2, page 256. Kluwer Academic Publisher Group, Chichester, 1994.

- J. C. GÉRARD, B. NEMRY, L. FRANÇOIS, & P. WARNANT. The internal change in atmospheric CO₂ : contribution of subtropical ecosystems? *Geophys. Res. Lett.*, 26(2):243–246, 1999.
- A. E. S. GREEN. Attenuation by ozone and the earth's albedo in the middle ultraviolet. *Appl. Opt.*, 3(2):203–208, 1964.
- K. M. GREGORY-WODZICKI. Uplift history of the Central and Northern Andes: A review. *Geol. Soc. Am. Bull.*, 112(7):1091–1105, 2000.
- K. GROSFELD, G. LOHMANN, N. RIMBU, K. FRAEDRICH, & F. LUNKEIT. Atmospheric multidecadal variations in the North Atlantic realm: proxy data, observations, and atmospheric circulation model studies. *Climate of the Past*, 3:39–50, 2007.
- G. GUYOT. *Climatologie de l'environnement*. Dunod, Paris, 1999.
- K. HABERKORN, F. SIELMANN, F. LUNKEIT, E. KIRK, A. SCHNEIDERREIT, & K. FRAEDRICH. Planet Simulator Climate. Scientific report, Meteorological Institute, University of Hamburg, Hamburg, Germany, 2009.
- S. HAGEMANN. An Improved Land Surface Parameter Dataset for Global and Regional Climate Models. Technical Report 336, Max-Planck-Institut für Meteorologie, Hamburg, 2002.
- S. HAGEMANN, M. BOTZET, L. DÜMENIL, & B. MACHENHAUER. Derivation of Global GCM Boundary Conditions From 1 km Land Use Satellite Data. Technical Report 289, Max-Planck-Institut für Meteorologie, Hamburg, 1999.
- S. HAGEMANN & A. KLEIDON. The Influence of Rooting Depth on the Simulated Hydrological Cycle of a GCM. *Phys. Chem. Earth*, 24(7):775–779, 1999.
- N. HARRIS. The elevation history of the Tibetan Plateau and its implication for the Asian monsoon. *Palaeogeogr., Palaeoclimatol., Palaeoecol.*, 241:4–15, 2006.
- S. HARRISON, P. BRACONNOT, C. HEWITT, & R. J. STOUFFER. Fourth International Workshop of the Palaeoclimate Modelling Intercomparison Project (PMIP): Launching PMIP2 Phase II. *EOS Trans. AGU*, 83:447–447, 2002.

- S. P. HARRISON, P. YU, H. TAKAHARA, & I. C. PRENTICE. Paleovegetation - Diversity of temperate plants in east Asia. *Nature*, 413:129–130, 2001.
- A. M. HAYWOOD, M. A. CHANDLER, P. J. VALDES, U. SALZMANN, D. J. LUNT, & H. J. DOWSETT. Comparison of mid-Pliocene climate predictions produced by the HadAM3 and GCMAM3 General Circulation Models. *Global Planet. Change*, 66:208–224, 2009a.
- A. M. HAYWOOD, H. J. DOWSETT, B. OTTO-BLIESNER, M.A. CHANDLER, A.M. DOLAN, D.J. HILL, D.J. LUNT, M.M. ROBINSON, N. ROSENBLUM, U. SALZMANN, & L.E. SOHL. Pliocene Model Intercomparison Project (PlioMIP): experimental design and boundary conditions (Experiment 1). *Geosci. Model Dev.*, 3:227–242, 2010.
- A. M. HAYWOOD, H. J. DOWSETT, P. J. VALDES, D. J. LUNT, J. E. FRANCIS, & B. W. SELLWOOD. Introduction. Pliocene climate, processes and problems. *Phil. Trans. R. Soc. London Ser. A*, 367:3–17, 2009b.
- A. M. HAYWOOD, B.W. SELLWOOD, & P. J. VALDES. Regional warming: Pliocene (3Ma) paleoclimate of Europe and the Mediterranean. *Geology*, 28(12):1063–1066, 2000a.
- A. M. HAYWOOD & P. J. VALDES. Modelling Pliocene warmth: contribution of atmosphere, oceans and cryosphere. *Earth Planet. Sci. Lett.*, 218:363–377, 2004.
- A. M. HAYWOOD & P. J. VALDES. Vegetation cover in a warmer world simulated using a dynamic global vegetation model for the Mid-Pliocene. *Palaeogeogr., Palaeoclimatol., Palaeoecol.*, 237:412–427, 2006.
- A. M. HAYWOOD, P. J. VALDES, & V. L. PECK. A permanent El Niño-like state during the Pliocene? *Paleoceanography*, 22:PA1213, 2007.
- A. M. HAYWOOD, P. J. VALDES, & B.W. SELLWOOD. Global scale palaeoclimate reconstruction of the middle Pliocene climate using the UKMO GCM: initial results. *Global Planet. Change*, 25:239–256, 2000b.
- J. HENDERIKS & M. PAGANI. Coccolithophore cell size and the paleogene decline in atmospheric CO₂. *Earth Planet. Sci. Lett.*, 269:575–583, 2008.
- A. HENDERSON-SELLERS. Continental Vegetation as a Dynamic Component of a Global Climate Model: A Preliminary Assessment. *Climatic Change*, 23:337–377, 1993.

- A.-J. HENROT. Etude des impacts de la végétation sur le climat à l'aide d'un modèle climatique. Master's thesis, Université de Liège, Faculté des Sciences, Licence en Sciences Physiques, 2006.
- A.-J. HENROT. Impacts des changements des propriétés de la surface terrestre sur le climat du dernier maximum glaciaire. Etude avec un modèle climatique. Master's thesis, Université de Liège, Faculté des Sciences, DEA en Sciences Spatiales, 2007.
- A.-J. HENROT, L. FRANÇOIS, , E. FAVRE, M. BUTZIN, M. OUBERDOUS, & G. MUNHOVEN. Effects of CO₂, continental distribution, topography and vegetation changes on the climate at the Middle Miocene: a model study. *Climate of the Past*, 6:675–694, 2010.
- A.-J. HENROT, L. FRANÇOIS, S. BREWER, & G. MUNHOVEN. Impacts of land surface properties and atmospheric CO₂ on the Last Glacial Maximum climate: a factor separation analysis. *Climate of the Past*, 5:183–202, 2009.
- N. HEROLD, M. SETON, R. D. MÜLLER, Y. YOU, & M. HUBER. Middle Miocene tectonic boundary conditions for use in climate models. *Geochem., Geophys., Geosyst.*, 9(10):Q10009, 2008.
- N. HEROLD, Y. YOU, R. D. MÜLLER, & M. SETON. Climate model sensitivity to change in Miocene paleotopography. *Australian Journal of Earth Sciences*, 56:1049–1059, 2009.
- C. D. HEWITT & J. F. B. MITCHELL. Radiative forcing and response of a GCM to ice age boundary conditions : cloud feedback and climate sensitivity. *Climate Dyn.*, 13:821–834, 1997.
- C. D. HEWITT, R. J. STOUFFER, A. J. BROCCOLI, J. F. B. MITCHELL, & P. VALDES. The effect of ocean dynamics in a coupled GCM simulation of the Last Glacial Maximum. *Climate Dyn.*, 20:203–218, 2003.
- D. J. HILL, A. M. HAYWOOD, R. C. A. HINDMARSH, & P. J. VALDES. Characterising ice sheets during the mid Pliocene: evidence from data and models. In M. WILLIAMS, A. M. HAYWOOD, F. J. GREGORY, & D. N. SCHMIDT, editors, *Deep Time Perspective on Climate Change: Marrying the Signal from Computer Models and Biological Proxies*, pages 517–538, Geol. Soc. of London, London, UK, 2007. Micropalaeontological Soc., Spec. Pub.
- L. R. HOLDRIDGE. Determination of World Plant Formation from Simple Climatic Data. *Science*, 105:367–368, 1947.

- B. J. HOSKINS & A. J. SIMMONS. A multi-layer spectral model and the semi-implicit method. *Quart. J. R. Meteorol. Soc.*, 101(429):637–655, 1975.
- B. HUBERT, L. FRANÇOIS, P. WARNANT, & D. STRIVAY. Stochastic generation of meteorological variables and effects on global models of water and carbon cycles in vegetation and soils. *J. Hydrol.*, 212-213(1-4):318–334, 1998.
- M. Z. JACOBSON. *Fundamentals of atmospheric modeling*. Cambridge University Press, Cambridge, UK, 2 edition, 2005.
- A. JAHN, M. CLAUSSEN, A. GANOPOLSKI, & V. BROVKIN. Quantifying the effects of vegetation dynamics on the climate of the last glacial maximum. *Climate of the Past*, 1:1–7, 2005.
- E. JANSEN, J. OVERPECK, K. R. BRIFFA, J.-C. DUPLESSY, F. JOOS, V. MASSON-DELMOTTE, D. OLAGO, B. OTTO-BLIESNER, W. R. PELTIER, S. RAHMSTORF, R. RAMESH, D. RAYNAUD, D. RIND, O. SOLOMINA, R. VILLALBA, & D. ZHANG. Palaeoclimate. In S. SOLOMON, D. QIN, M. MANNING, Z. CHEN, M. MARQUIS, K. B. AVERYT, M. TIGNOR, & H. L. MILLER, editors, *Climate Change 2007. The Physical Science Basis. Contribution of Working Group I to the Fourth Assessment Report of the Intergovernmental Panel on Climate Change*, chapter 6. Cambridge University Press, Cambridge, 2007.
- N. JIAN, S. P. HARRISON, I. C. PRENTICE, J. KUTZBACH, & S. SITCH. Impact of climate variability on present and Holocene vegetation: A model-based study. *Ecol. Model.*, 191:469–486, 2005.
- D. JIANG, H. WANG, Z. DING, X. LANG, & H. DRANGE. Modelling the middle Pliocene climate with a global atmospheric general circulation model. *J. Geophys. Res.*, 110:D14107, 2005.
- D. JIANG, H. WANG, H. DRANGE, & X. LANG. Last Glacial Maximum over China: Sensitivities of climate to paleovegetation and Tibetan ice sheet. *J. Geophys. Res.*, 108:D34102, 2003.
- G. JIMENEZ-MORENO. Progressive substitution of a subtropical forest for a temperate one during the middle Miocene climate cooling in Central Europe according to palynological data from cores Tengelic-2 and Hidas-53 (Pannonian Basin, Hungary). *Rev. Palaeobot. Palynol.*, 142:1–14, 2006.
- G. JIMENEZ-MORENO, S. FAUQUETTE, & J.-P. SUC. Vegetation, climate and palaeoaltitude reconstructions of the Eastern Alps during the Miocene

- based on pollen records from Austria, Central Europe. *J. Biogeogr.*, 35: 1638–1649, 2008.
- G. JIMENEZ-MORENO & J-P. SUC. Middle Miocene latitudinal climatic gradient in Western Europe: Evidence from pollen records. *Palaeogeogr., Palaeoclimatol., Palaeoecol.*, 253:208–225, 2007.
- A. JOST, S. FAUQUETTE, M. KAGEYAMA, G. KRINNER, G. RAMSTEIN, J.-P. SUC, & S. VIOLETTE. High resolution climate and vegetation simulations of the Late Pliocene, a model-data comparison over western Europe and the Mediterranean region. *Climate of the Past*, 5:585–606, 2009.
- A. JOST, D. LUNT, M. KAGEYAMA, A. ABE-OUCHI, O. PEYRON, P. J. VALDES, & G. RAMSTEIN. High-resolution simulations of the last glacial maximum climate over Europe : a solution to discrepancies with continental palaeoclimatic reconstructions ? *Climate Dyn.*, 24(6):577–590, 2005.
- S. JOUSSAUME & K. TAYLOR. The Paleoclimate Modeling Intercomparison Project. In P. BRACONNOT, editor, *Paleoclimate Modeling Intercomparison Project (PMIP)*, number 1007 in WMO/TD, pages 9–24. WMO, Geneva (CH), 2000. (WCRP-111).
- S. JOUSSAUME, K. E. TAYLOR, P. BRACONNOT, J. F. B. MITCHELL, J. E. KUTZBACH, S. P. HARRISON, I. C. PRENTICE, A. J. BROCCOLI, A. ABE-OUCHI, P. J. BARTLEIN, C. BONFILS, B. DONG, J. GUIOT, K. HERTERICH, C. D. HEWITT, D. JOLLY, J. W. KIM, A. KISLOV, A. KITOH, M. F. LOUTRE, V. MASSON, B. MCAVANEY, N. MCFARLANE, N. DE NOBLET, W. R. PELTIER, J. Y. PETERSCHMITT, D. POLLARD, D. RIND, J. F. ROYER, M. E. SCHLESINGER, J. SYKTUS, & S. THOMPSON. Monsoon changes for 6000 years ago : Results of 18 simulations from the Paleoclimate Modeling Intercomparison Project (PMIP). *Geophys. Res. Lett.*, 26(7):859–862, 1999.
- J. H. JUNGCLAUS, N. KEENLYSIDE, M. BOTZET, H. HAAK, J.-J. LUO, M. LATIF, U. MAROTZKE, U. MIKOLAJEWICZ, & E. ROECKNER. Ocean circulation and tropical variability in the coupled model ECHAM5/MPI-OM. *J. Climate*, 19:3952–3972, 2006.
- M. M. JUNGE, F. LUNKEIT, K. FRAEDRICH, V. GAYLER, R. BLENDER, & U. LUKSCH. Atmospheric multidecadal variations in the North Atlantic realm: proxy data, observations, and atmospheric circulation model studies. *Climate Dyn.*, 24:297–307, 2005.

- R. J. G. KAANDORP, H. B. VONHOF, F. P. WESSELINGH, L. ROMERO PITTMAN, D. KROONA, & J. E. VAN HINTE. Seasonal Amazonian rainfall variation in the Miocene Climate Optimum. *Palaeogeogr., Palaeoclimatol., Palaeoecol.*, 221:1–6, 2005.
- M. KAGEYAMA, A. LAÏNÉ, A. ABE-OUCHI, P. BRACONNOT, E. CORTIJO, M. CRUCIFIX, A. DE VERNAL, J. GUIOT, C. D. HEWITT, A. KITOH, M. KUCERA O. MARTI, R. OHGAI, B. OTTO-BLIESNER, W. R. PELTIER, A. ROSELL-MELÉ, G. VETTORETTI, S. L. WEBER, Y. YU, & MARGO PROJECT MEMBERS. Last Glacial Temperatures over the North Atlantic, Europe and western Siberia : a comparison between PMIP models, MARGO sea-surface temperatures and pollen-based reconstructions. *Quat. Sci. Rev.*, 25:2082–2102, 2006.
- M. KAGEYAMA, O. PEYRON, S. PINOT, P. TARASOV, J. GUIOT, S. JOUSSAUME, & G. RAMSTEIN. The Last Glacial Maximum climate over Europe and western Siberia : a PMIP comparison between models and data. *Climate Dyn.*, 17:23–43, 2001.
- M. KAGEYAMA & P. J. VALDES. Impacts of the North American ice-sheet orography on the Last Glacial Maximum eddies and snowfall. *Geophys. Res. Lett.*, 27:1515–1518, 2000.
- E. KALNAY, M. KANAMITSU, R. KISTLER, W. COLLINS, D. DEAVEN, L. GANDIN, M. IREDELL, S. SAHA, G. WHITE, J. WOOLLEN, Y. ZHU, A. LEETMAA, B. REYNOLDS, M. CHELLIAH, W. EBISUZAKI, W. HIGGINS, J. JANOWIAK, K. C. MO, C. ROPELEWSKI, J. WANG, R. JENNE, & D. JOSEPH. The NCEP/NCAR 40-year reanalysis project. *Bull. Am. Meteorol. Soc.*, 77(3):437–471, 1996.
- J. O. KAPLAN. *Geophysical application of vegetation modelling*. PhD thesis, University of Lund, Lund, 2001.
- S.-J. KIM, G. M. FLATO, & G. J. BOER. A coupled climate model simulation of the Last Glacial Maximum, Part 2: approach to equilibrium. *Climate Dyn.*, 20:635–661, 2003.
- A. KLEIDON & M. HEIMANN. Optimised rooting depth and its impacts on the simulated climate of an atmospheric general circulation model. *Geophys. Res. Lett.*, 25(3):345–348, 1998.
- W. KÖPPEN. *Die Klimate des Erde*. Walter de Gruyter, Berlin, 1923.

- C. KUBATZKI & M. CLAUSSEN. Simulation of the global biogeophysical interactions during the Last Glacial Maximum. *Climate Dyn.*, 14:461–471, 1998.
- M. KUCERA, A. ROSELL-MELÉ, R. SCHNEIDER, C. WAELBROECK, & M. WEINELT. Multiproxy approach for the reconstruction of the glacial ocean surface (MARGO). *Quat. Sci. Rev.*, 24:813–819, 2005.
- J. KUHLEMANN, I. DUNKL, A. BRÜGEL, C. SPIEGEL, & W. FRISCH. From source terrains of the Eastern Alps to the Molasse Basin: Detrital record of non-steady-state exhumation. *Tectonophysics*, 413:301–316, 2006.
- H. L. KUO. On formation and intensification of tropical cyclones through latent heat release by cumulus convection. *J. Atmos. Sci.*, 22(1):40–63, 1965.
- H. L. KUO. Further studies of the parametrization of the influence of cumulus convection on large-scale flow. *J. Atmos. Sci.*, 31(5):1232–1240, 1974.
- W. M. KÜRSCHNER, J. VAN DER BURGH, H. VISSCHER, & D. L. DILCHER. Oak leaves as biosensors of late Neogene and early Pleistocene paleoatmospheric CO₂ concentrations. *Mar. Micropaleontol.*, 27(1/4):299–312, 1996.
- W. M. KÜRSCHNER, Z. KVACEK, & D. L. DILCHER. The impact of Miocene atmospheric carbon dioxide fluctuations on climate and the evolution of terrestrial ecosystems. *PNAS*, 105(2):449–453, 2008.
- J. E. KUTZBACH, W. F. RUDDIMAN, & W. L. PRELL. Sensitivity of Climate to late Cenozoic Uplift in Southern Asia and the American West: Numerical Experiments. *J. Geophys. Res.*, 94(15):393–407, 1989.
- A. A. LACIS & J. E. HANSEN. A parameterization for the absorption of solar radiation in the Earth's atmosphere. *J. Atmos. Sci.*, 31:118–133, 1974.
- J.-M. LAURENT, A. BAR-BEN, L. FRANÇOIS, M. GHISLAIN, & R. CHEDDADI. Refining vegetation simulation models. From plant functional types to bioclimatic affinity groups of plants. *J. Vegetation Sci.*, 15:739–746, 2004.
- J.-M. LAURENT, L. FRANÇOIS, A. BAR-HEN, L. BEL, & R. CHEDDADI. European Bioclimatic Affinity Groups: data-model comparisons. *Global Planet. Change*, 61:28–40, 2008.
- L. LAURSEN & E. ELISASEN. On the effect of the damping mechanism in an atmospheric general circulation model. *Tellus*, 41:385–400, 1989.

- H. LE TREUT, R. SOMERVILLE, U. CUBASCH, Y. DING, C. MAURITZEN, A. MOKSSIT, T. PETERSON, & M. PRATHER. Historical Overview of Climate Change. In S. SOLOMON, D. QIN, M. MANNING, Z. CHEN, M. MARQUIS, K. B. AVERYT, M. TIGNOR, & H. L. MILLER, editors, *Climate Change 2007. The Physical Science Basis. Contribution of Working Group I to the Fourth Assessment Report of the Intergovernmental Panel on Climate Change*, chapter 1. Cambridge University Press, Cambridge, 2007.
- R. LEEMANS & W. CRAMER. The IIASA database for mean monthly values of temperature, precipitation and cloudiness on a global terrestrial grid. IIASA-report RR-91-18, International Institute for Applied Systems Analysis, 1991.
- S. LEROY & L. DUPONT. Development of vegetation and continental aridity in northwestern Africa during the Late Pliocene: the pollen record of ODP site 658. *Palaeogeogr., Palaeoclimatol., Palaeoecol.*, 109:295–316, 1994.
- S. LEVIS, G. B. BONAN, M. VERTENSTEIN, & K. W. OLESON. The Community Land Model's Dynamic Global Vegetation Model (CLM-DGVM): Technical description and user's guide. Technical Report NCAR/TN-459+IA, Terrestrial Sciences Section, Climate and Global Dynamics Division, 2004.
- S. LEVIS, J. A. FOLEY, & D. POLLARD. CO₂, climate and vegetation feedbacks at the Last Glacial Maximum. *J. Geophys. Res.*, 104(24):31191–31198, 1999.
- S. LEVIS, J. A. FOLEY, & D. POLLARD. Large scale vegetation feedbacks on a doubled CO₂ climate. *J. Climate*, 13:1313–1325, 2000.
- L. LIU, J. T. ERONEN, & M. FORTELIUS. Significant mid-latitude aridity in the middle Miocene of East Asia. *Palaeogeogr., Palaeoclimatol., Palaeoecol.*, 279:201–206, 2009.
- J. F. LOUIS. A parametric model of vertical eddy fluxes. *Bound. Layer Meteor.*, 17:187–202, 1979.
- W. LUCHT, I. C. PRENTICE, R. B. MYNENI, S. SITCH, P. FRIEDLINGSTEIN, W. CRAMER, P. BOUSQUET, W. BUERMANN, & B. SMITH. Climatic control of the high-latitude vegetation greening trend and Pinatubo effect. *Science*, 296:1687–1689, 2002.

- W. LUCHT, S. SCHAPHOFF, T. ERBRECHT, U. HEYDER, & W. CRAMER. Terrestrial vegetation redistribution and carbon balance under climate change. *Carbon Balance and Management* 1, 6, 2006.
- F. LUNKEIT, M. BÖTTINGER, K. FRAEDRICH, H. JANSEN, E. KIRK, A. KLEIDON, & U. LUKSCH. Planet Simulator Reference Manual Version 15.0. Technical report, Meteorologisches Institut, Universität Hamburg, Hamburg, 2007.
- D. J. LUNT, P. J. VALDES, A. HAYWOOD, & I. C. RUTT. Closure of the Panama Seaway during the Pliocene: implications for climate and Northern Hemisphere glaciation. *Climate Dyn.*, 30:1–18, 2008.
- J. LYNCH-STIEGLITZ, J.F. ADKINS, W.B. CURRY, T. DOKKEN, I.R. HALL, J.C. HERGUERA, J.J.-M. HIRSCHI, E.V. IVANOVA, C. KISSEL, O. MARCHAL, T.M. MARCHITTO, I.N. MCCAVE, J. MCMANUS, S. MULITZA, U. NINNEMANN, F. PEETERS, E.-F. YU, & R. ZAHN. Atlantic Meridional Overturning Circulation during the Last Glacial Maximum. *Science*, 316:66–69, 2007.
- E. MAIER-REIMER, U. MIKOLAJEWICZ, & K. HASSELMANN. Mean circulation of the Hamburg LSG OGCM and its sensitivity to the thermohaline surface forcing. *J. Phys. Oceanog.*, 23:731–757, 1993.
- S. MANABE. Climate and ocean circulation. I. The atmospheric circulation and the hydrology of the earth's surface. *Mon. Wea. Rev.*, 97:739–774, 1969.
- S. MANABE & A. J. BROCCOLI. The influence of Continental Ice Sheets on the Climate of an Ice Age. *J. Geophys. Res.*, 90(1):2167–2190, 1985.
- B. G. MARK, S.P. HARRISON, A. SPESSA, M. NEW, D.J.A. EVANS, & K.F. HELMENS. Tropical snowline changes at the Last Glacial Maximum: A global assessment. *Quaternary International*, 138–139:168–201, 2005.
- H. A. MARTIN. Cenozoic climatic change and the development of the arid vegetation in Australia. *J. Arid. Environ.*, 66:533–563, 2006.
- P. J. MASON. The formation of areally-averaged roughness lengths. *Quart. J. R. Meteorol. Soc.*, 114:399–420, 1988.
- J. M. MELILLO, A. D. MCGUIRE, D. W. KICKLIGHTER, B. MOORE, C. J. VOROSMARTY, & A. L. SCHLOSS. Global climate change and terrestrial net primary production. *Nature*, 363:234–235, 1993.

- A. MICHEELS, A. BRUCH, & V. MOSBRUGGER. Miocene climate modelling sensitivity experiments for different CO₂ concentrations. *Palaeontologia Electronica*, 12(2), 2009a.
- A. MICHEELS, J. ERONEN, & V. MOSBRUGGER. The Late Miocene climate response to a modern Sahara desert. *Global Planet. Change*, 67:193–204, 2009b.
- Y. MINTZ & G. WALKER. Global fields of soil moisture and surface evapotranspiration derived from observed precipitation and surface air temperature. *J. Appl. Meteorol.*, 32:185–188, 1993.
- V. MOSBRUGGER & T. UTESCHER. The coexistence approach—a method for quantitative reconstructions of Tertiary terrestrial palaeoclimate data using plant fossils. *Palaeogeogr., Palaeoclimatol., Palaeoecol.*, 134:61–86, 1997.
- V. MOSBRUGGER, T. UTESCHER, & D. L. DILCHER. Cenozoic continental climatic evolution of Central Europe. *PNAS*, 102(42):14964–14969, 2005.
- G. MYHRE, E. J. HIGHWOOD, K. P. SHINE, & F. STORDAL. New estimates of radiative forcing due to well mixed greenhouse gases. *Geophys. Res. Lett.*, 25(14):2715–2718, 1998.
- T. NAISH, R. POWELL, R. LEVY, G. WILSON, R. SCHERER, F. TALARICO, L. KRISSEK, F. NIESSEN, M. POMPILIO, T. WILSON, L. CARTER, R. DE-CONTO, P. HUYBERS, R. MACKAY, D. POLLARD, J. ROSS, D. WINTER, P. BARETT, G. BROWNE, & R. CODY. Obliquity-paced Pliocene West Antarctic ice sheet oscillation. *Nature*, 458:322–328, 2009.
- R. R. NEMANI, C. D. KEELING, H. HASHIMOTO, W. M. JOLLY, S. C. PIPER, C. J. TUCKER, R. B. MYNENI, & S. W. RUNNING. Climate-driven increases in global terrestrial net primary production from 1982 to 1999. *Science*, 300:1560–1563, 2003.
- B. NEMRY, L. M. FRANÇOIS, P. WARNANT, F. ROBINET, & J.-C. GÉRARD. The seasonality of the CO₂ exchange between the atmosphere and the land biosphere : A study with a global mechanistic vegetation model. *J. Geophys. Res.*, 101(D3):7111–7125, 1996.
- M. NEW, D. LISTER, M. HULME, & I. MAKIN. A high-resolution data set of surface climate over global land areas. *Clim. Res.*, 21:1–25, 2002.

- M. NOTARO, Z. LIU, R. GALLIMORE, S. J. VAVRUS, J. E. KUTZBACH, I. C. PRENTICE, & R. L. JACOB. Simulated and Observed Preindustrial to Modern Vegetation and Climate Changes. *J. Climate*, 18:3650–3671, 2005.
- Y. M. OKUMURA, C. DESER, A. HU, A. TIMMERMANN, & S-P. XIE. North Pacific Climate Response to Freshwater Forcing in the Subarctic North Atlantic: Oceanic and Atmospheric Pathways. *J. Climate*, 22:1424–1445, 2009.
- J. D. OPSTEEGH, R. J. HAARSMA, F. M. SELTEN, & A. KATTENBERG. ECBilt: A dynamic alternative to mixed boundary conditions in ocean models. *Tellus*, 50:348–367, 1998.
- S. A. ORSZAG. Transform method for the calculation of vector-coupled sums : Application to the spectral form of the vorticity equation. *J. Atmos. Sci.*, 27(6):890–895, 1970.
- D. OTTO, D. RASSE, J. KAPLAN, P. WARNANT, & L. FRANÇOIS. Biospheric carbon stocks reconstructed at the Last Glacial Maximum : comparison between general circulation models using prescribed and computed sea surface temperatures. *Global Planet. Change*, 33(2-3):117–138, 2002.
- M. PAGANI, M. A. ARTHUR, & K. H. FREEMAN. Miocene evolution of atmospheric carbon dioxide. *Paleoceanography*, 14(3):273–292, 1999.
- M. PAGANI, L. ZHONGHUI, J. LARIVIERE, & A. C. RAVELO. High Earth-system climate sensitivity determined from Pliocene carbon dioxide concentrations. *Nature Geoscience*, 3:27–30, 2010.
- K. A. PATTERSON. Global distributions of total and total-available soil water-holding capacities. Master's thesis, University of Delaware, Newark, DE, USA, 1990.
- P. N. PEARSON & M. R. PALMER. Atmospheric carbon dioxide concentrations over the past 60 million years. *Nature*, 406(6797):695–699, 2000.
- P. N. PEARSON, B. E. VAN DONGEN, C. J. NICHOLAS, R. D. PANCOST, S. SCHOUTEN, J. M. SINGANO, & B. S. WADE. Stable warm tropical climate through the Eocene Epoch. *Geology*, 35(3):211–214, 2007.
- T. F. PEDERSEN, R. FRANÇOIS, L. FRANÇOIS, K. D. ALVERSON, & J. MC-MANUS. The Late Quaternary History of Biogeochemical Cycling of Carbon. In K. D. ALVERSON, R. S. BRADLEY, & T. F. PEDERSEN, edi-

- tors, *Paleoclimate, Global Change and the Future*, chapter 4, pages 63–78. Springer-Verlag, Berlin, Germany, 2003.
- S. F. PEKAR & R. M. DECONTO. High-resolution ice-volume estimates for the early Miocene: Evidence for a dynamic ice sheet in Antarctica. *Palaeogeogr., Palaeoclimatol., Palaeoecol.*, 231(1-2):101–109, 2006.
- W. R. PELTIER. Global glacial isostasy and the surface of the ice-age earth : the ICE-5G (VM2) model and GRACE. *Annu. Rev. Earth Planet. Sci.*, 32:49–111, 2004.
- J.-R. PETIT, J. JOUZEL, D. RAYNAUD, N. I. BARKOV, J.-M. BARNOLA, I. BASILE, M. BENDER, J. CHAPPELLAZ, M. DAVIS, G. DELAYGUE, M. DELMOTTE, V. M. KOTLYAKOV, M. LEGRAND, V. Y. LIPENKOV, C. LORIUS, L. PÉPIN, C. RITZ, E. SALTZMAN, & M. STIEVENARD. Climate and atmospheric history of the past 420,000 years from the Vostok ice core, Antarctica. *Nature*, 399:429–436, 1999.
- V. PETOUKHOV, A. GANOPOLSKI, V. BROVKIN, M. CLAUSSEN, A. ELISEEV, C. KUBATZKI, & S. RAHMSTORF. CLIMBER-2: A climate system model of intermediate complexity. *Climate Dyn.*, 16:1–17, 2000.
- E. PICKETT, S. P. HARRISON, G. HOPE, K. HARLE, J. R. DODSON, A. P. KERSHAW, I. C. PRENTICE, J. BACKHOUSE, E. A. COLHOUN, D. D’COSTA, J. FLENLEY, J. GRINDROD, S. HABERLE, C. HASSELL, C. KENYON, M. MACPHAIL H. MARTIN, A. H. MARTIN, M. MCKENZIE, J. C. NEWSOME, D. PENNY, J. POWELL, I. RAINE, W. SOUTHERN, J. SUTRA, I. THOMAS, S. VAN DER KAARS, & J. WARD. Pollen-based reconstructions of biome distributions for Australia, South East Asia and the Pacific (SEAPAC region) at 0, 6000 and 18,000 14c yr B.P. *J. Biogeogr.*, 31:1381–1444, 2004.
- A. J. PITMAN, Z. L. YANG, J. C. COGLEY, & A. H. SELLERS. Description of bare essentials of surface transfer for the Bureau of Meteorology Research Center AGCM. BMRC Research Report, Bureau of Meteorology Research Center, Melbourne, Australia, 1991.
- C. PRENTICE, J. GUIOT, B. HUNTLEY, D. JOLLY, & R. CHEDDADI. Reconstructing biomes from palaeoecological data: a general method and its application to european pollen data at 0 and 6 ka. *Climate Dyn.*, 12: 185–194, 2000a.

- I. C. PRENTICE, J. GUIOT, & S. P. HARRISON. Mediterranean vegetation, lake levels and palaeoclimate at the Last Glacial Maximum. *Nature*, 360: 658–660, 1992.
- I. C. PRENTICE, D. JOLLY, & BIOME 6000 PARTICIPANTS. Mid-Holocene and glacial-maximum vegetation geography of the northern continents and Africa. *J. Biogeogr.*, 27(3):507–519, 2000b.
- G. RAMSTEIN, M. KAGEYAMA, J. GUIOT, H. WU, C. HÉLY, G. KRINNER, & S. BREWER. How cold was Europe at the Last Glacial Maximum? a synthesis of the progress achieved since the first PMIP model-data comparison. *Climate of the Past*, 3:331–339, 2007.
- M. E. RAYMO, B. GRANT, M. HOROWITZ, & G. H. RAU. Mid-Pliocene warmth: Stronger greenhouse and stronger conveyor. *Mar. Micropaleontol.*, 27:313–326, 1996.
- H. RENNSSEN, V. BROVKIN, T. FICHEFET, & H. GOOSSE. Holocene climate instability during the termination of the African Humid Period. *Geophys. Res. Lett.*, 30(4):1184, 2003.
- G. J. RETALLACK. Middle Miocene fossil plants from Fort Ternan (Kenia) and evolution of African grasslands. *Paleobiology*, 18(4):383–400, 1992.
- G. J. RETALLACK. Refining a pedogenic-carbonate CO₂ paleobarometer to quantify a middle Miocene greenhouse spike. *Palaeogeogr., Palaeoclimatol., Palaeoecol.*, 281(2):57–65, 2009.
- R. W. REYNOLDS & T. M. SMITH. A high resolution global sea surface temperature climatology. *J. Climate*, 8:1571–1583, 1995.
- D. RIND. Components of the Ice Age Circulation. *J. Geophys. Res.*, 92(4): 4241–4281, 1987.
- D. RIND & M. CHANDLER. Increased ocean heat transports and warmer climate. *J. Geophys. Res.*, 96:7437–7461, 1991.
- A. J. ROBERT. A stable numerical integration scheme for the primitive meteorological equations. *Atmos. Ocean*, 19:35–46, 1981.
- M. M. ROBINSON, H. J. DOWSETT, G. S. DWYER, & K. T. LAWRENCE. Reevaluation of mid-Pliocene North Atlantic sea surface temperatures. *Paleoceanography*, 23:1–9, 2008.

- E. ROECKNER, K. ARPE, & L. BENGTSSON. Simulation of present-day climate with the ECHAM model: Impact of model physics and resolution. Tech. rep. 93, Max-Planck Institute, Hamburg, Germany, 1992.
- E. ROECKNER, K. ARPE, L. BENGTSSON, M. CHRISTOPH, M. CLAUSSEN, L. DUMENIL, M. ESCH, M. GIORGETTA, & U. SCHLESE. The atmospheric general circulation model ECHAM4: model description and simulation of present day climate. Technical Report 218, Max-Planck-Institut für Meteorologie, Hamburg, 1996.
- E. ROECKNER, G. BÄUML, L. BONAVENTURA, R. BROKOPF, M. ESCH, M. GIORGETTA, S. HAGEMANN, I. KIRCHNER, L. KORNBUEH, E. MANZINI, A. RHODIN, U. SCHLESE, U. SCHULZWEIDA, & A. TOMPKINS. The atmospheric general circulation model ECHAM5. part I : Model description. Technical Report 349, Max-Planck-Institut für Meteorologie, Hamburg, 2003.
- V. ROMANOVA, G. LOHMANN, & K. GROSFELD. Effect of land albedo, CO₂, orography, and oceanic heat transport on extreme climates. *Climate of the Past*, 2:31–42, 2006.
- W. F. RUDDIMAN, editor. *Tectonic Uplift and Climate Change*. Plenum Press, New York, NY, 1997.
- U. SALZMANN, A. M. HAYWOOD, D.J. LUNT, P. J. VALDES, & D.J. HILL. A new Global Biome Reconstruction and Data-Model Comparison for the middle Pliocene. *Global Ecol. Biogeogr.*, 17:432–447, 2008.
- T. SASAMORI. The radiative cooling calculation for application to general circulation experiments. *J. Appl. Meteorol.*, 7(5):721–729, 1968.
- R. SAUSEN, S. SCHUBERT, & L. DÜMENIL. A model of river runoff for use in coupled atmosphere-ocean models. *J. Hydrol.*, 155:337–352, 1994.
- K. EK SAXTON, W. J. RAWLS, J. S. ROMBERGER, & R. I. PAPENDICK. Estimating generalized soil-water characteristics from texture. *Soil Sci. Soc. Am. J.*, 50:1031–1036, 1986.
- H. J. SCHENK & R. B. JACKSON. The global biogeography of roots. *Ecol. Monogr.*, 72(3):311–328, 2002.
- B. SCHNEIDER & A. SCHMITTNER. Simulating the impact of the panamanian seaway closure on ocean circulation, marine productivity and nutrient cycling. *Earth Planet. Sci. Lett.*, 246:367–380, 2006.

- T. SCHNEIDER VON DEIMLING, A. GANOPOLSKI, & H. HELD. How cold was the Last Glacial Maximum? *Geophys. Res. Lett.*, 33:L14709, 2006.
- A. J. SEMTNER. A model for the thermodynamic growth of sea ice in numerical investigations of climates. *J. Phys. Oceanog.*, 6:379–389, 1976.
- C. J. SHELLITO, L. C. SLOAN, & M. HUBER. Climate model sensitivity to atmospheric CO₂ levels in the Early-Middle Paleogene. *Palaeogeogr., Palaeoclimatol., Palaeoecol.*, 193(1):113–123, 2003.
- A. J. SIMMONS, B. J. HOSKINS, & D. BURRIDGE. Stability of the semi-implicit method of time integration. *Mon. Wea. Rev.*, 106(3):405–412, 1978.
- S. SITCH, B. SMITH, I. C. PRENTICE, A. ARNETH, A. BONDEAU, W. CRAMER, J. O. KAPLAN, S. LEVIS, W. LUCHT, M. T. SYKES, K. THONICKE, & S. VENEVSKY. Evaluation of ecosystems dynamics, plant geography and terrestrial carbon cycling in the LPJ Dynamic Global Vegetation Model. *Global Change Biol.*, 9:161–185, 2003.
- A. SLINGO & M. SLINGO. Response of the National Center for Atmospheric Research community climate model to improvements in the representation of clouds. *J. Geophys. Res.*, 96:341–357, 1991.
- L.C. SLOAN, T.J. CROWLEY, & D. POLLARD. Modelling of middle Pliocene climate with the NCAR GENESIS general circulation model. *Mar. Micropaleontol.*, 27:57–61, 1996.
- A. SLUIJS, G. J. BOWEN, H. BRINKHUIS, L. J. LOURENS, & E. THOMAS. The Paleocene-Eocene Thermal Maximum super greenhouse: Biotic and geochemical signatures, age models and mechanisms of global change. In M. WILLIAMS, A. M. HAYWOOD, J. GREGORY, & D. N. SCHMIDT, editors, *Deep-time perspectives on climate change: Marrying the signal from computer models and biological proxies*, pages 267–293, Geol. Soc. of London, London, UK, 2007. Micropalaeontological Soc., Spec. Pub.
- L. E. SOHL, M. A. CHANDLER, R. B. SCHMUNK, K. MANKOFF, J. A. JONAS, K. M. FOLEY, & H. J. DOWSETT. PRISM3/GISS topographic reconstruction. *U. S. Geological Survey Data Series*, 419:6p., 2009.
- U. STEIN & P. ALPERT. Factor separation in numerical simulations. *J. Atmos. Sci.*, 50(14):2107–2115, 1993.

- G. L. STEPHENS. The parametrization of radiation for numerical weather prediction and climate models. *Mon. Wea. Rev.*, 112(4):826–867, 1984.
- C. A. E. STRÖMBERG. The origin and spread of grass-dominated ecosystems in the late Tertiary of North America: preliminary results concerning the evolution of hypsodonty. *Palaeogeogr., Palaeoclimatol., Palaeoecol.*, 177: 59–75, 2002.
- J. SUN & Z. ZHANG. Palynological evidence for the Mid-Miocene Climatic Optimum recorded in Cenozoic sediments of the Tian Shan Range, north-western China. *Global Planet. Change*, 64:53–68, 2008.
- Q.-G. SUN, M. E. COLLINSON, C.-S. LI, Y.-F. WANG, & D. J. BEERLING. Quantitative reconstruction of palaeoclimate from the Middle Miocene Shanwang flora, eastern China. *Palaeogeogr., Palaeoclimatol., Palaeoecol.*, 180:315–329, 2002.
- G. THOMAS & P. R. ROWNTREE. The boreal forests and climate. *Q. J. R. Meteorol. Soc.*, 118:496–497, 1992.
- R. S. THOMPSON & R. F. FLEMING. Middle Pliocene vegetation: reconstructions, paleoclimatic inferences, and boundary conditions for climate modelling. *Mar. Micropaleontol.*, 27:27–49, 1996.
- J. A. TONG, Y. YOU, R. D. MÜLLER, & M. SETON. Climate model sensitivity to atmospheric CO₂ concentrations for the middle Miocene. *Global Planet. Change*, 67:129–140, 2009.
- P. TSCHUCK, F. CHAUVIN, B. DONG, & K. ARPE. Impact of sea-surface temperature anomalies in the Equatorial Indian Ocean and Western Pacific on the Asian summer monsoon in three general circulation models. *International Journal of Climatology*, 24(2):181–191, 2004.
- T. UTESCHER, B. ERDEI, L. FRANÇOIS, & V. MOSBRUGGER. Tree diversity in the Miocene forests of Western Eurasia. *Palaeogeogr., Palaeoclimatol., Palaeoecol.*, 253:226–250, 2007.
- T. UTESCHER, V. MOSBRUGGER, & A.R. ASHRAF. Terrestrial climate evolution in Northwest Germany over the last 25 million years. *Palaeogeogr., Palaeoclimatol., Palaeoecol.*, 15(5):430–449, 2000.
- J. A. VAN DAM. Geographic and temporal patterns in the late Neogene (12–3 Ma) aridification of Europe. the use of small mammals as paleoprecipitation proxies. *Palaeogeogr., Palaeoclimatol., Palaeoecol.*, 238:190–218, 2006.

- A. VON DER HEYDT & H. A. DIJKSTRA. Effect of ocean gateways on the global ocean circulation in the late Oligocene and early Miocene. *Paleoceanography*, 21:PA1011, 2006.
- A. VON DER HEYDT & H. A. DIJKSTRA. The effect of ocean gateways on ocean circulation patterns in the Cenozoic. *Global Planet. Change*, 62: 132–146, 2008.
- Y. WANG, T. DENG, & D. BIASATTI. Ancient diets indicate significant uplift of southern Tibet after ca. 7 Ma. *Geology*, 34(4):309–312, 2006.
- P. WARNANT. *Modélisation du cycle du carbone dans la biosphère continentale à l'échelle globale*. PhD thesis, Université de Liège, Liège, 1999. (In French.).
- P. WARNANT, L. M. FRANÇOIS, D. STRIVAY, & J.-C. GÉRARD. CARAIB : A global model of terrestrial biological productivity. *Global Biogeochem. Cycles*, 8(3):255–270, 1994.
- S. L. WEBER, S.S. DRIJFHOUT, A. ABE-OUCHI, M. CRUCIFIX, M. EBY, A. GANOPOLSKI, S. MURAKAMI, B. OTTO-BLIESNER, & W.R. PELTIER. The modern and glacial overturning circulation in the Atlantic ocean in PMIP coupled model simulations. *Climate of the Past*, 3:51–64, 2007.
- P. WETZEL, E. MAIER-REIMER, M. BOTZET, J. H. JUNGCLAUS, N. KEENLYSIDE, & M. LATIF. Effects of ocean biology on the penetrative radiation in a coupled climate model. *J. Climate*, 19:3973–3987, 2006.
- J. M. WHITE, T. A. AGER, D. P. ADAM, E. B. LEOPOLD, G. LIU, H. JETTÉ, & C. E. SCHWEGER. An 18 million year record of vegetation and climate change in northwestern Canada and Alaska: tectonic and global climatic correlates. *Palaeogeogr., Palaeoclimatol., Palaeoecol.*, 130: 293–306, 1997.
- V. M. VAN WIJK, S. DEKKER, W. BOUTEN, F. BOSVELD, W. KOHSIEK, K. KRAMER, & G. MOHREN. Modeling daily gas exchange of a douglas-fir forest : comparison of three stomatal conductance models with and without a soil water stress function. *Tree Physiol.*, 20:115–122, 2000.
- J. W. WILLIAMS, T. WEBB III, P. H. RICHARD, & P. NEWBY. Late quaternary biomes of Canada and the eastern United States. *J. Biogeogr.*, 27(3):585–607, 2000.

- M. WILLIAMS, A. M. HAYWOOD, S. P. TAYLOR, P. J. VALDES, B. W. SELLWOOD, & C. D. HILLENBRAND. Evaluating the efficacy of planktonic foraminifer calcite $\delta^{18}\text{O}$ data for sea surface temperature reconstruction for the Late Miocene. *Geobios*, 38(6):843–863, 2005.
- F. I. WOODWARD, M. R. LOMAS, & C. K. KELLY. Global climate and the distribution of plant biomes. *Phil. Trans. R. Soc. London Ser. B*, 359: 1465–1476, 2004.
- H. WU, J. GUIOT, S. BREWER, & Z. GUO. Climatic changes in Eurasia and Africa at the last glacial maximum and mid-Holocene: reconstruction from pollen data using inverse vegetation modelling. *Climate Dyn.*, 29: 211–229, 2007.
- U. WYPUTTA & B. J. MCAVENEY. Influence of vegetation changes during the Last Glacial Maximum using the BMRC atmospheric general circulation model. *ClimateDyn*, 17:923–932, 2001.
- W. YANASE & A. ABE OUCHI. The LGM surface climate and atmospheric circulation over East Asia and the North Pacific in the PMIP2 coupled model simulations. *Climate of the Past*, 3:439–451, 2007.
- Y. YOU, M. HUBER, R. D. MÜLLER, C. J. POULSEN, & J. RIBBE. Simulation of the Middle Miocene Climate Optimum. *Geophys. Res. Lett.*, 36 (4):L04702, 2009.
- J. ZACHOS, M. PAGANI, L. SLOAN, E. THOMAS, & K. BILLUPS. Trends, rhythms and aberrations in global climate 65 Ma to present. *Science*, 292 (5517):686–693, 2001.
- L. ZHOU, R. K. KAUFMANN, Y. TIAN, R. B. MYNENI, & C. J. TUCKER. Relation between interannual variations in satellite measures of northern forest greenness and climate between 1982 and 1999. *J. Geophys. Res.*, 108:4004, 2003.